Prediction and optimization of the mechanical and thermal properties of bio-based concrete : analytical and numerical multi-scale approaches.

Gang Huang

Université Fédérale
Toulouse Midi-Pyrénées

THÈSE

En vue de l'obtention du
DOCTORAT DE L'UNIVERSITÉ DE TOULOUSE

Délivré par l'Institut National des Sciences Appliquées de Toulouse

Présentée et soutenue par

Gang HUANG

Le 17 mai 2023

Prédiction et optimisation des propriétés mécaniques et thermiques des bétons biosourcés : approches multi-échelles analytiques et numériques.

Ecole doctorale : **MEGEP - Mécanique, Energétique, Génie civil, Procédés**

Spécialité : **Génie civil**

Unité de recherche :
LMDC - Laboratoire Matériaux et Durabilité des Constructions de Toulouse

Thèse dirigée par
Sandrine GEOFFROY et Ariane ABOU CHAKRA

Jury

M. Frédéric GRONDIN, Rapporteur
M. Farid BENBOUDJEMA, Rapporteur
M. Thibaut LECOMPTE, Examinateur
Mme Sandrine GEOFFROY, Directrice de thèse
M. Joseph ABSI, Directeur de thèse
Mme Ariane ABOU CHAKRA, Co-directrice de thèse

Abstract

Energy consumption and carbon emissions are challenging the current construction industry. The development of sustainable building materials has thus become increasingly crucial, given the high environmental impact of traditional construction materials, such as cement and ordinary concrete. Bio-based concrete has emerged as a promising solution to alleviate these issues due to high insulation performance and sustainability. This material recycles agricultural waste as aggregates and addresses the negative effects of waste accumulation and incineration. Multiscale modeling has advantages in studying the connection between microstructure and macroscopic performance. However, current models are unable to meet the complex structural characteristics of bio-based concrete.

In this study, we developed a novel homogenization model based on multi-scale structural features to predict, evaluate, and optimize the mechanical and thermal properties of a wide range of bio-based concretes. The proposed model considers various factors, including the volume fraction of each phase, the shape and orientation of bio-aggregates, different pore sizes, moisture, and imperfect contact. To validate the model, we conducted a series of verifications at different scales, working conditions, and sources of bio-aggregates. The intercomparison shows a good agreement between the analytical, numerical, and experimental data.

Next, we used the verified model for parametric analysis to quantify the effect of structural features on macroscopic performance. While all the factors mentioned above have an influence on the concrete properties, the effects on the mechanical and thermal behaviors may be reversed. For instance, increasing the volume fraction of bio-aggregate reduces the mechanical performance but increases the thermal insulation. Moreover, the type of binder and the moisture have a strong influence on the mechanical properties and the thermal insulation, respectively, while the volume fraction of bio-aggregates has a significant effect on both. Also, the anisotropy of bio-based concrete is not negligible due to orientation, shape, pore distribution, and imperfect contact. Additionally, the influence of bio-aggregate shape decreases with aspect ratio, but it also depends on volume fraction, orientation, moisture, etc. Therefore, evaluating and optimizing the performance of bio-based concrete requires systematic and comprehensive work.

Finally, we combined models of mechanical and thermal behavior to optimize the comprehensive performance of bio-based concrete through a multi-objective optimization approach, in order to find the best tradeoff between competing objectives. The results of the optimization analysis illustrate the optimal solution and recommendations corresponding to three main practical applications of bio-based concrete.

Overall, this study provides a comprehensive framework for predicting, evaluating, and optimizing the mechanical and thermal properties of bio-based concrete. The developed model has the potential to be a valuable tool for designing and optimizing bio-based concrete for a wide range of applications, thus reducing

the carbon footprint of concrete production, and promoting sustainable and efficient development in the construction industry.

Keywords: Bio-based concrete; Mechanical and thermal properties; Homogenization; Multi-scale modeling; Finite Element Analysis; Multi-Objective Optimization.

Résumé

La réduction de la consommation d'énergie et émissions de carbone est, actuellement, un défi pour l'industrie de la construction. Le développement de matériaux de construction durables est donc devenu de plus en plus crucial, étant donné l'impact environnemental élevé des matériaux de construction traditionnels, tels que les matériaux cimentaires et les bétons ordinaires. Le béton biosourcé est apparu comme une solution prometteuse pour atténuer ces problèmes grâce à ses performances d'isolation élevées et à sa durabilité. Ce matériau recycle les déchets agricoles comme agrégats et s'attaque aux effets négatifs de l'accumulation et de l'incinération des déchets. La modélisation multi-échelle présente des avantages pour l'étude du lien entre la microstructure et la performance macroscopique. Toutefois, les modèles actuels ne sont pas en mesure de répondre aux caractéristiques structurelles complexes du béton biosourcé.

Dans cette étude, nous avons développé un nouveau modèle d'homogénéisation basé sur des caractéristiques structurelles multi-échelles pour prédire, évaluer et optimiser les propriétés mécaniques et thermiques d'une large gamme de bétons biosourcés. Le modèle proposé prend en compte différents facteurs, notamment la fraction volumique de chaque phase, la forme et l'orientation des bio-agrégats, les différentes tailles de pores, l'humidité et le contact imparfait. Pour valider le modèle, nous avons effectué une série de vérifications à différentes échelles, processus industriel et sources de bio-agrégats. L'inter-comparaison montre un bon accord entre les données analytiques, numériques et expérimentales.

Ensuite, nous avons utilisé le modèle vérifié pour une analyse paramétrique afin de quantifier l'effet des caractéristiques structurelles sur les performances macroscopiques. Bien que tous les facteurs mentionnés ci-dessus aient une influence sur les propriétés du béton, les effets sur les comportements mécaniques et thermiques peuvent être inversés. Par exemple, l'augmentation de la fraction volumique de bio-agrégat réduit les performances mécaniques mais augmente l'isolation thermique. De plus, le type de liant et l'humidité ont une forte influence sur les propriétés mécaniques et l'isolation thermique, respectivement, alors que la fraction volumique des bio-agrégats a un effet significatif sur les deux. En outre, l'anisotropie du béton biosourcé n'est pas négligeable en raison de l'orientation, de la forme, de la distribution des pores et du contact imparfait. En outre, l'influence de la forme des bio-agrégats diminue avec le rapport d'aspect, mais elle dépend également de la fraction volumique, de l'orientation, de l'humidité, etc. Par conséquent, l'évaluation et l'optimisation des performances des bétons biosourcés nécessitent un travail systématique et complet.

Enfin, nous avons combiné des modèles de comportement mécanique et thermique pour optimiser la performance globale du béton biosourcé par le biais d'une approche d'optimisation multi-objectifs, afin de trouver le meilleur compromis entre des objectifs concurrents. Les résultats de l'analyse d'optimisation illustrent la solution optimale et les recommandations correspondant à une utilisation de ces bétons biosourcés à l'échelle de la structure selon trois configurations.

Dans l'ensemble, cette étude fournit un cadre complet pour prédire, évaluer et optimiser les propriétés mécaniques et thermiques du béton biosourcé. Le modèle développé a le potentiel d'être un outil précieux pour concevoir et optimiser le béton biosourcé pour une large gamme d'applications, réduisant ainsi l'empreinte carbone de la production de béton, et promouvant un développement durable et efficace dans l'industrie de la construction.

Mots-clés : Béton biosourcé ; Propriétés mécaniques et thermiques ; Homogénéisation ; Modélisation multi-échelle ; Analyse par éléments finis ; Optimisation multi-objectif.

Contents

Abstract ..... **iii**

Résumé ..... **v**

Contents ..... **vii**

List of Figures ..... **xiii**

List of Tables ..... **xix**

Introduction ..... **xxi**

CHAPTER I: Literature review **23**

Chapter introduction 23

1.1. Background 24

1.2. Bio-based concrete 24

1.2.1. Definition 24

1.2.2. Composition 25

1.2.3. Application review 27

1.3. Characteristics of bio-based concrete 31

1.3.1. Physical properties 31

1.3.2. Mechanical properties 35

1.3.3. Thermal properties 39

1.3.4. Hygrothermal properties 40

1.4. Factors affecting mechanical and thermal properties of bio-based concrete 42

1.4.1. Type of plants 42

1.4.2. Type of binder 44

1.4.3. Fiber shape and percentage 46

1.4.4. Fiber orientation 47

1.4.5. Moisture 50

1.4.6. Density 50

1.4.7. Plant surface treatment 51

1.4.8. Temperature 53

1.4.9. Aging 54

1.5. Modeling of bio-based concrete 54

1.6. Conclusion 60

1.7. References 61

CHAPTER II ..... : Modeling the mechanical properties of bio-based concrete 77

Chapter introduction 77

Article A: Optimization of mechanical properties in anisotropic bio-based building materials by a multiscale homogenization model 78

Abstract 78

1. Introduction 79

2. Material definition 81

2.1. Description of micro structure of bio-based concrete 81

2.2. Particularities and individual characteristics of components 84

3. Model description 86

3.1. Inclusions with a parallel orientation 86

3.2. Basis transformation 87

3.3. Uniformly distributed but arbitrarily oriented inclusions (Isotropic case) 88

3.4. Inclusions with anisotropic distribution 90

4. Application and validation in bio-based building materials 91

4.1. Scale 1: Porous bio-aggregate and porous binder 91

4.2. Scale 2: Bio-based building materials 92

5. Parametric study 95

5.1. Influence of volume fraction 95

5.2. Influence of modulus of components 96

5.3. Influence of fiber shape 98

5.4. Influence of fiber orientation 99

5.5. Weights of parameters 101

6. Conclusion 104

Appendix A. Bechterew Notation 105

Appendix B. Eshelby tensor with different inclusion shapes 107

Appendix C. Numerical implementation of φ 108

References: 109

CHAPTER III.....: Modeling the thermal conductivity of bio-based concrete 115

Chapter introduction 115

Article B: A Multi-Scale Numerical Simulation on Thermal Conductivity of Bio-Based Construction Materials 117

Abstract 117

1. Introduction 117

2. Materials and Methods 120

2.1. Materials 120

2.2. Methods 121

3. Results and Discussion 125

3.1. Effective Thermal Conductivity of Binder 125

3.2. Effective Thermal Conductivity of Individual Hemp Shiv 125

3.3. Effective Thermal Conductivity of Bio-Based Construction Materials 127

4. Conclusions 132

References 134

Article C: A multiscale homogenization model on thermal conductivity of bio-based building composite considering anisotropy, imperfect interface and moisture 139

Abstract 139

1. Introduction 139

2. Theoretical basis of the multi-scale homogenization method 144

2.1. Heat conduction problem 144

2.2. Tensor transformation of inclusions between global and local coordinate systems 145

2.3. Multi-scale homogenization of bio-based building materials 146

2.4. Shape of bio-aggregates 151

3. Model verification and application 152

3.1. Effective aspect ratio of bio-aggregates 152

3.2. Effective thermal conductivity of porous binder 153

3.3. Effective thermal conductivity of porous bio-aggregates 154

3.4. Effective thermal conductivity of bio-based composite 155

4. Conclusion 160

CRediT authorship contribution statement 161

Declaration of Competing Interest 161

Appendix A. Depolarization tensor 161

Appendix B. Effective thermal conductivity of porous binder 162

References 163

CHAPTER IV .... : Performance optimization of bio-based concrete through a multi-objective approach 171

Chapter introduction 171

Article D: Improving the Mechanical and Thermal Performance of Bio-Based Concrete Through Multi-Objective Optimization 172

Abstract 172

1. Introduction 172

2. Methodology 174

2.1. Multi-scale models 174

2.2. Multi-objective optimization problem 175

2.3. Optimization strategy for bio-based concrete 175

2.4. Decision variables and constraints 176

3. Results and discussions 178

3.1. Sampling density (SD) 178

3.2. Point distribution of the objectives 180

3.3. Sensitivity analysis and multi-objective optimization in the general case 181

3.3.1. BB 181

3.3.2. BR 183

3.3.3. BS 184

3.4. Constraints on bio-aggregates 185

3.5. Performance Constraints 187

3.6. Density constraint 189

3.7. Optimization in humid environments 190

3.8. Summary of optimal solutions for varied requirements 191

4. Conclusion 193

CRediT authorship contribution statement 193

Declaration of Competing Interest 194

References 194

Conclusions and perspectives 199

List of Figures

List of Figures: CHAPTER I

Figure 1.1. Spraying of bio-based concrete [69]. 28

Figure 1.2. Construction methods for hemp concrete [21]. 29

Figure 1.3. Various applications of bio-based concrete. (a) wall with load-bearing blocks [68,74], (b) firewall [68,74], (c) soundproof wall [68,74], (d) roof [72], (e) floor [68,74], (f) frame filling [73]. 30

Figure 1.4. Microstructure of hemp concrete [76]. 31

Figure 1.5. Pores at different scales in bio-based concrete [43]. 34

Figure 1.6. Stress-strain curves of bio-based concrete in different directions [82,83]. 37

Figure 1.7. Flexural load-deflection test of industrial hemp fiber-reinforced beam [84]. 38

Figure 1.8. Triaxial shearing behaviour of bio-based concrete [85]. 38

Figure 1.9. Tensile stress-strain curves of bio-based concrete [86]. 39

Figure 1.10. Sorption capacity of bio-aggregates. Hemp shiv (HS), sunflower pith (SP), sunflower bark (SB), corn bark (CB), corn cob (CC), and barley straw (BS) [57]. 41

Figure 1.11. Hourly temperature and relative humidity of hemp concrete wall [92]. 42

Figure 1.12. Ten plant fibers in the study from [57]. 43

Figure 1.13. Thermal conductivity of ten types of bio-concrete [57] (Left: dry, right: 55±5% relative humidity). 44

Figure 1.14. Effect of binder type on mechanical (left) and thermal (right) properties [93]. 46

Figure 1.15. Effect of flax fiber size (a) on thermal conductivity (b) and compressive strength (c). Fi-j, i = (1, 2, 3) denotes BS, MS, and LS, respectively. j = (1, 2, 3) denotes the mass percentage of 11.5%, 14.5%, and 17.5%, respectively. (Adapted from [97]). 47

Figure 1.16. Orientation of plant fibers in concrete [18,82]. 48

Figure 1.17. Mechanical properties (a) (b) and thermal conductivity (c) of hemp concrete at different compaction levels and layer thickness [99]. 50

Figure 1.18. Effect of moisture on the thermal conductivity [45]. 50

Figure 1.19. Thermal conductivity of hemp concrete with dry density [23]. 51

Figure 1.20. Surface treatment of apricot shell and compressive strength of corresponding concrete [54]. 52

Figure 1.21. Effect of pretreatment on the thermal properties of corn stalk concrete [45]..... 53

Figure 1.22. Thermal conductivity of corn stalk (top) and hemp (bottom) concrete with temperature [23,45]. 54

Figure 1.23. Effect of aging on compressive strength test [100]. 54

Figure 1.24. Self-consistent scheme in the modelling of bio-based concrete..... 56

Figure 1.25. Mathematical description of the orientation of ellipsoidal inclusions [118]. 57

Figure 1.26. Iterative homogenization method from [131]. 59

Figure 1.27. FEM models for straw concrete [132]..... 60

Figure 1.28. 3D X-ray tomography reconstruction [76]. 60

List of Figures: CHAPTER II, Article A

Fig. 1. Elementary volume of bio-based concretes, (a) [26], (b) [46]. 82

Fig. 2. Aspect ratio (R=a/b) for cylindrical and ellipsoidal fibers..... 83

Fig. 3. Inclusion orientation depend on φ and θ. 84

Fig. 4. Elementary representation of hemp, sunflower pith and maize pith fibers, (a) [26], (b) [46], (c) [60], (d) [32]..... 85

Fig. 5. Inclusions arranged in an initial direction. 87

Fig. 6. Transformation between the global coordinate system (X, Y, Z) and local coordinate system (x, y, z). 88

Fig. 7. Inclusions uniformly distributed and arbitrarily oriented in the matrix. 89

Fig. 8. Inclusions with anisotropic distribution in bio-based concrete. 91

Fig. 9. Young's modulus of individual bio-aggregate (Left) and binder (Right) with porosity (E_A: Young's modulus in the axial direction, E_T: Young's modulus in the transverse direction). 92

Fig. 10. Young's modulus of bio-aggregates and binder with porosity (Anisotropy of hemp=(E_A-Hemp/E-Binder)-(E_T-Hemp-/E-Binder)). 92

Fig. 11. Comparison of Young's modulus from homogenization theory and experiments. (Experimental data was from Abbas et al. [26]) 94

Fig. 12. Comparison of Young's modulus of hemp concretes based on density. (Experimental data are from [58]) 95

Fig. 13. Effective modulus with volume fraction of bio-aggregates in the isotropic case. 96

Fig. 14. Effective modulus with volume fraction of bio-aggregates in the anisotropic case. (R=3 and θ=75º) 96

Fig. 15. Effective modulus with E-Binder and E-Aggregate in the anisotropic case. (Cylindrical inclusions, θ=75º, volume fraction=0.5) 97

Fig. 16. Poisson's ratio with E-Binder and E-Aggregate in the anisotropic case. (Cylindrical inclusions, θ=75º, volume fraction=0.5) 98

Fig. 17. Influence of aspect ratio of ellipsoidal inclusion in the anisotropic case. (θ=75º, volume fraction=0.20, the dashed line is for cylinder) 98

Fig. 18. Comparison between cylinders and ellipsoids with different aspect ratio in the different case. (Left: Isotropic case. Right: Inclusions with φ and θ=45º, volume fraction=0.20, the first six curves are related to ellipsoidal inclusions.) 99

Fig. 19. Influence of R for ellipsoidal inclusions when θ=0º and 45º. (Volume fraction=0.20) 99

Fig. 20. Influence of angle θ and φ for cylindrical inclusions with a given θ and φ orientation. (Cylindrical inclusions, volume fraction=0.20) 100

Fig. 21. Influence of φ and θ for cylindrical inclusions. (Volume fraction=0.20) 101

Fig. 22. Influence of θ for cylindrical inclusions in bio-based concrete. (Volume fraction=0.16) 101

Fig. 23. Weights of the parameters affecting the effective modulus of bio-based concrete..... 103

Fig. 24. Differences in optimization for different aspect ratios (Vertical (E1) and parallel (E3) directions. Low aspect ratio: R=3, high aspect ratio R=8, low volume fraction: 0.2, high volume fraction: 0.5). 104

List of Figures: CHAPTER III, Article B

Figure 1. Microstructure of hemp shiv is reprinted with permission from Ref. [32]. 2018. Elsevier.-A, reprinted with permission from Ref. [12]. 2018. Elsevier.-B, (**A-1**,**B-1**) cross-section, (**A-2**,**B-2**) longitudinal section..... 120

Figure 2. Multi-scale homogenization model for the thermal conductivity (The photograph of the sample on the right is reprinted with permission from Ref. [41]. 2020. Elsevier). 122

Figure 3. Multi-scale homogenization model for scale 2-binder..... 122

Figure 4. Multi-scale homogenization model for scale 2. 123

Figure 5. Multi-scale homogenization model for scale 3-bio-aggregate. 123

Figure 6. Multi-scale homogenization model for scale 3-bio-based composite. 124

Figure 7. Multiple shapes of bio-aggregates in numerical models. 125

Figure 8. Effective thermal conductivity of binder (Experimental results as a comparison are from [21,38,40]). 125

Figure 9. Effective thermal conductivity of pore-moisture (Anisotropy = $\lambda^{\perp}$)..... 126

Figure 10. Effective thermal conductivity of hemp with porosity in various water saturation (WS: water saturation, $\lambda^{\parallel}$ and $\lambda^{\perp}$ denote the axial direction of hemp and the direction perpendicular to the axial direction, respectively). 127

Figure 11. Variation in effective thermal conductivity with water saturation for hemp shiv. 127

Figure 12. Testing of mesh element size. 128

Figure 13. Comparison of numerical simulation with experimental data from [23,40]. 129

Figure 14. Effective thermal conductivity of composite with water saturation. 130

Figure 15. Comparison of (**A**) thermal conductivity and (**B**) anisotropy in multiple homogenization steps. 130

Figure 16. Comparison of bio-aggregates in various shapes. 131

Figure 17. Analysis of plant fiber orientation based on finite element results (the compaction direction is in the X-axis. (**A**)—thermal flux X, (**B**)—thermal flux Z). 132

List of Figures: CHAPTER III, Article C

Fig. 1. Definition of inclusion direction. 146

Fig. 2. Multi-scale structure of bio-based building materials for modeling (The photograph of the sample on the right: [62]). 147

Fig. 3. Process of the iterative homogenization approach. 150

Fig. 4. Flowchart of the iterative computation. 151

Fig. 5. Iteration test. 151

Fig. 6. Comparison of experimental data [61] and fitting based on Weibull functions. 153

Fig. 7. Fitting of the size of hemp (Experimental data: [60]). 153

Fig. 8. Model validation on binder: I-MFH versus FEM [67]. 154

Fig. 9. Model validation on bio-aggregates with intra-particle pores (FEM: [67], experimental data: [72]). 155

Fig. 10. Model verification on binder-aggregates with orientation. 156

Fig. 11. Model validation on dry hemp concrete with density (Experimental data: [31,43,44,65]). 157

Fig. 12. Calibration of the thermal conductivity of wheat straw concrete with imperfect contact. 158

Fig. 13. Calibration of the thermal conductivity of wheat straw concrete with moisture. 159

Fig. 14. Validation on various plant aggregates (Experimental data: [28,76–79]). 160

List of Figures: CHAPTER IV, Article D

Fig. 1. Three optimization strategies for bio-based concrete. 176

Fig. 2. Point distribution and Pareto front (Line) at varying sampling densities. 179

Fig. 3. Comparison of Pareto fronts at different sampling densities for three applications (Icons × and ✓ represent inadequate and adequate sampling density in the comparison). 180

Fig. 4. Density plot of the objective values. 181

Fig. 5. Color-coded point distribution of objectives in BB (PM: preference for mechanical properties, BP: balanced performance, PI: preference for insulation)..... 182

Fig. 6. Color-coded point distribution of objectives in BR. 184

Fig. 7. Color-coded point distribution of objectives in BS. 185

Fig. 8. Point distribution in high-volume bio-aggregates. 186

Fig. 9. Optimization under performance constraints. 188

Fig. 10. Optimization of bio-based concrete for lightweight roofing. 189

Fig. 11. Optimization of bio-based concrete under dry, low humidity, and high humidity conditions for three industrial applications. 191

Fig. 12. Optimal solutions for varied requirements. 192

List of Tables

List of Tables: CHAPTER I

Table 1.1. Mix proportions of bio-based concretes [57]. 27

Table 1.2. Chemical composition of hemp [65]. 27

Table 1.3. Microstructure of various bio-aggregates [77]. 33

Table 1.4. Porosity of bio-based concrete [78]. 34

Table 1.5. Relationship between porosity and density [79]. 35

Table 1.6. Compressive strength and young's modulus of hemp concrete [34,81]. 36

Table 1.7. Thermal conductivity of different insulation materials [88]. 40

Table 1.8. Sources of five unfired binders to replace lime [93]. 46

Table 1.9. Mechanical properties of apricot shell concrete after surface treatment [54]. 52

List of Tables: CHAPTER II, Article A

Table 1. Approximate volume fraction of phase 2 according to [26]. 93

Table 2. Some experimental data [58,69,70] and results of calculations of fiber volume fractions for hemp concrete. 95

Table 3. Data input for weighting analysis. 102

List of Tables: CHAPTER III, Article B

Table 1. Properties of hemp shiv. 120

Table 2. Properties of binder. 121

Table 3. Volume fraction of each phase in hemp construction material from [12]. 124

List of Tables: CHAPTER III, Article C

Table 1. Parameters of hemp concrete. 156

Table 2. Volume fraction of each component of wheat straw concrete [54,61]. 157

Table 3. Properties of wheat straw concrete [54,61]..... 158

CHAPTER IV, Article D

Table 1. Decision variables and boundaries. 177

Table 2. Fixed parameters in this model. 177

Table 3. Optimal solution for the general case. 183

Table 4. Optimal solution in high-volume bio-aggregates. 186

Table 5. Optimal solution under performance constraints. 188

Table 6. Optimal solution for lightweight roofing. 189

Introduction

The construction industry significantly contributes to carbon emissions and energy consumption, and buildings account for a large portion of this. Bio-based concrete, made from recycled agricultural waste and low-carbon binders, has the potential to reduce these impacts due to lower embodied carbon and thermal insulation properties.

Bio-based materials exhibit lower mechanical performance and higher thermal insulation than conventional building materials. These macroscopic characteristics arise from their complex microscopic multi-scale structure, such as the shape, orientation, and porosity of bio-aggregates. Establishing quantitative macro-micro relationships can enable the prediction and optimization of material behavior, especially the mechanical and thermal properties, from a perspective of multi-scale structure.

Multiscale homogenization models can help to solve this issue. Therefore, this study developed a novel multiscale homogenization model applicable to the mechanical properties of bio-based concrete. The model performed well in the application of hemp, sunflower, and corn concrete, and was subsequently used to optimize the weak mechanical performance of bio-based concrete.

Optimizing the mechanical properties with a single-objective approach has the potential to enhance the load-bearing capacity of bio-based concrete, enabling its application to moderately loaded building components. However, such an approach could negatively impact its thermal insulation, which is a crucial factor in the widespread adoption of bio-based concrete. To address this, the study then presented a thermal model of bio-based concrete.

Detailed analysis of the mechanical and thermal models suggests that the microscopic features that contribute to improved mechanical performance can actually compromise thermal insulation, and vice versa. To achieve a perfectly balanced bio-based material that exhibits both superior strength and excellent thermal insulation, we combined the two models by a multi-objective optimization approach to obtain a balanced material.

This thesis comprises four chapters. The first chapter is a literature review, while chapters two to four consist of journal articles that have either been published or are in the process of being submitted. As of writing this manuscript, chapter 2 contains a published journal article, and chapter 3 includes a published article and another article scheduled for publication on May 9, 2023. Chapter 4 is an unpublished manuscript that is currently being prepared for submission, and its final version will depend on the requirements of the target journal. A brief overview of each chapter is provided below.

Chapter 1 introduces the current challenges in the construction industry and identifies bio-based concrete as the focus of the study. Then, a review of the literature revealed that existing models are inadequate for predicting and optimizing the complex structure of this material. Therefore, this study aims to develop a novel model for bio-based concrete that can accurately predict, evaluate, and optimize its mechanical and thermal properties.

Chapter 2 presents a multiscale model of the mechanical properties by a two-step homogenization. This model considered the effects of pores, modulus of binder and aggregate, shape, orientation, and volume fraction on mechanical properties. It was then verified by comparison with experimental data from the literature. Further, this model was used for parametric analysis and single-objective optimization.

Chapter 3 presents a multiscale model of the thermal conductivity of bio-based concrete by numerical and analytical approaches, respectively. They were verified on multiple scales, various bio-aggregates, and humid environments.

In Chapter 4, the two models developed in Chapters 2 and 3 were integrated to optimize the combined mechanical and thermal properties of bio-based concrete using a multi-objective optimization approach. The resulting optimal solutions were tailored to meet the demands of various industrial applications and practical needs.

In conclusion, the models proposed in this study can effectively predict, evaluate, and optimize the mechanical and thermal properties of bio-concrete. By a multi-objective optimization approach, it is possible to achieve a balanced bio-based material with both high mechanical performance and excellent thermal insulation, expanding its potential applications in the building industry.

CHAPTER I : Literature review

Chapter introduction

Chapter 1 provides a comprehensive literature review to contextualize the study and identify research gaps in the field of bio-based concrete. The review first highlights the significance of bio-based concrete as a solution to environmental and sustainability challenges in the construction industry due to its low carbon footprint and high insulation properties.

Then, the physical, mechanical, thermal, and hygrothermal properties of bio-based concrete were investigated in detail, revealing that its porous structure, weak mechanical properties, and moisture-sensitive low thermal conductivity are key characteristics.

The microstructure of bio-based concrete affects its macroscopic properties. Therefore, the literature review delves into the micro-macro linkages between the material's microstructure and its mechanical and thermal properties, considering factors such as plant and binder type, fiber volume fraction, orientation and shape, moisture, density, treatment, temperature, and age. However, the review finds that current multiscale homogenization models are not sufficient for complex bio-based concrete structures. Thus, the main objective of this study is to develop a novel multiscale model to predict, analyze, and optimize the mechanical and thermal properties of bio-based concrete.

1.1. Background

In recent years, the global community has been increasingly concerned with issues related to environmental protection, energy crisis, and sustainability. The building industry plays a significant role in these issues because of the large amount of carbon emissions and energy consumption [1–3]. From 1990 and 2019, global CO_2 emissions from buildings increased by 50% [4]. In the UK, buildings are responsible for 50% of CO_2 emissions [5]. Moreover, buildings account for about 30-40% of total energy consumption in developed countries [6]. In France, this sector accounts for 43% and 25% of energy consumption and greenhouse gases [7]. In 2021, the International Energy Agency (IEA) reported that building operations were responsible for 30% of global final energy consumption, while building space heating and cooling account for the largest share [8,9]. In 2019, heating and cooling was the largest residential energy demand in Europe and Eurasia [4]. Net-Zero Energy Buildings (NZEB) [10,11] and Net-Zero Carbon Buildings (NZCB) [12,13] are becoming increasingly popular, making these issues even more challenging.

Globally, a significant amount of agricultural waste is generated every year, and over 30% of waste from crop straw and forest crop is burned and discarded [14,15], leading to environmental pollution and human health risks [16]. In fact, they can be used as aggregates for concrete, known as bio-based concrete [17–19]. The use of recycled agricultural waste in the construction industry can reduce waste accumulation and environmental hazards [20]. Also, buildings made of bio-based materials consume less energy and contribute to carbon emissions reduction. Firstly, bio-based concrete has excellent thermal insulation [19,21–23], which reduces energy consumption for space heating and cooling of buildings. For example, the application of bio-based materials significantly reduces the annual electricity consumption of buildings [24]. Secondly, plants are good materials for carbon sequestration, and many life cycle assessments demonstrate the advantages of bio-based buildings in reducing emissions [25–29].

1.2. Bio-based concrete

1.2.1. Definition

Many studies [22,30–33] have shown that these agricultural wastes or by-products can be reused in the construction industry. This material, partially derived from biomass, is an effective means of reducing energy consumption, carbon emissions, and the accumulation of agricultural waste, thus contributing to the NZEB and NZCB processes. It offers many advantages over traditional building materials: high insulation, high acoustic absorption, high porosity, light weight, moisture regulation, low carbon footprint, and energy savings [21,34], etc. They will be discussed separately in section 1.3. Although the mechanical strength of this material is very low, it is mainly used in non-load-bearing structures such as floors, roofs, and walls [34,35].

Up to now, there is no clear definition of this material. Various terms have been used to denote this concept. According to the European Commission's definition, “bio-based products” are materials derived in whole or in part from biological sources, excluding materials embedded in geological formations and/or fossils [36]. It includes products produced through bio-catalysis and fermentation, as well as biodegradable plastics, etc. Therefore, the concept of bio-based products is too broad to describe this study, and it is not limited to uses in the construction industry. Another concept is “lightweight concrete”, which is classified according to unit weight. The density of lightweight concrete is not higher than 1920 kg/m^3 [37]. It can be further divided into “aerated or foam concrete” and “lightweight aggregate or structural lightweight concrete” [37–40]. Lightweight aggregates contain natural aggregates such as perlite, shale ceramsite, scoria, pumice, plant, and artificial aggregates such as expanded glass, expanded shale, expanded polystyrene, expanded clay, waste rubber, waste plastic, and fly ash [41]. The concept of lightweight concrete includes not only plant aggregate concrete, but also a variety of materials. Similarly, for the concept of natural fiber concrete, it involves all fibers of natural origin: plant origin (e.g., hemp fibers), animal origin (e.g., animal hair), and mineral origin (e.g., basalt and asbestos fibers) [42].

Therefore, it is necessary to define this type of material before starting this study. It can contribute to standardize the classification of scientific research. This manuscript uses “bio-based concrete” as a term to represent this type of material, which refers to the use of plant particles or fibers in whole or in part as aggregates and combined with binders to form lightweight concrete for construction purposes. Sometimes it is also called bio-based building material because it is mainly used for building roofs, walls, and floors, etc. Generally, bio-based concrete consists of recycled plant fibers and a lime-based binder, without the addition of mineral aggregates. Depending on the type of crop, there are a variety of bio-based concretes, such as hemp [43], sunflower [44], corn stalk [45], flax [46], rape straw [47], date palm [48], jute [49], coconut [50], wheat straw [51], lavender [52], rice husk [53], miscanthus [22], apricot shell [54], pine needle [55], wood-aggregate [56], etc. These aggregates used in construction materials are called bio-aggregates. In particular, hemp concrete is the most widely studied bio-based material [57,58] and it is abbreviated as “Hempcrete” in some studies [59,60]. Also, hemp concrete usually consists of a lime-based binder and hemp fibers, so it is also called “hemp-lime” in some articles [61,62]. Due to pozzolanic reactivity, plant waste can also be used as an additive in the form of ash [21,63]. Note that this study only focuses on plants as fibers or aggregates in construction materials.

1.2.2. Composition

Bio-based concrete usually consists of binder and bio-aggregate, while very few studies use both mineral and bio-aggregate. Various recycled agricultural wastes are used in place of traditional mineral aggregates, such as sand and gravel. Due to the different applications, the density, porosity, mechanical properties,

thermal conductivity, and acoustic properties of bio-based concrete are required differently. Moreover, plant fibers themselves have multiple sizes, shapes, porosities, and pore structures depending on the source. Therefore, a variety of mix proportions for bio-based concrete appeared in the experimental study. Researchers tried to find a ratio that meets the needs. It is clear that a lightweight, high mechanical properties, high thermal insulation, and high acoustic absorption material was the common goal. As shown in **Table 1.1**, an experimental study from [57] used two types of binders. Binder 1 is a commercial lime, which consists of 60% natural lime, 40% hydraulic and pozzolanic binder. Binder 2 contains 70% metakaolin and 30% air lime. In addition, potassium sulfate and superplasticizer were used as additives to the concrete of Binder 2. In order to compare the performance of concrete with different bio-aggregates and to find suitable reuse solutions for the corresponding plant fibers, ten plant aggregates were studied: hemp, linseed shives, sunflower pith, sunflower bark, coriander straw, wheat straw, wheat chaff, corn spat, miscanthus stalk, vine shoots. It can be seen from **Table 1.1** that the binder and water requirements in the casting procedure are related to the type of bio-aggregate. Moreover, the density of different bio-aggregate concrete varies, especially the dry density.

Binder	Bio-aggregates	mixing sequence	Bio-aggregate / binder ratio	Water / binder ratio	Fresh density (Kg/m^3)	Dry density (Kg/m^3)
Binder 1	Hemp	1	0.43	1.40	731	391 ± 5
Binder 1	Linseed shives	1	0.58	1.29	742	413 ± 7
Binder 1	Sunflower pith	1	0.14	1.36	647	333 ± 10
Binder 1	Sunflower bark	1	0.64	1.20	734	425 ± 9
Binder 1	Coriander straw	1	0.37	1.34	700	385 ± 6
Binder 1	Wheat straw	1	0.28	1.25	655	386 ± 9
Binder 1	Wheat chaff	1	0.35	1.23	665	406 ± 18
Binder 1	Corn spat	1	0.37	1.35	704	398 ± 5
Binder 1	Miscanthus stalk	1	0.73	1.33	790	381 ± 10
Binder 1	Vine shoots	1	1.21	1.22	886	513 ± 17
Binder 1	Hemp	2	0.43	1.40	731	399 ± 8
Binder 1	Sunflower pith	2	0.14	1.36	647	321 ± 8
Binder 1	Sunflower bark	2	0.64	1.20	734	412 ± 5
Binder 1	Wheat straw	2	0.28	1.25	655	378 ± 6

Binder 2	Hemp	1	0.43	0.98	622	352 ± 14
Binder 2	Sunflower pith	1	0.14	1.28	625	313 ± 12
Binder 2	Sunflower bark	1	0.64	1.11	711	406 ± 8
Binder 2	Wheat straw	1	0.28	0.83	547	349 ± 7
Binder 2	Vine shoots	1	1.23	0.80	773	453 ± 19

Table 1.1. Mix proportions of bio-based concretes [57].

Most agricultural plant aggregates used in construction materials are composed of lignin, hemicellulose, and cellulose. These components are less compatible with conventional binders [45,64]. Therefore, researchers commonly use lime-based binders in bio-based concrete to improve compatibility and achieve light weight and low carbon emissions. In general, the binders associated with bio-aggregates are natural and Portland cements, aerial limes, hydraulic limes, dolomite limes, formulated crystallization, etc [21].

Bio-aggregates are derived from natural plants and the determination of their chemical composition facilitates the study of surface treatments. Although there are various plant species, their main composition consists of hemicellulose, cellulose, and lignin (see **Table 1.2**).

Sample	Soluble	Hemicellulose	Cellulose	Lignin	Ash	Humidity of samples
Flax Shiv	9.1 ± 1.9	17.6 ± 2.4	43.5 ± 4.7	27.1 ± 4.5	2.7 ± 0.9	4.7 ± 0.7
Hemp Shiv	17.2 ± 1.1	21.6 ± 1.8	49.0 ± 2.8	8.1 ± 0.6	4.1 ± 1.6	3.1 ± 0.4
Maize Bark	15.3 ± 0.2	34.8 ± 0.9	42.8 ± 1.0	3.3 ± 0.2	3.8 ± 0.2	2.8 ± 0.1
Miscanthus	7.2 ± 0.5	27.8 ± 1.4	43.6 ± 9.8	19.0 ± 10.8	2.4 ± 0.1	3.5 ± 1.5
Reed	9.6 ± 1.5	28.3 ± 1.3	47.6 ± 1.2	10.5 ± 1.5	4.0 ± 0.1	2.4 ± 0.1
Rice Husk	7.7 ± 0.3	19.8 ± 0.5	42.1 ± 0.6	16.8 ± 0.2	13.7 ± 0.1	1.9 ± 0.1
Sunflower Bark	6.0 ± 2.2	18.1 ± 2.8	30.3 ± 6.2	41.7 ± 8.5	3.8 ± 0.5	6.5 ± 0.1
Sunflower Pith	38.6 ± 1.1	5.0 ± 1.9	23.3 ± 6.8	21.4 ± 6.4	11.7 ± 0.3	8.7 ± 0.3
Wheat	10.5 ± 0.1	34.1 ± 4.5	45.3 ± 4.3	6.2 ± 0.3	3.9 ± 0.1	5.5 ± 0.1

Table 1.2. Chemical composition of hemp [65].

1.2.3. Application review

Human cultivation of hemp can be traced back to 8000 BCE [66]. Hemp concrete is the most widely researched and applied bio-based concrete. As early as the 1990s, hemp concrete came to be used in historic

timber buildings, repair works, and new construction in France [21,67]. Due to its excellent thermal insulation properties, bio-based concrete is mostly used as a building insulation material. On the other hand, the strength of bio-based concrete is very low and it is mainly used for non-load-bearing structures, while the frame provides the support of the building. Depending on where it is processed and cast, bio-based concrete can be manufactured on site or off site [34]. Off-site construction is further subdivided into spraying and molding. For the spraying process, the dry lime and hemp mixture is delivered to the spray gun by a high-pressure air stream. Then water is mixed with the dry material at the nozzle, as shown in **Figure 1.1**. For the casting through the mold, the mixture of bio-based concrete is mixed in a mixer and transported to the construction site. It is then injected into the prepared formwork. Note that the tamping operation is generally necessary, as self-healing or gravity compaction is difficult to achieve on bio-based concrete [68]. Precast blocks are the main method of off-site construction. **Figure 1.2** shows the various methods of construction of hemp concrete. The use of several types of precast blocks can be seen to enhance the aesthetics of the building.

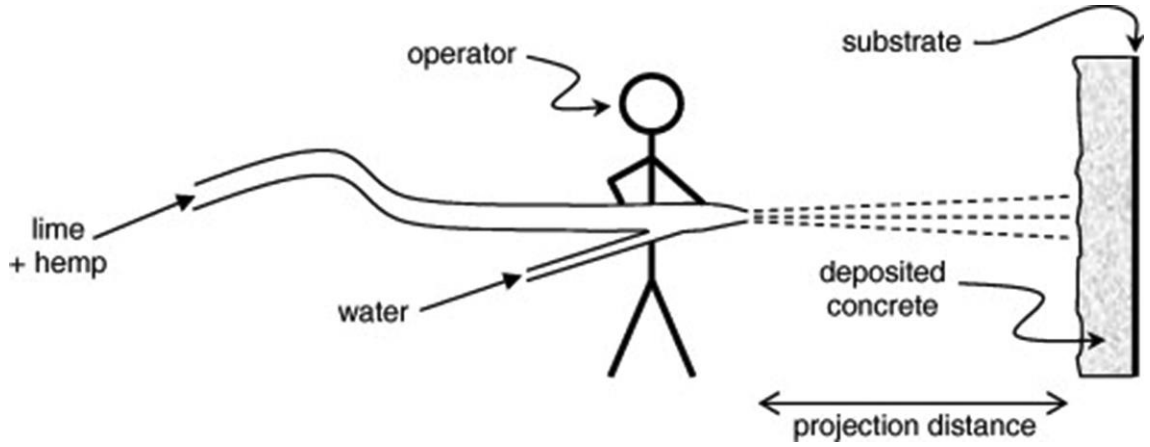

Figure 1.1. Spraying of bio-based concrete [69].

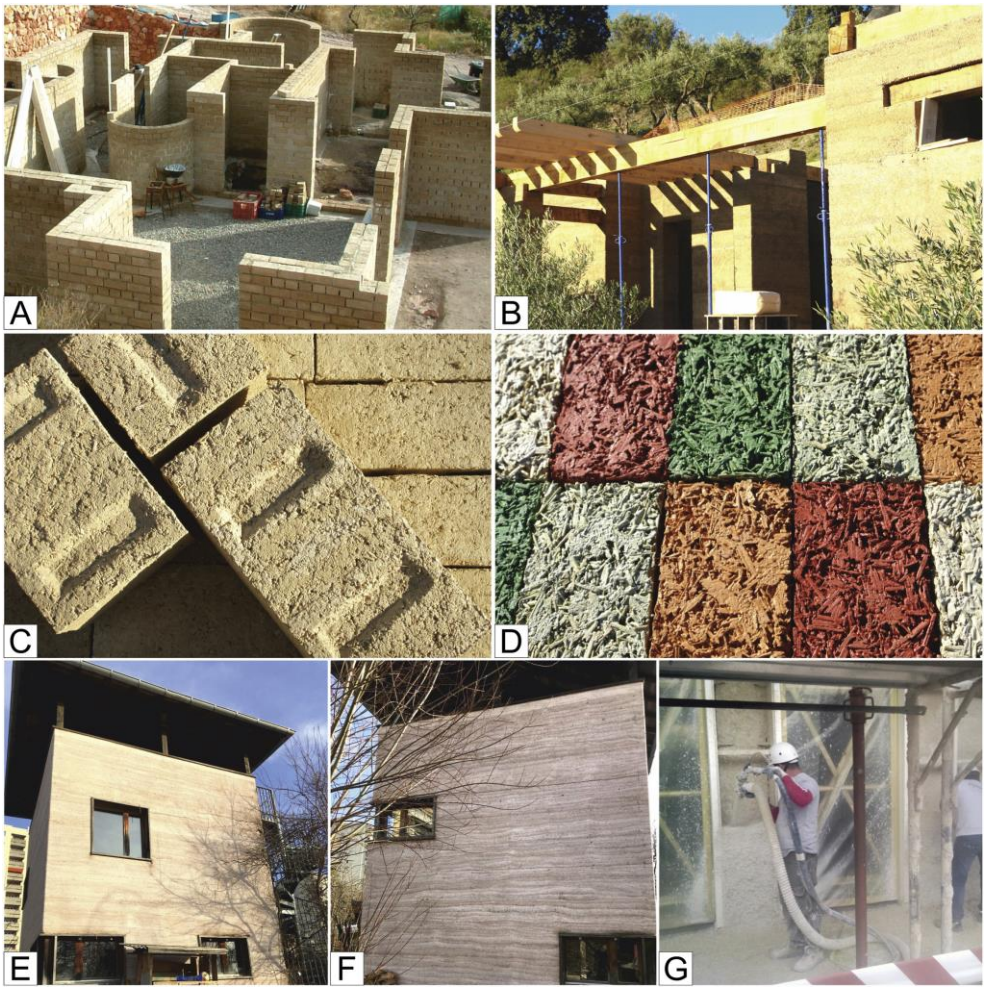

Figure 1.2. Construction methods for hemp concrete [21].

Moreover, depending on the structural composition of the building, bio-based concrete can be used for walls, roof, floor, window frame filling, and render.

Wall. The bio-based concrete used for walls is usually filled within a load-bearing frame, as shown in **Figure 1.3** (a). Moreover, bio-based concrete walls are also used in firewalls, soundproof walls, and interior partition walls because of its high thermal insulation, high sound absorption, aesthetics, and low toxicity of the bio-based material [68], as shown in **Figure 1.3** (b) and (c). The density used for this formulation is between 350 and 550 kg/m^3 [70]. This provides a balance of mechanical properties and insulation.

Roof. Bio-based concrete can be filled in the frame of a building roof as an insulating material, and it also has a pest-proof function [34,71]. The formulation used for roof has the lowest binder content. It therefore has a high porosity and a low density, generally not exceeding 300 kg/m^3 [70]. **Figure 1.3** (d) illustrates the construction process of a bio-based concrete roof from Tradical® [72].

Floor. As an important part of the heat transfer between the building and the outside world, bio-based concrete floors are also one of the applications, as shown in **Figure 1.3** (e). The density of hemp-based concrete used for flooring is 300-500 kg/m³ [70], which is heavier than hemp-based concrete used for roof. This is because it increases the load-bearing capacity of the floor, while the lighter roof reduces the burden on the building's support structure [34,71].

Window frame filling. The gaps between building windows and frames are weak spots for insulation. Bio-based concrete can be used to fill this gap instead of synthetic materials [34]. **Figure 1.3** (f) shows an example from Tradical® [73].

Render. For some buildings with high load-bearing requirements and subsequent building renovations, bio-based concrete can be used for walls in the form of plaster mortar. In this case, a high binder content is required to provide adequate adhesion [34]. Its density is usually greater than 800 kg/m³ [70].

Figure 1.3. Various applications of bio-based concrete. (a) wall with load-bearing blocks [68,74], (b) firewall [68,74], (c) soundproof wall [68,74], (d) roof [72], (e) floor [68,74], (f) frame filling [73].

1.3. Characteristics of bio-based concrete

1.3.1. Physical properties

Bio-based concrete is a mixture of binder, bio-aggregates, and water, which then becomes a porous composite. X-ray tomography is an important way to study the complex microstructure of bio-based concrete [75], as shown in **Figure 1.4**. At this scale bio-based materials have three phases: bio-aggregates, binders, and air pores. Due to the special shape of the bio-aggregate, i.e., generally elongated fibers, larger pores are formed between the bio-aggregates. These pores are referred to as inter-particle pores.

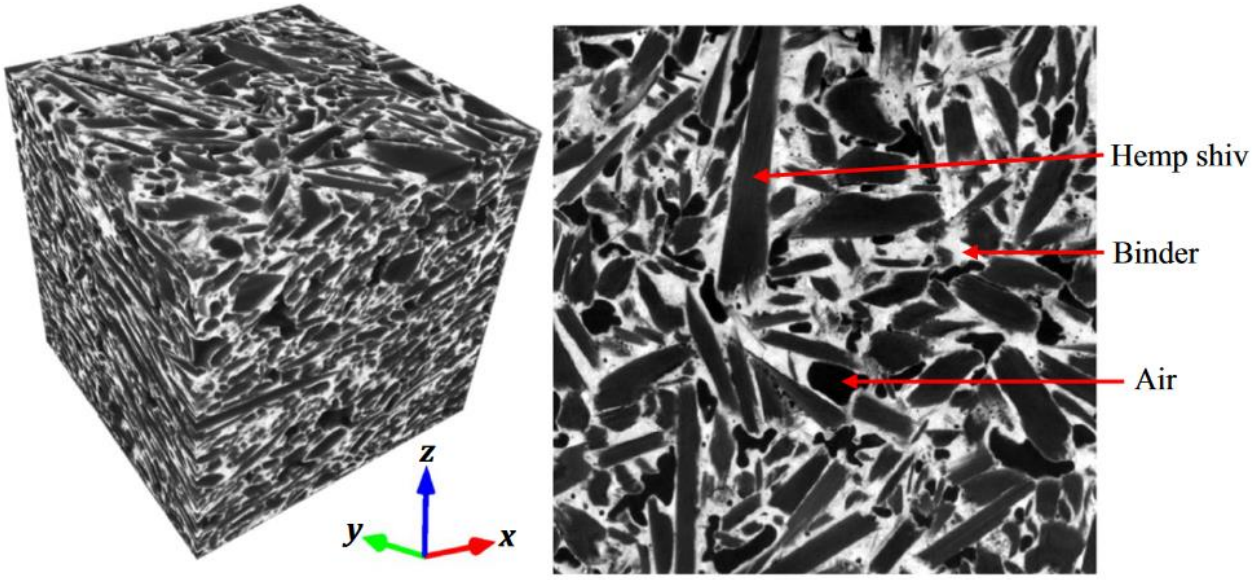

Figure 1.4. Microstructure of hemp concrete [76].

Further, there are micropores in the binder paste. Moreover, the bio-aggregate itself is a porous material and the pores located inside the bio-aggregate are called intra-particle pores. The shape and size of the intra-particle pores depend on the type of bio-aggregate. **Figure 1.5** illustrates the microstructure of five types of agricultural wastes commonly used in construction materials: hemp shiv, flax shiv, rape straw, wheat straw, and corn cob. The five bio-aggregates mentioned above have different epidermis, phloem layer, vascular cambium, xylem layer, and pith layer, which result in different porosity. Moreover, most of the bio-aggregates have tubular pores except for corn cob.

		Epidermis (Ep)	Phloem layer (PL)			Vascular cambium (VC)	Xylem layer (XL)		Pith (Pi) or Hollow space (HS)	Micro-structure
			Parenchyma cells (PC)	Sieve tubes (ST)	Starch granules (SG)		Tracheids (Tr)	Vessels (Ve)		
Hemp shiv	**Type**	Rectangular	-	-	Spherical (simple or compound)	Rectangular	Pitted	Annular	Hollow space	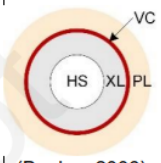 (Bouloc, 2006)
	Ø (µm)	l_1 : 6 - 8 l_2 : 10 - 12	10 - 20	35 - 50	3 - 7	l_1 : 6 - 8 l_2 : 14 - 18	10	50		
	L (µm)	-	50 - 70	-	-	-	100 - 150	90 - 110		
Flax shiv	**Type**	Purposeless	Purposeless			Purposeless	Pitted	Reticulate	Hollow space	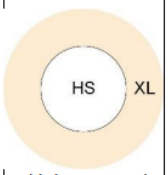 (Johnson and Kerr, 2015)
	Ø (µm)						9 - 12	15 - 35		
	L (µm)						130 - 150	-		
Rape straw	**Type**	Not measurable	-	-	Spherical (simple)	Not observed	Pitted	Reticulate	Pith	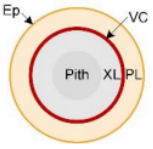
	Ø (µm)		10 - 20	-	3 - 5		10	15 - 50	50 - 100	
	L (µm)		130	-	-		100 - 130	30 - 50	-	
Wheat straw	**Type**	Rectangular	-	-	Spherical (simple)	Purposeless	Pitted	Annular	Hollow space	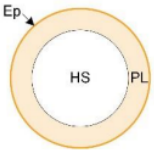 (Ghaffar, 2017)
	Ø (µm)	l_1 : 5 - 8 l_2 : 10 - 12	5 - 25	50	20		6 - 15	25 - 30		
	L (µm)	-	160 - 220	100	-		-	-		
Corn Cob	**Type**	Purposeless	Polyhedral	-	Polyhedral (simple)	Purposeless	Purposeless		Not observed	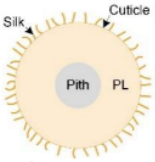 (Pinto et al., 2012)
	Ø (µm)		40	-	5					
	L (µm)		100	-	-					

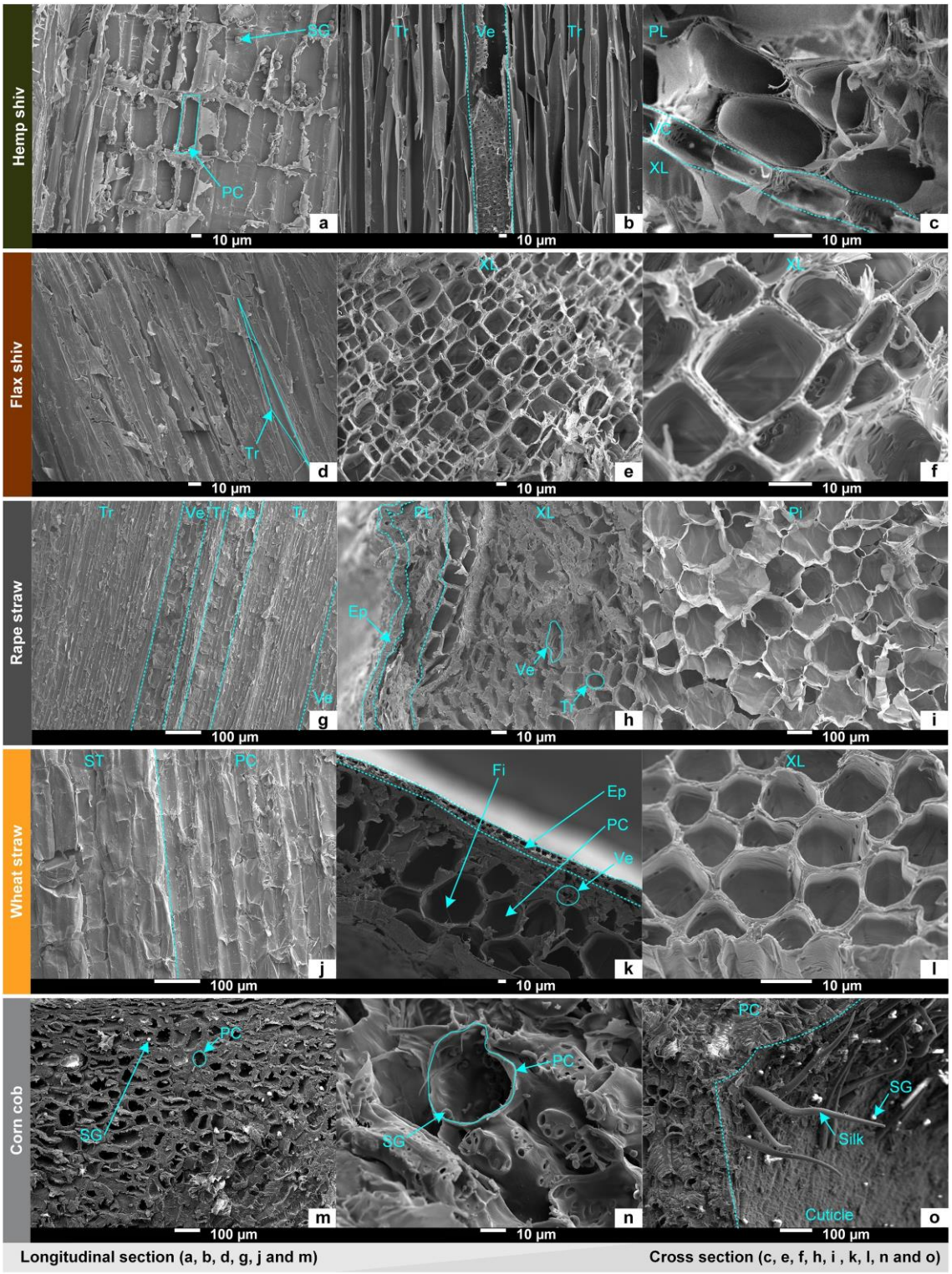

Table 1.3. Microstructure of various bio-aggregates [77].

Therefore, the total porosity of bio-based concrete is a sum of inter-particle pores, intra-particle pores and macropores. **Figure 1.5** illustrates the pores in the bio-based material at different scales and they all show

three different sizes of pores. The comparison between the left and right of **Figure 1.5** shows the difference in the illustration of the binder, which acts as a surface layer for the bio-aggregate on the right. This difference depends on the ratio of binder to bio-aggregate in the casting. [78] defined the total open porosity of bio-based concrete as the sum of intra-particle porosity and inter-particle porosity. As shown in **Table 1.4**, binder type (C1 and C2), bio-aggregate type (sunflower: S, four sources of hemp: F, H, G, and UK), and compaction (*) can all affect the porosity of bio-based concrete. Also, the total open porosity of bio-based concrete is higher than 70% regardless of the formulation, and this is without considering the microscopic pores inside the binder. High porosity is the key to bio-based concrete as a thermal and acoustic insulation material. Therefore, the study of porosity is naturally the key to improve the performance of the material.

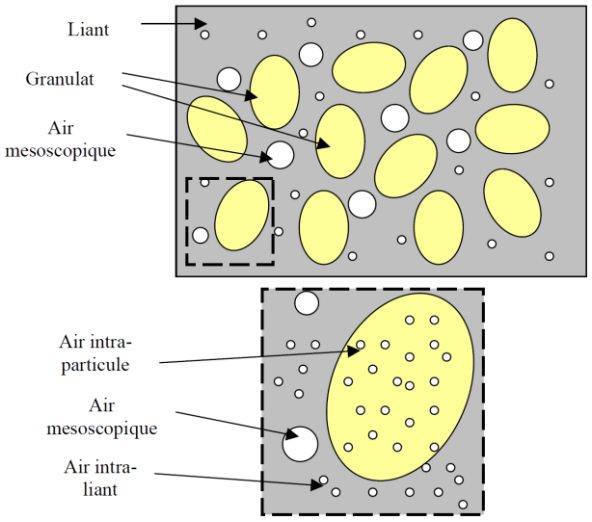

Figure 1.5. Pores at different scales in bio-based concrete [43].

Formulation	C2-H*	C2-S	C2-H + S	S	H	H98-G	H98-UK	H98-F	CLIN-UK	CLIN-G	C1-F
Total open porosity	0.7	0.77	0.7	0.99	0.87	0.786	0.715	0.719	0.739	0.814	0.75
Inter-particle porosity	0.41	0.36	0.43	0.76	0.66	0.5	0.53	0.47	0.47	0.49	0.43
Intra-particle porosity	0.49	0.63	0.48	0.96	0.61	0.58	0.4	0.47	0.51	0.64	0.56
Aggregate's grain density	296	59	–	59	296	460	486	523	486	460	523

Table 1.4. Porosity of bio-based concrete [78].

The high porosity of bio-based concrete results in low density. **Table 1.5** demonstrates the relationship between porosity and sample density for hemp, sunflower, flax, and rape straw concrete. Compared to conventional concrete, which has a density of 2400 kg/m^3, bio-based concrete has a much lower density. Therefore, these concretes using natural fibers are a type of lightweight concrete.

Particle	Sample density (Kg/m^3)	Total open porosity (%)	Inter-particle porosity (%)	Intra-particle porosity (%)	Particle density (kg/m^3)	Skeletal density (kg/m^3)
Hemp (shiv)	133	87	66.2	61.5	394	1020
Sunflower (bark)	168	82.5	62.5	53.3	448	960
Sunflower (pith)	34	99	76.3	95.8	144	3400
Flax (shiv)	115	90.5	82.6	45.3	663	1120
Rape (straw)	115	90	78.1	54.3	526	1150

Table 1.5. Relationship between porosity and density [79].

1.3.2. Mechanical properties

Compressive strength and young's modulus. Compressive strength and young's modulus are two of the most important properties of the material. **Table 1.6** shows the measurements of compressive strength and young's modulus of dry cannabis concrete by different researchers. It can be seen that the strength of bio-based concrete is very low compared to conventional concrete. This is mainly attributed to the strength, imperfect alignment, and porosity of the plant fibers [34,80]. Low strength is a limitation for its use in a wider range of structural materials. In other words, improving the mechanical properties of bio-based materials can expand its range of applications.

Authors	Binder Composition	Density (kg/m3)	Compressive strength (MPa)	Young's modulus (MPa)
Nguyen et al. (2009)	NA	850	–	131
		670	–	113
Arnaud and Gourlay, (2012)	NHL 3.5[a]	460	0.18	9
	NHL 3.5-Z[b]	480	0.31	36

	NHL 2.5[c]	480	0.10–0.22	5–24
	Commercial pre-formulated lime-based binder	460–500	0.30–0.34	–
Kioy, (2005)	NA	610	1.88	43
		830	1.98	52
Cerezo, (2005)	NA	356	0.3	14
		391	0.35	44
		504	0.7	15
Tronet et al., (2016)	Commercial pre-formulated lime-based binder	–	1.36	43
		–	1.63	51
		–	2.13	70
		–	4.74	147
		–	3.95	122
Sutton et al., (2011)	Commercial pre-formulated lime-based binder	270–330	0.10–0.20	–
Sassoni et al., (2014)	Patented MgO based binder with water-soluble vegetable protein (Canti, 2013)	330	1.15	–
		640	3.04	–
Sinka et al., (2014)	60% Dolomitic Lime + 40% Metakaolin	540	0.266	–
		397	0.154	–
		330	0.133	–
Sinka et al., (2014)	Pure Dolomitic Lime	461	0.181	–
		367	0.136	–
		345	0.125	–
Sassu et al., (2016)	NHL 3.5	643	0.414	12.495
		698	0.146	3.387
Sassu et al., (2016)	85% NHL 3.5 + 15% Portland cement	753	0.357	12.19
Sassu et al., (2016)	Portland cement	638	0.622	15.07

Table 1.6. Compressive strength and young's modulus of hemp concrete [34,81].

In particular, the stress-strain curves of the bio-based concrete differ in the direction perpendicular and parallel to the compaction, as shown in **Figure 1.19**. In the direction perpendicular to compaction, the young's modulus in the elastic stage is higher but the ultimate strength is lower. This can be explained by the heterogeneity of the bio-based concrete. The heterogeneity of the fibers themselves, the fiber arrangement, the pore structure, etc. all contribute to this heterogeneity.

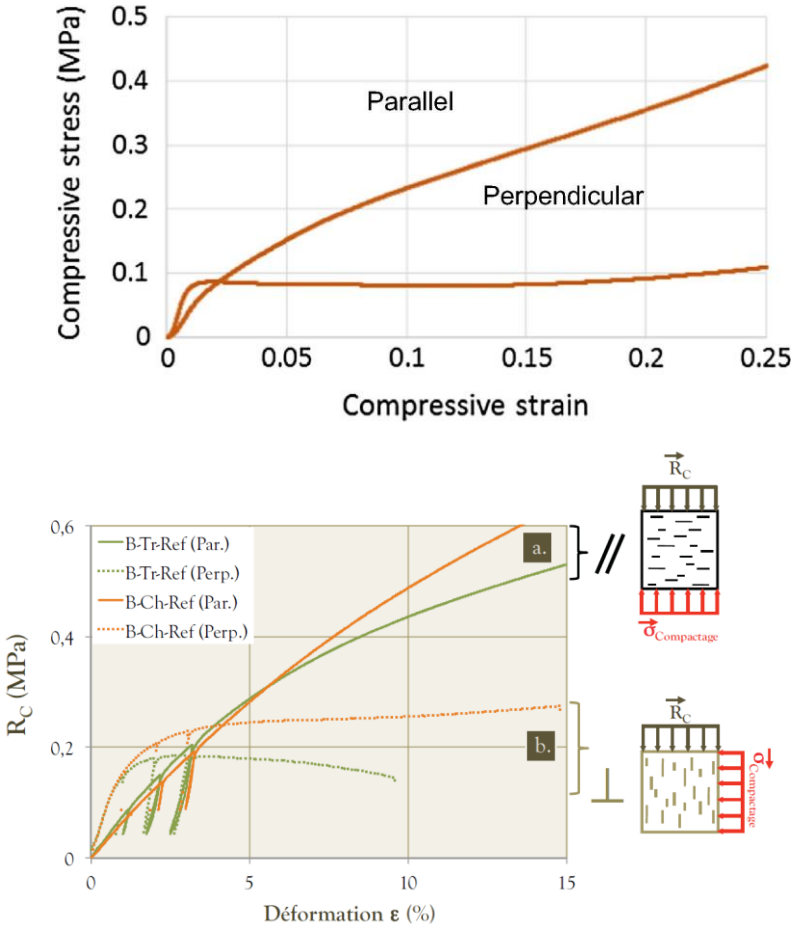

Figure 1.6. Stress-strain curves of bio-based concrete in different directions [82,83].

Flexural strength. Awwad et al. [84] studied the flexural behavior of industrial hemp fiber-reinforced beam specimens, as shown in **Figure 1.7**. The results showed that industrial hemp was enhanced in flexural strength and ductile post-cracking behavior. Moreover, the fibers showed a more obvious reinforcement of 28-day flexural strength than 7-day.

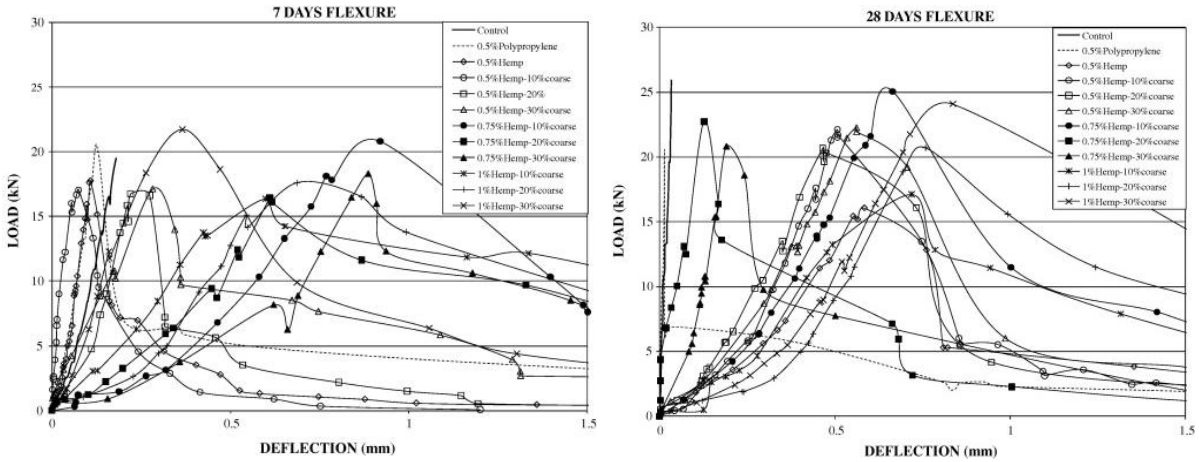

Figure 1.7. Flexural load-deflection test of industrial hemp fiber-reinforced beam [84].

Shear behavior. The shear behavior of concrete is determined by the resistance of the material to shear stress, which is the stress that acts parallel to the surface of the material. The study of shear behavior contributes to the understanding of shear damage in bio-based material walls [34]. Chabannes et al. [85] studied the shear behavior of hemp and rice husk concrete by triaxial compression and found two failure modes, as shown in **Figure 1.8**. The peak deviatoric stress increases with the confining pressure.

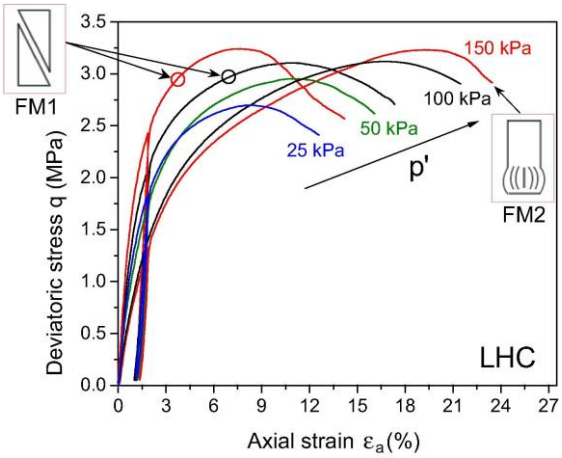

Figure 1.8. Triaxial shearing behaviour of bio-based concrete [85].

Tensile strength. Zhao et al. [86] investigated the tensile behavior of pineapple leaf fiber and ramie fiber concrete. As shown in **Figure 1.9**, P1-2 represent different volume fractions. The results showed that the incorporation of plant fibers changed the failure mode of the material from brittle to ductile. The curve can be divided into three stages: linear rise, linearly ascending stage, nearly horizontal stage, and descending stage [86,87]. In the first stage, the matrix bears the main load. In the second stage, the matrix cannot resist the load and then cracks, so the fibers bear the load until they are pulled out. In the third stage, the crack extends further until it fails.

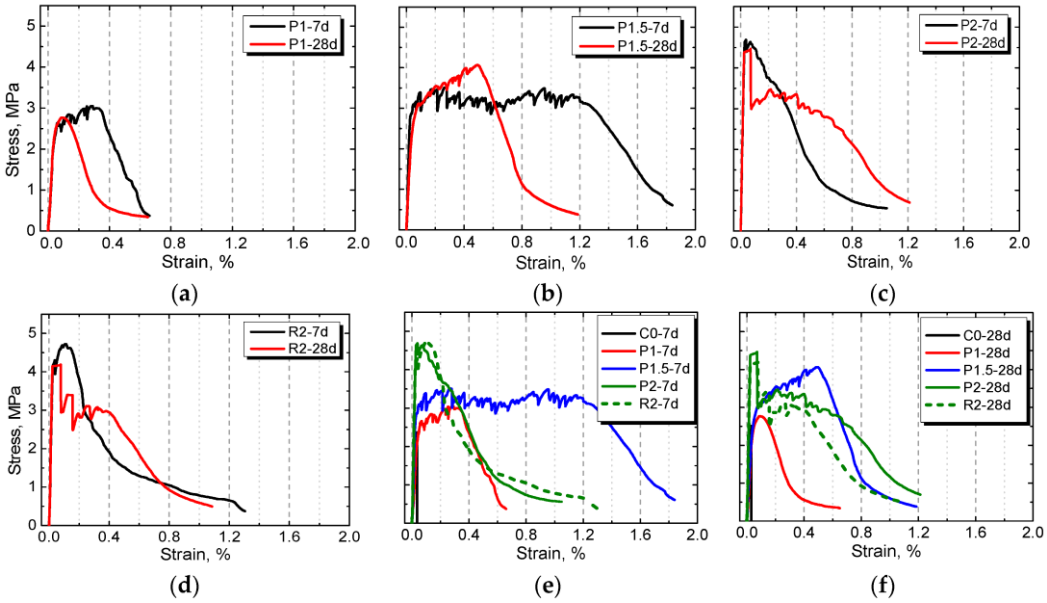

Figure 1.9. Tensile stress-strain curves of bio-based concrete [86].

1.3.3. Thermal properties

Insulation materials are broadly classified as organic, inorganic, combined, and advanced materials [88]. Plant fibers belong to organic insulation materials, which have good insulation properties and are not inferior to other insulation materials, as shown in **Table 1.7**. The thermal conductivity of organic materials ranges from 0.02 to 0.055 W/(m·K), which is lower than that of inorganic materials.

Main group	Subgroup	Insulation Material	Temperature (°C)	Density (kg/m^3)	Thermal conductivity (W/(m·K))
Inorganic	Fibrous	Glass wool	−100–500	13–100	0.03–0.045
		Rock wool	−100–750	30–180	0.033–0.045
	Cellular	Calcium silicate	300	115–300	0.045–0.065
		Cellular glass	−260–430	115–220	0.04–0.06
		Vermiculite	700–1600	70–160	0.046–0.07
		Ceramic	N.A.	120–560	0.03–0.07
Organic	Foamed	EPS	−80–80	15–35	0.035–0.04
		XPS	−60–75	25–45	0.03–0.04
		PUR	−50–120	30–100	0.024–0.03

		PIR	−20–100	30–45	0.018–0.028
	Foamed, expanded	Cork	110–120	110–170	0.037–0.050
		Melamine foam	N.A.	8–11	0.035
		Phenolic foam	150	40–160	0.022–0.04
		Polyethylene foam	−40–105	25–45	0.033
	Fibrous	Fiberglass	−4–350	24–112	0.033–0.04
		Sheep wool	130–150	25–30	0.04–0.045
		Cotton	100	20–60	0.035–0.06
		Cellulose fibers	60	30–80	0.04–0.045
		Jute	N.A.	35–100	0.038–0.055
		Rice straw	24	154–168	0.046–0.056
		Hemp	100–120	20–68	0.04–0.05
		Bagasse	160–200	70–350	0.046–0.055
		Coconut	180–220	70–125	0.04–0.05
		Flax	N.A.	20–80	0.03–0.045
Combined	Boards	Gypsum foam	N.A.	N.A.	0.045
		Wood wool	110–180	350–600	0.09
		Wood fibers	110	30–270	0.04–0.09
Advanced materials		VIPs	N.A.	150–300	0.002–0.008
		Aerogel	N.A.	60–80	0.013–0.014

Table 1.7. Thermal conductivity of different insulation materials [88].

1.3.4. Hygrothermal properties

Bio-based concrete is a high porosity material with high water vapor permeability and high moisture storage [3,89,90]. **Figure 1.10** demonstrates the sorption capacity of a variety of plant fibers: hemp shiv (HS), sunflower pith (SP), sunflower bark (SB), corn bark (CB), corn cob (CC), and barley straw (BS), it increases with the relative humidity of the environment and increases more rapidly when it is almost saturated. Among

the above-mentioned bio-aggregates, sunflower pith and sunflower bark have higher water absorption on average. For corn bark, it has the lowest water absorption at low relative humidity and increases fastest at high relative humidity. It regulates and moderates building humidity changes, thus balancing indoor and outdoor temperature and humidity changes and suppressing external weather [91].

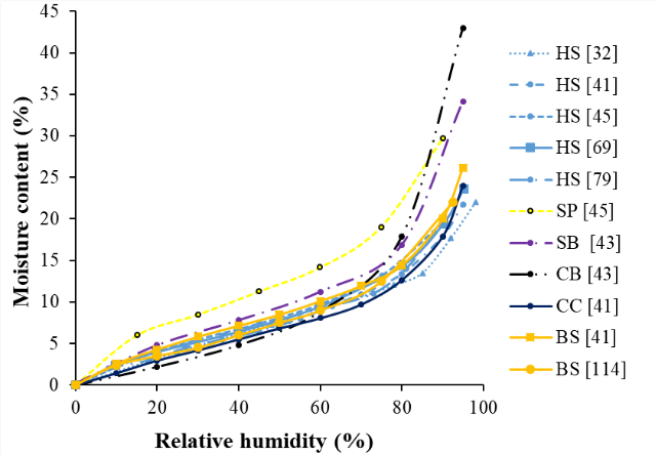

Figure 1.10. Sorption capacity of bio-aggregates. Hemp shiv (HS), sunflower pith (SP), sunflower bark (SB), corn bark (CB), corn cob (CC), and barley straw (BS) [57].

Long-term case studies [92] of hemp concrete buildings have also shown that 30 cm hemp concrete walls can suppress 90% of external temperature and humidity changes and delay the effects of peaks by about a dozen hours, as shown in **Figure 1.11**.

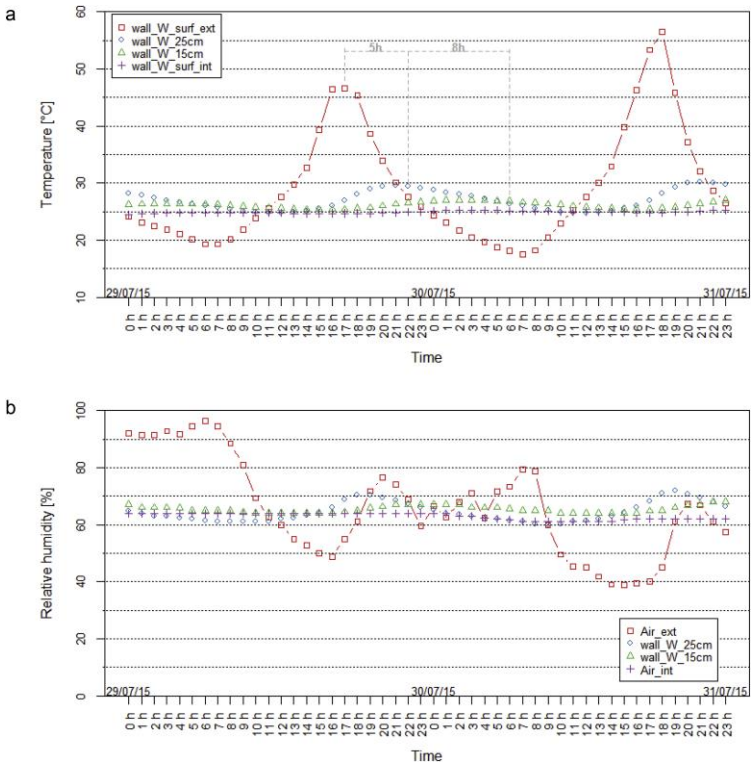

Figure 1.11. Hourly temperature and relative humidity of hemp concrete wall [92].

Bennai et al. [90] compared the hygrothermal behavior of hemp concrete with that of conventional brick and aerated concrete at the building scale. The results showed that hemp concrete buildings have an advantage over traditional building materials in terms of energy consumption. Hemp concrete mitigates the variation in relative humidity and improves the thermal comfort of the building in summer and winter.

1.4. Factors affecting mechanical and thermal properties of bio-based concrete

1.4.1. Type of plants

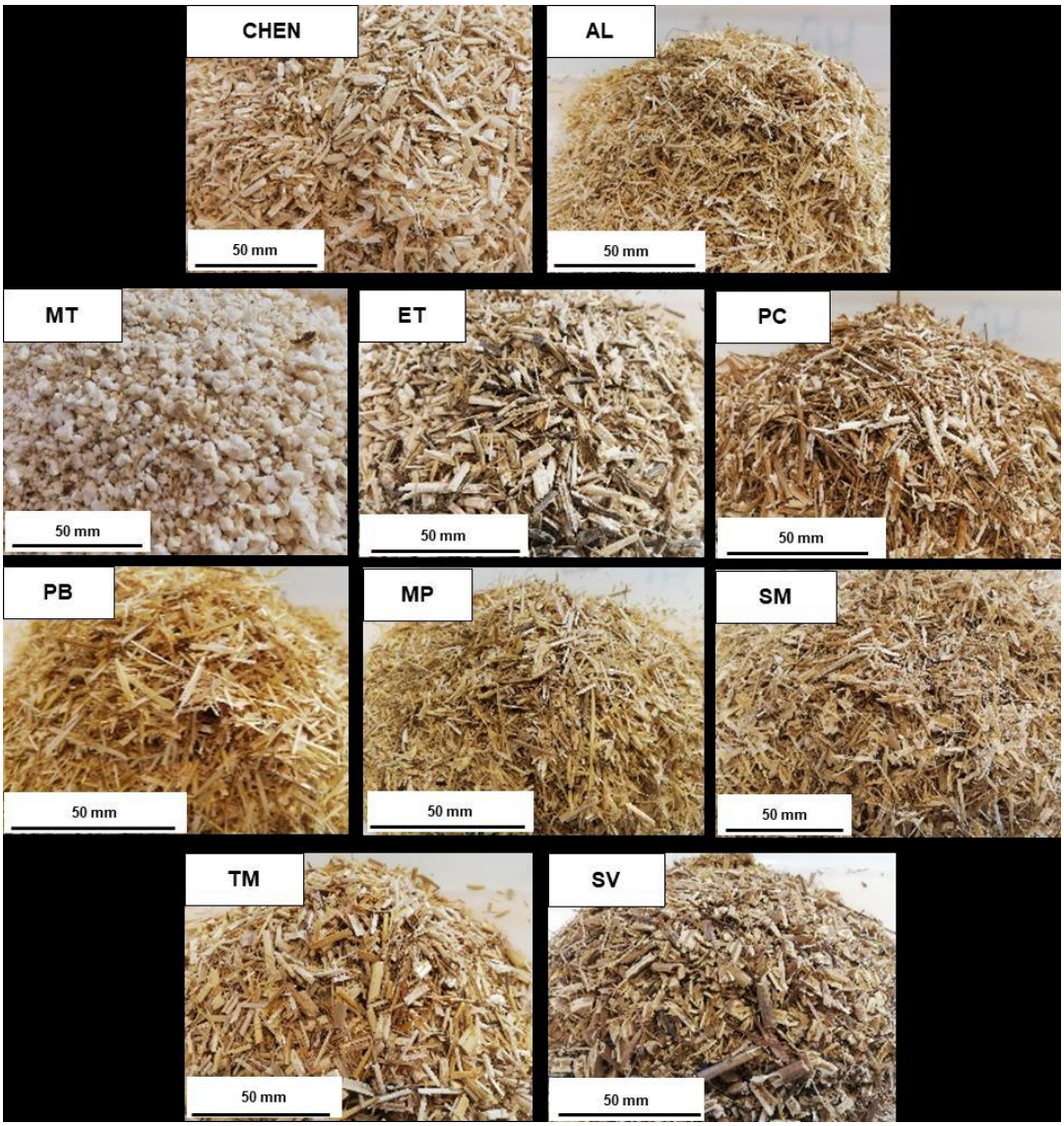

Figure 1.12. Ten plant fibers in the study from [57].

The combination of bio-aggregates and binder provides both the bonding and excellent insulation properties required. RATSIMBAZAFY [57] investigated the thermal conductivity of ten types of plant concrete listed in **Table 1.1**. As shown in **Figure 1.12**, blue represents dry thermal conductivity and orange represents thermal conductivity at 55±5% relative humidity. Their dry thermal conductivity ranges from 0.060 to 0.087, while the thermal conductivity in a humid environment is relatively higher, as shown in **Figure 1.13**.

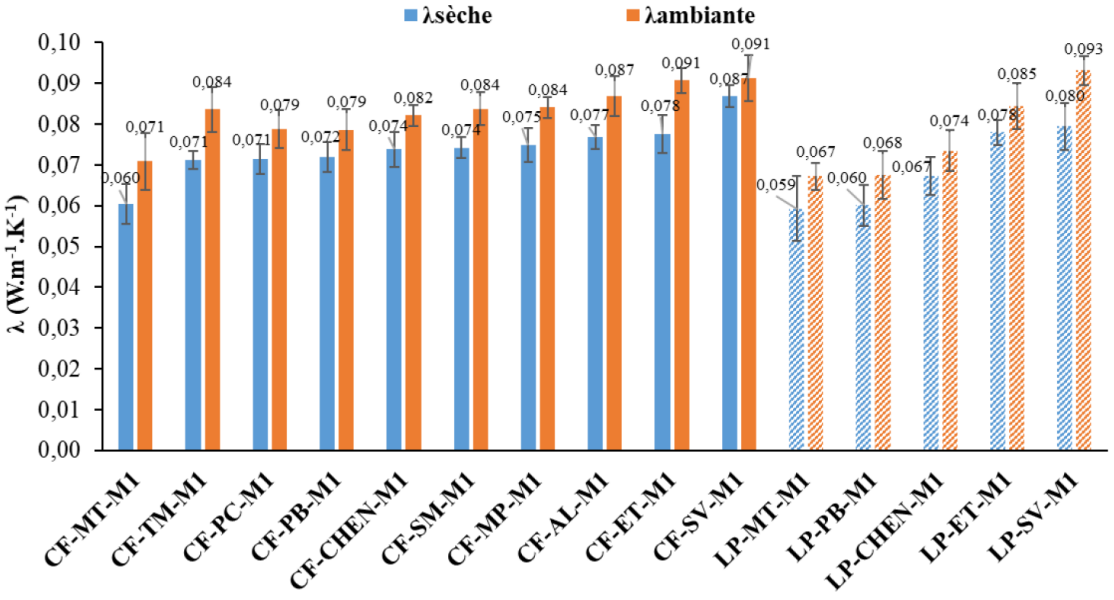

Figure 1.13. Thermal conductivity of ten types of bio-concrete [57] (Left: dry, right: 55±5% relative humidity).

1.4.2. Type of binder

Lime based binders are the preferred choice for bio-based construction materials due to its low embodied carbon (EC), embodied energy (EE) and better compatibility with bio-aggregates compared to cement. The kiln temperature for the production of lime is lower than that of cement, they are generally not higher than 900 and 1450 °C [93]. High temperature calcination turns calcium carbonate into calcium oxide (quicklime) through a chemical reaction. This process releases about 0.7 tons of CO_2 per ton of quicklime produced [28,94]. The calcium oxide then combines with water during the construction process to form calcium hydroxide (slaked lime). Finally, during the life of the building, the calcium hydroxide reabsorbs CO_2 and reverts to calcium carbonate. This carbonation process is accompanied by the hardening of the lime-based binder and has a positive carbon sequestration. Moreover, this carbonizes 90% of the CO_2 released by the calcination process [95].

The compatibility of binders and bio-aggregates is closely related to the performance of bio-based materials. Ahmad et al. [64] compared Portland cement, magnesium phosphate cement, and geopolymer binders in corn stalk concrete and tried to find a substitute for conventional binders to solve the compatibility problem. Their study found that the compressive strength of geopolymer-based and magnesium phosphate cement-based concrete was 150% and 550% higher than that of Portland cement-based concrete for the case of untreated corn stalk. For the comparison of thermal conductivity, magnesium phosphate cement-based concrete was significantly higher than the other two materials, while geopolymer-based concrete was slightly lower than Portland cement-based concrete.

Although lime-based binders have lower carbon emissions and calcination energy consumption compared to ordinary Portland cement, unfired binders have a greater advantage in this regard. Haik et al. [93] investigated the potential of five unfired binders (Kalgir, Mamshit, Motza, Amiad, and Basalt, **Table 1.8**) to partially replace lime in hemp concrete. The lime-based binder used in the experiment was Tradical® PF70 [96] which is a widely used binder for hemp concrete and as a reference for the five alternative binders. The mechanical properties of the different binders and hemp concrete from that study are shown in **Figure 1.14** (left). For the pure binder sample, the compressive strength of all five alternative binders was lower than that of the reference sample (100% lime). However, after the addition of hemp, the compressive strengths of 50% Kalgir and 50% Mamshit were 134% and 124% higher than the reference concrete, and their stress-strain curves also showed better mechanical performance. Authors Haik et al. [93] explained this phenomenon by the absorption of water by hemp in the mixture. Then, the hydration reaction of lime was not sufficient to reach the maximum potential strength. In contrast to the mechanical properties, the thermal conductivity and heat capacity of hemp concrete with different binders are almost the same, as shown in **Figure 1.14** (right).

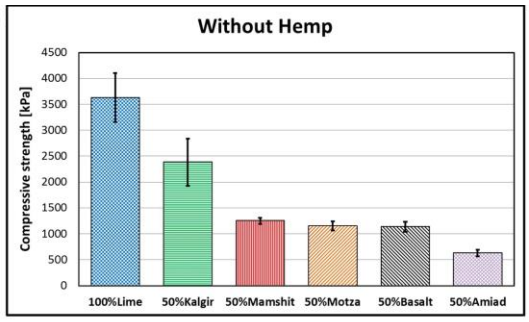

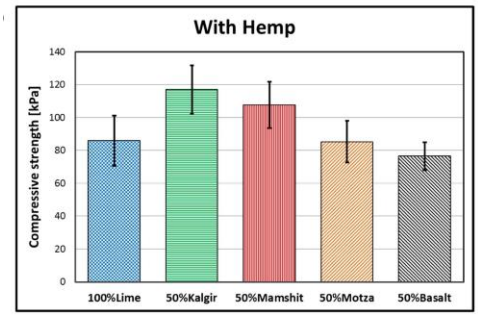

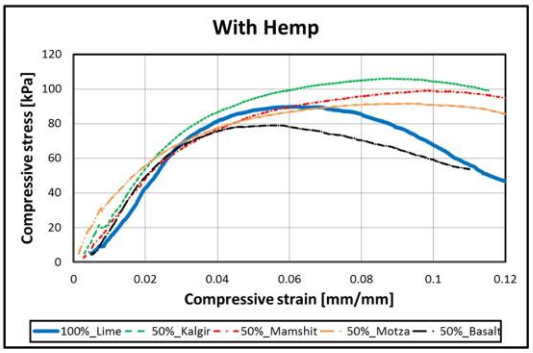

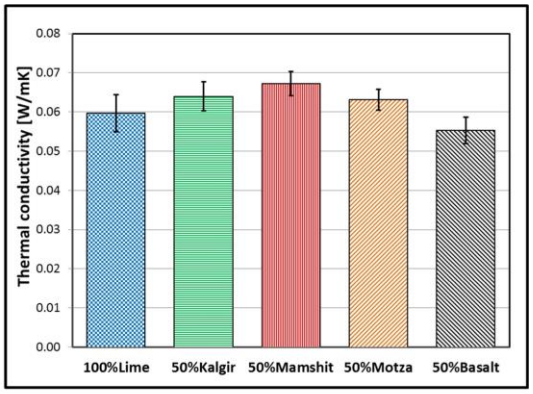

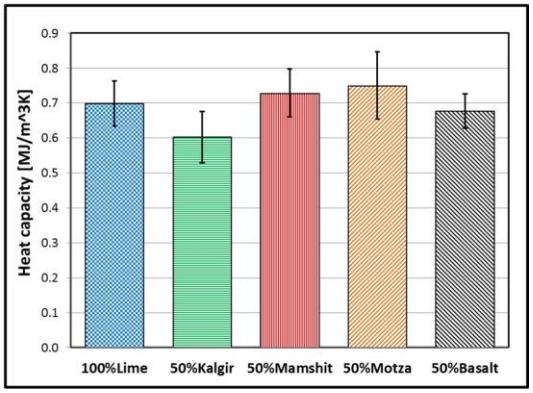

Figure 1.14. Effect of binder type on mechanical (left) and thermal (right) properties [93].

Binder designation	Source	Basis	Place of origin in Israel
Kalgir	Commercial product	Limestone	Negev
Mamshit	Commercial product	Clay	Mamshit, Negev
Motza	Commercial product	Dolomitic clay	Motza, Yehuda mountains
Amiad	Waste material	Limestone	Amiad quarry, Galilee
Basalt	Waste material	Basalt	Daliot quarry, Golan

Table 1.8. Sources of five unfired binders to replace lime [93].

1.4.3. Fiber shape and percentage

The sources and production processes of bio-aggregates lead to differences in shape. Understanding the effect of bio-aggregate shape on concrete properties facilitates the better use of a wide range of agricultural wastes. In addition, the percentage of bio-aggregate is an important parameter in the formulation.

Benmahiddine et al. [97] used three sizes of flax fibers: bulk size (BS), medium size (MS), and large size (LS) in their study, and the length distribution is shown in **Figure 1.15** (a). Different lengths of flax fibers have different aspect ratios and are thus associated with fiber shape. Also, three flax fiber percentages in that study: 11.5%, 14.5%, and 17.5% by mass. Three shapes and three percentages make up nine flax fiber concrete formulations. nine formulations are denoted by Fi-j, with i denoting the three shapes and j denoting the three percentages, as illustrated in **Figure 1.1**. The effect of flax shape and percentage on the thermal conductivity of concrete is shown in **Figure 1.15** (b). The comparison of j=1,2,3 shows that the thermal conductivity of flax concrete decreases with the percentage of bio-aggregate. This can be explained by the lower thermal conductivity of porous flax particles compared to the binder. The comparison of i=1,2,3 demonstrates that the thermal conductivity decreases with flax size generally. Authors Benmahiddine et al. [97] explained this by the differences in the arrangement and anisotropy of flax due to shape. **Figure 1.15** (c) illustrates that the compressive strength of flax concrete decreases with volume fraction, while the effect of the flax shape on the compressive strength is almost negligible. The effect of the high percentage can be explained by the increase in porosity and the weak bonding of the binder/bio-aggregate.

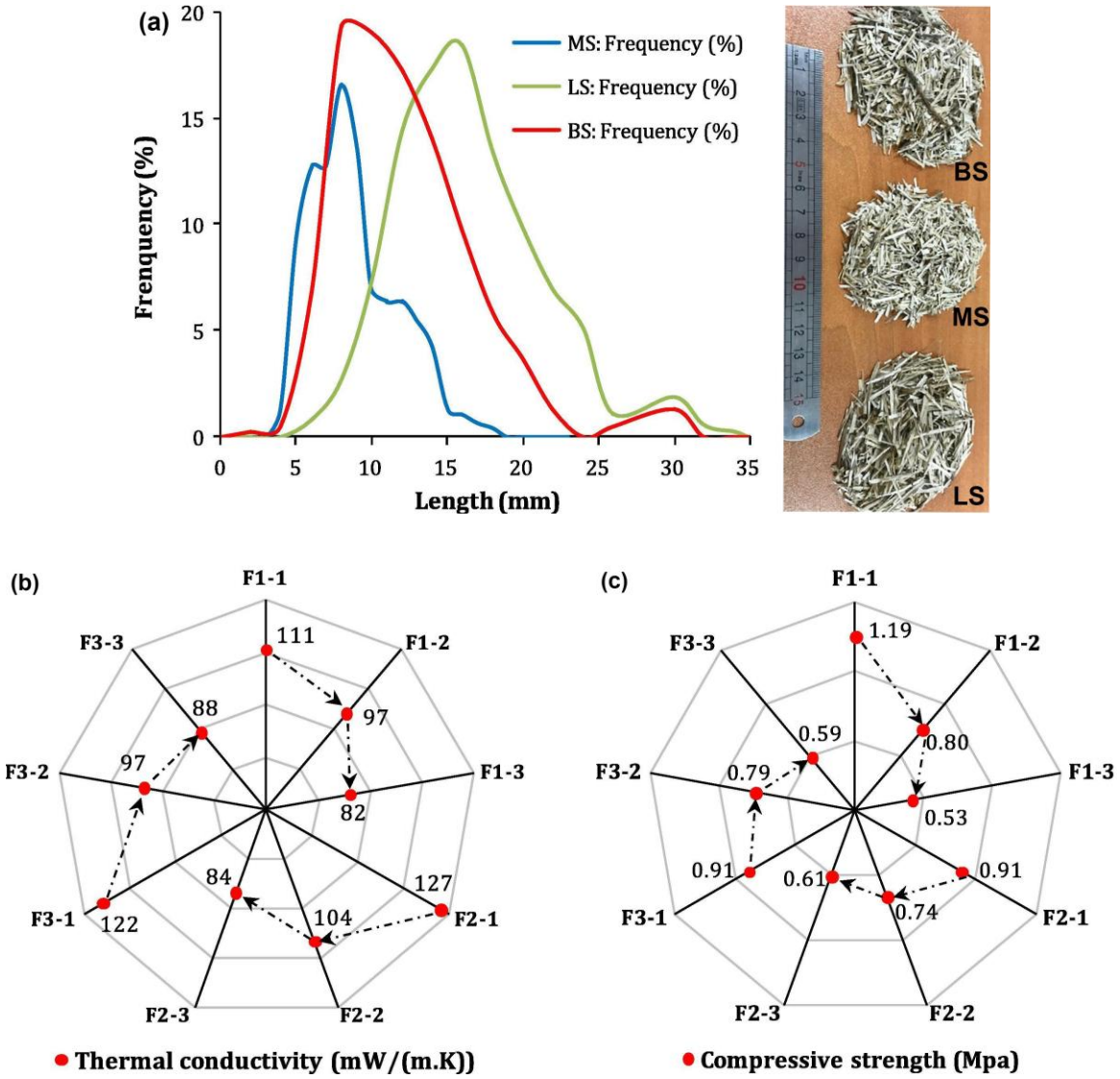

Figure 1.15. Effect of flax fiber size (a) on thermal conductivity (b) and compressive strength (c). Fi-j, i = (1, 2, 3) denotes BS, MS, and LS, respectively. j = (1, 2, 3) denotes the mass percentage of 11.5%, 14.5%, and 17.5%, respectively. (Adapted from [97]).

1.4.4. Fiber orientation

Bio-based materials are not isotropic, which is reflected in the different thermal conductivity and mechanical properties of the concrete specimens in the vertical and horizontal directions [98,99]. Because of the effect of compaction, it was found that the plant fibers tended to be distributed in the plane perpendicular to the compaction, as shown in **Figure 1.16**. Due to compaction, the biological fibers tend to be randomly and uniformly distributed in the plane perpendicular to the compaction, while the angle between the fibers and the compaction tends to be 90°. It is important to note that 90° is in an ideal situation and impossible to achieve in reality.

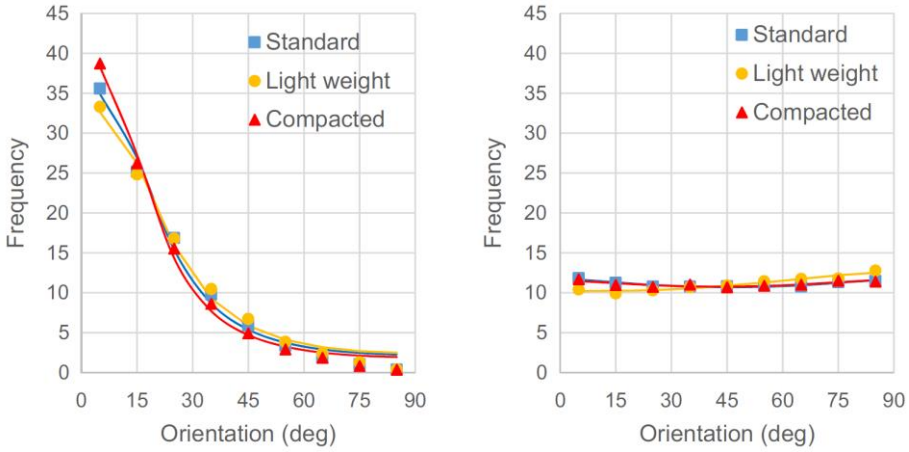

(a) Measured by image analysis [82].

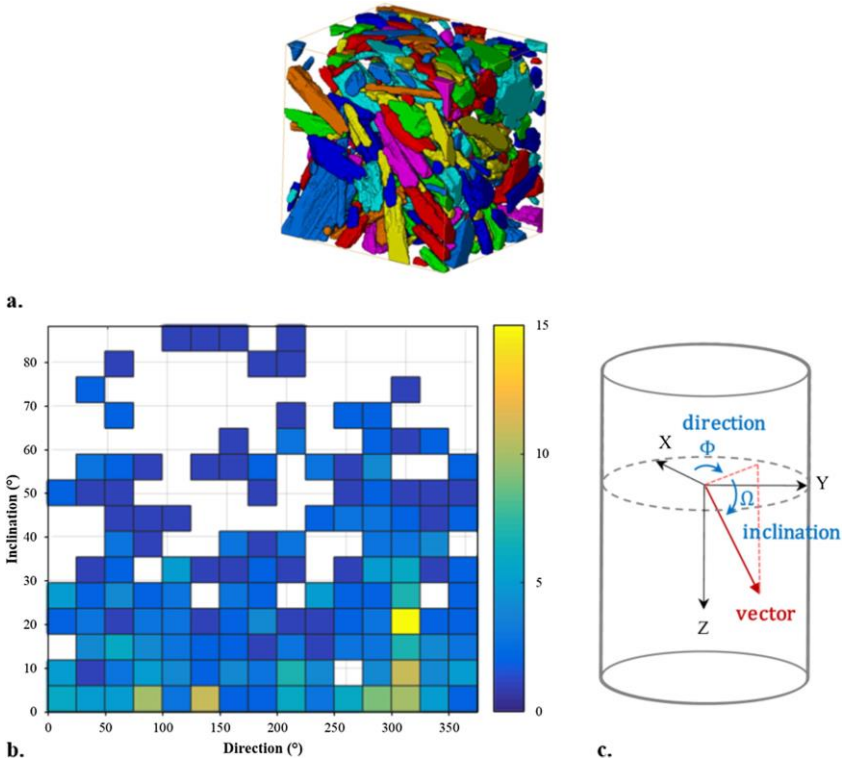

(b) Measured by X-ray tomography [18].

Figure 1.16. Orientation of plant fibers in concrete [18,82].

The orientation of the bio-aggregate in the concrete is closely related to the compaction process. Williams et al. [99] investigated the effect of three layer thicknesses (25, 50, and 150 mm) and three compaction levels (30%, 45%, and 60% volume reduction compared to the non-compacted state) on the mechanical and thermal properties of the concrete. **Figure 1.17** (a) shows the relationship between the

compressive rupture stress of hemp concrete and the degree of compaction and layer thickness. The compressive rupture stress of hemp concrete increases significantly with the compaction level and has no clear relationship with the layer thickness. Also, there is a significant difference in the failure mode of the hemp concrete in parallel and perpendicular directions as shown in **Figure 1.17** (b). This is related to the specific arrangement of plant fibers. It can be seen from **Figure 1.17** (c) that the vertical thermal conductivity of hemp concrete is greater than the parallel thermal conductivity, which is on average 16% higher. This difference is greater than that in compressive rupture stress. Moreover, both parallel and vertical thermal conductivities increase with the compaction level and approximately do not vary with layer thickness. Overall, the orientation of the bio-aggregate can influence the behavior of the concrete.

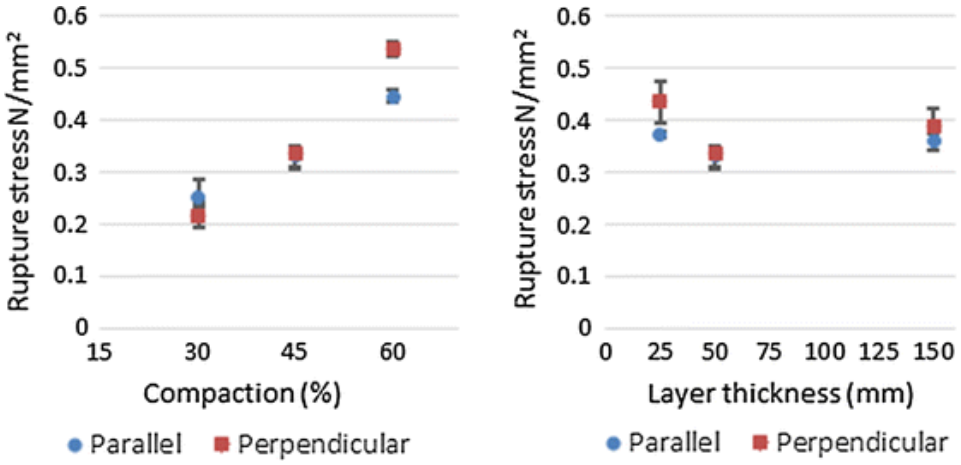

(a) Compressive rupture stress.

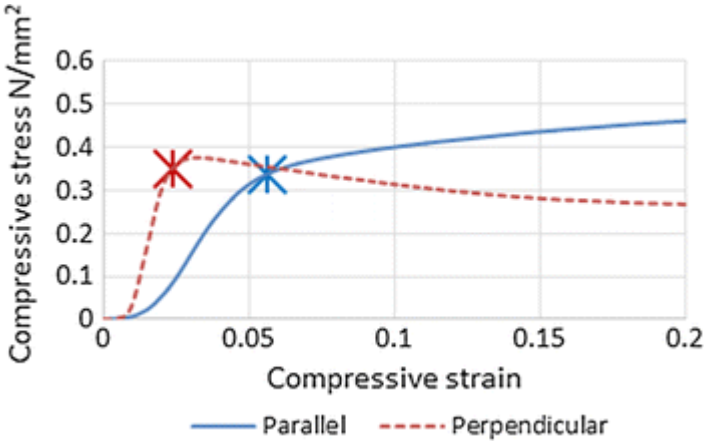

(b) Stress-strain curves of hemp concrete in parallel and perpendicular directions.

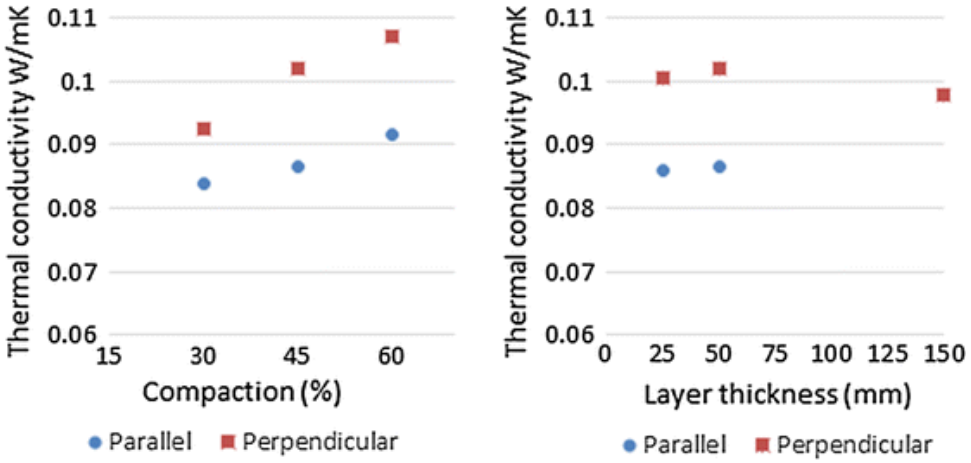

(c) Thermal conductivity.

Figure 1.17. Mechanical properties (a) (b) and thermal conductivity (c) of hemp concrete at different compaction levels and layer thickness [99].

1.4.5. Moisture

Bio-based concrete has strong water absorption. The thermal conductivity of water is much higher than that of dry concrete. Moisture has a significant effect on the thermal conductivity of concrete. **Figure 1.18** shows the significant increase in thermal conductivity of corn stalk concrete with moisture in three binders (OPC: ordinary Portland cement, GP: geopolymer, MPC: magnesium phosphate cement) and three pretreatment methods (UCS: untreated corn stalk, ACS: alkalization process, LCS: hydrophobization process).

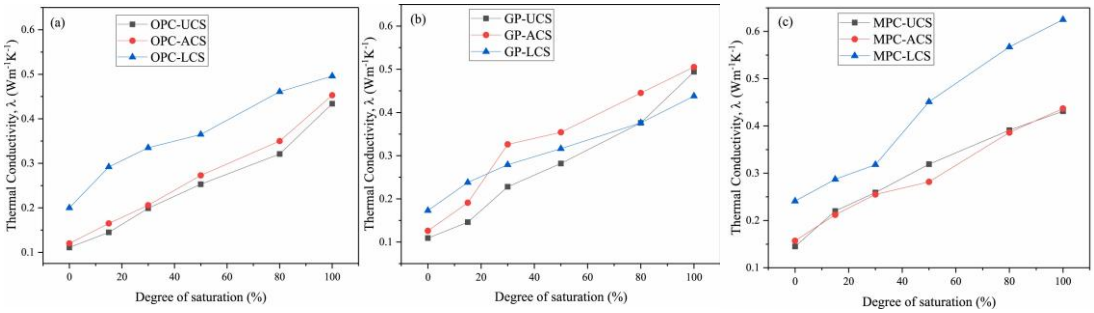

Figure 1.18. Effect of moisture on the thermal conductivity [45].

The effect of moisture on the mechanical properties of bio-based concrete is more on the setting. Humid environments like 75% and 98% RH greatly slow down the setting of hemp concrete [100]. This is the fact that high moisture impedes the diffusion of carbon dioxide in the pores of the lime mortar [101].

1.4.6. Density

The density of bio-based concrete is an indicator that combines several factors such as the type, shape and percentage of bio-aggregates, degree of compaction, porosity, moisture, etc. The variation of thermal conductivity of hemp concrete with dry density in the literature was summarized by Seng et al [23], as shown in **Figure 1.19**. Although the change in density may be due to a variety of factors. In general, the higher the density, the higher the thermal conductivity.

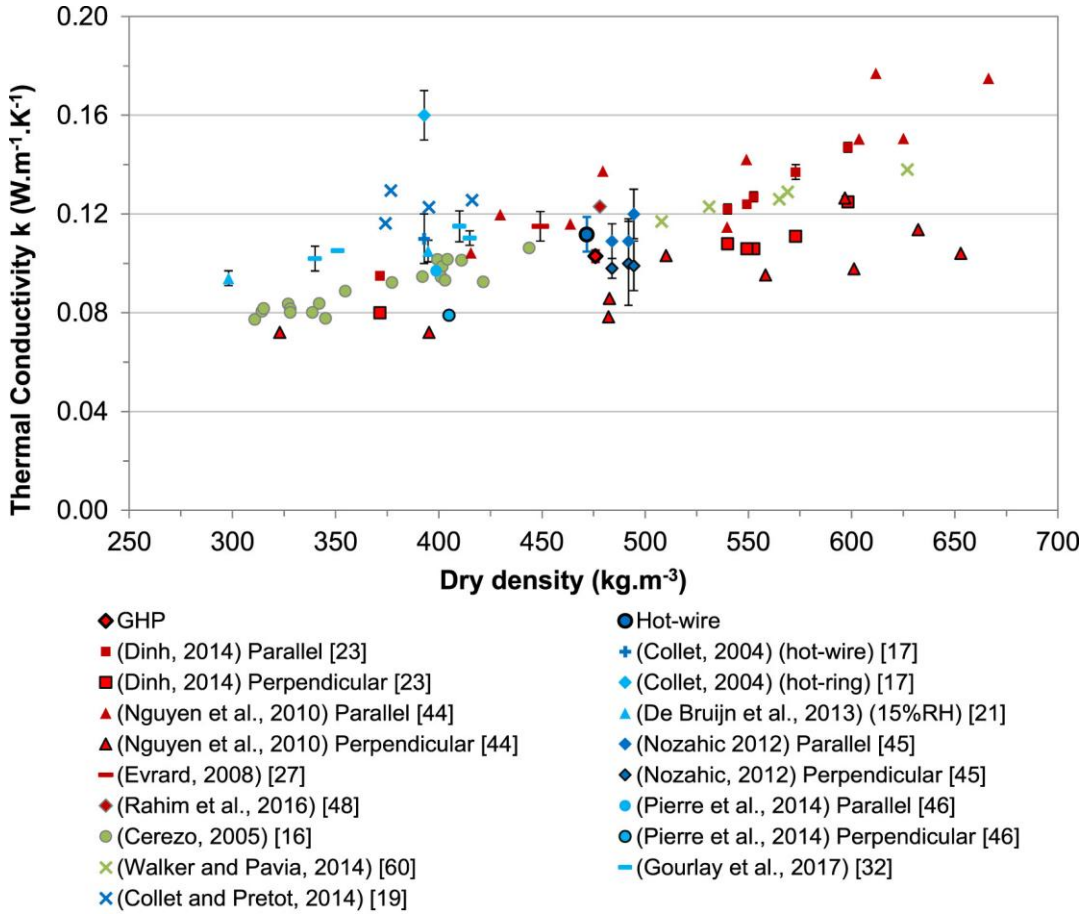

Figure 1.19. Thermal conductivity of hemp concrete with dry density [23].

1.4.7. Plant surface treatment

Due to porosity, surface properties, biodegradability, and sugar leaching, the bonding in the interfacial transition zone between the bio-aggregate and the binder is weak [54,102–104]. Wu et al. [54] pretreated apricot shell by five methods: cement solution (CS), waterproof agent (WP), wood oil (WO), sodium silicate (SS), white latex (WL), as shown in **Figure 1.20**. It can be seen that WP and CS can improve the compressive strength of concrete while WO decreases it. The fact that WO impairs mechanical properties can also be found on splitting tensile strength, flexural strength and elasticity modulus (**Table 1.9**). The WO treatment

forms a hydrophobic film, which increases the porosity of the concrete [54,105]. The positive effect of the WP treatment comes from the waterproof agent, which promotes the hydration of the binder [54].

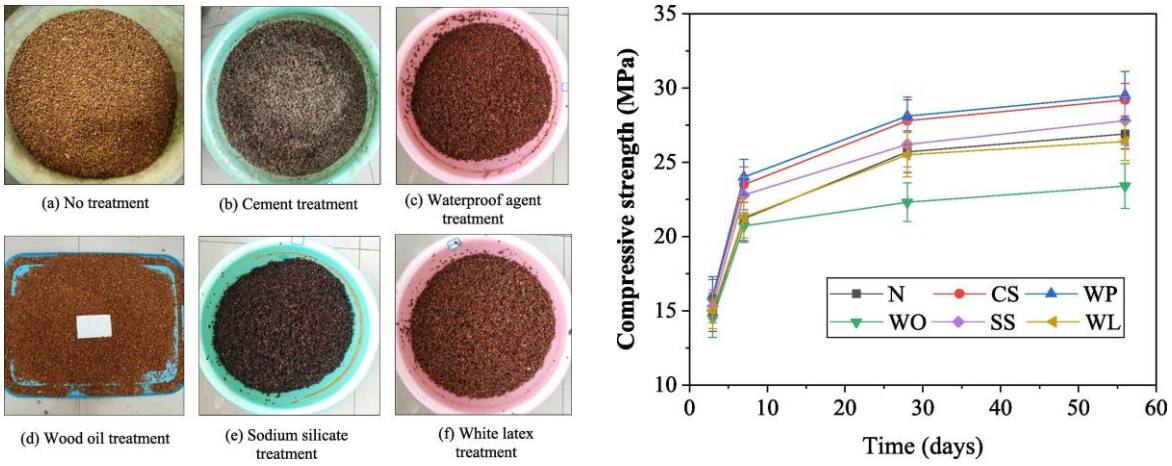

Figure 1.20. Surface treatment of apricot shell and compressive strength of corresponding concrete [54].

Mix code	Splitting tensile strength (MPa)	Flexural strength (MPa)	Modulus of elasticity (GPa)
N	2.21 ± 0.14	3.65 ± 0.22	10.4 ± 0.4
CS	2.43 ± 0.15	3.97 ± 0.20	12.1 ± 0.5
WP	2.57 ± 0.17	4.20 ± 0.24	12.4 ± 0.3
WO	1.91 ± 0.20	3.24 ± 0.25	9. 7 ± 0.5
SS	2.31 ± 0.16	3.82 ± 0.23	10.6 ± 0.4
WL	2.30 ± 0.13	3.72 ± 0.29	10.3 ± 0.3

Table 1.9. Mechanical properties of apricot shell concrete after surface treatment [54].

The study from [45] compared the effects of pretreatment methods on the thermal properties of corn stalk concrete, as shown in **Figure 1.21**. The abbreviations on this figure refer to Section 1.4.5. The thermal conductivity and heat capacity of ACS (alkalization with NaOH) and LCS (hydrophobic with linseed oil) concrete are higher compared to that of the untreated concrete. In detail, the enhancement effect of LCS was more significant than ACS, especially for thermal conductivity. The authors [45] explained this as pretreatment increasing the density of the concrete. Considering that bio-based concrete is generally used for building insulation, the pretreatment reduces the thermal insulation although it increases the mechanical properties as well. In practical applications, a balance between mechanical properties and thermal insulation

should be obtained. For example, ACS pretreatment can increase the mechanical properties of concrete while maintaining approximately no decrease in thermal insulation.

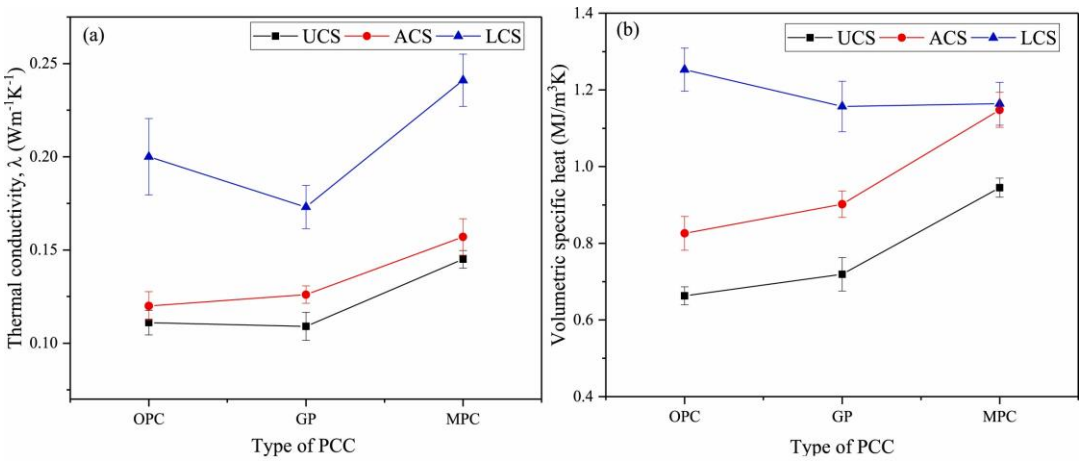

Figure 1.21. Effect of pretreatment on the thermal properties of corn stalk concrete [45].

1.4.8. Temperature

Figure 1.22 (top) illustrates the effect of temperature on the thermal conductivity of corn stalk concrete with three binders and three pretreatment methods for nine formulations as described in Section 1.4.5. It can be seen that the thermal conductivity increases with temperature from 20°C to 50°C regardless of the binder and pretreatment. This can be explained by the fact that high temperatures enhance the heat transfer in the pores [45,106]. Seng et al. [23] gave an empirical equation for dry hemp concrete with temperature as shown in **Figure 1.22** (bottom).

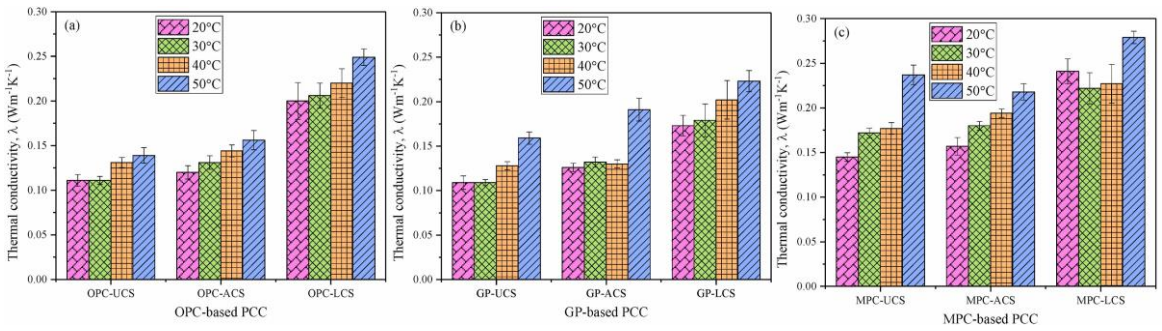

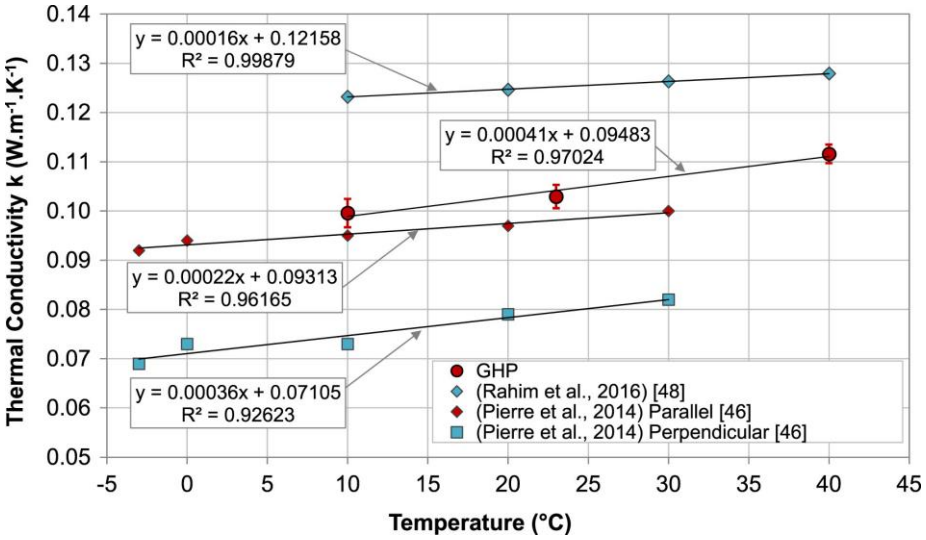

Figure 1.22. Thermal conductivity of corn stalk (top) and hemp (bottom) concrete with temperature [23,45].

1.4.9. Aging

The study as in **Figure 1.23** shows the stress-strain curves of hemp concrete at five ages (21 days, 3 months, 6 months, 15 months, 24 months). The hardening kinetics of bio-based concrete is slower compared to normal concrete. Hemp concrete has good ductility at early ages. As the age increases, the ductility of the concrete decreases but the compressive strength increases. The authors [100] explained that at early ages the binder hydrate does not form a network of connections and at this time the behavior of the concrete is more reflected in the hemp. After a long time of setting, the binder takes the main stress under strain.

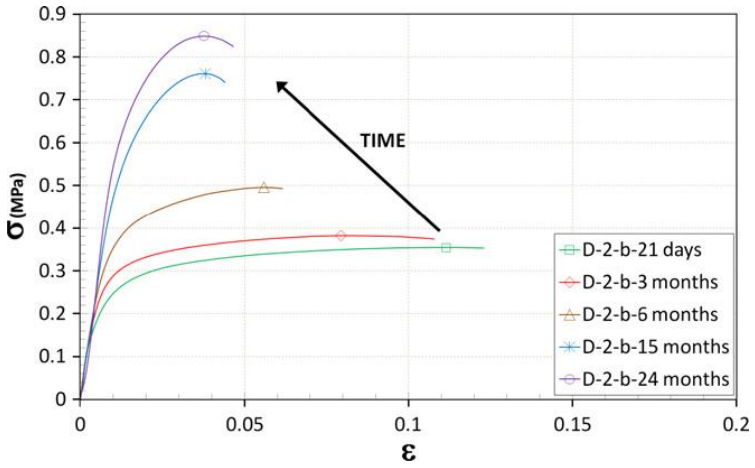

Figure 1.23. Effect of aging on compressive strength test [100].

1.5. Modeling of bio-based concrete

As mentioned above, numerous factors can influence the mechanical and thermal conductivity of bio-based materials. Understanding the mechanisms by which these factors affect macroscopic behavior can help to analyze, predict, and optimize material properties. However, figuring out the impact of these micro- and meso-level factors on macro-level behavior requires enormous time and economic costs in experimental campaigns. Moreover, some factors are difficult to characterize experimentally and control quantitatively. For example, it is difficult to set a planned bio-aggregate distribution through the manufacturing process. Thus, quantitative study of the effect of bio-aggregate distribution on macroscopic behavior cannot be achieved through experiments. Analytical and numerical simulations are attractive alternatives to experiments. Analytical methods based on micromechanics have been widely used for various heterogeneous composite materials. However, it is rarely involved in the field of bio-based construction materials. Due to the complex microstructure of bio-based building materials, i.e., heterogeneity of bio-aggregates, orientation distribution of fibers or particles, shape of fibers, pores of different sizes, high water absorption, imperfect contact between bio-aggregates and binders, etc. Therefore, it is difficult to apply existing models from other materials directly to bio-based materials. It is necessary to develop an applicable and novel model according to the specificity of bio-based materials.

Although micromechanical models based on micro-geometric features on bio-based concrete have not been studied much so far, they serve as an important reference for the development of novel models. Most of the current analytical models in this field are based on conventional mean field homogenization methods (MFH), which is derived from the Eshelby solution [107]. Several classical theories have been developed according to different assumptions about the interaction between inclusions. The most commonly used of these is the Mori-Tanaka (MT) scheme [108]. In addition, self-consistent scheme (SC) [109] and double inclusion scheme (DI) [110,111] are also widely used for the micromechanics and homogenization of heterogeneous materials [112]. SC schemes based on the assumption of composite spheres have long been used for modeling building materials such as aerated concrete [113] and rubber waste concrete [114]. The same approach has been applied directly to bio-based concrete. It was applied by Cerezo [43] back in 2005 for modeling the mechanics and thermal conductivity of hemp concrete. Subsequently, it appeared on the modeling of various plant fiber concretes [19,115–117]. In the SC scheme the phases of the heterogeneous material are assumed to be an assembly of composite spheres [19], as shown in **Figure 1.24** (a). Most of these models are in the dry state. In this case, the bio-based concrete is considered to contain three phases, with the small, medium, and large spheres in **Figure 1.24** (b) representing air, bio-aggregate, and binder, respectively. Further, Onésippe-Potiron et al. [116] developed SC to be used in wet bio-based concrete (**Figure 1.24** (c)). This homogenization process consists of two steps. First step: homogenization of bio-aggregate (f) and binder to form a medium (sf), second step: medium (sf) is homogenized with air (a), water (w). The SC scheme can roughly estimate the equivalent mechanical properties and thermal conductivity of bio-based materials, and

the calculation process is simple and easy to understand with concise formulas. However, it ignores the orientation distribution and shape of the bio-aggregates, the shape of the voids inside the bio-aggregates, the different scales of the pores, and the homogenization sequence does not consider the effect of scale.

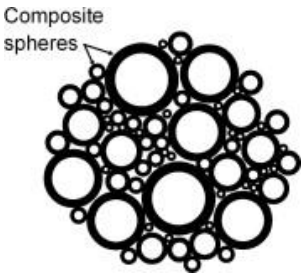

(a) Assumption of composite spheres for multiple phases

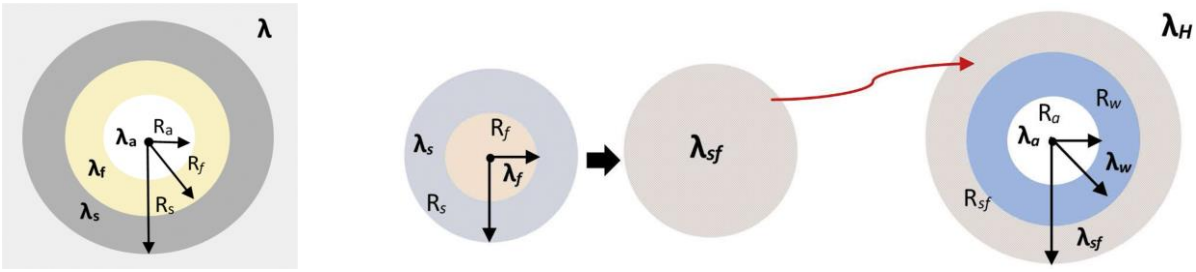

(b) Modeling in dry state

(c) Modeling in wet state

Figure 1.24. Self-consistent scheme in the modelling of bio-based concrete.

In fact, mathematical descriptions of the orientation and shape of the fibers have been provided in the studies of other composites. a series of papers by Giraud et al. [118–120] and a Ph.D. thesis by Huynh [121] described the orientation distribution function (ODF, denoted by W (θ_φ, φ_α)) to define the fiber orientation and the aspect ratio of the ellipsoid to define the fiber shape. Specifically, an ellipsoidal inclusion of arbitrary orientation is embedded in the matrix to form a two-phase heterogeneous material. The coordinate system associated with the matrix is the global coordinate system, while the coordinate system associated with the inclusions is the local coordinate system. The arbitrarily oriented inclusion is realized by a two-step rotation φ_α and θ_φ between the two coordinate systems, as shown in **Figure 1.25** (a). For inclusions in multiple directions, the contributions of all inclusions can be accounted by integration over the unit sphere [118]:

$$\frac{1}{4\pi}\int_{\varphi_\alpha=0}^{2\pi}\int_{\theta_\alpha=0}^{\pi} W(\theta_\alpha,\varphi_\alpha)\sin\theta_\alpha d\theta_\alpha d\varphi_\alpha = 1 \qquad (1)$$

For the transversely isotropic orientation distribution, ODF depends only on θ_α and can be expressed as [118]:

$$W(\theta_\alpha) = \frac{\sigma \cosh(\sigma \cos(\theta_\alpha))}{\sinh(\sigma)} \quad (2)$$

σ is the parameter related to the degree of the preferred alignment. $\sigma = 0$ represents the average distribution of fibers over 0 to 180°, and A→∞ indicates an aligned distribution. The effect of parameter σ on the fiber orientation distribution is shown in **Figure 1.25** (b).

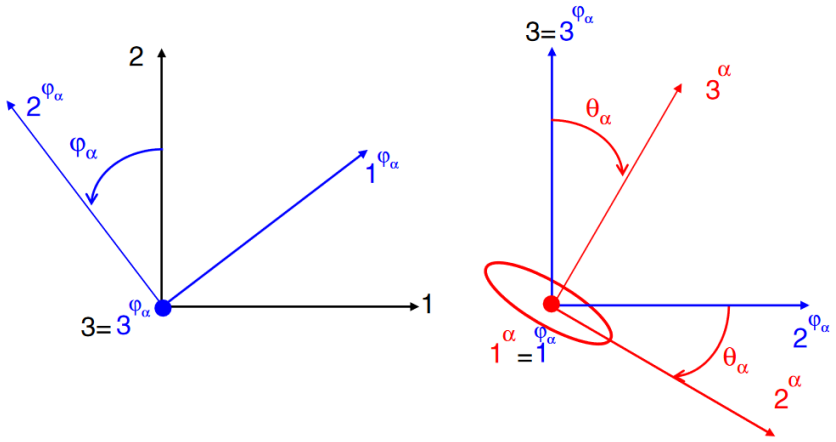

(a) Transformation between local (associated to the inclusion) and global coordinate (associated to the matrix).

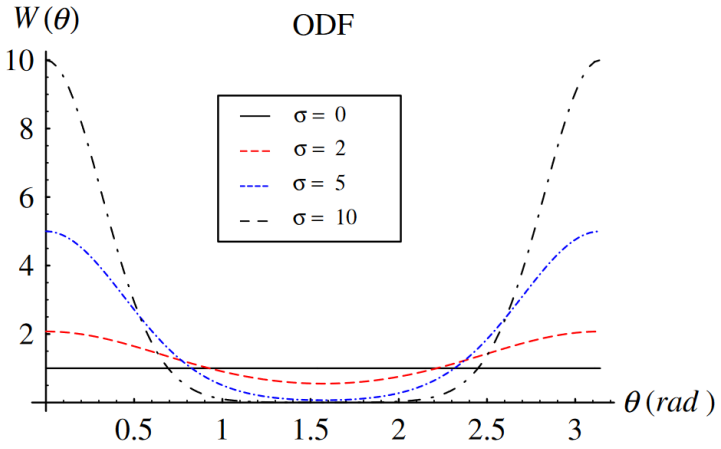

(b) Orientation distribution function.

Figure 1.25. Mathematical description of the orientation of ellipsoidal inclusions [118].

Accordingly, the above-mentioned approach to the shape and orientation of inclusions is used for bio-based materials although there are only a few examples up to now. Nguyen-Sy et al. [122] and Tran-Le et al. [123] developed a multiscale model to predict the effective thermal conductivity of dry hemp concrete by the

MFH method. In that model, the hemp particles are considered as two-phase materials containing a solid phase and oriented pores, and the lime-based binder is considered to consist of an isotropic solid phase and pores. The homogenization process was executed on porous binder, porous hemp, and dry hemp concrete, respectively. The comparison of simulated data with experimental data showed the reliability of this model in terms of parallel and perpendicular thermal conductivity. Note that ODF was used to measure the orientation distribution of the hemp particles in the binder. However, the parameters of the ODF were obtained after several inverse analyses. This may only work under similarly formulated hemp concrete and processing conditions, while the applicability of fiber distribution for a wide range of bio-based materials is yet to be investigated. By the fact, it was mentioned in Section 1.4.4 that plant fiber orientation can now be characterized by image analysis or X-ray tomography. However, the ODF approach in this model cannot directly utilize the data from fiber orientation measurements. Moreover, the above model is only used for dry bio-based materials. The high-water absorption of bio-based concrete can have a significant effect on the thermal conductivity.

Another study [124] developed a multiscale model of the effective thermal conductivity for wet hemp shives in bulk. Individual hemp shiv was assumed to be a three-phase composite of solid phase, air, and water. This study introduced the effect of moisture into the modeling of hemp materials and provided ideas for this purpose. However, this study only focused on hemp shives in bulk and no binder was involved. As far as I have shown, subsequent studies have not taken moisture into account for the multi-scale micromechanical modeling of bio-based concrete. Furthermore, this study obtained by inverse analysis a thermal conductivity of 0.5755 $W \cdot m^{-1} \cdot K^{-1}$ for the solid phase of individual hemp, which is a very critical parameter for the modeling of hemp materials. Most studies have focused on the properties of hemp concrete rather than individual hemp fibers, but data on individual hemp fiber for multi-scale modeling. Experimental measurements of the thermal properties of small-thickness materials are difficult, especially when samples are millimeter-scale or smaller [125]. Pierre et al. [125] measured the longitudinal thermal conductivity of individual hemp fiber to be 0.124 ± 0.023 $W \cdot m^{-1} \cdot K^{-1}$ by the original method developed by Rémy et al [126]. This study performed transient temperature measurements through an infrared camera and circumvented the boundary condition problem [125,126]. Then on this basis, Glé et al. [127] calculated the thermal conductivity of the hemp solid phase based on the density difference using the MHF method. As a result, the density and longitudinal thermal conductivity of individual porous hemp are 265 ± 15 $kg \cdot m^{-3}$ and 0.124 ± 0.023 $W \cdot m^{-1} \cdot K^{-1}$, while they are 1454 $kg \cdot m^{-3}$ and 0.564 ± 0.126 $W \cdot m^{-1} \cdot K^{-1}$ for the solid phase. It can be seen that this result is close to the one obtained by the inverse analysis of hemp shivs in bulk. Of course, this varies on hemp samples from different sources due to the varying porosity.

In addition, MFH methods have good approximations at low-volume fractions. In contrast, its prediction for high inclusions volume has been criticized [112,128]. For instance, the study in the literature [129] demonstrated that the Mori-Tanaka-based micromechanical model well predicts the effective piezoelectric strain constants at low volume fractions (0.15). But beyond this, the average relative difference is up to about 30%. Although when the volume of the inclusions is higher than that of the matrix, the "inverse Mori-Tanaka method" [130] can be used, i.e., the matrix is considered as an inclusion. However, this is only a compromise solution because it does not completely solve the problem of high volume and the inclusions may have a complex orientation distribution and shape. The iterative approach can reduce the volume fraction at each step. [131] implemented an iterative homogenization for hemp concrete, but the macropores were not counted, as shown in **Figure 1.26**. Generally, the macropore increases with the percentage of plant aggregates due to its elongated shape. Thus, it is more realistic to consider both macropore and aggregate in each step of the iteration.

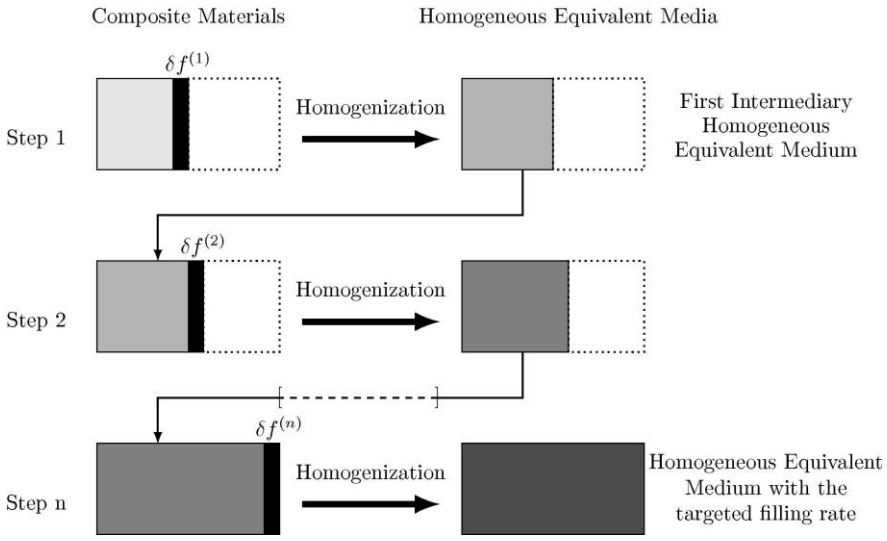

Figure 1.26. Iterative homogenization method from [131].

Some methods based on 3D numerical models are also applicable to bio-based concrete. [132] developed a numerical model with spatial distribution, size, and shape to predict the thermal conductivity and mechanical behavior of straw concrete, as shown in **Figure 1.27**. This model performs well with an intuitive visualization, but has limitations in terms of volume fraction and computational cost compared to the analytical method. With the development of 3D X-ray reconstruction techniques, a 3D realistic structure (see **Figure 1.28**) based on a bio-based concrete sample can also be used for modeling various properties [76]. It is closer to the real material structure than the traditional numerical model. Nevertheless, this model cannot be used for parametric analysis and material optimization because of the immutability of the structure.

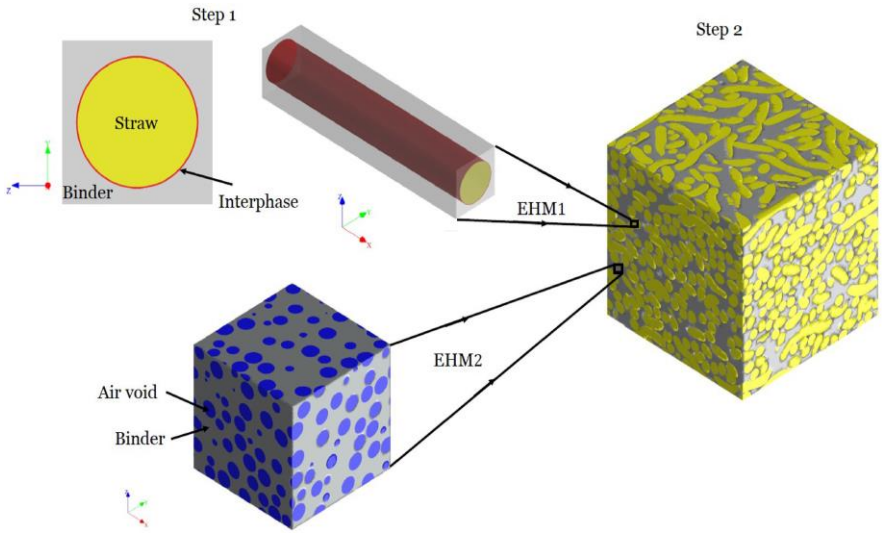

Figure 1.27. FEM models for straw concrete [132].

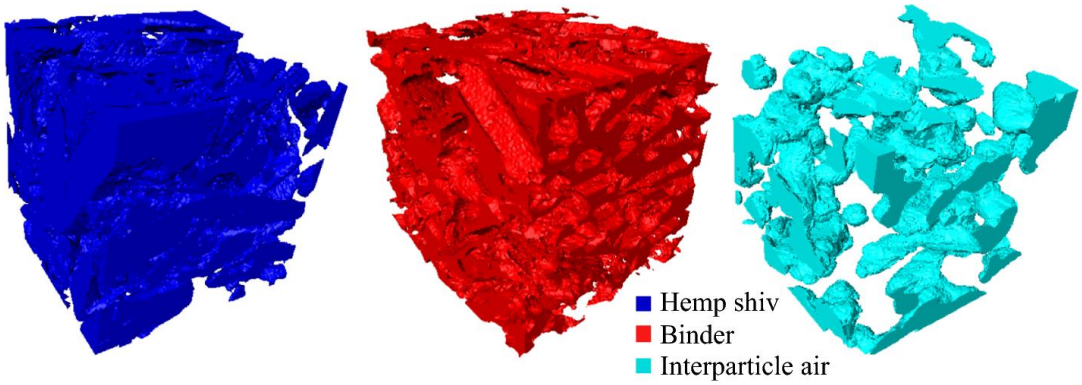

Figure 1.28. 3D X-ray tomography reconstruction [76].

1.6. Conclusion

Carbon emissions and energy consumption in the construction industry are a growing concern. Bio-based concrete has great potential to address these issues. However, the current modeling of bio-based concrete has many shortcomings as follows.

a) Compared to other materials, including fiber reinforced materials, there are fewer models for bio-based concrete.

b) Existing models of bio-based materials focus on hygrothermal properties rather than mechanical properties and thermal conductivity.

c) Few studies consider factors such as moisture, imperfect contact, anisotropy and shape of bio-aggregates in the model of bio-based materials.

d) A multiscale structure is necessary in the model of bio-based concrete because of the complex microstructures. However, existing models are not detailed enough to study the multiscale structure, such as the difference of pore structure in different plants and three sizes of pores in the material.

e) Existing models are developed based on only one type of bio-aggregate.

f) Plant fiber orientation is usually defined with probability density functions in existing studies, but this method cannot utilize data from X-ray tomography.

g) Existing iterative methods lack consideration of macropores.

Therefore, this study proposes a multi-scale homogenization model for mechanical properties and thermal conductivity applicable to a wide range of bio-based construction materials. This model considers the above issues and predicts, evaluates, and optimizes the macroscopic behavior of bio-based materials in terms of microscopic morphological characteristics. Chapter 2 describes the mechanical behavior of the bio-based material, while Chapter 3 deals with the thermal conductivity. Chapter 4 combines the mechanical behavior and thermal insulation to optimize the bio-based material by a multi-objective optimization method.

1.7. References

[1] Is cooling the future of heating? – Analysis, IEA. (n.d.). https://www.iea.org/commentaries/is-cooling-the-future-of-heating (accessed November 2, 2022).

[2] A. Arrigoni, D.K. Panesar, M. Duhamel, T. Opher, S. Saxe, I.D. Posen, H.L. MacLean, Life cycle greenhouse gas emissions of concrete containing supplementary cementitious materials: cut-off vs. substitution, Journal of Cleaner Production. 263 (2020) 121465. https://doi.org/10.1016/j.jclepro.2020.121465.

[3] F. Benmahiddine, F. Bennai, R. Cherif, R. Belarbi, A. Tahakourt, K. Abahri, Experimental investigation on the influence of immersion/drying cycles on the hygrothermal and mechanical properties of hemp concrete, Journal of Building Engineering. 32 (2020) 101758. https://doi.org/10.1016/j.jobe.2020.101758.

[4] Climate Change 2022: Mitigation of Climate Change, (n.d.). https://www.ipcc.ch/report/ar6/wg3/ (accessed May 16, 2022).

[5] E.A.J. Hirst, P. Walker, K.A. Paine, T. Yates, Characteristics of low-density hemp-lime building materials, Proceedings of the Institution of Civil Engineers - Construction Materials. 165 (2012) 15–23. https://doi.org/10.1680/coma.1000021.

[6] X. Li, W. Wu, C.W.F. Yu, Energy demand for hot water supply for indoor environments: Problems and perspectives, Indoor and Built Environment. 24 (2015) 5–10. https://doi.org/10.1177/1420326X14564285.

[7] B. Mazhoud, F. Collet, S. Pretot, C. Lanos, Mechanical properties of hemp-clay and hemp stabilized clay composites, Construction and Building Materials. 155 (2017) 1126–1137. https://doi.org/10.1016/j.conbuildmat.2017.08.121.

[8] O. Kaynakli, A review of the economical and optimum thermal insulation thickness for building applications, Renewable and Sustainable Energy Reviews. 16 (2012) 415–425. https://doi.org/10.1016/j.rser.2011.08.006.

[9] Buildings, IEA. (2022). https://www.iea.org/reports/buildings (accessed October 31, 2022).

[10] B. Lin, Z. Chen, Net zero energy building evaluation, validation and reflection – A successful project application, Energy and Buildings. 261 (2022) 111946. https://doi.org/10.1016/j.enbuild.2022.111946.

[11] W. Wu, H.M. Skye, Residential net-zero energy buildings: Review and perspective, Renewable and Sustainable Energy Reviews. 142 (2021) 110859. https://doi.org/10.1016/j.rser.2021.110859.

[12] Green Buildings, World Economic Forum. (2021). https://www.weforum.org/realestate/green-buildings/ (accessed November 2, 2022).

[13] E. Ohene, A.P.C. Chan, A. Darko, Prioritizing barriers and developing mitigation strategies toward net-zero carbon building sector, Building and Environment. 223 (2022) 109437. https://doi.org/10.1016/j.buildenv.2022.109437.

[14] N. Asim, Z. Emdadi, M. Mohammad, M.A. Yarmo, K. Sopian, Agricultural solid wastes for green desiccant applications: an overview of research achievements, opportunities and perspectives, Journal of Cleaner Production. 91 (2015) 26–35. https://doi.org/10.1016/j.jclepro.2014.12.015.

[15] D. Jiang, S. Lv, S. Cui, S. Sun, X. Song, S. He, J. Zhang, P. An, Effect of thermal insulation components on physical and mechanical properties of plant fibre composite thermal insulation mortar, Journal of Materials Research and Technology. 9 (2020) 12996–13013. https://doi.org/10.1016/j.jmrt.2020.09.009.

[16] G. He, T. Liu, M. Zhou, Straw burning, PM2.5, and death: Evidence from China, Journal of Development Economics. 145 (2020) 102468. https://doi.org/10.1016/j.jdeveco.2020.102468.

[17] M.R. Ahmad, B. Chen, S. Yousefi Oderji, M. Mohsan, Development of a new bio-composite for building insulation and structural purpose using corn stalk and magnesium phosphate cement, Energy and Buildings. 173 (2018) 719–733. https://doi.org/10.1016/j.enbuild.2018.06.007.

[18] M. Lagouin, C. Magniont, P. Sénéchal, P. Moonen, J.-E. Aubert, A. Laborel-préneron, Influence of types of binder and plant aggregates on hygrothermal and mechanical properties of vegetal concretes, Construction and Building Materials. 222 (2019) 852–871. https://doi.org/10.1016/j.conbuildmat.2019.06.004.

[19] F. Collet, S. Pretot, Thermal conductivity of hemp concretes: Variation with formulation, density and water content, Construction and Building Materials. 65 (2014) 612–619. https://doi.org/10.1016/j.conbuildmat.2014.05.039.

[20] World Agricultural Production, USDA Foreign Agricultural Service. (2022). https://www.fas.usda.gov/data/world-agricultural-production (accessed June 13, 2022).

[21] M.P. Sáez-Pérez, M. Brümmer, J.A. Durán-Suárez, A review of the factors affecting the properties and performance of hemp aggregate concretes, Journal of Building Engineering. 31 (2020) 101323. https://doi.org/10.1016/j.jobe.2020.101323.

[22] Y.X. Chen, F. Wu, Q. Yu, H.J.H. Brouwers, Bio-based ultra-lightweight concrete applying miscanthus fibers: Acoustic absorption and thermal insulation, Cement and Concrete Composites. 114 (2020) 103829. https://doi.org/10.1016/j.cemconcomp.2020.103829.

[23] B. Seng, C. Magniont, S. Lorente, Characterization of a precast hemp concrete. Part I: Physical and thermal properties, Journal of Building Engineering. 24 (2019) 100540. https://doi.org/10.1016/j.jobe.2018.07.016.

[24] J. Zhao, S. Li, Life cycle cost assessment and multi-criteria decision analysis of environment-friendly building insulation materials - A review, Energy and Buildings. 254 (2022) 111582. https://doi.org/10.1016/j.enbuild.2021.111582.

[25] G. Churkina, A. Organschi, C.P.O. Reyer, A. Ruff, K. Vinke, Z. Liu, B.K. Reck, T.E. Graedel, H.J. Schellnhuber, Buildings as a global carbon sink, Nat Sustain. 3 (2020) 269–276. https://doi.org/10.1038/s41893-019-0462-4.

[26] F. Ntimugura, R. Vinai, A.B. Harper, P. Walker, Environmental performance of miscanthus-lime lightweight concrete using life cycle assessment: Application in external wall assemblies, Sustainable Materials and Technologies. 28 (2021) e00253. https://doi.org/10.1016/j.susmat.2021.e00253.

[27] G.M. Cappucci, V. Ruffini, V. Barbieri, C. Siligardi, A.M. Ferrari, Life cycle assessment of wheat husk based agro-concrete block, Journal of Cleaner Production. 349 (2022) 131437. https://doi.org/10.1016/j.jclepro.2022.131437.

[28] K. Ip, A. Miller, Life cycle greenhouse gas emissions of hemp–lime wall constructions in the UK, Resources, Conservation and Recycling. 69 (2012) 1–9. https://doi.org/10.1016/j.resconrec.2012.09.001.

[29] A. Galimshina, M. Moustapha, A. Hollberg, P. Padey, S. Lasvaux, B. Sudret, G. Habert, Bio-based materials as a robust solution for building renovation: A case study, Applied Energy. 316 (2022) 119102. https://doi.org/10.1016/j.apenergy.2022.119102.

[30] R. Hasan, Md.H.R. Sobuz, A.S.M. Akid, Md.R. Awall, M. Houda, A. Saha, Md.M. Meraz, Md.S. Islam, N.M. Sutan, Eco-friendly self-consolidating concrete production with reinforcing jute fiber, Journal of Building Engineering. 63 (2023) 105519. https://doi.org/10.1016/j.jobe.2022.105519.

[31] J. Pokorný, R. Ševčík, J. Šál, L. Fiala, L. Zárybnická, L. Podolka, Bio-based aggregate in the production of advanced thermal-insulating concrete with improved acoustic performance, Construction and Building Materials. 358 (2022) 129436. https://doi.org/10.1016/j.conbuildmat.2022.129436.

[32] R. Belloum, B. Agoudjil, N. Chennouf, A. Boudenne, Hygrothermal performance assessment of a bio-based building made with date palm concrete walls, Building and Environment. 223 (2022) 109467. https://doi.org/10.1016/j.buildenv.2022.109467.

[33] E. Krasny, S. Klarić, A. Korjenić, Analysis and comparison of environmental impacts and cost of bio-based house versus concrete house, Journal of Cleaner Production. 161 (2017) 968–976. https://doi.org/10.1016/j.jclepro.2017.05.103.

[34] T. Jami, S.R. Karade, L.P. Singh, A review of the properties of hemp concrete for green building applications, Journal of Cleaner Production. 239 (2019) 117852. https://doi.org/10.1016/j.jclepro.2019.117852.

[35] S. Barbhuiya, B. Bhusan Das, A comprehensive review on the use of hemp in concrete, Construction and Building Materials. 341 (2022) 127857. https://doi.org/10.1016/j.conbuildmat.2022.127857.

[36] Bio-based products, (n.d.). https://ec.europa.eu/growth/sectors/biotechnology/bio-based-products_en (accessed June 16, 2022).

[37] M.F. Junaid, Z. ur Rehman, M. Kuruc, I. Medveď, D. Bačinskas, J. Čurpek, M. Čekon, N. Ijaz, W.S. Ansari, Lightweight concrete from a perspective of sustainable reuse of waste byproducts, Construction and Building Materials. 319 (2022) 126061. https://doi.org/10.1016/j.conbuildmat.2021.126061.

[38] F. Wu, Q. Yu, C. Liu, Durability of thermal insulating bio-based lightweight concrete: Understanding of heat treatment on bio-aggregates, Construction and Building Materials. 269 (2021) 121800. https://doi.org/10.1016/j.conbuildmat.2020.121800.

[39] H. Zhang, Y. He, C. Wang, Y. Guan, Z. Ge, R. Sun, Y. Ling, B. Šavija, Statistical mixture design for carbide residue activated blast furnace slag foamed lightweight concrete, Construction and Building Materials. 342 (2022) 127840. https://doi.org/10.1016/j.conbuildmat.2022.127840.

[40] J. Shi, B. Liu, Y. Liu, E. Wang, Z. He, H. Xu, X. Ren, Preparation and characterization of lightweight aggregate foamed geopolymer concretes aerated using hydrogen peroxide, Construction and Building Materials. 256 (2020) 119442. https://doi.org/10.1016/j.conbuildmat.2020.119442.

[41] S.K. Adhikary, D.K. Ashish, H. Sharma, J. Patel, Ž. Rudžionis, M. Al-Ajamee, B.S. Thomas, J.M. Khatib, Lightweight self-compacting concrete: A review, Resources, Conservation & Recycling Advances. 15 (2022) 200107. https://doi.org/10.1016/j.rcradv.2022.200107.

[42] R. Merli, M. Preziosi, A. Acampora, M.C. Lucchetti, E. Petrucci, Recycled fibers in reinforced concrete: A systematic literature review, Journal of Cleaner Production. 248 (2020) 119207. https://doi.org/10.1016/j.jclepro.2019.119207.

[43] V. CEREZO, Propriétés mécaniques, thermiques et acoustiques d'un matériau à base de particules végétales : approche expérimentale et modélisation théorique, These de doctorat, INSA Lyon, 2005. https://www.theses.fr/2005ISAL0037.

[44] H. Binici, M. Eken, M. Dolaz, O. Aksogan, M. Kara, An environmentally friendly thermal insulation material from sunflower stalk, textile waste and stubble fibres, Construction and Building Materials. 51 (2014) 24–33. https://doi.org/10.1016/j.conbuildmat.2013.10.038.

[45] M.R. Ahmad, B. Chen, M.A. Haque, S.M. Saleem Kazmi, M.J. Munir, Development of plant-concrete composites containing pretreated corn stalk bio-aggregates and different type of binders, Cement and Concrete Composites. 121 (2021) 104054. https://doi.org/10.1016/j.cemconcomp.2021.104054.

[46] M. Rahim, O. Douzane, A.D. Tran Le, T. Langlet, Effect of moisture and temperature on thermal properties of three bio-based materials, Construction and Building Materials. 111 (2016) 119–127. https://doi.org/10.1016/j.conbuildmat.2016.02.061.

[47] M. Rahim, O. Douzane, A.D. Tran Le, G. Promis, T. Langlet, Characterization and comparison of hygric properties of rape straw concrete and hemp concrete, Construction and Building Materials. 102 (2016) 679–687. https://doi.org/10.1016/j.conbuildmat.2015.11.021.

[48] B. Haba, B. Agoudjil, A. Boudenne, K. Benzarti, Hygric properties and thermal conductivity of a new insulation material for building based on date palm concrete, Construction and Building Materials. 154 (2017) 963–971. https://doi.org/10.1016/j.conbuildmat.2017.08.025.

[49] M. Asim, G.M. Uddin, H. Jamshaid, A. Raza, Z. ul Rehman Tahir, U. Hussain, A.N. Satti, N. Hayat, S.M. Arafat, Comparative experimental investigation of natural fibers reinforced light weight concrete as thermally efficient building materials, Journal of Building Engineering. 31 (2020) 101411. https://doi.org/10.1016/j.jobe.2020.101411.

[50] S. Janani, P. Kulanthaivel, G. Sowndarya, H. Srivishnu, P.G. Shanjayvel, Study of coconut shell as coarse aggregate in light weight concrete- a review, Materials Today: Proceedings. 65 (2022) 2003–2006. https://doi.org/10.1016/j.matpr.2022.05.329.

[51] B. Ismail, N. Belayachi, D. Hoxha, Optimizing performance of insulation materials based on wheat straw, lime and gypsum plaster composites using natural additives, Construction and Building Materials. 254 (2020) 118959. https://doi.org/10.1016/j.conbuildmat.2020.118959.

[52] R.V. Ratiarisoa, C. Magniont, S. Ginestet, C. Oms, G. Escadeillas, Assessment of distilled lavender stalks as bioaggregate for building materials: Hygrothermal properties, mechanical performance and chemical interactions with mineral pozzolanic binder, Construction and Building Materials. 124 (2016) 801–815. https://doi.org/10.1016/j.conbuildmat.2016.08.011.

[53] M. Chabannes, J.-C. Bénézet, L. Clerc, E. Garcia-Diaz, Use of raw rice husk as natural aggregate in a lightweight insulating concrete: An innovative application, Construction and Building Materials. 70 (2014) 428–438. https://doi.org/10.1016/j.conbuildmat.2014.07.025.

[54] F. Wu, Q. Yu, C. Liu, H.J.H. Brouwers, L. Wang, Effect of surface treatment of apricot shell on the performance of lightweight bio-concrete, Construction and Building Materials. 229 (2019) 116859. https://doi.org/10.1016/j.conbuildmat.2019.116859.

[55] W. Long, Y. Wang, Effect of pine needle fibre reinforcement on the mechanical properties of concrete, Construction and Building Materials. 278 (2021) 122333. https://doi.org/10.1016/j.conbuildmat.2021.122333.

[56] A. Akkaoui, S. Caré, M. Vandamme, Experimental and micromechanical analysis of the elastic properties of wood-aggregate concrete, Construction and Building Materials. 134 (2017) 346–357. https://doi.org/10.1016/j.conbuildmat.2016.12.084.

[57] H.H. Ratsimbazafy, Évaluation du potentiel de co-produits agricoles locaux valorisables dans le domaine des matériaux de construction (PALOMAC), phdthesis, Université Paul Sabatier - Toulouse III, 2022. https://tel.archives-ouvertes.fr/tel-03699668 (accessed September 30, 2022).

[58] Herinjaka Haga Ratsimbazafy, Aurélie Laborel-Préneron, Camille Magniont, Philippe Evon, A Review of the Multi-Physical Characteristics of Plant Aggregates and Their Effects on the Properties of Plant-Based Concrete, RPM. 03 (2021) 1–1. https://doi.org/10.21926/rpm.2102026.

[59] M. Birjukovs, M. Sinka, A. Jakovics, D. Bajare, Combined in situ and in silico validation of a material model for hempcrete, Construction and Building Materials. 321 (2022) 126051. https://doi.org/10.1016/j.conbuildmat.2021.126051.

[60] Y. Shang, F. Tariku, Hempcrete building performance in mild and cold climates: Integrated analysis of carbon footprint, energy, and indoor thermal and moisture buffering, Building and Environment. 206 (2021) 108377. https://doi.org/10.1016/j.buildenv.2021.108377.

[61] O. Kinnane, A. Reilly, J. Grimes, S. Pavia, R. Walker, Acoustic absorption of hemp-lime construction, Construction and Building Materials. 122 (2016) 674–682. https://doi.org/10.1016/j.conbuildmat.2016.06.106.

[62] J. Williams, M. Lawrence, P. Walker, The influence of constituents on the properties of the bio-aggregate composite hemp-lime, Construction and Building Materials. 159 (2018) 9–17. https://doi.org/10.1016/j.conbuildmat.2017.10.109.

[63] K.H. Mo, U.J. Alengaram, M.Z. Jumaat, S.P. Yap, S.C. Lee, Green concrete partially comprised of farming waste residues: a review, Journal of Cleaner Production. 117 (2016) 122–138. https://doi.org/10.1016/j.jclepro.2016.01.022.

[64] M.R. Ahmad, B. Chen, S.F. Ali Shah, Mechanical and microstructural characterization of bio-concrete prepared with optimized alternative green binders, Construction and Building Materials. 281 (2021) 122533. https://doi.org/10.1016/j.conbuildmat.2021.122533.

[65] S. Arufe, A. Hellouin de Menibus, N. Leblanc, H. Lenormand, Physico-chemical characterisation of plant particles with potential to produce biobased building materials, Industrial Crops and Products. 171 (2021) 113901. https://doi.org/10.1016/j.indcrop.2021.113901.

[66] S. Allegret, The history of hemp., Hemp: Industrial Production and Uses. (2013) 4–26. https://doi.org/10.1079/9781845937935.0004.

[67] S. Allin, Building with Hemp, SeedPress, 2005.

[68] A.T.M.F. Ahmed, M.Z. Islam, M.S. Mahmud, M.E. Sarker, M.R. Islam, Hemp as a potential raw material toward a sustainable world: A review, Heliyon. 8 (2022) e08753. https://doi.org/10.1016/j.heliyon.2022.e08753.

[69] S. Elfordy, F. Lucas, F. Tancret, Y. Scudeller, L. Goudet, Mechanical and thermal properties of lime and hemp concrete (“hempcrete”) manufactured by a projection process, Construction and Building Materials. 22 (2008) 2116–2123. https://doi.org/10.1016/j.conbuildmat.2007.07.016.

[70] S. Mom, Modèle d’homogénéisation itérative numérique pour des milieux non linéaires morphologiquement riches : application aux comportements de bétons de chanvre, These de doctorat, Paris 6, 2013. https://www.theses.fr/2013PA066558 (accessed December 16, 2022).

[71] C. Magwood, Essential Hempcrete Construction: The Complete Step-by-Step Guide, New Society Publishers, 2016.

[72] How to Insulate a Roof ?, Weber Tradical. (n.d.). https://www.weber-tradical.com/en/hempcrete/beton-de-chanvre-toiture-isolante/ (accessed December 12, 2022).

[73] What is Hempcrete and How to Use It for Construction ?, Weber Tradical. (n.d.). https://www.weber-tradical.com/en/hempcrete/what-is-hempcrete-2/ (accessed December 12, 2022).

[74] IsoHemp - Sustainable building and renovating with hempcrete blocks, IsoHemp - Sustainable Building and Renovating with Hempcrete Blocks. (n.d.). https://www.isohemp.com/en (accessed November 25, 2022).

[75] F. Bennai, C. El Hachem, K. Abahri, R. Belarbi, Microscopic hydric characterization of hemp concrete by X-ray microtomography and digital volume correlation, Construction and Building Materials. 188 (2018) 983–994. https://doi.org/10.1016/j.conbuildmat.2018.08.198.

[76] F. Bennai, K. Abahri, R. Belarbi, Contribution to the Modelling of Coupled Heat and Mass Transfers on 3D Real Structure of Heterogeneous Building Materials: Application to Hemp Concrete, Transp Porous Med. 133 (2020) 333–356. https://doi.org/10.1007/s11242-020-01426-9.

[77] M. Viel, F. Collet, C. Lanos, Chemical and multi-physical characterization of agro-resources' by-product as a possible raw building material, Industrial Crops and Products. 120 (2018) 214–237. https://doi.org/10.1016/j.indcrop.2018.04.025.

[78] M.S. Abbas, E. Gourdon, P. Glé, F. McGregor, M.Y. Ferroukhi, A. Fabbri, Relationship between hygrothermal and acoustical behavior of hemp and sunflower composites, Building and Environment. 188 (2021) 107462. https://doi.org/10.1016/j.buildenv.2020.107462.

[79] P.A. Chabriac, E. Gourdon, P. Gle, A. Fabbri, H. Lenormand, Agricultural by-products for building insulation: Acoustical characterization and modeling to predict micro-structural parameters, Construction and Building Materials. 112 (2016) 158–167. https://doi.org/10.1016/j.conbuildmat.2016.02.162.

[80] P. Bouloc, Le chanvre industriel: production et utilisations, France Agricole Editions, 2006.

[81] T. Jami, D. Rawtani, Y.K. Agrawal, Hemp concrete: carbon-negative construction, Emerging Materials Research. 5 (2016) 240–247. https://doi.org/10.1680/jemmr.16.00122.

[82] J. Williams, M. Lawrence, P. Walker, A method for the assessment of the internal structure of bio-aggregate concretes, Construction and Building Materials. 116 (2016) 45–51. https://doi.org/10.1016/j.conbuildmat.2016.04.088.

[83] V. Nozahic, Vers une nouvelle démarche de conception des bétons de végétaux lignocellulosiques basée sur la compréhension et l'amélioration de l'interface liant / végétal : application à des granulats de chenevotte et de tige de tournesol associés à un liant ponce / chaux, phdthesis, Université Blaise Pascal - Clermont-Ferrand II, 2012. https://tel.archives-ouvertes.fr/tel-00822142 (accessed October 10, 2022).

[84] E. Awwad, M. Mabsout, B. Hamad, M.T. Farran, H. Khatib, Studies on fiber-reinforced concrete using industrial hemp fibers, Construction and Building Materials. 35 (2012) 710–717. https://doi.org/10.1016/j.conbuildmat.2012.04.119.

[85] M. Chabannes, F. Becquart, E. Garcia-Diaz, N.-E. Abriak, L. Clerc, Experimental investigation of the shear behaviour of hemp and rice husk-based concretes using triaxial compression, Construction and Building Materials. 143 (2017) 621–632. https://doi.org/10.1016/j.conbuildmat.2017.03.148.

[86] K. Zhao, S. Xue, P. Zhang, Y. Tian, P. Li, Application of Natural Plant Fibers in Cement-Based Composites and the Influence on Mechanical Properties and Mass Transport, Materials. 12 (2019) 3498. https://doi.org/10.3390/ma12213498.

[87] L. Li, Z. Cai, K. Yu, Y.X. Zhang, Y. Ding, Performance-based design of all-grade strain hardening cementitious composites with compressive strengths from 40 MPa to 120 MPa, Cement and Concrete Composites. 97 (2019) 202–217. https://doi.org/10.1016/j.cemconcomp.2019.01.001.

[88] L.D. Hung Anh, Z. Pásztory, An overview of factors influencing thermal conductivity of building insulation materials, Journal of Building Engineering. 44 (2021) 102604. https://doi.org/10.1016/j.jobe.2021.102604.

[89] F. Bennai, N. Issaadi, K. Abahri, R. Belarbi, A. Tahakourt, Experimental characterization of thermal and hygric properties of hemp concrete with consideration of the material age evolution, Heat Mass Transfer. 54 (2018) 1189–1197. https://doi.org/10.1007/s00231-017-2221-2.

[90] F. Bennai, M.Y. Ferroukhi, F. Benmahiddine, R. Belarbi, A. Nouviaire, Assessment of hygrothermal performance of hemp concrete compared to conventional building materials at overall building scale, Construction and Building Materials. 316 (2022) 126007. https://doi.org/10.1016/j.conbuildmat.2021.126007.

[91] M. Rahim, O. Douzane, A.D. Tran Le, G. Promis, B. Laidoudi, A. Crigny, B. Dupre, T. Langlet, Characterization of flax lime and hemp lime concretes: Hygric properties and moisture buffer capacity, Energy and Buildings. 88 (2015) 91–99. https://doi.org/10.1016/j.enbuild.2014.11.043.

[92] B. Moujalled, Y. Aït Ouméziane, S. Moissette, M. Bart, C. Lanos, D. Samri, Experimental and numerical evaluation of the hygrothermal performance of a hemp lime concrete building: A long term case study, Building and Environment. 136 (2018) 11–27. https://doi.org/10.1016/j.buildenv.2018.03.025.

[93] R. Haik, G. Bar-Nes, A. Peled, I.A. Meir, Alternative unfired binders as lime replacement in hemp concrete, Construction and Building Materials. 241 (2020) 117981. https://doi.org/10.1016/j.conbuildmat.2019.117981.

[94] A. Williams, Essential guides for building designers: lime green–traditional mortar mixes for today–NBS shortcut 88, (2009).

[95] Ecology of Building Materials, Routledge, 2007. https://doi.org/10.4324/9780080504988.

[96] Tradical - Building lime innovation, (n.d.). https://www.tradical.com/tradical-pf70.html (accessed January 11, 2023).

[97] F. Benmahiddine, R. Cherif, F. Bennai, R. Belarbi, A. Tahakourt, K. Abahri, Effect of flax shives content and size on the hygrothermal and mechanical properties of flax concrete, Construction and Building Materials. 262 (2020) 120077. https://doi.org/10.1016/j.conbuildmat.2020.120077.

[98] T.T. Nguyen, V. Picandet, P. Carre, T. Lecompte, S. Amziane, C. Baley, Effect of compaction on mechanical and thermal properties of hemp concrete, European Journal of Environmental and Civil Engineering. 14 (2010) 545–560. https://doi.org/10.1080/19648189.2010.9693246.

[99] J. Williams, M. Lawrence, P. Walker, The influence of the casting process on the internal structure and physical properties of hemp-lime, Mater Struct. 50 (2017) 108. https://doi.org/10.1617/s11527-016-0976-4.

[100] L. Arnaud, E. Gourlay, Experimental study of parameters influencing mechanical properties of hemp concretes, Construction and Building Materials. 28 (2012) 50–56. https://doi.org/10.1016/j.conbuildmat.2011.07.052.

[101] K. Van Balen, D. Van Gemert, Modelling lime mortar carbonation, Materials and Structures. 27 (1994) 393–398. https://doi.org/10.1007/BF02473442.

[102] F. Wu, C. Liu, W. Sun, L. Zhang, Y. Ma, Mechanical and Creep Properties of Concrete containing Apricot Shell Lightweight Aggregate, KSCE J Civ Eng. 23 (2019) 2948–2957. https://doi.org/10.1007/s12205-019-0738-2.

[103] G.C.H. Doudart de la Grée, Q.L. Yu, H.J.H. Brouwers, Assessing the effect of CaSO4 content on the hydration kinetics, microstructure and mechanical properties of cements containing sugars, Construction and Building Materials. 143 (2017) 48–60. https://doi.org/10.1016/j.conbuildmat.2017.03.067.

[104] F. Wu, C. Liu, L. Zhang, Y. Lu, Y. Ma, Comparative study of carbonized peach shell and carbonized apricot shell to improve the performance of lightweight concrete, Construction and Building Materials. 188 (2018) 758–771. https://doi.org/10.1016/j.conbuildmat.2018.08.094.

[105] M. Bederina, M. Gotteicha, B. Belhadj, R.M. Dheily, M.M. Khenfer, M. Queneudec, Drying shrinkage studies of wood sand concrete – Effect of different wood treatments, Construction and Building Materials. 36 (2012) 1066–1075. https://doi.org/10.1016/j.conbuildmat.2012.06.010.

[106] Y. Xu, D. Sun, Z. Zeng, H. Lv, Temperature dependence of apparent thermal conductivity of compacted bentonites as buffer material for high-level radioactive waste repository, Applied Clay Science. 174 (2019) 10–14. https://doi.org/10.1016/j.clay.2019.03.017.

[107] J.D. Eshelby, R.E. Peierls, The determination of the elastic field of an ellipsoidal inclusion, and related problems, Proceedings of the Royal Society of London. Series A. Mathematical and Physical Sciences. 241 (1957) 376–396. https://doi.org/10.1098/rspa.1957.0133.

[108] T. Mori, K. Tanaka, Average stress in matrix and average elastic energy of materials with misfitting inclusions, Acta Metallurgica. 21 (1973) 571–574. https://doi.org/10.1016/0001-6160(73)90064-3.

[109] R. Hill, A self-consistent mechanics of composite materials, Journal of the Mechanics and Physics of Solids. 13 (1965) 213–222. https://doi.org/10.1016/0022-5096(65)90010-4.

[110] S. Nemat-Nasser, M. Hori, Micromechanics: overall properties of heterogeneous materials, North Holland, Amsterdam, 1993.

[111] G. Lielens, Micro-macro modeling of structured materials, Université Catholique de Louvain, Belgium. (1999).

[112] A. Jain, Micro and mesomechanics of fibre reinforced composites using mean field homogenization formulations: A review, Materials Today Communications. 21 (2019) 100552. https://doi.org/10.1016/j.mtcomm.2019.100552.

[113] C. Boutin, Conductivité thermique du béton cellulaire autoclavé: modélisation par méthode autocohérente, Mat. Struct. 29 (1996) 609–615. https://doi.org/10.1007/BF02485968.

[114] A. Benazzouk, O. Douzane, K. Mezreb, B. Laidoudi, M. Quéneudec, Thermal conductivity of cement composites containing rubber waste particles: Experimental study and modelling, Construction and Building Materials. 22 (2008) 573–579. https://doi.org/10.1016/j.conbuildmat.2006.11.011.

[115] A. Djoudi, M.M. Khenfer, A. Bali, T. Bouziani, Effect of the addition of date palm fibers on thermal properties of plaster concrete: experimental study and modeling, Journal of Adhesion Science and Technology. 28 (2014) 2100–2111. https://doi.org/10.1080/01694243.2014.948363.

[116] C. Onésippe-Potiron, K. Bilba, A. Zaknoune, M.-A. Arsène, Auto-coherent homogenization applied to the assessment of thermal conductivity: Case of sugar cane bagasse fibers and moisture content effect, Journal of Building Engineering. 33 (2021) 101537. https://doi.org/10.1016/j.jobe.2020.101537.

[117] S.C. Somé, A. Ben Fraj, A. Pavoine, M. Hajj Chehade, Modeling and experimental characterization of effective transverse thermal properties of hemp insulation concrete, Construction and Building Materials. 189 (2018) 384–396. https://doi.org/10.1016/j.conbuildmat.2018.08.210.

[118] A. Giraud, D. Hoxha, Q.V. Huynh, D.P. Do, V. Magnenet, Effective porothermoelastic properties of transversely isotropic rock-like composites, International Journal of Engineering Science. 46 (2008) 527–550. https://doi.org/10.1016/j.ijengsci.2008.01.010.

[119] A. Giraud, Q.V. Huynh, D. Hoxha, D. Kondo, Effective poroelastic properties of transversely isotropic rock-like composites with arbitrarily oriented ellipsoidal inclusions, Mechanics of Materials. 39 (2007) 1006–1024. https://doi.org/10.1016/j.mechmat.2007.05.005.

[120] A. Giraud, I.-C. Gruescu, D.P. Do, F. Homand, D. Kondo, Effective thermal conductivity of transversely isotropic media with arbitrary oriented ellipsoïdal inhomogeneities, International Journal of Solids and Structures. 44 (9) (2007) 2627–2647. https://doi.org/10.1016/j.ijsolstr.2006.08.011.

[121] Q.V. Huynh, ESTIMATION DES PROPRIETES POROMECANIQUES EFFECTIVES DES ARGILITES: APPORT DES METHODES D'HOMOGENEISATION, phdthesis, Institut National Polytechnique de Lorraine - INPL, 2006. https://theses.hal.science/tel-00180319 (accessed December 23, 2022).

[122] T. Nguyen-Sy, A.D. Tran-Le, T. Nguyen-Thoi, T. Langlet, A multi-scale homogenization approach for the effective thermal conductivity of dry lime–hemp concrete, Journal of Building Performance Simulation. 11 (2018) 179–189. https://doi.org/10.1080/19401493.2017.1323009.

[123] A.D. Tran-Le, S.-T. Nguyen, T. Langlet, A novel anisotropic analytical model for effective thermal conductivity tensor of dry lime-hemp concrete with preferred spatial distributions, Energy and Buildings. 182 (2019) 75–87. https://doi.org/10.1016/j.enbuild.2018.09.043.

[124] Modeling thermal conductivity of hemp insulation material: A multi-scale homogenization approach, Building and Environment. 107 (2016) 127–134. https://doi.org/10.1016/j.buildenv.2016.07.026.

[125] T. Pierre, M. Carin, Characterization of the thermal properties of millimeter-sized insulating materials, International Journal of Thermal Sciences. 135 (2019) 247–255. https://doi.org/10.1016/j.ijthermalsci.2018.09.009.

[126] B. Rémy, A. Degiovanni, D. Maillet, Measurement of the In-plane Thermal Diffusivity of Materials by Infrared Thermography, Int J Thermophys. 26 (2005) 493–505. https://doi.org/10.1007/s10765-005-4511-z.

[127] P. Glé, T. Lecompte, A. Hellouin de Ménibus, H. Lenormand, S. Arufe, C. Chateau, V. Fierro, A. Celzard, Densities of hemp shiv for building: From multiscale characterisation to application, Industrial Crops and Products. 164 (2021) 113390. https://doi.org/10.1016/j.indcrop.2021.113390.

[128] M. Ferrari, Asymmetry and the high concentration limit of the Mori-Tanaka effective medium theory, Mechanics of Materials. 11 (1991) 251–256. https://doi.org/10.1016/0167-6636(91)90006-L.

[129] N. Mishra, K. Das, A Mori–Tanaka Based Micromechanical Model for Predicting the Effective Electroelastic Properties of Orthotropic Piezoelectric Composites with Spherical Inclusions, SN Appl. Sci. 2 (2020) 1206. https://doi.org/10.1007/s42452-020-2958-y.

[130] A.F. Fedotov, Mori-Tanaka experimental-analytical model for predicting engineering elastic moduli of composite materials, Composites Part B: Engineering. 232 (2022) 109635. https://doi.org/10.1016/j.compositesb.2022.109635.

[131] S. Dartois, S. Mom, H. Dumontet, A. Ben Hamida, An iterative micromechanical modeling to estimate the thermal and mechanical properties of polydisperse composites with platy particles: Application to anisotropic hemp and lime concretes, Construction and Building Materials. 152 (2017) 661–671. https://doi.org/10.1016/j.conbuildmat.2017.06.181.

[132] B. Ismail, N. Belayachi, D. Hoxha, L. Arbaret, Modelling of thermal conductivity and nonlinear mechanical behavior of straw insulation composite by a numerical homogenization approach, Journal of Building Engineering. 43 (2021) 103144. https://doi.org/10.1016/j.jobe.2021.103144.

CHAPTER II : Modeling the mechanical properties of bio-based concrete

Chapter introduction

The weak mechanical property of bio-based concrete is a potential limitation compared to traditional construction materials, making it primarily suitable for non-structural purposes in the construction industry. The microstructure of bio-based concrete plays a crucial role in determining its mechanical properties. Although optimizing mechanical properties through microstructure is feasible, quantifying the link between the two through experimental methods is challenging. Therefore, it is necessary to propose a model to predict and optimize the mechanical properties of bio-based concrete.

Homogenization using micromechanical methods can establish macro-micro connections. In this study, a multiscale model applicable to bio-based concrete is developed, taking into account the shape and orientation of the bio-aggregate, volume fraction, properties of each phase, and other characteristics on the multiscale structure. The model is validated using hemp, sunflower, and corn concrete. Furthermore, the developed model is used for parametric analysis and optimization to improve the mechanical performance of bio-based concrete. This research contributes to the development of a model that can assist in the prediction and optimization of bio-based concrete for practical applications in the construction industry.

This study was published in *Journal of Building Engineering* on October 1, 2022.

Article A: Optimization of mechanical properties in anisotropic bio-based building materials by a multiscale homogenization model

Gang Huang[a], Ariane Abou-Chakra[a, *], Joseph Absi[b], Sandrine Geoffroy[a]

[a] *Université de Toulouse, UPS, INSA, LMDC (Laboratoire Matériaux et Durabilité des Constructions), 135 Avenue de Rangueil, 31077 Toulouse Cedex 04, France*

[b] *Université de Limoges, IRCER, UMR CNRS 7315, 12 rue Atlantis, 87068 Limoges, France*

Abstract

Bio-based building material is derived mainly from waste agricultural by-products and has been intensively studied for its role in mitigating carbon emissions. This study aims to optimize its mechanical properties of bio-based building materials by a multiscale model based on micro-geometric characteristics. This model considered three common agricultural by-products: hemp, sunflower, and maize. Then the predicted results were compared with the experimental data. Moreover, the influence of the following parameters on the effective mechanical properties was investigated: volume fraction, modulus of binder and aggregate, shape, and orientation. In order to quantify the priority of each parameter in the optimization, a weight evaluation method was proposed. The analysis of the weight of these parameters shows that the modulus of the binder and the volume fraction of the plant aggregates have the greatest influence on improving the mechanical properties of the composites. When the aspect ratio of the plant particles is greater than 8, the change in their shape almost does not affect the results. Furthermore, this weight evaluation method was used in the case of bio-aggregates with high and low aspect ratios and volume fractions. The analysis shows that in the composite with a low aspect ratio, the optimization by orientation can take into account the performance in both vertical and horizontal directions. The higher the volume fraction, the better the optimization by shape and orientation. These findings provide a theoretical reference to improve the mechanical properties of bio-based building materials containing different agricultural by-products.

Keywords: Bio-based building materials, Multiscale modeling, Homogenization, Fiber orientation, Optimization.

https://doi.org/10.1016/j.jobe.2022.104890

Highlights:

· A multiscale model containing the shape and orientation of the inclusions is created.

· Various representative volume elements are developed based on the characteristics of different types of plants.

· The following parameters are studied: volume fraction, modulus of binder and aggregate, shape, and orientation.

· A weight evaluation method is proposed to quantify the influence of each parameter.

· Methods to optimize the mechanical properties of bio-based building materials are proposed.

1. Introduction

Over the past century, there has been a dramatic increase in natural resources due to the increasing population. The fastest growth from 1900 to 2005 came from construction minerals, as the most important component in the building sector, which increased by a factor of 34 [1]. These products in the building sector, especially concrete, lead to copious greenhouse gas emissions, thus aggravate climate change [2]. In the UK, 50% of carbon dioxide emissions come from buildings [3]. In the OECD countries, the building sector accounts for 40% of energy consumption and generates 36.2 trillion tonnes of carbon dioxide emissions [4]. When it comes to France, this sector accounts for 43% and 25% of energy consumption and greenhouse gases [5]. Moreover, cooling and heating of the building space require approximately 60% of the total energy consumed in the building [6].

The use of bio-based products can be an effective way to reduce carbon emissions. According to the European Commission's definition, bio-based products are materials derived partly or wholly from biological sources that can help reduce CO_2 emissions and dependence on fossil fuels [7]. On the one hand, the embodied carbon (EC) in plant aggregates is lower than that of conventional materials, i. e. the lower CO_2 emissions associated with the manufacture and construction throughout its life cycle [8]. The literature [9,10] on life cycle assessment (LCA) also demonstrates the lighter environmental impact of bio-based concrete. Moreover, it contributes to carbon sink in building materials due to the considerable amount of carbon that plants can store [11]. On the other hand, its outstanding thermal insulation [12–14] helps to save energy and thus indirectly reduces carbon emissions. Additionally, the plant aggregates used in bio-based building materials come from waste agricultural by-products, and their large deposition [15] can be a burden to industry. Therefore, this type of building material is also known as eco-friendly concrete or bio-based concrete.

Compared to conventional concrete, bio-based concrete has a high porosity, weak mechanical properties, and low density [16–18]. Therefore bio-based concrete is generally used as an insulation material for external walls, floors, and ceilings, rather than as a direct replacement for high-strength concrete due to its weak

mechanical properties [19–21]. In general, it has a high-volume fraction of plant fibers to achieve superior acoustic absorption and thermal insulation [12,13,22], which leads to a complex microstructure. These complex structures bring too many factors affecting the mechanical properties of bio-based concrete. In detail, firstly, various types of plant fibers have different shapes and internal pore structures [23–25], which requires a multi-scale analysis involving the distribution of pores inside the plant fiber. Secondly, some plant fibers such as hemp [26] and sunflower bark [27] have high aspect ratios, tamping or compaction during the manufacture of bio-based concrete can significantly affect the orientation of these fibers in the concrete. Several researchers [28,29] have investigated the effect of fiber orientation in straw bales on the properties of the material. However, the orientation distribution of fibers in bio-based concrete is more complex compared to straw bales. It has been previously observed that plant fibers tend to be perpendicular to the direction of compaction [30–32]. Most studies on orientation are based on experiments and it's difficult to quantify the relationship between orientation and material properties. Lastly, many factors affect the mechanical properties of bio-based concrete. A single-factor study is not comprehensive because of the interrelation of these factors. However, there is not an optimization scheme that simultaneously addresses all of the following factors: volume fraction, modulus of binder and aggregate, shape, and orientation.

Micromechanics is one of the effective solutions, which have been used to model a wide range of cement-based materials [33,34], but few have been carried out to predict bio-based material's behavior. Collet and Pretot [14] predicted the thermal conductivity of hemp concrete by self-consistent scheme with spherical inclusions. Somé et al. [35] developed a model containing one type of hemp shape to predict the thermal conductivity of concrete and assumed a random distribution of hemp fibers. However, most models are based on thermal conductivity and do not take into account the effects of different orientations or shapes. Studies conducted by Dartois et al. [36] and Tran-Le et al. [37] have considered the distribution of hemp fibers embedded in the concrete and include mechanical properties. But these studies only focused on hemp concrete since it has been applied in the construction industry in France as early as the 1990s [12,38,39], none of the predictions contain sunflower and maize. In fact, hemp is not produced on a large scale in the world. In detail, the global hemp area was 0.273 million ha [40] (2020), while sunflower and maize were 26 [41] (2019) and 197 [42] (average 2017–19) million ha respectively. The increase in transport distances results in additional carbon emissions. It is therefore necessary to find other locally available bio-aggregates. Recently, several experimental studies have been conducted to verify the potential of sunflower [43–45] and maize [26,27] in building materials. These two plants can be used as a substitute for conventional mineral aggregates because of their large availability in the world compared to hemp. Therefore, modeling on bio-based concrete should be expanded from hemp to more types of bio-aggregates to facilitate this substitution.

Moreover, the above-mentioned articles on modeling focus only on model development, and rarely use the model further for parametric analysis and optimization, especially involving the interconnection of multiple factors. Therefore, a multiscale model was developed, in this paper, to optimize the effective mechanical properties of bio-based building materials. This model was built on three representative volume elements (RVEs) and applied to hemp, sunflower, and maize concrete for validation. Then, the effects of volume fraction, modulus, orientation, and shape on bio-based concrete were investigated to figure out their detailed roles. It's an important step before incorporating the hygrothermal aspect to understand deeply the link between microstructure and macro behavior. Furthermore, in order to quantify the influence of these parameters, a weight evaluation method was proposed and used in the case of bio-aggregates with high and low aspect ratios and volume fractions. This evaluation method gave a priority to optimize bio-based building materials in different shapes and volume fractions. Moreover, this research took into account the shape, aspect ratio, and orientation distribution of different kinds of plant fibers, hence it is applicable to most bio-based building materials.

2. Material definition

2.1. Description of micro structure of bio-based concrete

Bio-based concrete has a more complex microstructure than ordinary concrete due to the diverse structure of plant fibers and high-volume fraction. Therefore, it is necessary to investigate the structural characteristics of bio-based concrete on multiscale before theoretical analysis. Representative elementary volume (RVE), commonly used to present the periodic structure of composite materials, was introduced to illustrate the structure of bio-based concrete. As shown in **Fig. 1**, a typical RVE concerning bio-based concrete contains binder, plant fibers, and pores. The binder has a porous structure with a random distribution of pores, its porosity depends on the types of binder and mix proportions. The plant fibers have a specific directional pore distribution, which depends on the plant species and the part of the stalk where they are located. Moreover, bio-based concrete has three types of pores, which were mentioned in other experimental studies [44]. **Fig. 1** shows only the approximate multiscale structures of three types of concrete with cylindrical and ellipsoidal fibers. The accurate shapes and orientations of fibers, which require statistical analysis, will be described in detail in the following sections.

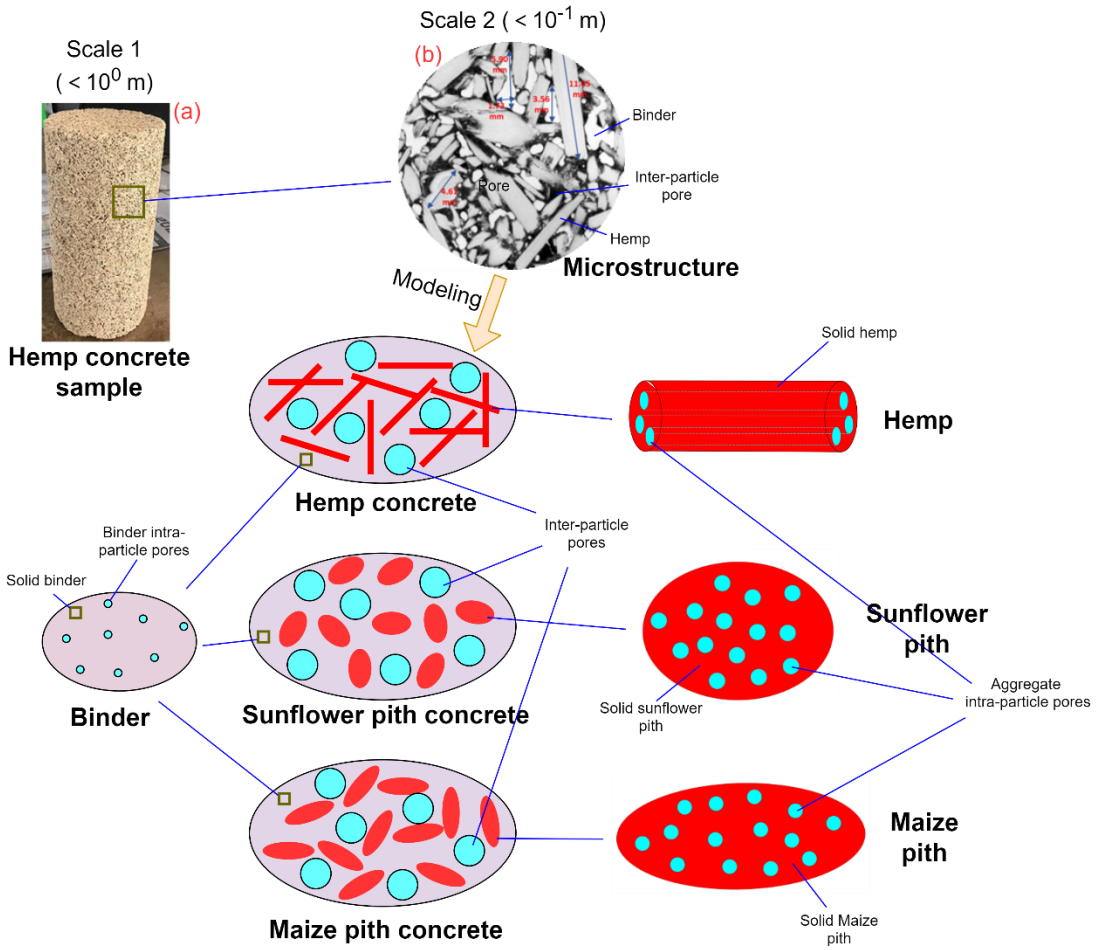

Fig. 1. Elementary volume of bio-based concretes, (a) [26], (b) [46].

2.1.1. Shape

Natural fibers have complex shapes due to their sources and manufacturing methods, so conventional gradation measurements are not sufficient to cover the exact characteristics of the fibers, which will introduce errors in the subsequent theoretical analysis. With the development of automated image analysis (AIA), it has become easier to obtain statistical characteristics such as area, diameter, and perimeter of irregular fibers [47]. Subsequently, the shape factors of the fibers can be calculated on the basis of these measurements. Aspect ratio (R) and circularity (f_{circ}) are two of the most common components of the shape factor, which only depends on the relative size, not absolute size. Circularity describes the degree of roundness of fiber and is defined in Eq. (1).

$$f_{Circ} = 4\pi \frac{S}{P^2} \quad (1)$$

The value of f_{circ} varies from 0 (infinitely elongated particle) to 1 (Circle) [48]. Aspect ratio is defined as the ratio of its maximum directed diameter to perpendicular directed diameter [47]. For ellipsoidal fibers, it is the ratio of the major axis to the minor axis. For cylindrical fibers, it is the ratio of height to diameter. **Fig. 2** illustrates this definition for both cases, i.e., the aspect ratio R=a/b. Moreover, circularity can be transformed into an aspect ratio when the shape of the inclusions is determined.

Where S and P are the area and perimeter of the projection perpendicular to A-A, as shown in **Fig. 2**. These measurements [48] require the use of the foregoing AIA method that is based on the statistics of numerous fibers. It is worth mentioning that cylinders and ellipsoids are self-symmetric, which allows parameters from two dimensions can be used in three dimensions to evaluate the shape of the fibers.

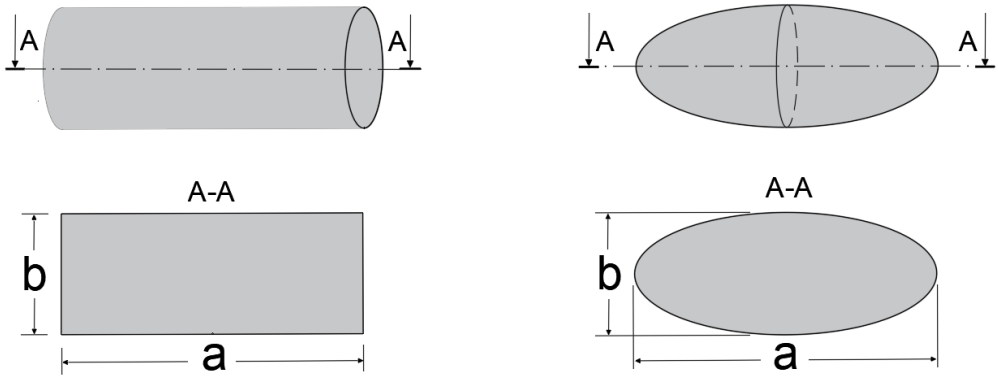

(a) Cylinder inclusion. (b) Ellipsoid inclusion.

Fig. 2. Aspect ratio (R=a/b) for cylindrical and ellipsoidal fibers.

The shape of the appearance of plant fibers can be obtained from the experimental observations, which will be described separately in **Section 2.2**. When the shape of the appearance is cylindrical, there is the following relationship between circularity and aspect ratio.

$$f_{Circ} = \frac{\pi R}{[1+R]^2} \tag{2}$$

When it has an ellipsoidal shape, the equation about circularity and aspect ratio is as follows.

$$f_{Circ} = \frac{4\pi^2 R}{\left[2\pi+4(R-1)\right]^2} \tag{3}$$

2.1.2. Orientation

Data from several studies [12,49] suggest that plant fiber concrete has different properties in the parallel direction and perpendicular direction. The reason for this is that inclusion orientation is a key factor in the anisotropy of a composite. The orientation of the fiber in the matrix is influenced by many factors, such as manufacturing method, fiber properties, boundary forms, and placing methods, etc. [50]. Therefore, it is essential to investigate the distribution of inclusions in the matrix for bio-based concrete. Since the beginning of the 21st century and especially in the last few years, x-ray tomography has been rapidly applied in cementitious materials [51]. Several researchers [27,52] have used it to observe the fiber orientation in the concrete and to obtain statistical data by computer analysis. The distribution of fibers in the bio-based concrete can be represented by two angles φ and θ, as shown in **Fig. 3**. According to Lagouin et al. [27] and Williams et al. [31,49], the orientation of the fibers in the concrete is greatly influenced by the compaction. To be specific, when the compaction direction is along the Z-axis, the elongated fibers always tend to be logically distributed in the direction perpendicular to the Z-axis. This means that the number of fibers increases with θ as can be found from the statistical results, and most fibers have a θ greater than 40° [27]. On the other hand, the fibers are not subjected to external forces in the X-Y plane, so θ is randomly but uniformly distributed in every possible value.

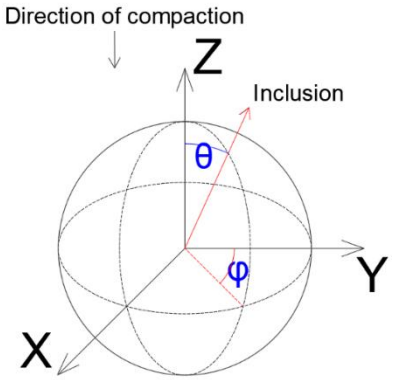

Fig. 3. Inclusion orientation depend on φ and θ.

2.2. Particularities and individual characteristics of components

2.2.1. Binder

Due to low emissions [20,21] and better compatibility with plant particles [53], lime-based binders are used in this study instead of ordinary Portland cement. This binder contains hydraulic lime, pozzolanic lime, air lime or their mixture, etc. [12,44,54]. The Young's modulus of this binder is approximately between 180 and 500 MPa [25,36,55] due to variations in components and water content. As a comparison, Young's modulus of ordinary Portland cement varies from approximately 20 to 27 GPa [56]. Nevertheless, bio-based concrete is mainly used as an insulation layer rather than for structural applications [21].

2.2.2. Hemp

From the literature [57,58], hemp is the most common plant aggregate studied for bio-based concrete despite the fact that its total mass production is the lower one in the world. In contrast, relatively few papers have been published on other agricultural by-products regardless of their proven viability in the construction industry [57]. Therefore, in this paper, hemp was selected for a benchmark in order to enrich the research on other plant aggregates. It can be found from the literature that different sources yield distinctive shapes of hemp, such as platy [36] and cylindrical particles [12,35]. Considering that the experimental data used as a comparison in **Section 4** is from near-cylindrical hemp, cylindrical fiber is used in this model. Moreover, two shapes bring the same performance when the volume fraction is low [36]. Hemp has a porous structure with internal pore distribution characteristics with reference to [58,59]. The density of hemp is 100Kg/m^3. Two types of hemp concrete, i. e. dry density of 410Kg/m^3 (porosity of 0.78) and 600Kg/m^3 (porosity of 0.70), are used in **section 4.2** [26]. **Figs. 1 and 4** show elementary representations of hemp concrete and hemp fiber.

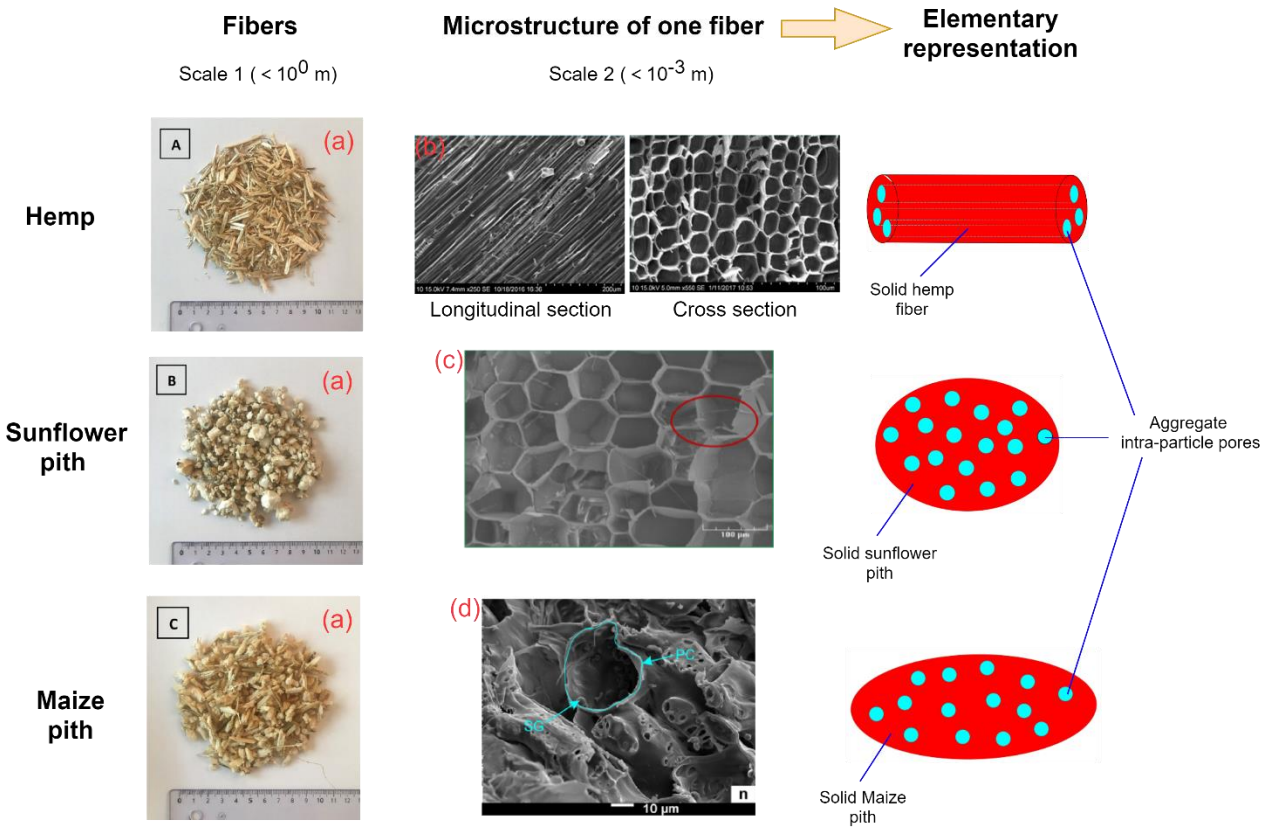

Fig. 4. Elementary representation of hemp, sunflower pith and maize pith fibers, (a) [26], (b) [46], (c) [60], (d) [32].

2.2.3. Sunflower pith

Sunflower pith has a different structure from hemp, it has an approximately ellipsoidal shape and a low aspect ratio [26]. In **Section 4**, the estimated aspect ratio according to an inverse calculation is set to 2.2. SEM photographs from [60] show that sunflower pith has a honeycomb pore structure. Therefore, elementary representations of sunflower pith concrete and sunflower pith fiber are shown in **Figs. 1 and 4**. Additionally, the density of sunflower pith is 14 Kg/m^3. In **section 4.2**, there are two types of sunflower pith concrete: dry density of 150 Kg/m^3 (porosity of 0.94) and 550 Kg/m^3 (porosity of 0.77) [26].

2.2.4. Maize pith

The maize pith particles used in Abbas et al. [26]'s experiment show a non-uniformity in size. But in general, most of the particles have a similar shape to sunflower pith, i.e., ellipsoid. Additionally, it is more elongated. Thus, its aspect ratio is set to 3. Maize and sunflower pith are located in similar locations in the plant and have densities of 18 and 14 kg/m³ [26], respectively, so their internal structures are considered similar, as shown in **Fig. 4**. Moreover, the dry density and porosity of the maize pith concrete used in **Section 4.2** are 160 Kg/m^3 and 0.92 [26].

3. Model description

According to classical theory by Eshelby [61], the fourth-order effective stiffness tensor of a composite material containing matrix and inclusions can be expressed by the following equation:

$$\mathbb{C}_{hom} = \mathbb{C}_M + \sum_{i=1}^{N} f_i \, (\mathbb{C}_i - \mathbb{C}_M) : \mathbb{A}_i \qquad (4)$$

Where the subscript M represents matrix. The subscript i represents the number of families, a family is defined as a group of inclusions with identical orientation and mechanical properties. When i is equal to 1, all inclusions have the same orientation and stiffness tensor. $\mathbb{C}_{hom}$ represents the effective stiffness tensor, $\mathbb{C}_M$, $\mathbb{C}_i$ represents the stiffness tensor in the matrix and i-th family (from 1 to N), the calculation of the stiffness tensor for homogenized material is shown in **Appendix A**. f_i represents the volume fraction of the i-th family, $\mathbb{A}_i$ represents the concentration tensor. A modified Mori-Tanaka scheme (MT) with reference to [45–47] was used in this study, which specifically took into account the orientation and shape of the inclusions embedded in the bio-based matrix. In particular, all calculations were based on the Bechterew notation [65], which will be described in **Appendix A**.

3.1. Inclusions with a parallel orientation

As shown in **Fig. 5**, two kinds of composites are considered to contain matrix and cylindrical or ellipsoidal inclusions arranged in an initial direction.

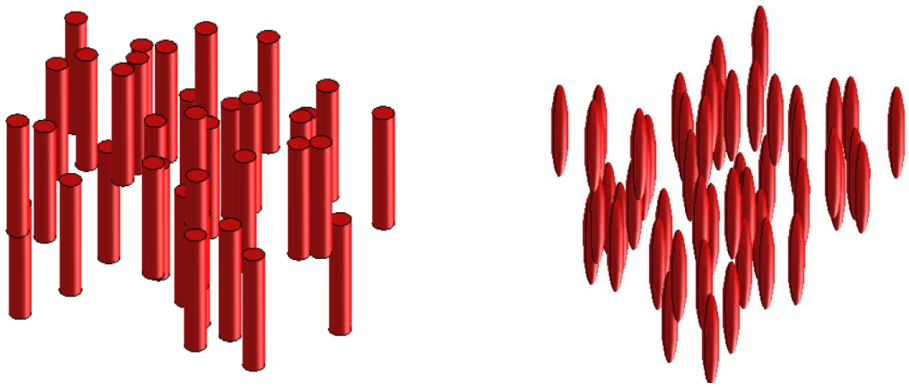

(a) Cylinder inclusions. (b) Ellipsoid inclusions.

Fig. 5. Inclusions arranged in an initial direction.

In this case, the number of families is equal to 1 because of the same orientation of all inclusions. Therefore, Eq. (4) can be recast as:

$$\mathbb{C}_{hom} = \mathbb{C}_M + f_1(\mathbb{C}_1 - \mathbb{C}_M) : \mathbb{A}_1^{MT} \quad (5)$$

In Eq. (5), $\mathbb{A}_1^{MT}$ is the concentration tensor of MT scheme and can be expressed as:

$$\mathbb{A}_1^{MT} = [\mathbb{I} + \mathbb{P}_1 : (\mathbb{C}_1 - \mathbb{C}_M)]^{-1} : [(1 - f_1)\mathbb{I} + f_1[\mathbb{I} + \mathbb{P}_1 : (\mathbb{C}_1 - \mathbb{C}_M)]^{-1}] \quad (6)$$

Where $\mathbb{P}_1$ is the Hill tensor, which depends on the stiffness tensor of the matrix and the Eshelby tensor $\mathbb{S}^E$, while the Eshelby tensor depends on the shape of the inclusions. The relationship between them can be expressed by the following equation.

$$\mathbb{P}_1 = \mathbb{S}^E : {\mathbb{C}_M}^{-1} \quad (7)$$

The components of Eshelby tensor $\mathbb{S}^E$ in Eq. (7) for cylindrical and ellipsoidal inclusions can be calculated according to Toshio Mura's book [66] and shown in **Appendix B**.

3.2. Basis transformation

$\mathbb{P}_1$ in Eq. (6) is on a local basis, but in the case of the inclusions with a given θ and φ orientation, $\mathbb{P}_1$ should be replaced by $\mathbb{P}_1(\theta,\varphi)$ that corresponds to a global basis. So, Eq. (6) can be recast as:

$$\mathbb{A}_1^{MT} = [\mathbb{I} + \mathbb{P}_1(\theta,\varphi) : (\mathbb{C}_1 - \mathbb{C}_M)]^{-1} : [(1 - f_1)\mathbb{I} + f_1[\mathbb{I} + \mathbb{P}_1(\theta,\varphi) : (\mathbb{C}_1 - \mathbb{C}_M)]^{-1}]^{-1} \quad (8)$$

In this case, the inclusions are not along the initial orientation, but the given θ and φ orientation, as shown in **Fig. 3**. Therefore, a transformation from local to global is necessary. Based on the classical Euler angles and

the shape of the inclusions in this study, two angles φ ($0< \varphi <2\ \pi$) and θ ($0< \theta < \pi$) were introduced in this study [67,68], as shown in **Fig. 6**. The process of transformation in Bechterew notation is shown in the following equation.

$$P_1(\theta,\varphi) = MP_1M^T \tag{9}$$

Where M is a rotation matrix and is given in the following equation, M^T is a transpose matrix of M.

$$M = \begin{bmatrix} g_{11}^2 & g_{12}^2 & g_{13}^2 & \sqrt{2}g_{12}g_{13} & \sqrt{2}g_{13}g_{11} & \sqrt{2}g_{11}g_{12} \\ g_{12}^2 & g_{22}^2 & g_{23}^2 & \sqrt{2}g_{22}g_{23} & \sqrt{2}g_{23}g_{21} & \sqrt{2}g_{21}g_{22} \\ g_{13}^2 & g_{23}^2 & g_{33}^2 & \sqrt{2}g_{32}g_{33} & \sqrt{2}g_{33}g_{31} & \sqrt{2}g_{31}g_{32} \\ \sqrt{2}g_{21}g_{31} & \sqrt{2}g_{22}g_{32} & \sqrt{2}g_{23}g_{33} & g_{22}g_{33}+g_{23}g_{32} & g_{23}g_{31}+g_{21}g_{33} & g_{21}g_{32}+g_{22}g_{31} \\ \sqrt{2}g_{31}g_{11} & \sqrt{2}g_{32}g_{12} & \sqrt{2}g_{33}g_{13} & g_{32}g_{13}+g_{33}g_{12} & g_{33}g_{11}+g_{31}g_{13} & g_{31}g_{12}+g_{32}g_{11} \\ \sqrt{2}g_{11}g_{21} & \sqrt{2}g_{12}g_{22} & \sqrt{2}g_{13}g_{23} & g_{12}g_{23}+g_{13}g_{22} & g_{13}g_{21}+g_{11}g_{23} & g_{11}g_{22}+g_{12}g_{21} \end{bmatrix} \tag{10}$$

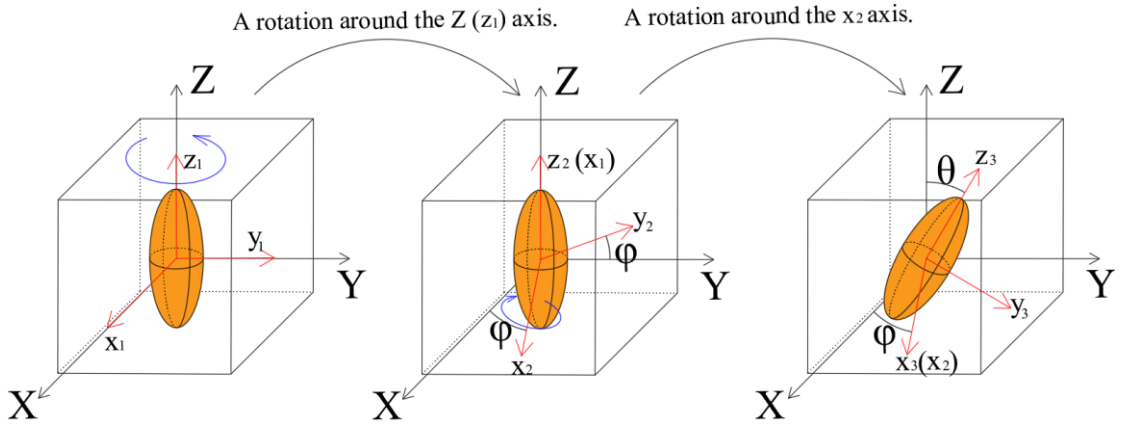

Fig. 6. Transformation between the global coordinate system (X, Y, Z) and local coordinate system (x, y, z).

Where the rotation matrix M depends on a matrix g, which is related to the Euler angles between a global and a local coordinate. g in Eq. (10) can be expressed as:

$$g = \begin{bmatrix} \cos(\varphi) & \sin(\varphi)\cos(\theta) & \sin(\varphi)\sin(\theta) \\ -\sin(\varphi) & \cos(\varphi)\cos(\theta) & \cos(\varphi)\sin(\theta) \\ 0 & -\sin(\theta) & \cos(\theta) \end{bmatrix} \tag{11}$$

3.3. Uniformly distributed but arbitrarily oriented inclusions (Isotropic case)

In this case, there is no effect of compaction on the fiber distribution, thus the inclusions are uniformly distributed but arbitrarily oriented in the matrix, as shown in **Fig. 7**. Moreover, the inclusions are rotated by

different angles based on the initial orientation to develop different new families. Therefore, in this case, the number i of families of inclusions should be considered infinite, this indicates that it covers all directions.

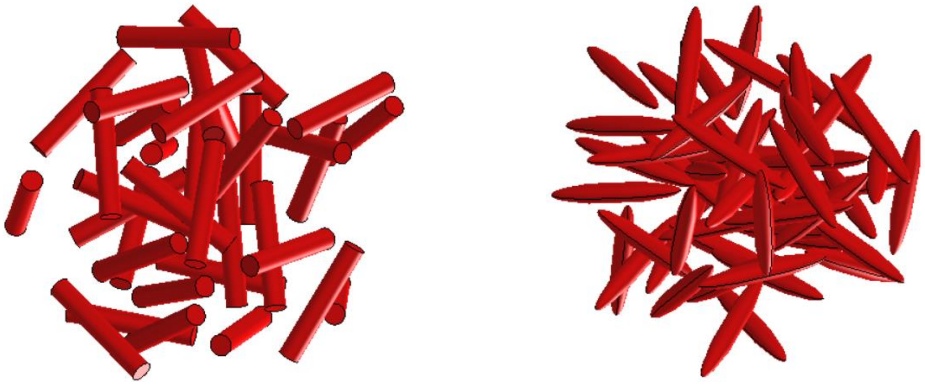

(a) Cylinder inclusions. (b) Ellipsoid inclusions.

Fig. 7. Inclusions uniformly distributed and arbitrarily oriented in the matrix.

Based on Eq. (4), the fourth-order stiffness tensor by MT scheme can be rewritten as:

$$\mathbb{C}_{hom} = \mathbb{C}_M + \sum_{i=1}^{N} f_i\,(\mathbb{C}_i - \mathbb{C}_M) : \mathbb{A}_i = \mathbb{C}_M + \sum_{i=1}^{N} f_i\,(\mathbb{C}_i - \mathbb{C}_M) : [\mathbb{I} + \mathbb{P}_i(\theta,\varphi) : (\mathbb{C}_i - \mathbb{C}_M)]^{-1} : \left[f_M \mathbb{I} + \sum_{i=1}^{N} f_i [\mathbb{I} + \mathbb{P}_i(\theta,\varphi) : (\mathbb{C}_i - \mathbb{C}_M)]^{-1}\right]^{-1} \quad (12)$$

Where f_M is the volume fraction of the matrix.

For the convenience of the calculation, $\langle \mathbb{T} \rangle$ was introduced here with reference to the literature [63], which is defined as follows:

$$\langle \mathbb{T} \rangle = \sum_{i=1}^{N} f_i \mathbb{T}_i,\ \mathbb{T}_i = [\mathbb{P}_i(\theta,\varphi) + (\mathbb{C}_i - \mathbb{C}_M)^{-1}]^{-1} \quad (13)$$

In Eq. (13), the mechanical properties of the inclusions in each family are absolutely the same and only the directions are different. Therefore, $\mathbb{C}_i$ in the i-th family can be replaced by $\mathbb{C}_1$ and Eq. (13) can be rewritten as:

$$\langle \mathbb{T} \rangle = \sum_{i=1}^{N} f_i [\mathbb{P}_i(\theta,\varphi) + (\mathbb{C}_1 - \mathbb{C}_M)^{-1}]^{-1} \quad (14)$$

Then substituting Eq. (14) into (12) and simplifying it, the effective stiffness tensor (12) can be recast as [63]:

$$\mathbb{C}_{hom} = \mathbb{C}_M + [f_M \langle \mathbb{T} \rangle^{-1} + (\mathbb{C}_1 - \mathbb{C}_M)^{-1}]^{-1} \quad (15)$$

$\langle \mathbb{T} \rangle$ in Eq. (15) is difficult to calculate, so transform it into an integral as follows:

$$\langle \mathbb{T} \rangle = \frac{f_I}{4\pi} \int_{\theta=0}^{\pi} \int_{\varphi=0}^{2\pi} [\mathbb{P}_i(\theta,\varphi) + (\mathbb{C}_1 - \mathbb{C}_M)^{-1}]^{-1} \sin\theta d\varphi d\theta \quad (16)$$

f_I in Eq. (16) is the total volume fraction of all families. For the convenience of calculation, Gauss-Legendre quadrature was introduced to calculate the double integral in Eq. (16). Prior to application, intervals [0, 2π] of φ and [0, π] of θ should be transformed into [0,1]. Let

$$\theta = \frac{\pi}{2}\theta_t + \frac{\pi}{2}, \varphi = \pi\varphi_t + \pi \tag{17}$$

Where θ_t and φ_t are new variables in the integration by substitution method to replace θ and φ, respectively.

Then (16) can be recast as:

$$\langle \mathbb{T} \rangle = \frac{f_I}{4\pi}\int_{\theta_t=-1}^{1}\int_{\varphi_t=-1}^{1}\left[\mathbb{P}_i\left(\frac{\pi}{2}\theta_t+\frac{\pi}{2},\pi\varphi_t+\pi\right)+(\mathbb{C}_1-\mathbb{C}_M)^{-1}\right]^{-1}\sin\left(\frac{\pi}{2}\theta_t+\frac{\pi}{2}\right)d(\pi\varphi_t+\pi)d\left(\frac{\pi}{2}\theta_t+\frac{\pi}{2}\right) =$$
$$\frac{\pi f_I}{8}\int_{\theta_t=-1}^{1}\int_{\varphi_t=-1}^{1}\left[\mathbb{P}_i\left(\frac{\pi}{2}\theta_t+\frac{\pi}{2},\pi\varphi_t+\pi\right)+(\mathbb{C}_1-\mathbb{C}_M)^{-1}\right]^{-1}\sin\left(\frac{\pi}{2}\theta_t+\frac{\pi}{2}\right)d(\varphi_t)d(\theta_t) \tag{18}$$

Calculate by Gauss-Legendre quadrature.

$$\langle \mathbb{T} \rangle \approx \frac{\pi f_I}{8}\sum_{u=1}^{N_{\theta_t}}\sum_{v=1}^{N_{\varphi_t}}\omega_{\theta_t}^{u}\,\omega_{\varphi_t}^{v}\left[\mathbb{P}_i\left(\frac{\pi}{2}\theta_t+\frac{\pi}{2},\pi\varphi_t+\pi\right)+(\mathbb{C}_1-\mathbb{C}_M)^{-1}\right]^{-1}\sin\left(\frac{\pi}{2}\theta_t+\frac{\pi}{2}\right) \tag{19}$$

N_{θ_t} and N_{φ_t} denote the number of integrating points, N_{φ_t}=2N_{θ_t}. θ_t, $\omega_{\theta_t}^{u}$, φ_t, $\omega_{\varphi_t}^{v}$ denote the coordinates and Gauss–Legendre weights corresponding to the N_{θ_t} and N_{φ_t} integrating points which are comprised respectively in the intervals [-1,1]. Different inclusions shapes such as cylinder and ellipsoid can be achieved by altering the Eshelby tensor.

3.4. Inclusions with anisotropic distribution

[27,31,49] have shown that the specific distribution of plant fibers leads to an anisotropic behavior of bio-based concrete on a macroscopic scale. Through the study of the microstructure of bio-based concrete in **Section 2**, we will consider here the case of inclusion with anisotropic distribution and the same stiffness C_1 embedded in an isotropic matrix of stiffness C_M.

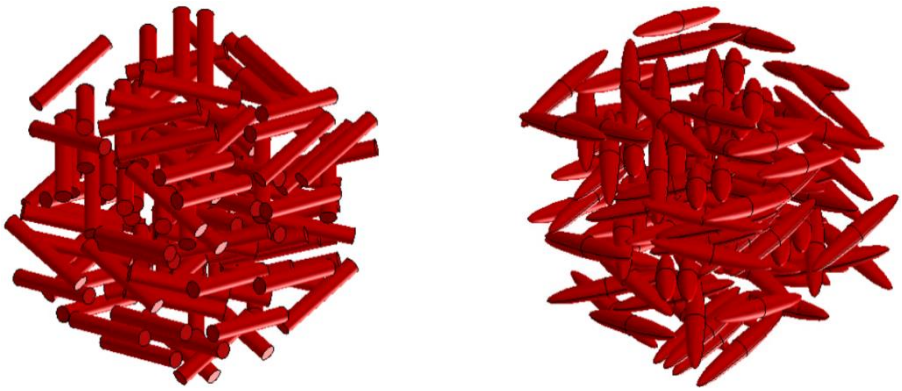

(a) Cylinder inclusions. (b) Ellipsoid inclusions.

Fig. 8. Inclusions with anisotropic distribution in bio-based concrete.

It can be seen in detail from **Section 2.1** that the plant fibers have a uniform distribution of φ on [0, 360º] and an average value of θ in bio-based concrete under the influence of compaction, as shown in **Fig. 8**. Therefore, in bio-based concrete, $\langle \mathbb{T} \rangle$ is replaced by $\langle \mathbb{T} \rangle_{bio}$, then Eq. (15) is rewritten as:

$$\mathbb{C}_{hom} = \mathbb{C}_M + \left[f_M \langle \mathbb{T} \rangle_{bio}{}^{-1} + (\mathbb{C}_1 - \mathbb{C}_M)^{-1} \right]^{-1} \tag{20}$$

With

$$\langle \mathbb{T} \rangle_{bio} = \sum_{i=1}^{N} f_i [\mathbb{P}_i(\theta^*, \varphi) + (\mathbb{C}_1 - \mathbb{C}_M)^{-1}]^{-1} \tag{21}$$

θ^* in Eq. (21) is a specific value that can be obtained from experimental observations, as detailed in **Section 2**. N should be infinite in Eq. (21), but the numerical method proves that N=50 is sufficient for this study (see **Appendix C** for details).

By the analysis above, Eq. (21) can be expressed as:

$$\langle \mathbb{T} \rangle_{bio} = \frac{f_I}{50} \sum_{i=1}^{50} \left[\mathbb{P}_i\left(\theta^*, \frac{2\pi}{50} i\right) + (\mathbb{C}_1 - \mathbb{C}_M)^{-1} \right]^{-1} \tag{22}$$

Finally, the homogenized stiffness tensor of bio-based concrete can be calculated by substituting Eq. (22) into (20).

4. Application and validation in bio-based building materials

4.1. Scale 1: Porous bio-aggregate and porous binder

The porosity and the arrangement of the pores in bio-aggregate depend on the type of plant. Also, binders with different mix proportions in the experiment also have different porosities. Therefore, it is necessary to investigate individual bio-aggregate and binder to make the model applicable to a wider range of bio-based materials. As described in **Section 2.2**, at the microscopic scale, both bio-aggregates and binder consist of microscopic pores and solid phases. The variation of Young's modulus with porosity for hemp, sunflower pith, and binder is shown in **Fig. 9**, where Young's modulus of the solid phase of bio-aggregates and binder are from [36]. It should be noted that the curves in **Fig. 9** are from the results of the model. It can be seen that the modulus of hemp differs in the axial and transverse directions because of the directional distribution of the pores. In contrast, the sunflower pith is isotropic and its Young's modulus is between the two curves of hemp.

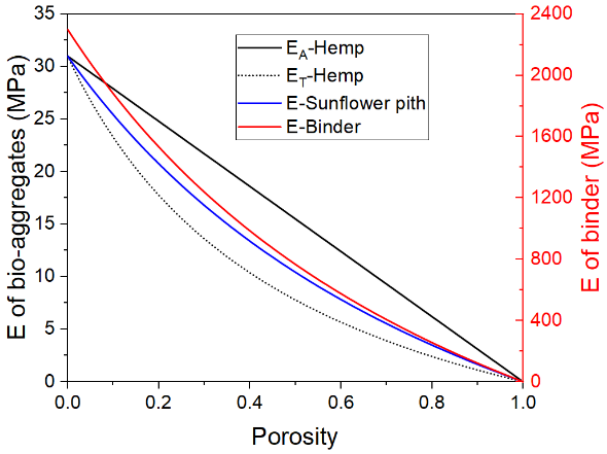

Fig. 9. Young's modulus of individual bio-aggregate (Left) and binder (Right) with porosity (E_A: Young's modulus in the axial direction, E_T: Young's modulus in the transverse direction).

Although hemp has heterogeneity in different directions, the high porosity greatly reduces this difference. Moreover, the modulus of the binder is much larger than that of the bio-aggregates, as shown in **Fig. 9**. In this case, this difference is further reduced. Literature [37] gives 82.5% porosity in hemp, then the anisotropy is only 0.48% (see **Fig. 10**).Therefore, the subsequent mechanical calculations consider the hemp to be isotropic. This assumption was also adopted in other literature [36]. Note that the anisotropy discussed here is for individual bio-aggregate rather than bio-based composites. In fact, both the elongated shape and the particular orientation distribution of the bio-aggregate increase the anisotropy of the composite.

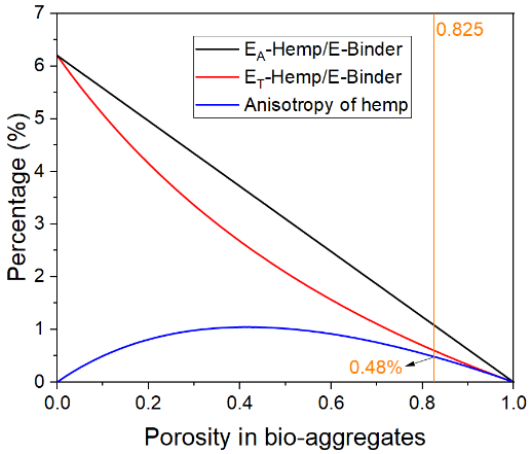

Fig. 10. Young's modulus of bio-aggregates and binder with porosity (Anisotropy of hemp=(E_A-Hemp/E-Binder)-(E_T-Hemp-/E-Binder)).

4.2. Scale 2: Bio-based building materials

On scale 1, the homogenized bio-aggregates and binder were obtained. On scale 2, these two homogenized phases are further homogenized for the effective properties of composites. To verify the accuracy of the multiscale model based on homogenization theory, the theoretical effective Young's modulus was compared with the experimental data from Abbas et al. [26], where there are three types of plant fiber: hemp, sunflower pith, and maize pith. The model has to be simplified before its application due to the lack of data. It is obvious from **Figs. 1 and 2** that bio-based concrete has a complex structure at different scales, which includes a variety of information such as volume fraction of each component, orientation, the shape of inclusions, etc. However, on the one hand, it is difficult to find researchers who have completed all these measurements with the same materials and mix proportions to get the whole information. On the other hand, the ratio of Young's modulus of hemp to binder is only 0.3% (1.5 MPa/500 MPa [36]), hence Young's modulus of hemp is assumed to be equal to that of the pore here. It should be noted that the original shape and orientation of the bio-aggregate are still preserved here. It is also noted that this assumption is only used in this section. The effect of E-Aggregate on mechanical properties will be studied in **Section 5.2** (see **Figs. 15 and 16)**. In summary, in order to use the available experimental data from Abbas et al. [26], in this section, there are some assumptions in the calculations as follows:

- Aggregates are considered to have the same properties as pores because of their negligible modulus and density compared to the binder, but the shape and orientation are preserved.

- Two-phase structure in this modeling, phase 1: 'binder', phase 2: 'pores'.

- The volume fraction of phase 2 is approximately equal to total open porosity in [26].

The approximate volume fraction of phase 2 for different types of plants is shown in **Table 1**.

Table 1. Approximate volume fraction of phase 2 according to [26].

Phase 2	H	S1	M	H+S2	S2
Volume fraction	0.78	0.94	0.92	0.70	0.77

Notes: From left to right, H: hemp, S1: sunflower pith in the case 1, M: maize, H+S2: hemp + the same sunflower in the case 2, S2: the same sunflower in the case 2.

Young's modulus of binder in this model is 500 MPa with reference to a classical lime-based binder [25,36]. On the other hand, the orientation distribution of plant fibers affects the effective mechanical properties of bio-based concrete (described in **Section 2**), but the paper of Abbas et al. [26] does not cover it. Therefore, theoretical results here are given in the form of a range, i.e., θ is from 0° to 90°. When θ is equal to 0, all plant fibers are directed towards the direction of compaction and the effective Young's modulus is maximum.

Conversely, when θ is equal to 90°, there is a minimum. These behaviors will be explained in **Section 5.4**. Based on these assumptions, a comparison between the effective modulus and the experimental data from Abbas et al. [26] is shown in **Fig. 11**.

As can be seen from **Fig. 11**, Young's modulus in the experiments of Abbas et al. [26] is between the maximum (θ=0) and minimum (θ=90°) values except for maize. As for maize, it can be seen from the data of maize that the relative error is acceptable because of the small modulus of this concrete. Another worthwhile point in **Fig. 11** is that the experimental value is closer to the theoretical value with θ of 90°. This can be explained by the aforementioned findings, under the influence of compaction, the fibers tend to be distributed in the plane perpendicular to the compaction direction, which results in a lower effective modulus parallel to the compaction direction than the modulus in the perpendicular direction. The relationship between compaction and plant fiber orientation is discussed in detail in **Section 5.3**.

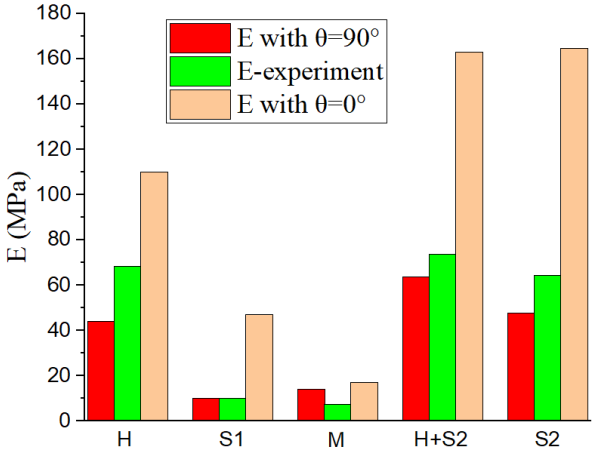

Fig. 11. Comparison of Young's modulus from homogenization theory and experiments. (Experimental data was from Abbas et al. [26])

Density is one of the most common parameters of bio-based concrete, and previous researchers [13,14,27] have related the thermal conductivity of concrete to density and obtained the corresponding mathematical equations to make some predictions. As for the effective modulus, its relationship with density can also be established. Therefore, in this section, the model predictions were also compared with experimental data [58] **(Table 2)** of hemp concrete based on densities.

Literature [20,58] has shown Young's modulus of hemp concrete corresponding to different densities, but it can be seen that the similar density may correspond to a far different Young's modulus. This is due to the different binders used by the experimenters, and it can also be seen in **Section 5.5** that the E-Binder has a significant effect on Young's modulus. Therefore, first of all, it is necessary to calculate Young's modulus of the binder with pores by inverse analysis: E-Binder (Kioy [69])=210MPa, E-Binder (Nguyen et al.

[70])=520MPa. In the inverse analysis, θ of the plant fibers was 75°, which was based on the average value of the X-ray tomography [27]. The volume fraction of hemp can be calculated from the dry density of lime (1760 kg/m^3 [71]) and the density of hemp-lime concrete, and thus the effective Young's modulus with a θ of 75° can be calculated. As a result, the volume fractions of hemp corresponding to the density in the two groups of experiments are shown in **Table 2**. As can be seen from the results in **Fig. 12**, the simulated curves are generally consistent with the experimental results. Moreover, for the same experimenter, the distribution of hemp fibers can be considered the same because of the similar compaction for each sample.

Table 2. Some experimental data [58,69,70] and results of calculations of fiber volume fractions for hemp concrete.

Experimenter	Kioy			Nguyen	
Density (Kg/m^3)	356	610	830	670	850
E (MPa)	14	43	52	113	131
Volume fraction	0.80	0.65	0.53	0.62	0.52

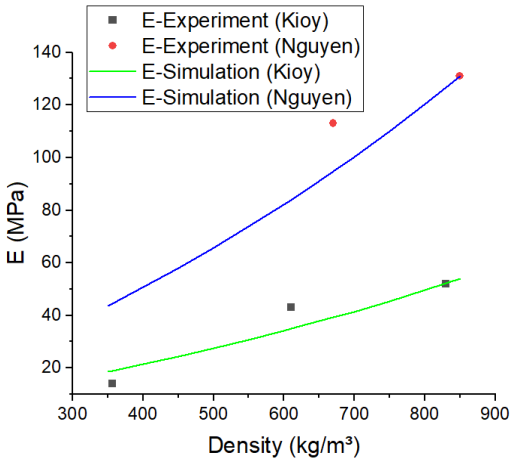

Fig. 12. Comparison of Young's modulus of hemp concretes based on density. (Experimental data are from [58])

5. Parametric study

In order to optimize the mechanical properties of bio-based building materials, these main parameters that can affect the mechanical property are investigated in this section: volume fraction, modulus of binder and aggregate, shape, and orientation. The initial Young's modulus and Poisson's ratio of matrix and inclusion are 500 MPa, 1.5 MPa, 0.2, and 0.1 [36], respectively. E1, E2, and E3 represent Young's modulus along the X, Y, and Z axes in **Fig. 2**, respectively, and the compaction direction is along the Z axis.

5.1. Influence of volume fraction

Figs. 13 and 14 show the variation of effective modulus with volume fraction for different shapes of inclusions. Young's modulus E and shear modulus G decrease with the volume fraction of plant aggregates. There are similar decreasing curves for different shapes between the isotropic case and the anisotropic case. Despite this, the effective modulus of inclusions with different shapes or aspect ratios are different, which can be found in **Section 5.3**. In the anisotropic case, E3 along the direction of compaction is less than E1 and E2 perpendicular to the direction of compaction, this can be explained by the fact that θ is 75° and greater than 45°. If θ is less than 45° the result will be reversed. A detailed analysis of this is discussed in **Section 5.4**.

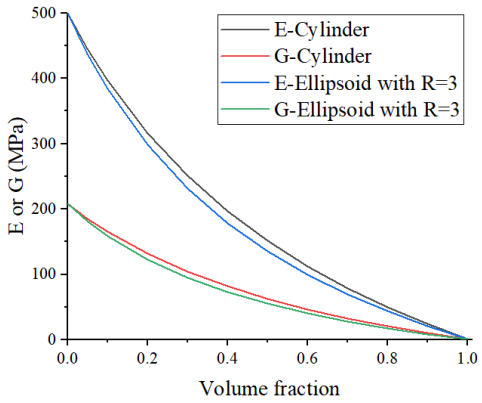

Fig. 13. Effective modulus with volume fraction of bio-aggregates in the isotropic case.

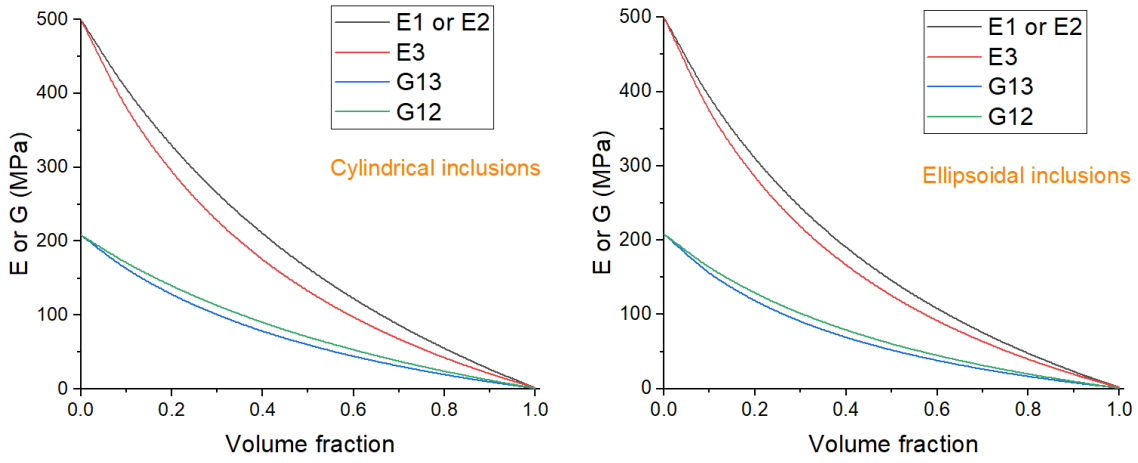

Fig. 14. Effective modulus with volume fraction of bio-aggregates in the anisotropic case. (R=3 and θ=75º)

5.2. Influence of modulus of components

Binder and plant aggregates are the two main components of bio-based concrete and their properties directly influence the effective elastic properties of the composite. Since similar curves are found for both ellipsoidal and cylindrical inclusions, only cylinders have been chosen as a representative to illustrate the influence of the modulus of the components, as shown in **Fig. 15**. Modulus has a linear relationship both with E-Binder and with E-Aggregate comparing the non-linear relationship of aggregate volume fraction. The difference in the slopes of Young's modulus and shear modulus in **Fig. 15** also indicates that the modulus of components has a greater effect on Young's modulus. A comparison of **Fig. 15** left and right shows that the effect of the aggregate on the effective elastic properties is slight while the binder can affect it significantly, this is logical and explained by the fact that Young's modulus varies considerably with the types of binder.

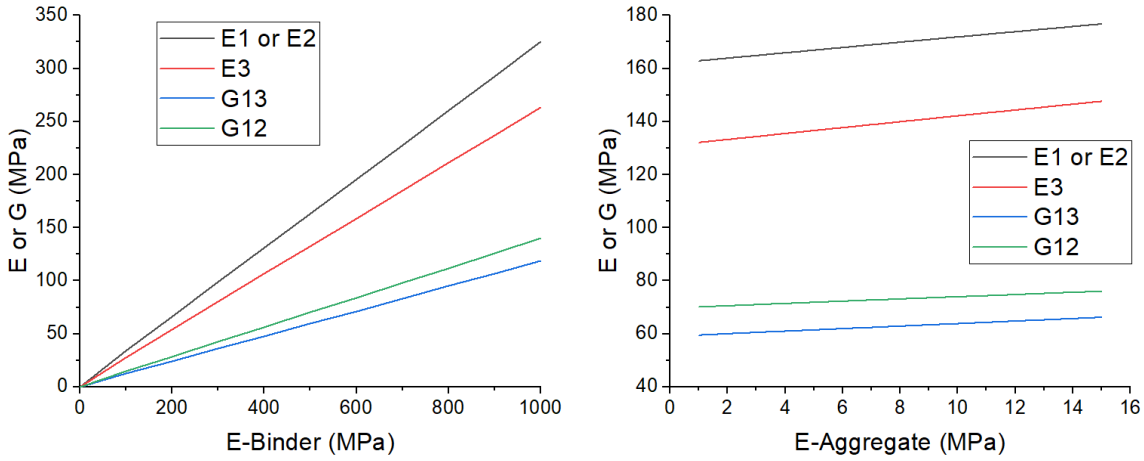

Fig. 15. Effective modulus with E-Binder and E-Aggregate in the anisotropic case. (Cylindrical inclusions, θ=75°, volume fraction=0.5)

Fig. 16 shows the opposite effects of E-Binder and E-Aggregate on the Poisson's ratio of concrete, where ν13 decreases with E-Aggregate and increases with E-Binder. Nevertheless, this effect on the Poisson's ratio is very weak and negligible relative to the modulus, especially on ν12.

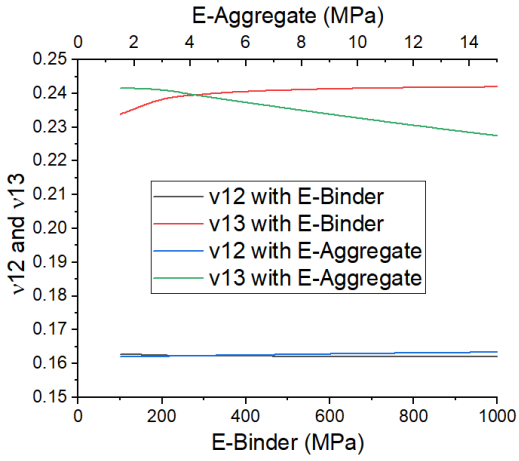

Fig. 16. Poisson's ratio with E-Binder and E-Aggregate in the anisotropic case. (Cylindrical inclusions, θ=75°, volume fraction=0.5)

5.3. Influence of fiber shape

As shown in **Fig. 17**, Young's and share modulus increase with aspect ratio but at a decreasing rate. This behavior can be understood as the larger the R, the thinner and longer the fibers when the volume fraction is fixed. As a weak part of the heterogeneous structure, external stress generates less strain in this slender weak part and the binder acts as a better framework and support in this case. In detail, the growth rate is large at the beginning of the curve, then the modulus can be considered to be independent of R when R is greater than about 8-9. On the other hand, from **Fig. 17** we can see that the curve of the ellipsoid gets closer to the cylinder as R increases. When R is greater than 8 or 9, it can be assumed to have the same modulus regardless of whether it is an ellipsoid or a cylinder. This is because the cylindrical case of the MT scheme is based on the ellipsoidal case and the assumption that the major axis of the ellipsoid is infinite. This does not affect the study of the fiber shape on the effective elastic properties.

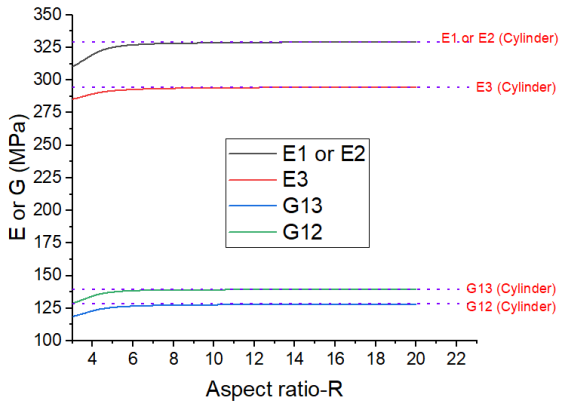

Fig. 17. Influence of aspect ratio of ellipsoidal inclusion in the anisotropic case. (θ=75°, volume fraction=0.20, the dashed line is for cylinder)

The same conclusion can be found in other cases in **Fig. 18**, modulus has a positive correlation with aspect ratio, wherever the fiber is oriented in the matrix. According to this finding, the researcher can appropriately select fibers with a high aspect ratio to obtain concrete with better mechanical properties. However, two points need to be noted, firstly, that it is futile to try to increase the mechanical properties by increasing R when R is greater than 8. As for the modeling of bio-based concrete, it is crucial to get an accurate value of R when it is less than 5, because small alterations in R can significantly affect the effective modulus. Secondly, an improvement in the aspect ratio may lead to an increase in the porosity of the concrete, which in turn reduces its mechanical properties. Therefore, the experimenter has to take these factors into account and optimize the concrete proportion according to the shape of the plant fibers.

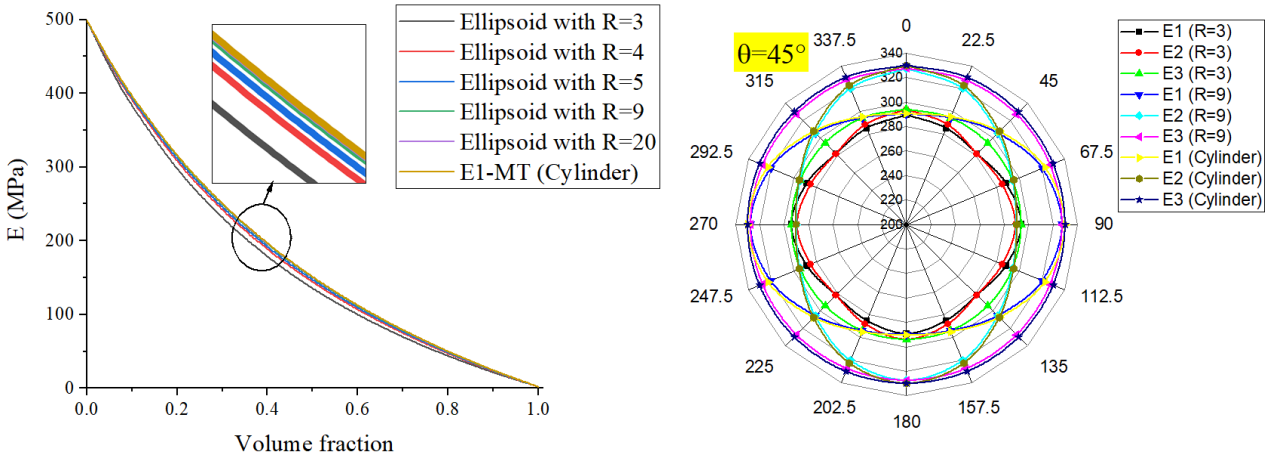

Fig. 18. Comparison between cylinders and ellipsoids with different aspect ratio in the different case. (Left: Isotropic case. Right: Inclusions with φ and θ=45º, volume fraction=0.20, the first six curves are related to ellipsoidal inclusions.)

In addition, it can be seen from **Fig. 19**, R only affects E2 and E3 when φ is equal to 0. In this case, the value of E1 is independent of θ and R. In other words, the effective modulus perpendicular to the direction of the fiber is not affected by R. So, if the experimenter compacts the concrete specimen sufficiently so that the fibers are completely distributed in a plane perpendicular to the direction of compaction, the effective modulus along the direction of compaction is independent of the fiber shapes. Although this situation is difficult to be realized, it can still be suggested that the effective modulus along the compaction direction is minimally affected by R when there is adequate compaction.

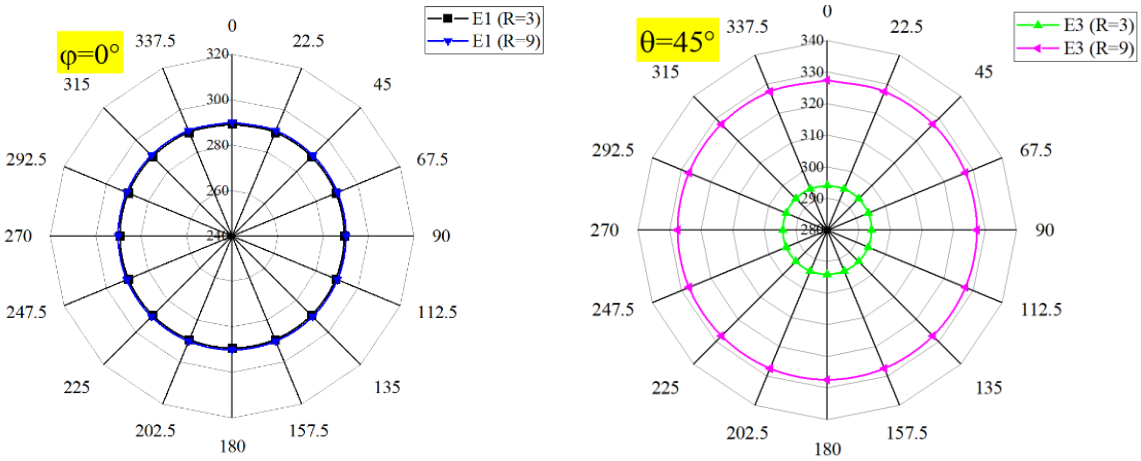

Fig. 19. Influence of R for ellipsoidal inclusions when θ=0º and 45º. (Volume fraction=0.20)

5.4. Influence of fiber orientation

Fig. 20 presents the influence of θ and φ on effective Young's modulus E1, E2, and E3. Over the interval [0, 360º], E1 has 4 maximum values, E2 has 6 maximum values, and E3 has an infinite number of maximum

values. The angles corresponding to these maximum values can be found in **Fig. 20**, and the curvature at the maximum value on the surface is 0. Furthermore, E3 only depends on the angle θ, this is also verified in **Fig. 21** when θ is equal to 0º, 45º, and 90º. The curves in the radar **Fig. 21** indicate that E1, E2, and E3 have symmetry with axes of 0-180º and 90-270º, while E1 has the same value as E2 when φ=45° or θ=0. This provides a reference to optimize the orientation of the fiber-reinforced concrete.

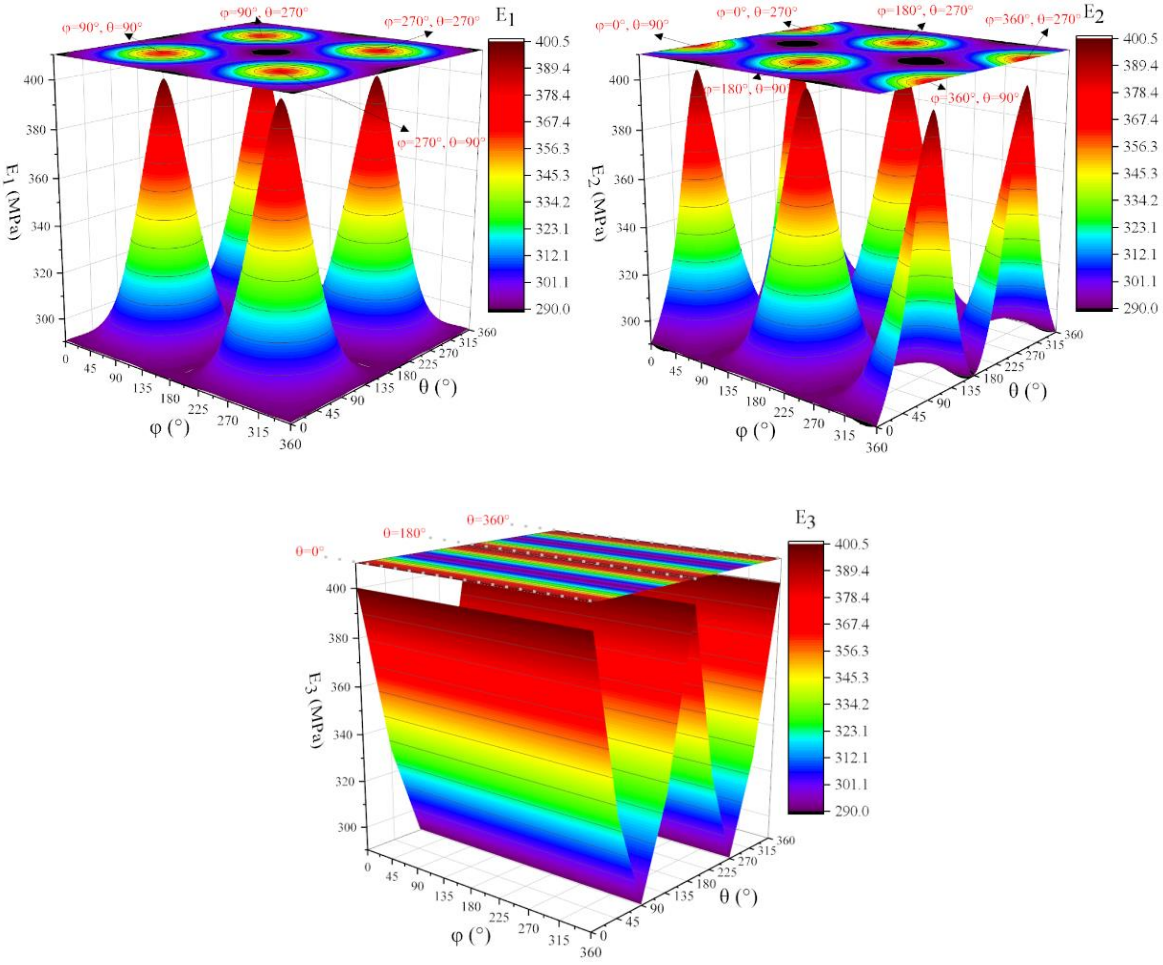

Fig. 20. Influence of angle θ and φ for cylindrical inclusions with a given θ and φ orientation. (Cylindrical inclusions, volume fraction=0.20)

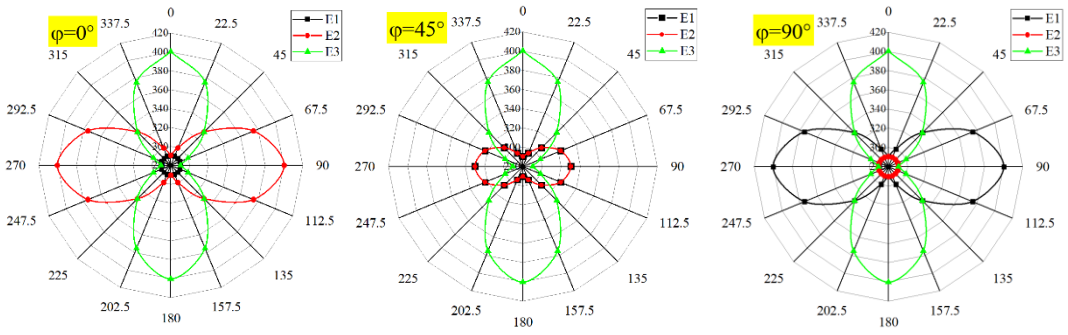

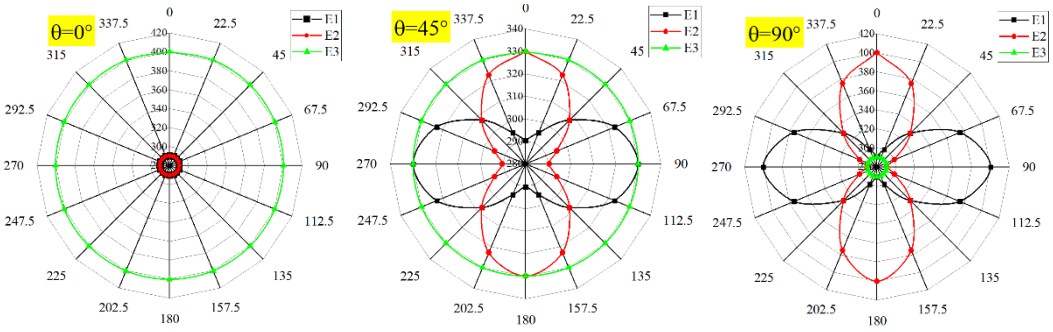

Fig. 21. Influence of φ and θ for cylindrical inclusions. (Volume fraction=0.20)

In bio-based concrete, the degree of compaction along the Z-axis causes a variation in θ, while φ is not affected by it. As can be seen from **Fig. 22,** the modulus and Poisson's ratio of bio-based concrete increase or decrease with θ, but the derivatives of different curves are similar, which increases and then decreases with θ, regardless of Young's modulus, shear modulus, or Poisson's ratio. This finding is helpful for the improvement of the compaction process of the specimens. The compaction process, which ensures that the majority of the fibers have a θ greater than 75°, is sufficient to achieve a high value of E1 or E2. Further improvements in the manufacturing process are not worthwhile.

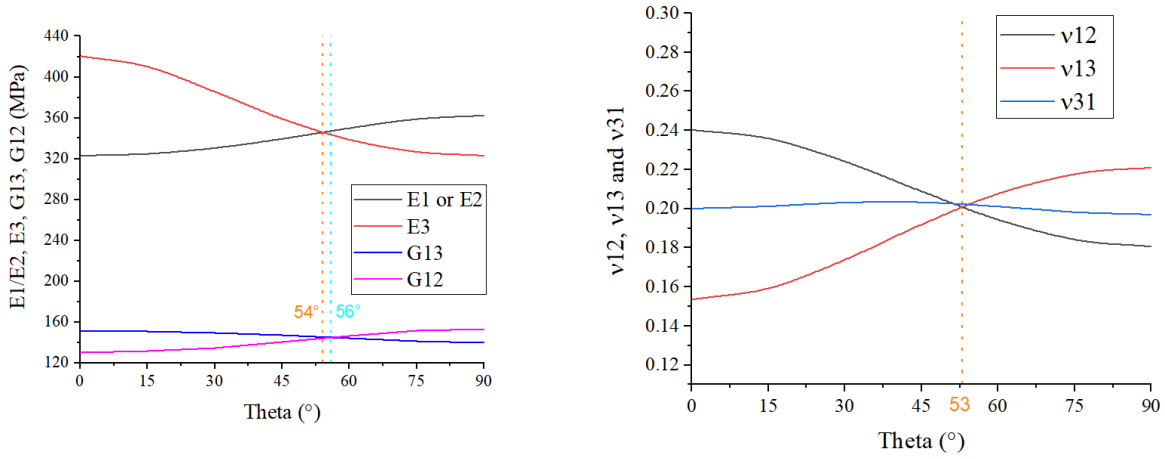

Fig. 22. Influence of θ for cylindrical inclusions in bio-based concrete. (Volume fraction=0.16)

5.5. Weights of parameters

All the parameters covered in the foregoing section can influence the effective properties of bio-based building materials. However, the weight of each parameter is unclear. Hence a method of measuring parameter weight is presented in this section.

When the weight of a parameter is studied, the value of this parameter is replaced by a contrast value in **Table 3**, and other parameters remain the benchmark values. In these two cases, the modulus in the compaction direction is Ea and Eb, respectively. Then the weight of this parameter is as follows.

$$Weight = \frac{|Eb-Ea|}{Ea} \times 100\% \quad (23)$$

Table 3. Data input for weighting analysis.

Parameters	E-Binder	E-Aggregate	Volume fraction	Orientation	Shape (When R>8)	Shape (When R<8)
Benchmark	500 MPa	1.5 MPa	0.5	θ=45º	R=8	R=8
Contrast	1000 MPa	3 MPa	0.8	θ=90º	R=16	R=3

The selection of the values in **Table 3** was based on the following principles:

- Try to ensure that the value of 'Contrast' is twice or nearly twice the value of 'Benchmark'.

- The selection of the volume fraction: **Section 3** shows that bio-based concrete has a high-volume fraction of fibers, so 0.5 and 0.8 were chosen here to make this evaluation method more applicable to real bio-based concrete.

- The selection of R: **Fig. 17** shows that R=8 is an important point to measure the effect of aspect ratio on the effective mechanical properties. Moreover, the slope of the curve is large when R=3 and close to 0 when R=16.

- The selection of θ. In an ideal uncompacted case, θ of fibers in bio-based concrete is close to 45º. In a fully compacted case, θ is close to 90º.

As a result, the weight for each parameter is shown in **Fig. 23**. E-Binder has the greatest weight, followed by volume fraction. When R is less than 8, the factor of shape has a similar weight to orientation. The factors of shape (R>8) and E-Aggregate barely affect the bio-based modulus. In order to increase the modulus of bio-based concrete, the most important method is the alteration in binder types and plant fibers volume fraction. Afterward, the compaction process can be adjusted appropriately with reference to the conclusions in **Section 5.4**. When the aspect ratio of the plant fiber is less than 8, it is also important to note the influence of shape on the results. In this perspective, the influence of different plant aggregates on the modulus of bio-based concrete is more a reflection of its shape than its modulus. This method for weight evaluation of parameters is based on ellipsoidal plant fibers, so the above conclusions are applicable to all bio-based concretes with inclusion of similar shapes. In fact, in the previous discussion, ellipsoidal inclusions were shown to have

similar curves to cylinders. Therefore, the conclusions can be applied to most bio-based materials in consideration of the shapes of common plant fibers.

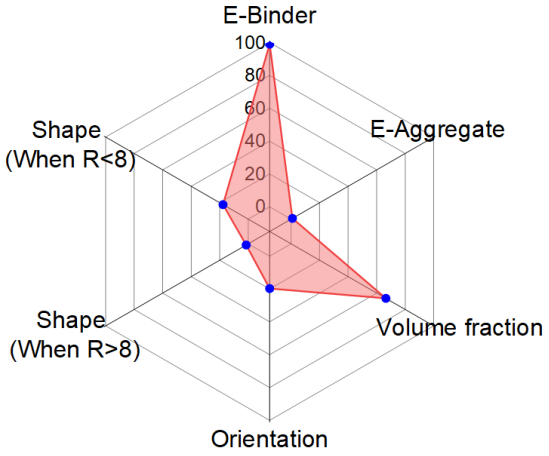

Fig. 23. Weights of the parameters affecting the effective modulus of bio-based concrete.

The aspect ratios of hemp, maize, and sunflower vary considerably, which affects the choice of the optimization method. Moreover, **Section 5.4** showed the opposite effect of orientation on Young's modulus in the parallel and perpendicular directions. Therefore, the evaluation method described above is further used to investigate the effect of different R and volume fractions on optimization. Since E-Binder has a large effect and E-Aggregate has a negligible effect on the results, these two parameters are not considered in the subsequent analysis. **Fig. 24** illustrates the effect of shape, orientation, and volume fraction in four cases: low (R=3) and high (R=8) aspect ratios, low (0.2) and high (0.5) volume fractions. A single-parameter analysis is utilized here, where one parameter is studied while holding the others constant.

As shown in **Fig. 24 (a)**, volume fraction has almost the same effect on different shapes of aggregates regardless of E1 or E2. For E3, orientation has a more negative effect in the case of a high aspect ratio (such as hemp), while for E1 there is an opposite trend. Therefore, for aggregates with low aspect ratios (such as sunflower pith and maize), orientation is a good choice for optimization, as an increase in orientation can increase E1 with a slight decrease in E3. As can be seen from **Fig. 24 (b)**, compared to low aggregate volume fractions, there is a more significant optimization in the high volume fraction both by shape and orientation. This can be explained by the fact that there are more plant fibers in this case, so the cumulative effect is greater.

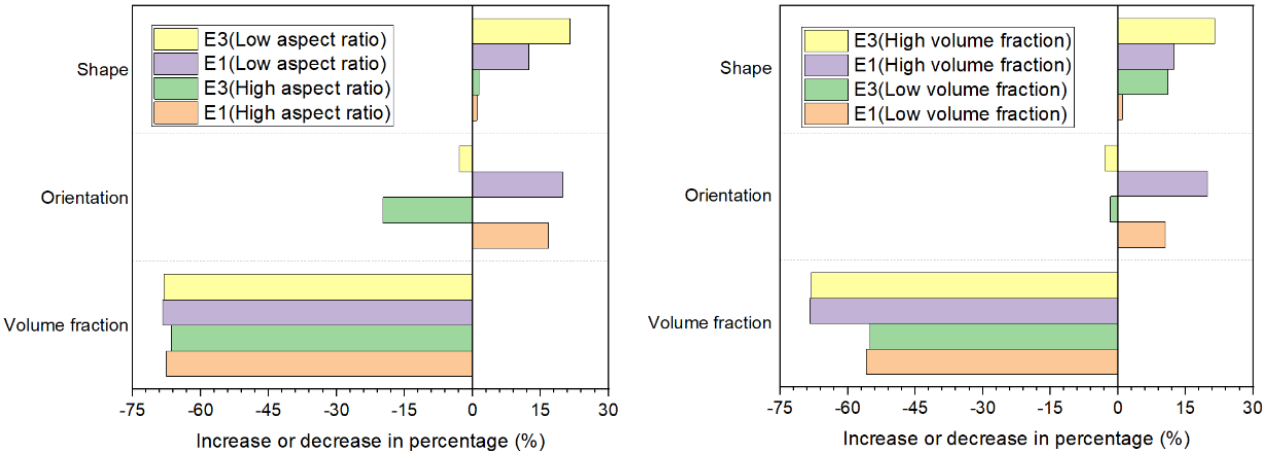

(a) Different aspect ratios. (b) Different volume fractions.

Fig. 24. Differences in optimization for different aspect ratios (Vertical (E1) and parallel (E3) directions. Low aspect ratio: R=3, high aspect ratio R=8, low volume fraction: 0.2, high volume fraction: 0.5).

Further, the above optimization method was applied to bio-based material with a low aspect ratio and high volume fraction. As a result, Young's modulus in the vertical direction can be increased by 32.1% through the optimization of orientation and shape, which is equivalent to the decrease in modulus caused by a 20% increase in volume fraction. It can be seen from this example that the optimization method can improve the mechanical performance of bio-based building materials without changing the volume of plant fibers.

6. Conclusion

This paper aims to optimize the mechanical properties of bio-based building materials by a multiscale model that takes into account the shape and orientation of plant fibers. This model established a connection between the micro-geometric characteristics and macroscopic mechanical properties of different bio-based building materials. Hemp is the most popular bio-aggregate in the building industry, but its planting area is much less than that of sunflower and maize. Therefore, hemp, sunflower pith, and maize were selected in this paper to verify the reliability of the models. Moreover, most of the previous models did not have a detailed study of the main factors affecting the mechanical properties, especially in terms of orientation and shape. Accordingly, this research considered the effect of the following parameters on the mechanical properties of the composites: volume fraction, modulus of binder and aggregate, shape, and orientation. To quantify the priority of these parameters in the optimization, a weight evaluation method was proposed. Further studies based on this evaluation method indicated that the optimization measures need to be adjusted for different bio-aggregate volume fractions and aspect ratios. Finally, suggestions and priorities were made for optimizing the mechanical properties of the composites in terms of the choice of the volume fraction and shape of bio-aggregates, the level of compaction, and the choice of binder.

The parametric study showed that the factors affecting the effective modulus of bio-based were E-Binder, volume fraction, orientation, shape (R<8), shape (R>8), E-Aggregate, from heavy to light. This provided suggestions for optimizing bio-based building materials, i.e., the mechanical properties are improved mainly by the volume fraction of plant fibers and E-Binder. In addition to this, further studies on shape, orientation, and volume fraction showed that optimizing by orientation, i.e., increasing the level of compaction, is a good choice for a low aspect ratio (such as sunflower pith and maize). Conversely, the volume fraction has almost the same effect regardless of the high or low aspect ratios. Moreover, there is a more significant optimization in the high volume fraction both by shape and orientation. According to this optimization method, the modulus perpendicular to the compaction direction can be increased theoretically by 32% through shape and direction for a given component characteristic.

In general, two significant ways to improve the mechanical properties of bio-based concrete are: firstly upgrading the binder and secondly reducing the volume fraction of the aggregates. However, the novelty of this article is to propose an alternative way to optimize the bio-based concrete, with constant aggregate proportion and binder properties, by selecting the aspect ratio and orientation of plant fibers. It was shown (see **Fig. 17**) that a greater aspect ratio (until 8) improves the mechanical properties. Moreover, this study highlighted the impact of the manufacturing processes on the overall behavior. For a constant mixture, heavy compaction gives unidirectional optimal mechanical properties, while moderate compaction achieves balanced optimal mechanical properties in all directions.

It should be noticed that a modification of one parameter affects not only the mechanical properties as shown in this work but also other properties, such as thermal and acoustic insulation. The significant added value of this article is that it proposes a calculation method able to investigate the usual other global characteristics and set out the basis to obtain a more balanced bio-sourced concrete.

Declaration of Competing Interest

The authors declare that they have no known competing financial interests or personal relationships that could have appeared to influence the work reported in this paper.

Appendix A. Bechterew Notation

According to Hooke's law $\boldsymbol{\sigma} = \mathbb{C}\boldsymbol{\varepsilon}$, the strain tensor $\boldsymbol{\sigma}$ and stress tensor $\boldsymbol{\varepsilon}$ are represented in Voigt notation by $\bar{\sigma}$ and $\bar{\varepsilon}$, each with six components [68].

$$\bar{\sigma} = \begin{bmatrix} \bar{\sigma}_1 \\ \bar{\sigma}_2 \\ \bar{\sigma}_3 \\ \bar{\sigma}_4 \\ \bar{\sigma}_5 \\ \bar{\sigma}_6 \end{bmatrix} = \begin{bmatrix} \sigma_{11} \\ \sigma_{22} \\ \sigma_{33} \\ \sigma_{23} \\ \sigma_{31} \\ \sigma_{12} \end{bmatrix} \qquad \bar{\varepsilon} = \begin{bmatrix} \bar{\varepsilon}_1 \\ \bar{\varepsilon}_2 \\ \bar{\varepsilon}_3 \\ \bar{\varepsilon}_4 \\ \bar{\varepsilon}_5 \\ \bar{\varepsilon}_6 \end{bmatrix} = \begin{bmatrix} \varepsilon_{11} \\ \varepsilon_{22} \\ \varepsilon_{33} \\ 2\varepsilon_{23} \\ 2\varepsilon_{31} \\ 2\varepsilon_{12} \end{bmatrix} \tag{A.1}$$

The fourth order stiffness tensor $\mathbb{C}$ is usually represented in Voigt notation by $\bar{C}$ in the form of 6×6 matrix.

$$\bar{C} = \begin{bmatrix} C_{1111} & C_{1122} & C_{1133} & C_{1123} & C_{1131} & C_{1112} \\ C_{2211} & C_{2222} & C_{2233} & C_{2223} & C_{2231} & C_{2212} \\ C_{3311} & C_{3322} & C_{3333} & C_{3323} & C_{3331} & C_{3312} \\ C_{2311} & C_{2322} & C_{2333} & C_{2323} & C_{2331} & C_{2312} \\ C_{3111} & C_{3122} & C_{3133} & C_{3123} & C_{3131} & C_{3112} \\ C_{1211} & C_{1222} & C_{1233} & C_{1223} & C_{1231} & C_{1212} \end{bmatrix} \tag{A.2}$$

When we describe Hooke's law in terms of the compliance tensor in Voigt notation, there is $\bar{\varepsilon} = \bar{S} : \bar{\sigma}$, which can be expressed in matrix form as follows:

$$\begin{bmatrix} \varepsilon_{11} \\ \varepsilon_{22} \\ \varepsilon_{33} \\ 2\varepsilon_{23} \\ 2\varepsilon_{31} \\ 2\varepsilon_{12} \end{bmatrix} = \begin{bmatrix} S_{1111} & S_{1122} & S_{1133} & 2S_{1123} & 2S_{1131} & 2S_{1112} \\ S_{2211} & S_{2222} & S_{2233} & 2S_{2223} & 2S_{2231} & 2S_{2212} \\ S_{3311} & S_{3322} & S_{3333} & 2S_{3323} & 2S_{3331} & 2S_{3312} \\ 2S_{2311} & 2S_{2322} & 2S_{2333} & 4S_{2323} & 4S_{2331} & 4S_{2312} \\ 2S_{3111} & 2S_{3122} & 2S_{3133} & 4S_{3123} & 4S_{3131} & 4S_{3112} \\ 2S_{1211} & 2S_{1222} & 2S_{1233} & 4S_{1223} & 4S_{1231} & 4S_{1212} \end{bmatrix} \begin{bmatrix} \sigma_{11} \\ \sigma_{22} \\ \sigma_{33} \\ \sigma_{23} \\ \sigma_{31} \\ \sigma_{12} \end{bmatrix} \tag{A.3}$$

One issue worth recognizing here is that $\mathbb{S}$ should be equal to $\mathbb{C}^{-1}$. But in Voigt notation, $\bar{S} \neq \bar{C}^{-1}$. This caused difficulties for the subsequent calculations in this paper, so a new notation called Bechterew, which replaces Voigt notation, is introduced here.

In Bechterew notation, the stress tensor and strain tensor are denoted by $\hat{\sigma}$ and $\hat{\varepsilon}$ as:

$$\hat{\sigma} = \begin{bmatrix} \hat{\sigma}_1 \\ \hat{\sigma}_2 \\ \hat{\sigma}_3 \\ \hat{\sigma}_4 \\ \hat{\sigma}_5 \\ \hat{\sigma}_6 \end{bmatrix} = \begin{bmatrix} \sigma_{11} \\ \sigma_{22} \\ \sigma_{33} \\ \sqrt{2}\sigma_{23} \\ \sqrt{2}\sigma_{31} \\ \sqrt{2}\sigma_{12} \end{bmatrix} \qquad \hat{\varepsilon} = \begin{bmatrix} \hat{\varepsilon}_1 \\ \hat{\varepsilon}_2 \\ \hat{\varepsilon}_3 \\ \hat{\varepsilon}_4 \\ \hat{\varepsilon}_5 \\ \hat{\varepsilon}_6 \end{bmatrix} = \begin{bmatrix} \varepsilon_{11} \\ \varepsilon_{22} \\ \varepsilon_{33} \\ \sqrt{2}\varepsilon_{23} \\ \sqrt{2}\varepsilon_{31} \\ \sqrt{2}\varepsilon_{12} \end{bmatrix} \tag{A.4}$$

In addition, the stiffness tensor denoted by $\hat{C}$ in Bechterew notation (or compliance tensor $\hat{S}$) can be represented by a 6×6 matrix of this form:

$$\hat{C} = \begin{bmatrix} C_{1111} & C_{1122} & C_{1133} & \sqrt{2}C_{1123} & \sqrt{2}C_{1131} & \sqrt{2}C_{1112} \\ C_{1112} & C_{2222} & C_{2233} & \sqrt{2}C_{2223} & \sqrt{2}C_{2231} & \sqrt{2}C_{2212} \\ C_{1133} & C_{2233} & C_{3333} & \sqrt{2}C_{3323} & \sqrt{2}C_{3331} & \sqrt{2}C_{3312} \\ \sqrt{2}C_{1123} & \sqrt{2}C_{2223} & \sqrt{2}C_{3323} & 2C_{2323} & 2C_{2331} & 2C_{2312} \\ \sqrt{2}C_{1131} & \sqrt{2}C_{2231} & \sqrt{2}C_{3331} & 2C_{3123} & 2C_{3131} & 2C_{3112} \\ \sqrt{2}C_{1112} & \sqrt{2}C_{2212} & \sqrt{2}C_{3312} & 2C_{2312} & 2C_{3112} & 2C_{1212} \end{bmatrix} \quad \text{(A.5)}$$

This notation is in accordance with Hooke's law and $\hat{\sigma} = \hat{C}\hat{\varepsilon}, \hat{\varepsilon} = \hat{S}\hat{\sigma}, \hat{S} = \hat{C}^{-1}$.

In the isotropic case, the stiffness tensor $\mathbb{C}$can be expressed by fourth-order decomposed tensors $\mathbb{J}$ and $\mathbb{K}$ [72].

$$\mathbb{C} = 3k\mathbb{J} + 2\mu\mathbb{K} \quad \text{(A.6)}$$

In Bechterew notation, $\mathbb{J}$ and $\mathbb{K}$ can be expressed as:

$$\mathbb{J} = \begin{bmatrix} \frac{1}{3} & \frac{1}{3} & \frac{1}{3} & 0 & 0 & 0 \\ \frac{1}{3} & \frac{1}{3} & \frac{1}{3} & 0 & 0 & 0 \\ \frac{1}{3} & \frac{1}{3} & \frac{1}{3} & 0 & 0 & 0 \\ 0 & 0 & 0 & 0 & 0 & 0 \\ 0 & 0 & 0 & 0 & 0 & 0 \\ 0 & 0 & 0 & 0 & 0 & 0 \end{bmatrix} \quad \mathbb{K} = \begin{bmatrix} \frac{2}{3} & -\frac{1}{3} & -\frac{1}{3} & 0 & 0 & 0 \\ -\frac{1}{3} & \frac{2}{3} & -\frac{1}{3} & 0 & 0 & 0 \\ -\frac{1}{3} & -\frac{1}{3} & \frac{2}{3} & 0 & 0 & 0 \\ 0 & 0 & 0 & 1 & 0 & 0 \\ 0 & 0 & 0 & 0 & 1 & 0 \\ 0 & 0 & 0 & 0 & 0 & 1 \end{bmatrix} \quad \text{(A.7)}$$

Appendix B. Eshelby tensor with different inclusion shapes

In transversely isotropic materials, the Eshelby tensor $\mathbb{S}^E$ can be represented in the Bechterew notation as:

$$\mathbb{S}^E = \begin{bmatrix} S^E{}_{1111} & S^E{}_{1122} & S^E{}_{1133} & 0 & 0 & 0 \\ S^E{}_{2211} & S^E{}_{2222} & S^E{}_{2233} & 0 & 0 & 0 \\ S^E{}_{3311} & S^E{}_{3322} & S^E{}_{3333} & 0 & 0 & 0 \\ 0 & 0 & 0 & 2S^E{}_{2323} & 0 & 0 \\ 0 & 0 & 0 & 0 & 2S^E{}_{1313} & 0 \\ 0 & 0 & 0 & 0 & 0 & 2S^E{}_{1212} \end{bmatrix} \quad \text{(B.1)}$$

The Eshelby tensor depends on the shape of the inclusions and the properties of the matrix. When the cylindrical inclusions are embedded in an isotropic matrix, and the inclusions are oriented along the z-axis in a cartesian coordinate system, the components of the Eshelby tensor can be expressed as [66]:

$$S^E_{1111} = \frac{\frac{5}{4} - \nu}{2 - 2\nu}, S^E_{1122} = \frac{-\frac{1}{4} + \nu}{2 - 2\nu}, S^E_{1133} = \frac{\nu}{2 - 2\nu},$$

$$S^E_{2211} = S^E_{1122}, S^E_{2222} = S^E_{1111}, S^E_{2233} = S^E_{1133},$$

$$S^E_{3311} = S^E_{3322} = S^E_{3333} = 0,$$

$$S^E_{2323} = S^E_{3131} = \frac{1}{4}, S^E_{1212} = \frac{\frac{3}{4} - \nu}{2 - 2\nu}.$$

(B.2)

In Eq. (B.2), ν is Poisson's ratio of the matrix.

In the case of ellipsoidal inclusions, the major axis of the ellipsoid is along the z-axis of the global coordinate system, and its shape can be described in the cartesian coordinate system as:

$$\frac{x^2}{{a_1}^2} + \frac{y^2}{{a_2}^2} + \frac{z^2}{{a_3}^2} = 1 \tag{B.3}$$

Where $a_1 = a_2 < a_3 \; with \; a_1 = a_2 = a, a_3 = Ra. (R{>}1)$.

The components of Eshelby tensor in this case can be expressed as [66]:

$$\begin{aligned} S^E_{iiii} &= \tfrac{3}{8\pi(1-\nu)} a_i^2 I_{ii} + \tfrac{1-2\nu}{8\pi(1-\nu)} I_i, \\ S^E_{iijj} &= \tfrac{1}{8\pi(1-\nu)} a_j^2 I_{ij} - \tfrac{1-2\nu}{8\pi(1-\nu)} I_i, \\ S^E_{ijij} &= \tfrac{1}{16\pi(1-\nu)} \left(a_i^2 + a_j^2\right) I_{ij} + \tfrac{1-2\nu}{16\pi(1-\nu)} \left(I_i + I_j\right). \end{aligned} \tag{B.4}$$

Where ν is the Poisson's ratio of the matrix, and I_{ii}, I_i, I_{ij} can be obtained by the following equations.

$$\begin{aligned} I_1 = I_2 &= \frac{2\pi a_1^2 a_3}{\left(a_3^2 - a_1^2\right)^{\frac{3}{2}}} \left[\frac{a_3}{a_1} \left(\frac{a_3^2}{a_1^2} - 1 \right)^{\frac{1}{2}} - \cosh^{-1} \frac{a_3}{a_1} \right], \\ I_3 &= 4\pi - 2I_1, I_{11} = I_{22} = I_{12}, \\ I_{12} &= \frac{\pi}{a_1^2} - \frac{1}{4} I_{13} = \frac{\pi}{a_1^2} - \frac{(I_1 - I_3)}{4\left(a_3^2 - a_1^2\right)}, \\ I_{31} = \tfrac{I_1 - I_3}{a_3^2 - a_1^2}, 3I_{33} &= \tfrac{4\pi}{a_3^2} - 2I_{31}, 3I_{11} = \tfrac{4\pi}{a_1^2} - I_{12} - \tfrac{I_1 - I_3}{a_3^2 - a_1^2}. \end{aligned} \tag{B.5}$$

Appendix C. Numerical implementation of φ

With reference to calculus theory, the distribution of φ in Eq. (21) is uniformly distributed over N families, i.e., $\varphi \in [0, 2\pi]$. Therefore, the value of N can be interpreted as the number of integration points in calculation, which affects the accuracy of the effective modulus. **Table C.1** presents that 50 is sufficient for this calculation. The value of E3 in **Table C.1** shows that it hardly depends on the number of integration points, which is consistent with the findings of **Section 5.4**.

Table C.1. A test of the accuracy of the integral. (In this case, the input of the parameters is shown in **Section 5,** and the volume fraction is 0.4, θ=75º, the shape is cylindrical.)

NI	2	5	50	100
E1 or E2 (MPa)	171.39	210.25	210.25	210.25
E3 (MPa)	175.23	175.21	175.21	175.21

Notes: NI is the number of the integration points, E1, E2 and E3 are Young's modulus along the X, Y and Z axis, respectively.

References:

[1] F. Krausmann, S. Gingrich, N. Eisenmenger, K.-H. Erb, H. Haberl, M. Fischer-Kowalski, Growth in global materials use, GDP and population during the 20th century, Ecological Economics. 68 (2009) 2696–2705. https://doi.org/10.1016/j.ecolecon.2009.05.007.

[2] A. Arrigoni, D.K. Panesar, M. Duhamel, T. Opher, S. Saxe, I.D. Posen, H.L. MacLean, Life cycle greenhouse gas emissions of concrete containing supplementary cementitious materials: cut-off vs. substitution, Journal of Cleaner Production. 263 (2020) 121465. https://doi.org/10.1016/j.jclepro.2020.121465.

[3] E.A.J. Hirst, P. Walker, K.A. Paine, T. Yates, Characteristics of low-density hemp-lime building materials, Proceedings of the Institution of Civil Engineers - Construction Materials. 165 (2012) 15–23. https://doi.org/10.1680/coma.1000021.

[4] F. Benmahiddine, F. Bennai, R. Cherif, R. Belarbi, A. Tahakourt, K. Abahri, Experimental investigation on the influence of immersion/drying cycles on the hygrothermal and mechanical properties of hemp concrete, Journal of Building Engineering. 32 (2020) 101758. https://doi.org/10.1016/j.jobe.2020.101758.

[5] B. Mazhoud, F. Collet, S. Pretot, C. Lanos, Mechanical properties of hemp-clay and hemp stabilized clay composites, Construction and Building Materials. 155 (2017) 1126–1137. https://doi.org/10.1016/j.conbuildmat.2017.08.121.

[6] O. Kaynakli, A review of the economical and optimum thermal insulation thickness for building applications, Renewable and Sustainable Energy Reviews. 16 (2012) 415–425. https://doi.org/10.1016/j.rser.2011.08.006.

[7] Bio-based products, (n.d.). https://ec.europa.eu/growth/sectors/biotechnology/bio-based-products_en (accessed June 16, 2022).

[8] L.F. Cabeza, L. Boquera, M. Chàfer, D. Vérez, Embodied energy and embodied carbon of structural building materials: Worldwide progress and barriers through literature map analysis, Energy and Buildings. 231 (2021) 110612. https://doi.org/10.1016/j.enbuild.2020.110612.

[9] F. Pittau, F. Krause, G. Lumia, G. Habert, Fast-growing bio-based materials as an opportunity for storing carbon in exterior walls, Building and Environment. 129 (2018) 117–129. https://doi.org/10.1016/j.buildenv.2017.12.006.

[10] M. Sinka, P. Van den Heede, N. De Belie, D. Bajare, G. Sahmenko, A. Korjakins, Comparative life cycle assessment of magnesium binders as an alternative for hemp concrete, Resources, Conservation and Recycling. 133 (2018) 288–299. https://doi.org/10.1016/j.resconrec.2018.02.024.

[11] G. Churkina, A. Organschi, C.P.O. Reyer, A. Ruff, K. Vinke, Z. Liu, B.K. Reck, T.E. Graedel, H.J. Schellnhuber, Buildings as a global carbon sink, Nat Sustain. 3 (2020) 269–276. https://doi.org/10.1038/s41893-019-0462-4.

[12] M.P. Sáez-Pérez, M. Brümmer, J.A. Durán-Suárez, A review of the factors affecting the properties and performance of hemp aggregate concretes, Journal of Building Engineering. 31 (2020) 101323. https://doi.org/10.1016/j.jobe.2020.101323.

[13] Y.X. Chen, F. Wu, Q. Yu, H.J.H. Brouwers, Bio-based ultra-lightweight concrete applying miscanthus fibers: Acoustic absorption and thermal insulation, Cement and Concrete Composites. 114 (2020) 103829. https://doi.org/10.1016/j.cemconcomp.2020.103829.

[14] F. Collet, S. Pretot, Thermal conductivity of hemp concretes: Variation with formulation, density and water content, Construction and Building Materials. 65 (2014) 612–619. https://doi.org/10.1016/j.conbuildmat.2014.05.039.

[15] World Agricultural Production, USDA Foreign Agricultural Service. (2022). https://www.fas.usda.gov/data/world-agricultural-production (accessed June 13, 2022).

[16] B. Belhadj, M. Bederina, Z. Makhloufi, R.M. Dheilly, N. Montrelay, M. Quéneudéc, Contribution to the development of a sand concrete lightened by the addition of barley straws, Construction and Building Materials. 113 (2016) 513–522. https://doi.org/10.1016/j.conbuildmat.2016.03.067.

[17] E. Chabi, A. Lecomte, E.C. Adjovi, A. Dieye, A. Merlin, Mix design method for plant aggregates concrete: Example of the rice husk, Construction and Building Materials. 174 (2018) 233–243. https://doi.org/10.1016/j.conbuildmat.2018.04.097.

[18] H. Fathi, A. Fathi, Sugar beet fiber and Tragacanth gum effects on concrete, Journal of Cleaner Production. 112 (2016) 808–815. https://doi.org/10.1016/j.jclepro.2015.06.072.

[19] H. Wadi, S. Amziane, E. Toussaint, M. Taazount, Lateral load-carrying capacity of hemp concrete as a natural infill material in timber frame walls, Engineering Structures. 180 (2019) 264–273. https://doi.org/10.1016/j.engstruct.2018.11.046.

[20] T. Jami, S.R. Karade, L.P. Singh, A review of the properties of hemp concrete for green building applications, Journal of Cleaner Production. 239 (2019) 117852. https://doi.org/10.1016/j.jclepro.2019.117852.

[21] S. Barbhuiya, B. Bhusan Das, A comprehensive review on the use of hemp in concrete, Construction and Building Materials. 341 (2022) 127857. https://doi.org/10.1016/j.conbuildmat.2022.127857.

[22] P.S. de Carvalho, M.D. Nora, L.C. da Rosa, Development of an acoustic absorbing material based on sunflower residue following the cleaner production techniques, Journal of Cleaner Production. 270 (2020) 122478. https://doi.org/10.1016/j.jclepro.2020.122478.

[23] V. Barbieri, M. Lassinantti Gualtieri, T. Manfredini, C. Siligardi, Lightweight concretes based on wheat husk and hemp hurd as bio-aggregates and modified magnesium oxysulfate binder: Microstructure and

technological performances, Construction and Building Materials. 284 (2021) 122751. https://doi.org/10.1016/j.conbuildmat.2021.122751.

[24] X. Zhang, M. Riaz Ahmad, B. Chen, Numerical and experimental investigation of the hygrothermal properties of corn stalk and magnesium phosphate cement (MPC) based bio-composites, Construction and Building Materials. 244 (2020) 118358. https://doi.org/10.1016/j.conbuildmat.2020.118358.

[25] C. Véronique, Propriétés mécaniques, thermiques et acoustiques d'un matériau à base de particules végétales : approche expérimentale et modélisation théorique, (n.d.) 248.

[26] M.S. Abbas, F. McGregor, A. Fabbri, M.Y. Ferroukhi, The use of pith in the formulation of lightweight bio-based composites: Impact on mechanical and hygrothermal properties, Construction and Building Materials. 259 (2020) 120573. https://doi.org/10.1016/j.conbuildmat.2020.120573.

[27] M. Lagouin, C. Magniont, P. Sénéchal, P. Moonen, J.-E. Aubert, A. Laborel-préneron, Influence of types of binder and plant aggregates on hygrothermal and mechanical properties of vegetal concretes, Construction and Building Materials. 222 (2019) 852–871. https://doi.org/10.1016/j.conbuildmat.2019.06.004.

[28] J.-P. Costes, A. Evrard, B. Biot, G. Keutgen, A. Daras, S. Dubois, F. Lebeau, L. Courard, Thermal Conductivity of Straw Bales: Full Size Measurements Considering the Direction of the Heat Flow, Buildings. 7 (2017) 11. https://doi.org/10.3390/buildings7010011.

[29] K.A. Sabapathy, S. Gedupudi, Straw bale based constructions: Measurement of effective thermal transport properties, Construction and Building Materials. 198 (2019) 182–194. https://doi.org/10.1016/j.conbuildmat.2018.11.256.

[30] J. Williams, M. Lawrence, P. Walker, The influence of the casting process on the internal structure and physical properties of hemp-lime, Mater Struct. 50 (2017) 108. https://doi.org/10.1617/s11527-016-0976-4.

[31] J. Williams, M. Lawrence, P. Walker, A method for the assessment of the internal structure of bio-aggregate concretes, Construction and Building Materials. 116 (2016) 45–51. https://doi.org/10.1016/j.conbuildmat.2016.04.088.

[32] M. Viel, F. Collet, C. Lanos, Chemical and multi-physical characterization of agro-resources' by-product as a possible raw building material, Industrial Crops and Products. 120 (2018) 214–237. https://doi.org/10.1016/j.indcrop.2018.04.025.

[33] G. Fang, Q. Wang, M. Zhang, Micromechanical analysis of interfacial transition zone in alkali-activated fly ash-slag concrete, Cement and Concrete Composites. 119 (2021) 103990. https://doi.org/10.1016/j.cemconcomp.2021.103990.

[34] T. Zhang, H. Zhu, L. Zhou, Z. Yan, Multi-level micromechanical analysis of elastic properties of ultra-high performance concrete at high temperatures: Effects of imperfect interface and inclusion size, Composite Structures. 262 (2021) 113548. https://doi.org/10.1016/j.compstruct.2021.113548.

[35] S.C. Somé, A. Ben Fraj, A. Pavoine, M. Hajj Chehade, Modeling and experimental characterization of effective transverse thermal properties of hemp insulation concrete, Construction and Building Materials. 189 (2018) 384–396. https://doi.org/10.1016/j.conbuildmat.2018.08.210.

[36] S. Dartois, S. Mom, H. Dumontet, A. Ben Hamida, An iterative micromechanical modeling to estimate the thermal and mechanical properties of polydisperse composites with platy particles: Application to anisotropic hemp and lime concretes, Construction and Building Materials. 152 (2017) 661–671. https://doi.org/10.1016/j.conbuildmat.2017.06.181.

[37] A.D. Tran-Le, S.-T. Nguyen, T. Langlet, A novel anisotropic analytical model for effective thermal conductivity tensor of dry lime-hemp concrete with preferred spatial distributions, Energy and Buildings. 182 (2019) 75–87. https://doi.org/10.1016/j.enbuild.2018.09.043.

[38] S. Allin, Building with Hemp, SeedPress, 2005.

[39] C. Ingrao, A. Lo Giudice, J. Bacenetti, C. Tricase, G. Dotelli, M. Fiala, V. Siracusa, C. Mbohwa, Energy and environmental assessment of industrial hemp for building applications: A review, Renewable and Sustainable Energy Reviews. 51 (2015) 29–42. https://doi.org/10.1016/j.rser.2015.06.002.

[40] Global Hemp Market - cannabusinessplans.com Business Plan templates, Business Plan Templates. (2022). https://cannabusinessplans.com/global-hemp-market/ (accessed February 6, 2022).

[41] TOP 10 Sunflower Seeds Producing Countries in 2019, Latifundist.Com. (2020). https://latifundist.com/en/rating/uzhe-razlili-maslo-rejting-proizvoditelej-podsolnechnika (accessed February 6, 2022).

[42] O. Erenstein, J. Chamberlin, K. Sonder, Estimating the global number and distribution of maize and wheat farms, Global Food Security. 30 (2021) 100558. https://doi.org/10.1016/j.gfs.2021.100558.

[43] N. Mati-Baouche, H. De Baynast, A. Lebert, S. Sun, C.J.S. Lopez-Mingo, P. Leclaire, P. Michaud, Mechanical, thermal and acoustical characterizations of an insulating bio-based composite made from sunflower stalks particles and chitosan, Industrial Crops and Products. 58 (2014) 244–250. https://doi.org/10.1016/j.indcrop.2014.04.022.

[44] M.S. Abbas, E. Gourdon, P. Glé, F. McGregor, M.Y. Ferroukhi, A. Fabbri, Relationship between hygrothermal and acoustical behavior of hemp and sunflower composites, Building and Environment. 188 (2021) 107462. https://doi.org/10.1016/j.buildenv.2020.107462.

[45] Y. Brouard, N. Belayachi, D. Hoxha, N. Ranganathan, S. Méo, Mechanical and hygrothermal behavior of clay – Sunflower (Helianthus annuus) and rape straw (Brassica napus) plaster bio-composites for building insulation, Construction and Building Materials. 161 (2018) 196–207. https://doi.org/10.1016/j.conbuildmat.2017.11.140.

[46] F. Bennai, C. El Hachem, K. Abahri, R. Belarbi, Microscopic hydric characterization of hemp concrete by X-ray microtomography and digital volume correlation, Construction and Building Materials. 188 (2018) 983–994. https://doi.org/10.1016/j.conbuildmat.2018.08.198.

[47] E.J. Kubel, J.J. Friel, ASM International, eds., Practical guide to image analysis, 1. print, ASM International, Materials Park, Ohio, 2000.

[48] H. Fares, A. Lecomte, Paramètres de composition des mélanges de particules de chènevotte pour l'élaboration de béton de chanvre, in: 2014. https://hal-enpc.archives-ouvertes.fr/hal-01144417 (accessed March 30, 2021).

[49] J. Williams, M. Lawrence, P. Walker, The influence of constituents on the properties of the bio-aggregate composite hemp-lime, Construction and Building Materials. 159 (2018) 9–17. https://doi.org/10.1016/j.conbuildmat.2017.10.109.

[50] R.A. Raju, S. Lim, M. Akiyama, T. Kageyama, Effects of concrete flow on the distribution and orientation of fibers and flexural behavior of steel fiber-reinforced self-compacting concrete beams, Construction and Building Materials. 262 (2020) 119963. https://doi.org/10.1016/j.conbuildmat.2020.119963.

[51] S. Brisard, M. Serdar, P.J.M. Monteiro, Multiscale X-ray tomography of cementitious materials: A review, Cement and Concrete Research. 128 (2020) 105824. https://doi.org/10.1016/j.cemconres.2019.105824.

[52] Z.J. Yang, A. Qsymah, Y.Z. Peng, L. Margetts, R. Sharma, 4D characterisation of damage and fracture mechanisms of ultra high performance fibre reinforced concrete by in-situ micro X-Ray computed tomography tests, Cement and Concrete Composites. 106 (2020) 103473. https://doi.org/10.1016/j.cemconcomp.2019.103473.

[53] R. Walker, A study of the properties of lime-hemp concrete with pozzolans, thesis, Trinity College (Dublin, Ireland). Department of Civil, Structural and Environmental Engineering, 2013. http://www.tara.tcd.ie/handle/2262/79389 (accessed June 7, 2021).

[54] V. Nozahic, S. Amziane, G. Torrent, K. Saïdi, H. De Baynast, Design of green concrete made of plant-derived aggregates and a pumice–lime binder, Cement and Concrete Composites. 34 (2012) 231–241. https://doi.org/10.1016/j.cemconcomp.2011.09.002.

[55] L. Arnaud, E. Gourlay, Experimental study of parameters influencing mechanical properties of hemp concretes, Construction and Building Materials. 28 (2012) 50–56. https://doi.org/10.1016/j.conbuildmat.2011.07.052.

[56] Y. Ding, J.-G. Dai, C.-J. Shi, Fracture properties of alkali-activated slag and ordinary Portland cement concrete and mortar, Construction and Building Materials. 165 (2018) 310–320. https://doi.org/10.1016/j.conbuildmat.2017.12.202.

[57] Herinjaka Haga Ratsimbazafy, Aurélie Laborel-Préneron, Camille Magniont, Philippe Evon, A Review of the Multi-Physical Characteristics of Plant Aggregates and Their Effects on the Properties of Plant-Based Concrete, RPM. 03 (2021) 1–1. https://doi.org/10.21926/rpm.2102026.

[58] P. Tronet, T. Lecompte, V. Picandet, C. Baley, Study of lime hemp concrete (LHC) – Mix design, casting process and mechanical behaviour, Cement and Concrete Composites. 67 (2016) 60–72. https://doi.org/10.1016/j.cemconcomp.2015.12.004.

[59] M. Rahim, O. Douzane, A.D. Tran Le, G. Promis, T. Langlet, Characterization and comparison of hygric properties of rape straw concrete and hemp concrete, Construction and Building Materials. 102 (2016) 679–687. https://doi.org/10.1016/j.conbuildmat.2015.11.021.

[60] N. Mati-Baouche, Conception d'isolants thermiques à base de broyats de tiges de tournesol et de liants polysaccharidiques, (n.d.) 269.

[61] J.D. Eshelby, R.E. Peierls, The determination of the elastic field of an ellipsoidal inclusion, and related problems, Proceedings of the Royal Society of London. Series A. Mathematical and Physical Sciences. 241 (1957) 376–396. https://doi.org/10.1098/rspa.1957.0133.

[62] T. Mori, K. Tanaka, Average stress in matrix and average elastic energy of materials with misfitting inclusions, Acta Metallurgica. 21 (1973) 571–574. https://doi.org/10.1016/0001-6160(73)90064-3.

[63] Q.V. Huynh, ESTIMATION DES PROPRIETES POROMECANIQUES EFFECTIVES DES ARGILITES: APPORT DES METHODES D'HOMOGENEISATION, (n.d.) 131.

[64] A. Giraud, D. Hoxha, Q.V. Huynh, D.P. Do, V. Magnenet, Effective porothermoelastic properties of transversely isotropic rock-like composites, International Journal of Engineering Science. 46 (2008) 527–550. https://doi.org/10.1016/j.ijengsci.2008.01.010.

[65] P. Bechterew, Analytical study of the generalized hooke's law. application of the method of coordinate transformation, Zh. Russ. Fiz.-Khim. Obshch. Leningrad. Univ., Fizika. 58 (1926) 415–416.

[66] T. Mura, Micromechanics of defects in solids, Springer Netherlands, Dordrecht, 1987. https://doi.org/10.1007/978-94-009-3489-4.

[67] S.-Z. Lin, L.-Y. Zhang, J.-Y. Sheng, B. Li, X.-Q. Feng, Micromechanics methods for evaluating the effective moduli of soft neo-Hookean composites, Arch Appl Mech. 86 (2016) 219–234. https://doi.org/10.1007/s00419-015-1116-2.

[68] S. Lemaitre, Modélisation des matériaux composites multiphasiques à microstructures complexes: Etude des propriétés effectives par des méthodes d'homogénéisation, n.d.

[69] S. Kioy, Lime-hemp composites: compressive strength and résistance to fungal attacks. MEng dissertation, recalled in Appendix 1: Resistance to compression and stress-strain properties, in: Hemp Lime Construction, A Guide to Building With Hemp Lime Composites, IHS BRE Press, 2013.

[70] T.T. Nguyen, V. Picandet, P. Carre, T. Lecompte, S. Amziane, C. Baley, Effect of compaction on mechanical and thermal properties of hemp concrete, European Journal of Environmental and Civil Engineering. 14 (2010) 545–560. https://doi.org/10.1080/19648189.2010.9693246.

[71] S. Pavía, E. Treacy, A comparative study of the durability and behaviour of fat lime and feebly-hydraulic lime mortars, Mater Struct. 39 (2007) 391–398. https://doi.org/10.1617/s11527-005-9033-4.

[72] L. Dormieux, D. Kondo, F.-J. Ulm, Microporomechanics, John Wiley & Sons, Chichester, West Sussex, England ; Hoboken, NJ, 2006.

CHAPTER III : Modeling the thermal conductivity of bio-based concrete

Chapter introduction

The construction industry is one of the largest consumers of energy, with heating and cooling of building operations being a major contributor. Bio-based concrete possesses the desirable property of thermal insulation, making it an attractive building material for reducing energy consumption during building operations.

Bio-based concrete offers an advantage in this area due to its low thermal conductivity, which can lead to significant energy savings. Understanding the microscopic mechanism of thermal conductivity in bio-based concrete is essential to optimize this property.

This chapter presents a multi-scale thermal model consisting of two journal papers (Articles B and C). Article B proposes a finite element model based on a multi-scale structure considering the volume fraction, shape, orientation, binders, and macroscopic pores. This model has four scales as follows.

1. Bio-based composite, which contains bio-aggregates, binders, and macropores. This scale involves factors such as volume fraction, shape, and orientation of the bio-aggregate.

2. Bio-aggregate, which contains bio-aggregate solids and intra-particle pores. The shape of the pores is considered.

3. Pore and moisture, which allows this model to be applied in a humid environment.

4. Binder, which consists of binder solids and microscopic pores.

This model accurately predicts the effective thermal conductivity of bio-based concrete. It visualizes the effect of the multi-scale structure on thermal conductivity and reveals the mechanism of heat flow through plant fibers. However, it requires significant computational resources and time.

As a complement and verification, article C develops an analytical model that considers the orientation and shape of plant fibers, moisture, imperfect contact, and pore size. A series of comparisons are then

performed between the analytical model, the finite element model, and experimental data from the literature. The results show that the analytical model accurately predicts the thermal conductivity of bio-based concrete and can be used to optimize its thermal insulation properties.

Overall, this chapter highlights the importance of understanding the microstructure of bio-based concrete and presents two models that can be used to predict and optimize its thermal conductivity. Articles B was published in *Construction Materials* on July 4, 2022, and article C will be published in *Construction and Building Materials* on May 9, 2023.

Article B: A Multi-Scale Numerical Simulation on Thermal Conductivity of Bio-Based Construction Materials

Gang Huang [1], Ariane Abou-Chakra [1,*], Sandrine Geoffroy [1] and Joseph Absi [2]

1 LMDC (Laboratoire Matériaux et Durabilité des Constructions), INSA, UPS, Université de Toulouse, 135 Avenue de Rangueil, 31077 Toulouse, France; ghuang@insa-toulouse.fr (G.H.); geoffroy@insa-toulouse.fr (S.G.)

2 UMR CNRS, IRCER, Université de Limoges, 12 rue Atlantis, 87068 Limoges, France; joseph.absi@unilim.fr

Abstract

Amid increasing concern about carbon emissions and ENERGY consumption in the building industry, bio-based construction materials are one of the solutions, especially considering their excellent thermal insulation. This study aims to develop a multi-scale numerical model to analyze the effect of microstructure on the thermal conductivity of a bio-based construction material. To achieve this**,** the size, shape, orientation, porosity, and water saturation of the bio-aggregate were considered in this study. The results show that the thermal conductivity of the bio-based material increases significantly and nonlinearly with water saturation, in contrast to the parallel thermal conductivity of the transversely isotropic bio-aggregate, which increases linearly. The thermal conductivity of the bio-based material shows an anisotropy in different directions and it obtains a maximum at water saturation of 0.4. Analysis of inclusions with different shapes shows that the thermal conductivity in the compaction direction is almost independent of the shape, but not in the direction perpendicular to the compaction. The finite element results show that the heat flow tends to transfer along the bio-aggregate rather than across it. These findings help to better understand the effect of microstructure on thermal conductivity and then promote the application of bio-based concrete as an insulation material in buildings.

Keywords: bio-based materials; thermal conductivity; moisture; microstructure; multi-scale homogenization; numerical modeling

https://doi.org/10.3390/constrmater2030011

1. Introduction

In recent years, there has been an increasing discussion on carbon emission, energy crisis, environmental protection, and sustainability. The building industry plays a vital role in these areas as global CO_2 emissions from building increased by 50% from 1990 to 2019 [1]. Moreover, in developing countries, buildings account for about 15–25% of total energy consumption, while in developed countries it is 30–40% [2]. Further investigations show that space heating was the largest residential energy demand in Europe and Eurasia,

exceeding 50% in 2019 [1].

The use of bio-based construction materials is one of the solutions to mitigate carbon emissions and energy consumption. This is due to the fact that bio-based construction materials have advantages over traditional concrete in these issues. On the one hand, plant aggregates have lower embodied carbon, which means lower CO_2 emissions are associated with the processes of construction and materials throughout their whole lifecycle [3]. Moreover, they promote carbon sink in building materials since plants store considerable amounts of carbon in a relatively small volume [1,4]. On the other hand, the excellent performance of bio-based materials in thermal insulation can save the energy consumption of space heating as mentioned above. Especially considering the growing global interest in net-zero energy buildings (NZEBs), more and more countries have set their own goal for NZEBs [5–7]. Obviously, the study of thermal conductivity helps to improve the thermal performance of bio-based materials, which thereby promotes environmental protection and reduces energy consumption.

Several experimental studies [8–10] have shown the low thermal conductivity of bio-based concrete. This is due to the high intra-particle porosity in plant particles and macro porosity in bio-based materials [11,12]. Moreover, bio-based materials are used in buildings because of their role as a humidity regulator, absorbing moisture in high-humidity environments and releasing it in the opposite case [13–15]. Many studies [15–20] have shown that the effect of moisture on the thermal conductivity of bio-based materials cannot be ignored because of their strong water absorption capacity. The thermal conductivity of dry plant particles (e.g., hemp: axial: 0.122 W/mK, transverse: 0.08 W/Mk [21]) is much lower than that of water (0.598 W/mK [22]). It is significant to consider the effect of moisture in the modeling of bio-based materials. In addition, compaction in the casting of bio-based materials affects the orientation of the plant fibers, and the plant fibers tend to be distributed in a plane perpendicular to the direction of compaction [23,24]. In this case, the fact that the thermal conductivity of bio-based materials depends on the orientation has been confirmed in research [21,23,25].

Numerical simulation has been widely used in fiber-reinforced construction materials, but most of them are related to steel fiber-reinforced concrete. For example, Rezakhani et al. [26] investigated the effect of size, shape, and strength of steel fiber on the quasi-static properties of concrete. Naderi and Zhang [27] studied the compression and tensile fracture behavior of steel fiber-reinforced concrete by a 3D fine-scale modeling approach. Liang and Wu [28] developed a model for the thermal conductivity of steel fiber concrete and then investigated these parameters: model thickness, steel fiber diameter, and volume fraction (0.5%, 1%, and 2%). However, these methods cannot be completely used for modeling bio-based building materials since there are more complex microstructures in bio-based materials compared to steel fiber concrete. Some plant fibers such as hemp [29] and wheat straw [30] have a transversely isotropic structure compared to the isotropic

steel fiber. The volume fraction of plant fiber in concrete is much higher than that of steel fiber, e.g., 55% in [12]. In addition, the porous structure leads to high water absorption of plant fiber [18,31], which affects the material properties, especially for thermal conductivity [16,17].

This paper aims to develop a multi-scale numerical model to investigate the effect of the microstructure of bio-based building materials on thermal conductivity. In this modeling, the bio-based material is considered to consist of three components, each of which can be subdivided into more components at the microscopic scale. The details of each component are as follows.

- Binder: binder solid and micropores;
- Bio-aggregates: intra-particle pores (air and water) embedded in a solid matrix;
- Macropores.

This model considers the size, shape, orientation, porosity, and water saturation of plant fibers. From the microscopic to the macroscopic scale, the microstructural characteristics of each component are linked to the macroscopic property by a successive numerical homogenization. This link can promote the application of bio-based concrete as an insulation material in buildings. In addition, the study of various porosities and shapes of bio-aggregate helps the model to be applied to a wider range of bio-based construction materials.

2. Materials and Methods

2.1. Materials

The material used in this model is bio-based construction material. Initially, hemp was selected as an example, which is one of the most widely studied plant fibers in bio-based construction materials. Then, the approach explores the application of this model to other types of bio-based materials by varying the shape and porosity of the bio-aggregate in the model.

Hemp is a porous transversely isotropic material from the microstructure due to the arrangement of the pores, as shown in Figure 1 from the literature [12,32]. It is essential to investigate the internal structure of hemp before multi-scale modeling. The cross-section in Figure 1(A-1) illustrates two diameters of the conduit: about 50 μm for the vessel and about 20 μm for the tracheid [32], while the longitudinal section (see Figure 1(A-2,B-2)) shows the elongated tubular structure. Additionally, Figure 1(B-1) clearly presents the nearly circular cross-section of the pores. Some of the physical and thermal properties of dry hemp shiv are shown in Table 1. In Table 1, the first value in multiple options is selected for the model. Aggregates used by different researchers may vary because of their source and manufacturing process, especially in terms of length and width. For specific heat capacity and thermal conductivity, the differences in values from various literature (Table 1) are slight, so the choices have little effect on the results. For length and width, the study of shape in Section 3.3.4 will compensate for this selection preference.

1. 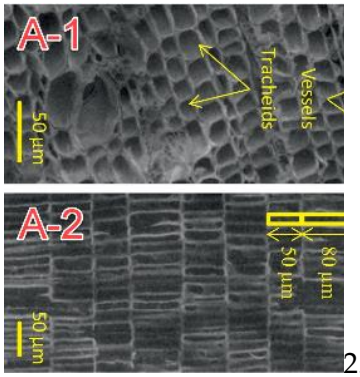

2. 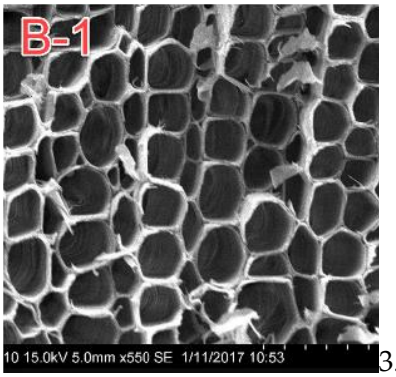

3. 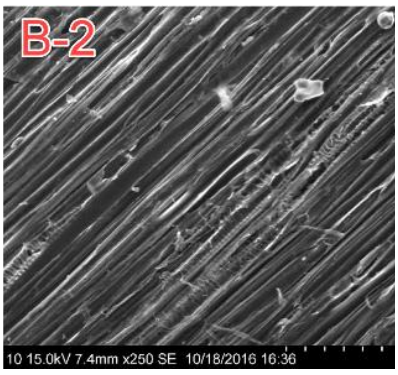

Figure 1. Microstructure of hemp shiv is reprinted with permission from Ref. [32]. 2018. Elsevier.-A, reprinted with permission from Ref. [12]. 2018. Elsevier.-B, (**A-1**,**B-1**) cross-section, (**A-2**,**B-2**) longitudinal section.

Table 1. Properties of hemp shiv.

Property	Value	Reference
Particle density (kg/m3)	265	[33]
Solid density (kg/m3)	1454	[34]
Length (mm)	4–8 mm	[34]
Width (mm)	1–2 mm	[34]

Porosity (%)	81.8	[34]
Specific heat capacity (J/(kg·K))	1320/1247/1272	[33,35,36]
Thermal conductivity of solid (W/(m·K))	0.564/0.576	[34,37]

Note: The first value in these multiple options is selected for the model.

Binders involving plant fibers are usually lime-based or metakaolin-based binders rather than cement. The former comes from high-temperature calcined limestone or kaolinite. At the microscopic scale, lime-based binder consists of binder solids and fine pores with most pore sizes distributed at 1 μm [38]. The physical and thermal properties are shown in Table 2.

Table 2. Properties of binder.

Property	Value	Reference
Density (kg/m^3)	1079	[38]
Porosity (%)	50.6/54.8	[21,38]
Specific heat capacity (J/(kg·K))	890/859	[35,39]
Thermal conductivity of solid (W/(m·K))	0.24/0.277	[38,40]
Pore size diameter (μm)	0.02–4	[38]

Note: The first value in these multiple options is selected for the model.

2.2. Methods

The microstructure of bio-based material and the dimensions of each part were investigated in the previous section and can be represented in Figure 2. At the macroscopic level (10^0–10^2 mm), bio-based building materials include a binder, bio-aggregates (Length: 4 mm, width: 1 mm), and macropores (1–3 mm). Further, the binder on a scale of 10^{-2}–10^0 μm includes micropores (0.02–4 μm) and binder solid, while the bio-aggregate on a scale of 10–10^2 μm includes intra-particle pores (20–50 μm) and bio-aggregate solid. In a humid environment, the porous structure of bio-aggregate absorbs moisture, which is distributed along the elongated pores, so water is assumed to be distributed in the air matrix as a cylinder in this model on a scale of 10^0–10 μm. Thus, in the present multi-scale model, binder, bio-aggregate, and bio-based composite are sequentially homogenized by numerical methods. Among them, bio-aggregate is homogenized in a humid environment involving intra-particle pores and moisture. The details of each homogenization step are

described in the next section.

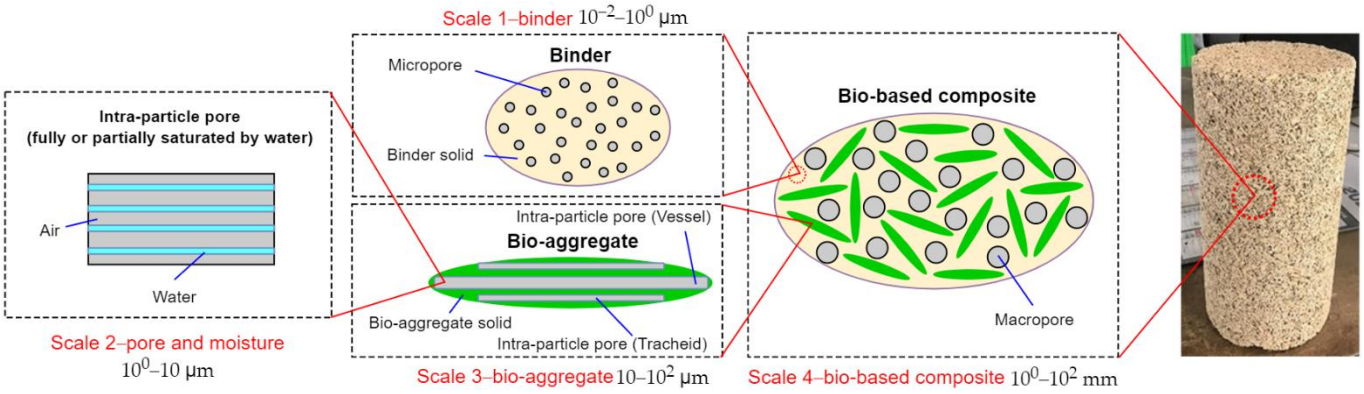

Figure 2. Multi-scale homogenization model for the thermal conductivity (The photograph of the sample on the right is reprinted with permission from Ref. [41]. 2020. Elsevier).

2.2.1. Modeling of Binder

Scale 1 (10−2–100 µm): the binder.

The binder is considered to consist of binder solids and micropores on scale 1 (10−2–100 µm), as shown in Figure 2. The micropores are considered to be randomly distributed in the solid. Micropores, with pore sizes in the range of 0.02–4 µm and mostly 1 µm [38], are considered to be randomly distributed in the solid. Note that there is only one homogenization step here. The model of the porous binder based on these data is shown in Figure 3. The pores were embedded in the binder solid to form a two-phase material, and then the mesh was applied to the whole. The nodes are shared at the interface of the two phases.

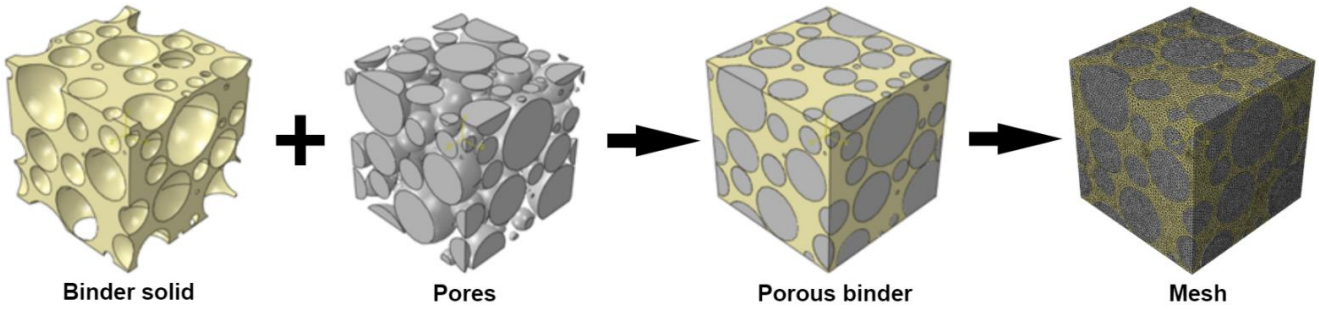

Figure 3. Multi-scale homogenization model for scale 2-binder.

2.2.2. Two-Scale Modeling of Individual Hemp Shiv

Scale 2 (100–10 µm): pore and moisture.

The porous structure of the hemp shown in Figure 1 facilitates the absorption of moisture. Moreover, the elongated cells allow the water to be distributed in a directional arrangement. Therefore, on scale 2 (Figure 2) of the numerical model, the moisture is assumed to be a cylinder embedded in the air matrix as shown in

Figure 4. Homogenized materials considering pores and moisture can be obtained through the homogenization in this step and used for modeling on the next scale. It is noted that water saturation (WS), i.e., the volume ratio of water to pore, is used to quantify the moisture value of the hemp.

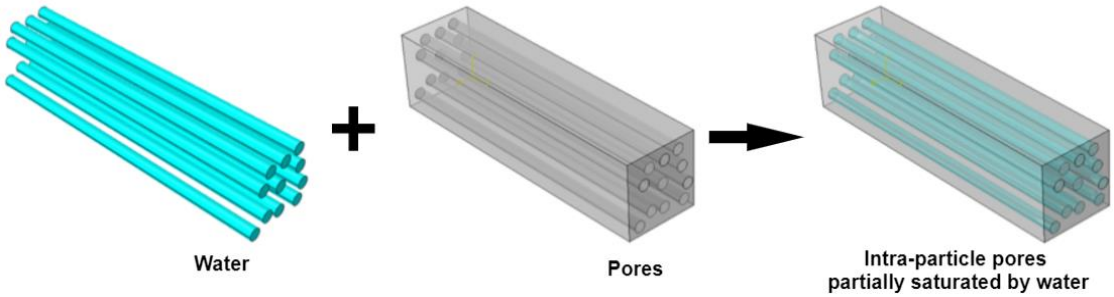

Figure 4. Multi-scale homogenization model for scale 2.

Scale 3 (10–102 μm): the bio-aggregates.

As shown in Figure 2, the homogenization at this scale aims to combine the homogenized material (moisture and voids) from the previous step with the hemp solid. Figure 1 shows that there are two types of pores inside the hemp: vessel (50 μm) and tracheid (20 μm). Therefore, the finite element models of tracheid and vessel were built according to their corresponding dimensions in Figure 5. It should be noted that the pores were generated randomly in the cross-section.

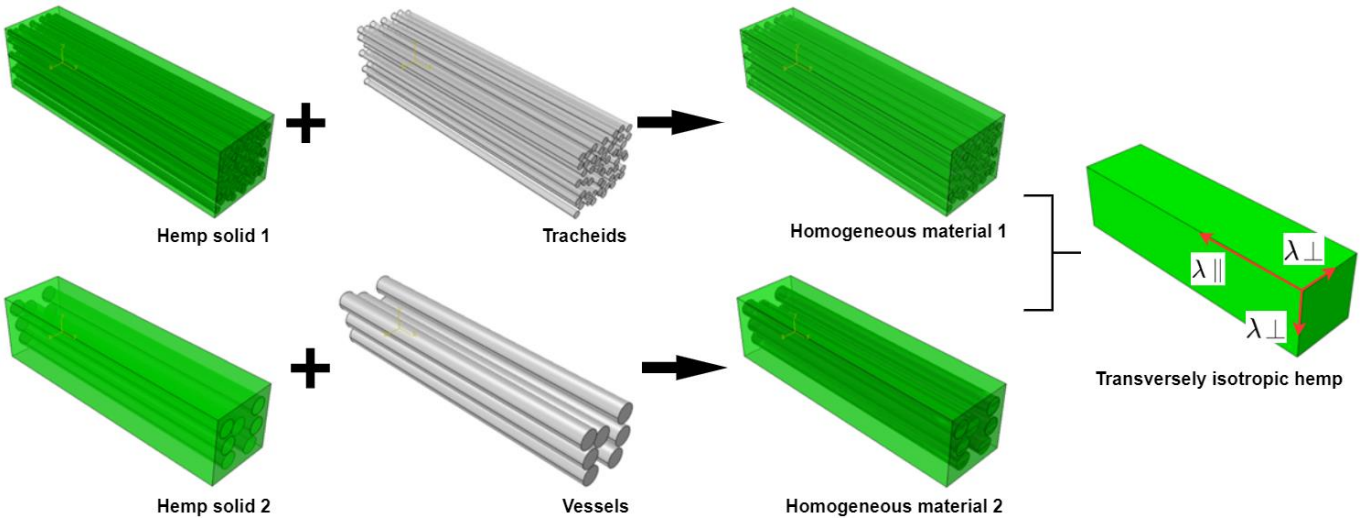

Figure 5. Multi-scale homogenization model for scale 3-bio-aggregate.

2.2.3. Modeling of Bio-Based Construction Materials

Scale 4 (100–102 mm): the bio-based composite.

The bio-based composite on scale 4 in Figure 2 is macroscopically composed of three components: binder,

hemp, and macropores. Macropores in the modeling are considered randomly distributed in the homogenized binder (binder solid and micropores). Therefore, prior to considering the hemp, the numerical homogenization was carried out between the binder and the macropores by a similar method as in Figure 3. After obtaining the homogenized binder, the final model containing the hemp is shown in Figure 6. The model was generated in the commercial software Digimat and then solved by Abaqus. As shown in Figure 6, the heat flow is transferred from the high-temperature side to the low-temperature side. In this process, the effective thermal conductivity of the composite can be calculated by applying the classical Fourier's law [42,43]. Note that the length and width of the hemp are 4 and 1 mm, respectively, according to Table 1. It is also worth noting that plant fibers in bio-based building materials usually tend to be distributed perpendicular to the compaction direction [24,44]. Therefore, in this model, the hemp is randomly distributed in the plane perpendicular to the compaction direction. For hemp construction material, the volume fraction of each component is essential for the modeling. This can be found in the literature [12] and listed in Table 3.

Table 3. Volume fraction of each phase in hemp construction material from [12].

Phases	Volume Fraction
Binder	0.30
Hemp	0.55
Macro pore	0.15

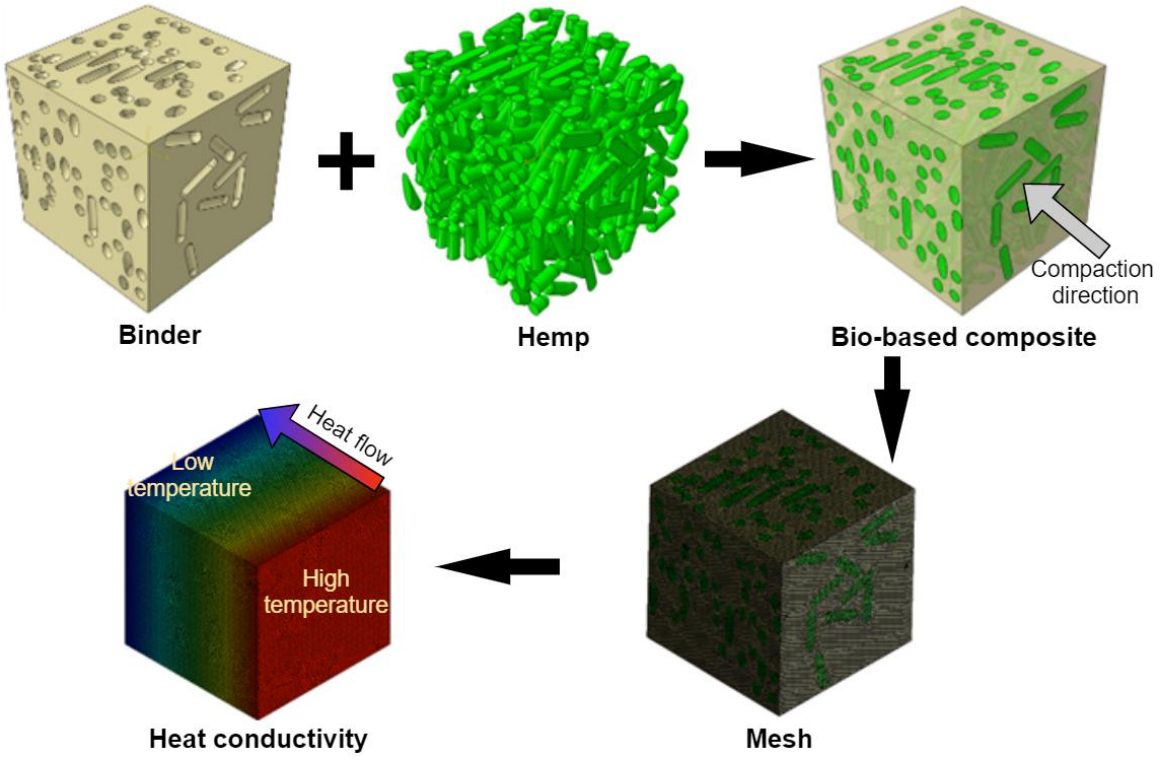

Figure 6. Multi-scale homogenization model for scale 3-bio-based composite.

To extend the present model from hemp to more types of bio-aggregates, three shapes of inclusions are compared in this numerical model. Their size information and particle distribution are shown in Figure 7.

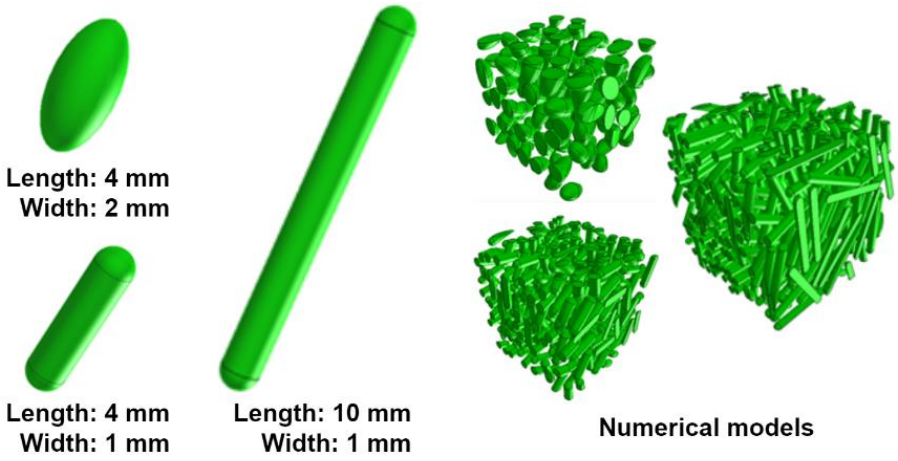

Figure 7. Multiple shapes of bio-aggregates in numerical models.

3. Results and Discussion

3.1. Effective Thermal Conductivity of Binder

The study of the effective thermal conductivity for a porous binder involves only one factor, i.e., the volume fraction of the micropores in Figure 2. The effective thermal conductivity of porous binder is presented in Figure 8. As the porosity increases, the thermal conductivity of the binder decreases. The results of the numerical simulations in this paper agree well with the experimental data from the literature [21,38,40].

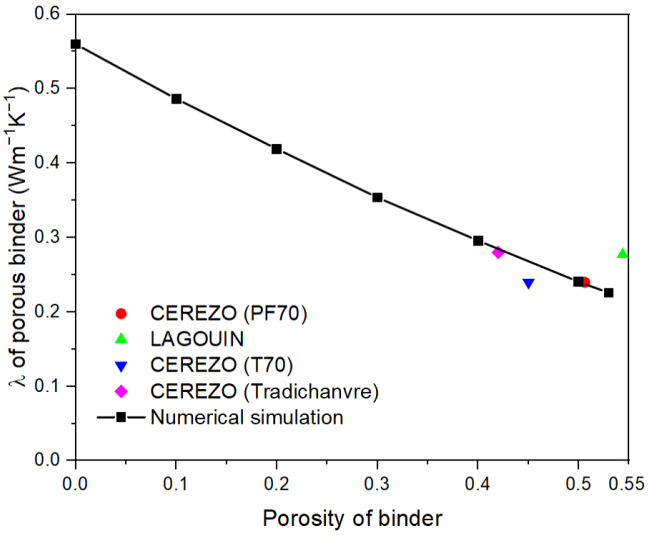

Figure 8. Effective thermal conductivity of binder (Experimental results as a comparison are from [21,38,40]).

3.2. Effective Thermal Conductivity of Individual Hemp Shiv

Figure 9 shows the thermal conductivity with water saturation in different directions on scale 2. Note that $\lambda_{\parallel}$ and $\lambda^{\perp}$ in Figure 9 denote the axial direction and the direction perpendicular to the axial direction, respectively. The axial direction is the revolution axis of the inclusion. The results in Figure 9 show that $\lambda_{\parallel}$ increases almost linearly with water saturation while $\lambda^{\perp}$ increases at an increasing rate. This difference makes the anisotropy increase initially, then decrease with water saturation. It takes a maximum of about 0.4. From this conclusion, it is known that water saturation affects the anisotropy of the pore-moisture, which in turn affects the anisotropy of the hemp and the bio-based composite. First, the orientation of the moisture illustrated in Figure 4 leads to differences in the thermal conductivity of the pore-moisture in different directions, i.e., anisotropy. Then, the orientation of the anisotropic pore-moisture in the hemp solid leads to the anisotropy of the hemp shiv, as shown in Figure 5. Finally, the anisotropic hemp is distributed in a specific direction in the composite, which results in the anisotropy of the composite.

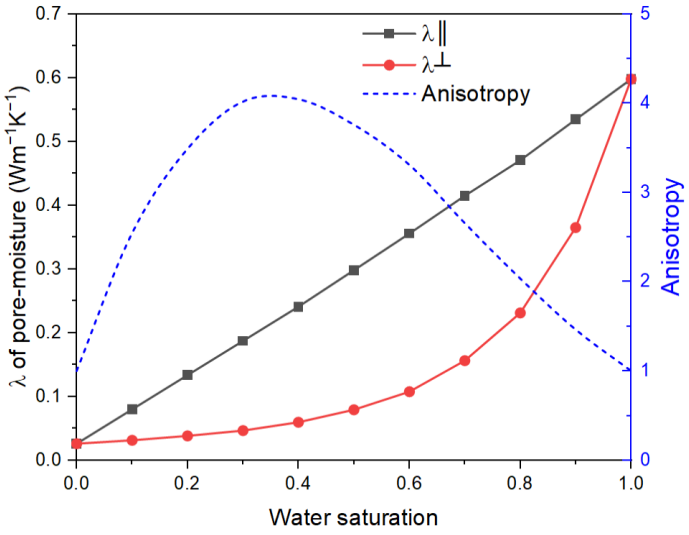

Figure 9. Effective thermal conductivity of pore-moisture (Anisotropy = $\lambda^{\perp}$).

After obtaining the properties of pore-moisture in the previous step, the hemp solid is homogenized with pore-moisture. The porosity of hemp varies with the source and processing method. Moreover, the study of porosity can also help to extend the present model to more plant fibers. So here the thermal conductivity of hemp with different porosity is studied as shown in Figure 10. As porosity increases, only at WS = 1.0, the thermal conductivity of hemp increases in 2 directions. This can be explained by the fact that the thermal conductivity of hemp solid is greater than that of pore-moisture when WS ≤ 0.8. Comparing $\lambda_{\parallel}$ and $\lambda^{\perp}$ in Figure 10 at the same WS, when WS = 1.0, $\lambda_{\parallel} = \lambda^{\perp}$ because the isotropic pore-moisture is embedded in the isotropic hemp solid. When WS ≤ 0.8, $\lambda_{\parallel} > \lambda^{\perp}$ owing to the anisotropy of pore-moisture, which can be seen in Figure 9. Another finding from Figure 10 is that water saturation significantly increases the transverse thermal conductivity of hemp when WS > 0.6. Finally, the experimental data on dry hemp from the literature

[33] agrees well with the numerical simulation.

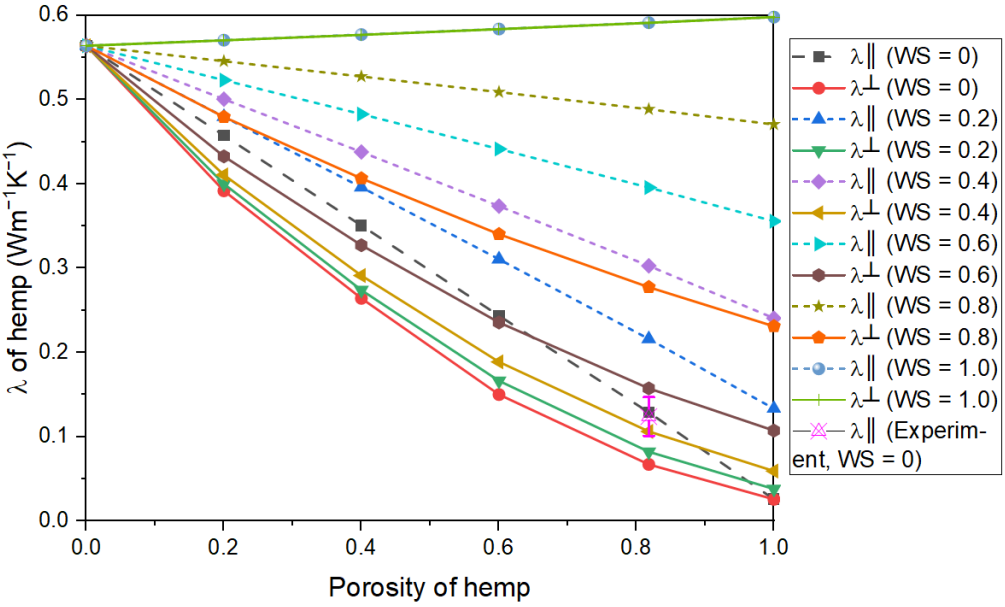

Figure 10. Effective thermal conductivity of hemp with porosity in various water saturation (WS: water saturation, $\lambda_{\parallel}$ and $\lambda_{\perp}$ denote the axial direction of hemp and the direction perpendicular to the axial direction, respectively).

Further, substituting the porosity 0.818 of hemp from the literature [34] into Figure 10 gives the variation of thermal conductivity of hemp with water saturation, as shown in Figure 11. The curves of hemp with WS are similar to the pore-moisture in Figure 9.

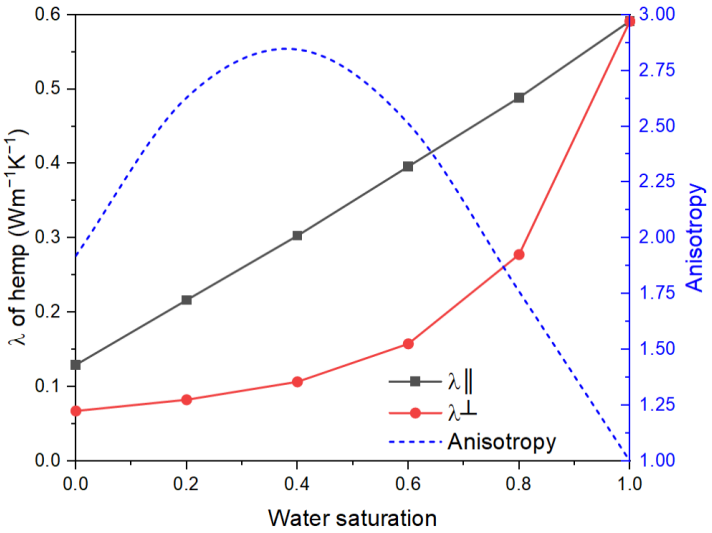

Figure 11. Variation in effective thermal conductivity with water saturation for hemp shiv.

3.3. Effective Thermal Conductivity of Bio-Based Construction Materials

3.3.1. Mesh Size Analysis

Figure 6 shows a complex numerical model of bio-based composite, and it is necessary to perform a mesh size analysis before studying the factors. A hemp volume fraction of 0.25 was selected here to investigate the effect of mesh element size on the thermal conductivity of the composite in horizontal and parallel directions. It should be noted that in the study of bio-based composites, $\lambda\|$ represents the thermal conductivity parallel to the compaction direction, and $\lambda\perp$ represents the thermal conductivity perpendicular to the compaction direction.

As shown in Figure 12, the thermal conductivity of the bio-based composite decreases as the mesh element size decreases. The thermal conductivity varies slightly when the mesh element size decreases from 0.2 to 0.1 mm. However, during this process, the number of elements in the finite element numerical simulation increases from 2,007,549 to 10,049,154. Therefore, a mesh element size of 0.2 mm was chosen in the study of bio-based composites. The dimensions of bio-aggregates can be found in Figure 7.

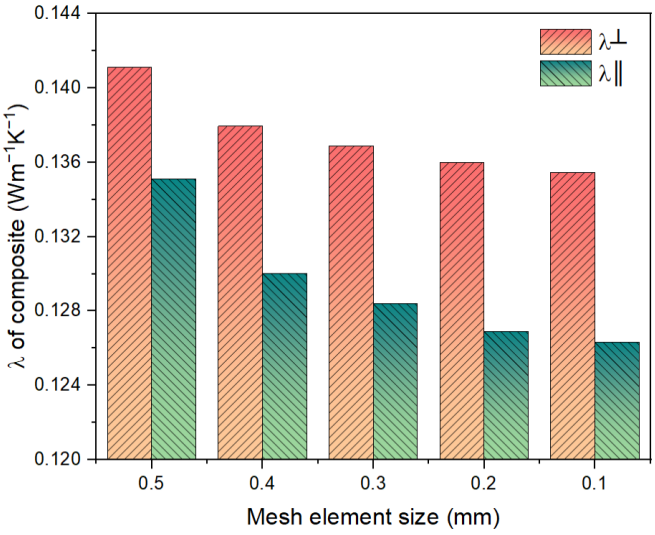

Figure 12. Testing of mesh element size.

3.3.2. Validation with Experimental Data

It is necessary to validate the model with the experimental results before conducting the parametric analysis. Figure 13 shows the comparison of the results of the numerical simulations with the experimental results from the literature [23,40]. It is important to note that the numerical simulation results in Figure 13 are based on the volume fraction of macropores in Table 3, i.e., macro-porosity was assumed to be a constant at different volume fractions of hemp, and then the density of the composite was calculated according to Tables 1 and 2. It should also be noted that for the experimental results from CEREZO [40], the authors did not distinguish the different thermal conductivity perpendicular and parallel to the compaction direction, so there is only one type of value in Figure 13. In contrast, the experiments from WILLIAMS [23] have different thermal conductivities in different directions. It can be seen that the results from CEREZO [40] are between

the two curves in Figure 13 when the density is approximately from 200 to 850 kg/m3. Moreover, the results of the numerical simulation agree approximately with the experimental results from WILLIAMS [23].

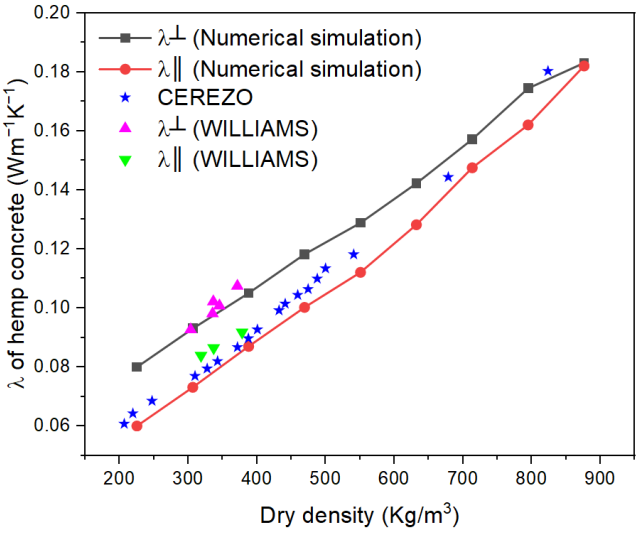

Figure 13. Comparison of numerical simulation with experimental data from [23,40].

3.3.3. Moisture

It is known from the previous sections that water saturation significantly affects the thermal conductivity of pore-moisture and hemp. In detail, in the multi-scale model, water saturation affects pore-moisture initially (Figure 9), then hemp (Figure 11), and finally bio-based composite. Figure 14 shows the effect of water saturation on the thermal conductivity of bio-based composites. Due to the high thermal conductivity of water compared to other components, the increase in water saturation reduces the thermal insulation of bio-based composite whether in the direction parallel or perpendicular to the compaction.

Further analysis in Figure 15A demonstrates the effect of water saturation on the thermal conductivity of the material at different scales. $\lambda\|$ increases approximately linearly with water saturation for pore-moisture and hemp shive. In contrast, it is nonlinear for the bio-based composite. This can be explained by the different arrangements of the inclusions. In bio-based composite, the inclusions are distributed randomly rather than linearly in the plane perpendicular to the compaction direction. In pore-moisture and hemp shiv, heat flow

can be transferred directly through the tubular inclusions.

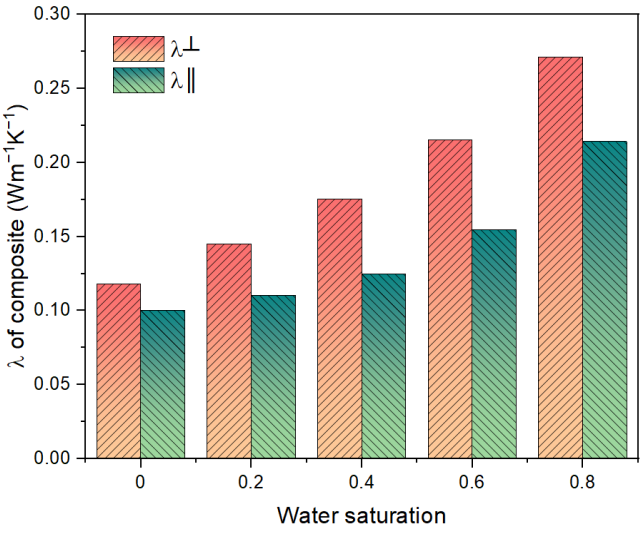

Figure 14. Effective thermal conductivity of composite with water saturation.

The effect of water saturation on the anisotropy of the pore-moisture, hemp shiv, and bio-based composites presented in Figure 15B. They have similar trends since the materials affect each other between different scales. This finding also illustrates that the macroscopic properties of a material depend on its microstructure state. Moreover, from pore-moisture to composite, anisotropy is decreasing as homogenization advances from microscopic to macroscopic scales (WS > 0.1). This is due to the fact that the new phases are isotropic materials at each step of homogenization, such as hemp solids and binders.

4.

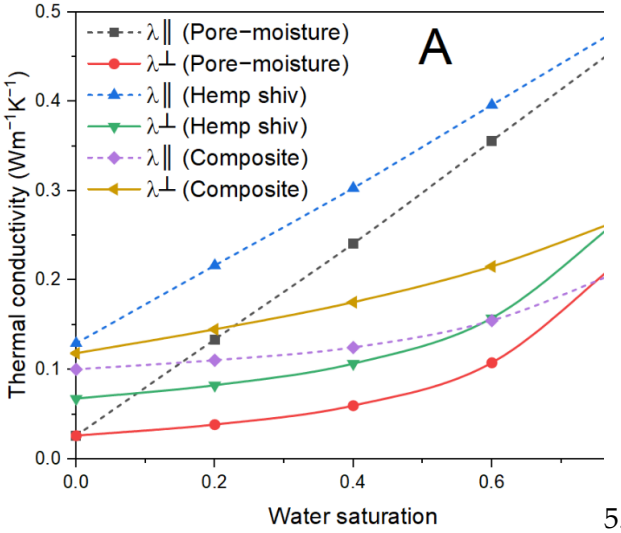

5.

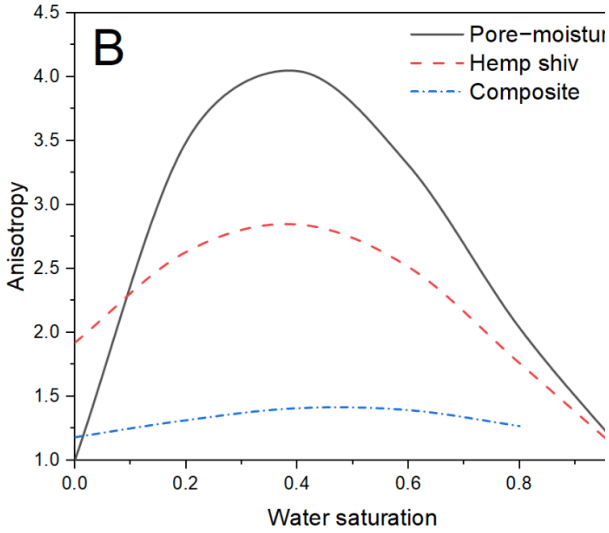

Figure 15. Comparison of (**A**) thermal conductivity and (**B**) anisotropy in multiple homogenization steps.

3.3.4. Shape of Bio-Aggregate

The multiscale homogenization models for inclusions with length and width of 4 and 1 mm has been discussed in the previous sections. However, on the one hand, the hemp size depends on the source and the manufacturing method. On the other hand, there are other local agricultural by-products specific to different countries and regions. Therefore, a comparison of three different shapes of bio-aggregates was undertaken and is shown in Figure 16. As can be seen from Figure 16, the thermal conductivity in the parallel direction is almost the same for different shapes. In contrast, with respect to the perpendicular direction, the thermal conductivity of inclusions with an aspect ratio (calculated by length/width) of 2 is lower than that of the other shapes. This relative difference increases with water saturation. These findings can be explained by the anisotropy and arrangement of the bio-aggregate. In the parallel direction, the transfer of heat flow needs to cross the cross-section of the plant fibers. In this case, the shape of the fibers in the perpendicular direction does not affect the properties in the parallel direction generally. On the contrary, in the perpendicular direction, the heat flow prefers to transfer along the plant fibers rather than cross them transversely, and the elongated plant fibers can better transfer the heat from one side of the specimen to the other side. Conversely, for plant fibers with a low aspect ratio, the heat flow from one side to the other side needs to cross more interparticle zones, which will undoubtedly increase the thermal resistance. This phenomenon will continue to be discussed in the next section based on finite element results.

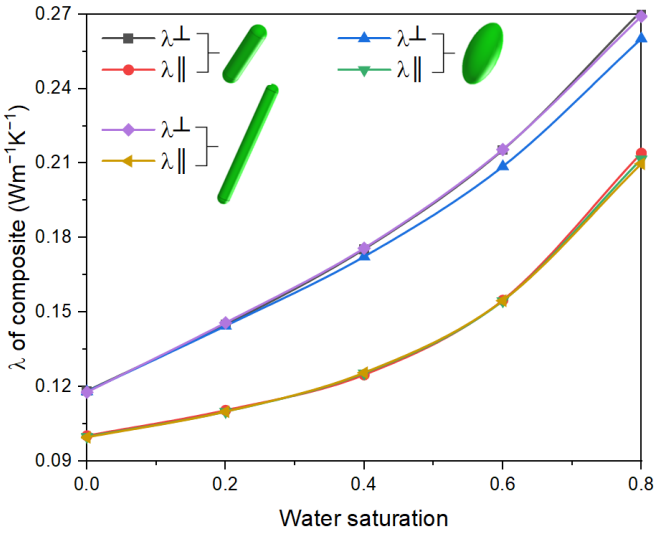

Figure 16. Comparison of bio-aggregates in various shapes.

3.3.5. Analysis of Fiber Orientation

Figure 17 shows the distribution of heat flux in the X- and Z-directions. Note that the compaction is along the X-axis. The distribution of the heat flux in the X-direction (Figure 17A) shows that the heat flux on each inclusion is almost the same. Moreover, it is less than the heat flux on the matrix. This is because, in the X-direction, the heat flow needs to pass through each inclusion transversely. Additionally, the transverse thermal

conductivity of the inclusions is lower than that of the matrix. As stated before, this arrangement of inclusions increases the thermal resistance in the X-direction and contributes to better insulation of the building material.

As for the distribution of the heat flux in the Z-direction, as shown in Figure 17B, the heat flux varies significantly on the inclusion in different orientations. In this case, the initial heat flow direction is along the Z-axis, so the inclusions oriented exactly in the Z-direction have the maximum heat flux, as shown in fiber A in Figure 17B. The heat flux is minimized when the fiber direction is perpendicular to the Z-axis, such as fiber D in Figure 17B. Moreover, the heat flux on fiber D is approximately equivalent to that of the fibers in Figure 17A, since the heat flow crosses the fibers transversely in both cases. In summary, the larger the angle (acute angle) between the fiber direction and the Z-axis (initial heat flow direction), the lower the heat flux. For example, the angle in fiber: C > B > A; as a result of heat flux: A < B < C. The heat flow tends to transfer along the bio-aggregate rather than across it because of its anisotropy.

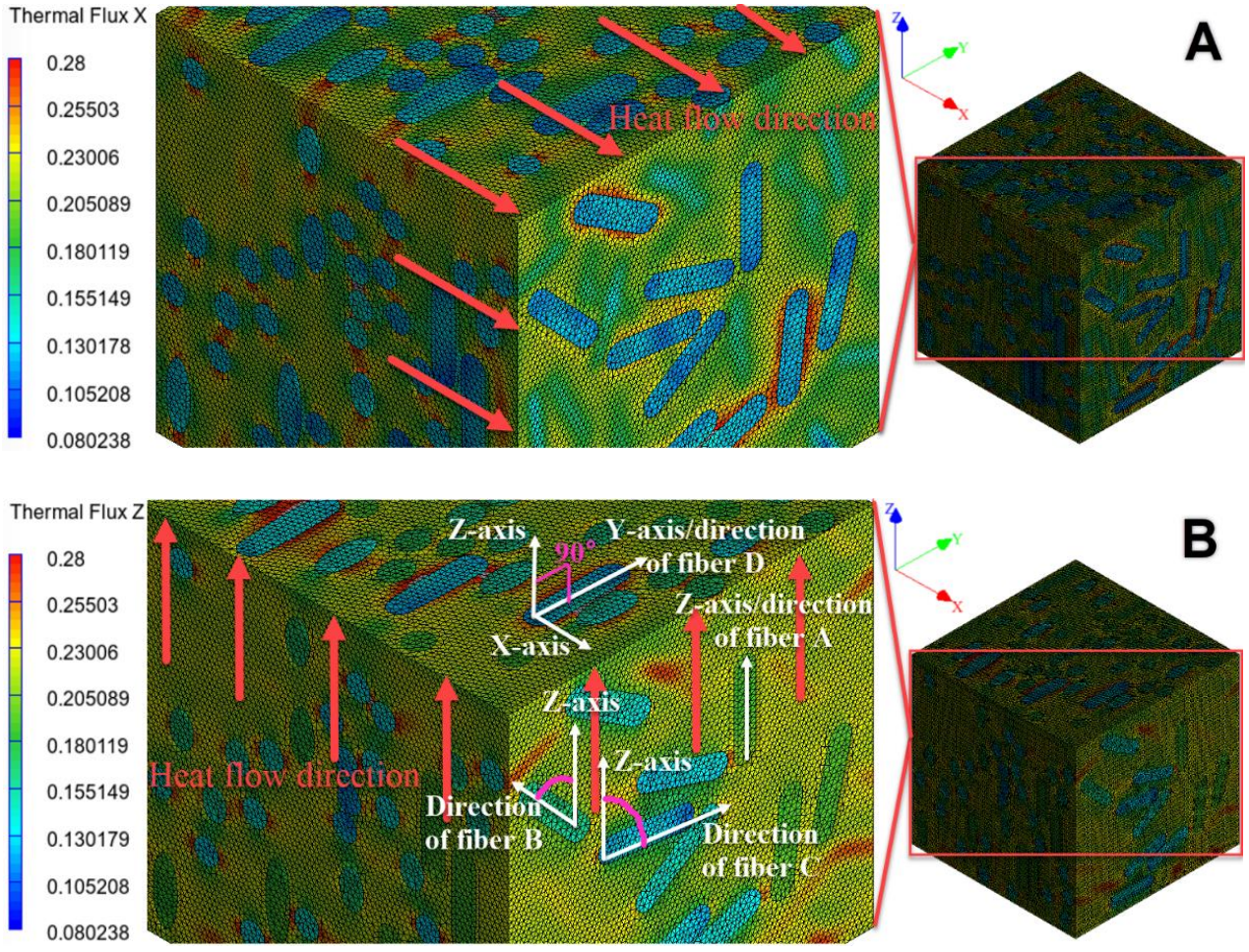

Figure 17. Analysis of plant fiber orientation based on finite element results (the compaction direction is in the X-axis. (**A**)—thermal flux X, (**B**)—thermal flux Z).

4. Conclusions

The purpose of this study is to develop a multi-scale numerical model to analyze the effect of the microstructure of bio-based construction materials on thermal conductivity. These factors were considered in this model: size, shape, orientation, porosity, and water saturation of plant fibers. The study of these factors can link microstructure and macroscopic thermal conductivity, which ultimately promotes the application of bio-based concrete as an insulation material in buildings. Moreover, considering the lack of research on numerical modeling, especially those involving multi-scale microstructures, in bio-based building materials, this study can make a contribution to the current literature. Additionally, the analysis of shape and porosity undertaken here can extend our modeling to more types of plant aggregates.

Based on the numerical simulation results, the main conclusions can be summarized as follows:

• For individual plant fiber, the thermal conductivity in the axial direction is greater than that in the transverse direction. For bio-based construction material, the thermal conductivity along the compaction direction is less than that perpendicular to the compaction direction.

• The anisotropy (the ratio of thermal conductivity in two directions) of both individual fiber and bio-based construction material increases initially, then decreases with water saturation. They take a maximum of about 0.4 water saturation.

• For transversely isotropic bio-aggregates, such as hemp, the thermal conductivity (WS $\leqslant$ 0.8) decreases with porosity. Moreover, the decline rate decreases with water saturation.

• The thermal conductivity of hemp and bio-based construction material increases with water saturation in both parallel and perpendicular directions. Further analysis shows that the parallel thermal conductivity of hemp increases linearly with water saturation, in contrast to the non-linear increase in thermal conductivity of bio-based material.

• Comparing the inclusions with different shapes (length/width = 2, 4, and 10), in the direction of compaction, the thermal conductivity of the bio-based material is almost independent of the shape. In the direction perpendicular to the compaction, the thermal conductivity at the length/width of two is lower than that of the other shapes, and the relative difference increases with water saturation.

• The analysis of the plant fiber orientation shows that the heat flow tends to transfer axially along the fiber rather than transversely across it. The heat flux on the fiber decreases with the angle (acute angle) between the fiber and the initial heat flow. This can be explained by the transversely isotropic structure of the plant

fibers.

Author Contributions: Conceptualization, A.A.-C., S.G. and J.A.; methodology, G.H., A.A.-C., S.G. and J.A.; software, G.H. and J.A.; validation, A.A.-C., S.G. and J.A.; formal analysis, G.H.; investigation, G.H.; resources, A.A.-C.; data curation, G.H.; writing—original draft preparation, G.H.; writing—review and editing, A.A.-C., S.G. and J.A.; visualization, G.H.; supervision, A.A.-C., S.G. and J.A.; project administration, S.G. All authors have read and agreed to the published version of the manuscript.

Funding: This research received no external funding.

Data Availability Statement: The data presented in this study are available on request from the corresponding author.

Conflicts of Interest: The authors declare no conflict of interest.

References

1. Climate Change 2022: Mitigation of Climate Change. Available online: https://www.ipcc.ch/report/ar6/wg3/ (accessed on 16 May 2022).
2. Li, X.; Wu, W.; Yu, C.W.F. Energy Demand for Hot Water Supply for Indoor Environments: Problems and Perspectives. *Indoor Built Environ.* **2015**, *24*, 5–10. https://doi.org/10.1177/1420326X14564285.
3. Cabeza, L.F.; Boquera, L.; Chàfer, M.; Vérez, D. Embodied Energy and Embodied Carbon of Structural Building Materials: Worldwide Progress and Barriers through Literature Map Analysis. *Energy Build.* **2021**, *231*, 110612. https://doi.org/10.1016/j.enbuild.2020.110612.
4. Churkina, G.; Organschi, A.; Reyer, C.P.O.; Ruff, A.; Vinke, K.; Liu, Z.; Reck, B.K.; Graedel, T.E.; Schellnhuber, H.J. Buildings as a Global Carbon Sink. *Nat. Sustain.* **2020**, *3*, 269–276. https://doi.org/10.1038/s41893-019-0462-4.
5. Wu, W.; Skye, H.M. Residential Net-Zero Energy Buildings: Review and Perspective. *Renew. Sustain. Energy Rev.* **2021**, *142*, 110859. https://doi.org/10.1016/j.rser.2021.110859.
6. Cabeza, L.F.; Chàfer, M. Technological Options and Strategies towards Zero Energy Buildings Contributing to Climate Change Mitigation: A Systematic Review. *Energy Build.* **2020**, *219*, 110009. https://doi.org/10.1016/j.enbuild.2020.110009.
7. Ürge-Vorsatz, D.; Khosla, R.; Bernhardt, R.; Chan, Y.C.; Vérez, D.; Hu, S.; Cabeza, L.F. Advances Toward a Net-Zero Global Building Sector. *Annu. Rev. Environ. Resour.* **2020**, *45*, 227–269. https://doi.org/10.1146/annurev-environ-012420-045843.

8. Amantino, G.M.; Hasparyk, N.P.; Tiecher, F.; Toledo Filho, R.D. Assessment of Bio-Aggregate Concretes' Properties with Rice Residue. *J. Build. Eng.* **2022**, *52*, 104348. https://doi.org/10.1016/j.jobe.2022.104348.
9. Bovo, M.; Giani, N.; Barbaresi, A.; Mazzocchetti, L.; Barbaresi, L.; Giorgini, L.; Torreggiani, D.; Tassinari, P. Contribution to Thermal and Acoustic Characterization of Corn Cob for Bio-Based Building Insulation Applications. *Energy Build.* **2022**, *262*, 111994. https://doi.org/10.1016/j.enbuild.2022.111994.
10. Costantine, G.; Maalouf, C.; Moussa, T.; Polidori, G. Experimental and Numerical Investigations of Thermal Performance of a Hemp Lime External Building Insulation. *Build. Environ.* **2018**, *131*, 140–153. https://doi.org/10.1016/j.buildenv.2017.12.037.
11. Chabriac, P.A.; Gourdon, E.; Gle, P.; Fabbri, A.; Lenormand, H. Agricultural By-Products for Building Insulation: Acoustical Characterization and Modeling to Predict Micro-Structural Parameters. *Constr. Build. Mater.* **2016**, *112*, 158–167. https://doi.org/10.1016/j.conbuildmat.2016.02.162.
12. Bennai, F.; El Hachem, C.; Abahri, K.; Belarbi, R. Microscopic Hydric Characterization of Hemp Concrete by X-Ray Microtomography and Digital Volume Correlation. *Constr. Build. Mater.* **2018**, *188*, 983–994. https://doi.org/10.1016/j.conbuildmat.2018.08.198.
13. Latif, E.; Lawrence, M.; Shea, A.; Walker, P. Moisture Buffer Potential of Experimental Wall Assemblies Incorporating Formulated Hemp-Lime. *Build. Environ.* **2015**, *93*, 199–209. https://doi.org/10.1016/j.buildenv.2015.07.011.
14. Colinart, T.; Lelievre, D.; Glouannec, P. Experimental and Numerical Analysis of the Transient Hygrothermal Behavior of Multilayered Hemp Concrete Wall. *Energy Build.* **2016**, *112*, 1–11. https://doi.org/10.1016/j.enbuild.2015.11.027.
15. Benmahiddine, F.; Bennai, F.; Cherif, R.; Belarbi, R.; Tahakourt, A.; Abahri, K. Experimental Investigation on the Influence of Immersion/Drying Cycles on the Hygrothermal and Mechanical Properties of Hemp Concrete. *J. Build. Eng.* **2020**, *32*, 101758. https://doi.org/10.1016/j.jobe.2020.101758.
16. Gourlay, E.; Glé, P.; Marceau, S.; Foy, C.; Moscardelli, S. Effect of Water Content on the Acoustical and Thermal Properties of Hemp Concretes. *Constr. Build. Mater.* **2017**, *139*, 513–523. https://doi.org/10.1016/j.conbuildmat.2016.11.018.
17. Collet, F.; Pretot, S. Thermal Conductivity of Hemp Concretes: Variation with Formulation, Density and Water Content. *Constr. Build. Mater.* **2014**, *65*, 612–619. https://doi.org/10.1016/j.conbuildmat.2014.05.039.
18. Ahmad, M.R.; Chen, B.; Haque, M.A.; Saleem Kazmi, S.M.; Munir, M.J. Development of Plant-Concrete Composites Containing Pretreated Corn Stalk Bio-Aggregates and Different Type of Binders. *Cem. Concr. Compos.* **2021**, *121*, 104054. https://doi.org/10.1016/j.cemconcomp.2021.104054.

19. Rahim, M.; Douzane, O.; Tran Le, A.D.; Langlet, T. Effect of Moisture and Temperature on Thermal Properties of Three Bio-Based Materials. *Constr. Build. Mater.* **2016**, *111*, 119–127. https://doi.org/10.1016/j.conbuildmat.2016.02.061.
20. Walker, R.; Pavía, S. Moisture Transfer and Thermal Properties of Hemp–Lime Concretes. *Constr. Build. Mater.* **2014**, *64*, 270–276. https://doi.org/10.1016/j.conbuildmat.2014.04.081.
21. Tran-Le, A.D.; Nguyen, S.-T.; Langlet, T. A Novel Anisotropic Analytical Model for Effective Thermal Conductivity Tensor of Dry Lime-Hemp Concrete with Preferred Spatial Distributions. *Energy Build.* **2019**, *182*, 75–87. https://doi.org/10.1016/j.enbuild.2018.09.043.
22. Water—Thermal Conductivity vs. Temperature. Available online: https://www.engineeringtoolbox.com/water-liquid-gas-thermal-conductivity-temperature-pressure-d_2012.html (accessed on 19 May 2022).
23. Williams, J.; Lawrence, M.; Walker, P. The Influence of the Casting Process on the Internal Structure and Physical Properties of Hemp-Lime. *Mater. Struct.* **2017**, *50*, 108. https://doi.org/10.1617/s11527-016-0976-4.
24. Williams, J.; Lawrence, M.; Walker, P. The Influence of Constituents on the Properties of the Bio-Aggregate Composite Hemp-Lime. *Constr. Build. Mater.* **2018**, *159*, 9–17. https://doi.org/10.1016/j.conbuildmat.2017.10.109.
25. Dartois, S.; Mom, S.; Dumontet, H.; Ben Hamida, A. An Iterative Micromechanical Modeling to Estimate the Thermal and Mechanical Properties of Polydisperse Composites with Platy Particles: Application to Anisotropic Hemp and Lime Concretes. *Constr. Build. Mater.* **2017**, *152*, 661–671. https://doi.org/10.1016/j.conbuildmat.2017.06.181.
26. Rezakhani, R.; Scott, D.A.; Bousikhane, F.; Pathirage, M.; Moser, R.D.; Green, B.H.; Cusatis, G. Influence of Steel Fiber Size, Shape, and Strength on the Quasi-Static Properties of Ultra-High Performance Concrete: Experimental Investigation and Numerical Modeling. *Constr. Build. Mater.* **2021**, *296*, 123532. https://doi.org/10.1016/j.conbuildmat.2021.123532.
27. Naderi, S.; Zhang, M. 3D Meso-Scale Modelling of Tensile and Compressive Fracture Behaviour of Steel Fibre Reinforced Concrete. *Compos. Struct.* **2022**, *291*, 115690. https://doi.org/10.1016/j.compstruct.2022.115690.
28. Liang, X.; Wu, C. Investigation on Thermal Conductivity of Steel Fiber Reinforced Concrete Using Mesoscale Modeling. *Int. J. Thermophys.* **2018**, *39*, 142. https://doi.org/10.1007/s10765-018-2465-1.
29. Mabrouk, Y.; Benazzouk, A.; Lahmar, A.; Azrour, M.; Mocerino, C.; Lahmar, A. Elaboration and Characterization of Lightweight Rammed Earth Containing Hemp Particles. *Mater. Today Proc.* **2022**, *58*, 1389–1396. https://doi.org/10.1016/j.matpr.2022.02.319.

30. Ismail, B.; Belayachi, N.; Hoxha, D. Optimizing Performance of Insulation Materials Based on Wheat Straw, Lime and Gypsum Plaster Composites Using Natural Additives. *Constr. Build. Mater.* **2020**, *254*, 118959. https://doi.org/10.1016/j.conbuildmat.2020.118959.
31. Fourmentin, M.; Faure, P.; Pelupessy, P.; Sarou-Kanian, V.; Peter, U.; Lesueur, D.; Rodts, S.; Daviller, D.; Coussot, P. NMR and MRI Observation of Water Absorption/Uptake in Hemp Shives Used for Hemp Concrete. *Constr. Build. Mater.* **2016**, *124*, 405–413. https://doi.org/10.1016/j.conbuildmat.2016.07.100.
32. Delannoy, G.; Marceau, S.; Glé, P.; Gourlay, E.; Guéguen-Minerbe, M.; Diafi, D.; Nour, I.; Amziane, S.; Farcas, F. Aging of Hemp Shiv Used for Concrete. *Mater. Des.* **2018**, *160*, 752–762. https://doi.org/10.1016/j.matdes.2018.10.016.
33. Pierre, T.; Carin, M. Characterization of the Thermal Properties of Millimeter-Sized Insulating Materials. *Int. J. Therm. Sci.* **2019**, *135*, 247–255. https://doi.org/10.1016/j.ijthermalsci.2018.09.009.
34. Glé, P.; Lecompte, T.; Hellouin de Ménibus, A.; Lenormand, H.; Arufe, S.; Chateau, C.; Fierro, V.; Celzard, A. Densities of Hemp Shiv for Building: From Multiscale Characterisation to Application. *Ind. Crops Prod.* **2021**, *164*, 113390. https://doi.org/10.1016/j.indcrop.2021.113390.
35. Seng, B.; Magniont, C.; Lorente, S. Characterization of a Precast Hemp Concrete. Part I: Physical and Thermal Properties. *J. Build. Eng.* **2019**, *24*, 100540. https://doi.org/10.1016/j.jobe.2018.07.016.
36. Bourdot, A.; Moussa, T.; Gacoin, A.; Maalouf, C.; Vazquez, P.; Thomachot-Schneider, C.; Bliard, C.; Merabtine, A.; Lachi, M.; Douzane, O.; et al. Characterization of a Hemp-Based Agro-Material: Influence of Starch Ratio and Hemp Shive Size on Physical, Mechanical, and Hygrothermal Properties. *Energy Build.* **2017**, *153*, 501–512. https://doi.org/10.1016/j.enbuild.2017.08.022.
37. Modeling thermal conductivity of hemp insulation material: A multi-scale homogenization approach. *Build. Environ.* **2016**, *107*, 127–134. https://doi.org/10.1016/j.buildenv.2016.07.026.
38. Lagouin, M.; Magniont, C.; Sénéchal, P.; Moonen, P.; Aubert, J.-E.; Laborel-préneron, A. Influence of Types of Binder and Plant Aggregates on Hygrothermal and Mechanical Properties of Vegetal Concretes. *Constr. Build. Mater.* **2019**, *222*, 852–871. https://doi.org/10.1016/j.conbuildmat.2019.06.004.
39. Zaknoune, A. Etude du Comportement Thermohydrique de Matériaux « Chanvre-Chaux » Lors de la Phase de Séchage—Estimation par Technique Inverse des Propriétés Hydriques. Ph.D. Thesis, Université de Bretagne Sud, Lorient, France, 2011.
40. Véronique, C. Propriétés Mécaniques, Thermiques et Acoustiques d'un Matériau à Base de Particules Végétales: Approche Expérimentale et Modélisation Théorique. Ph.D. Thesis, INSA, Lyon, France, 2005; p. 248.
41. Abbas, M.S.; McGregor, F.; Fabbri, A.; Ferroukhi, M.Y. The Use of Pith in the Formulation of Lightweight Bio-Based Composites: Impact on Mechanical and Hygrothermal Properties. *Constr. Build. Mater.* **2020**, *259*, 120573, doi:10.1016/j.conbuildmat.2020.120573.

42. Asadi, I.; Shafigh, P.; Abu Hassan, Z.F.B.; Mahyuddin, N.B. Thermal Conductivity of Concrete—A Review. *J. Build. Eng.* **2018**, *20*, 81–93. https://doi.org/10.1016/j.jobe.2018.07.002.
43. Cannon, J.R. *The One-Dimensional Heat Equation*; Cambridge University Press: Cambridge, UK, 1984; ISBN 0-521-30243-9.
44. Williams, J.; Lawrence, M.; Walker, P. A Method for the Assessment of the Internal Structure of Bio-Aggregate Concretes. *Constr. Build. Mater.* **2016**, *116*, 45–51. https://doi.org/10.1016/j.conbuildmat.2016.04.088.

Article C: A multiscale homogenization model on thermal conductivity of bio-based building composite considering anisotropy, imperfect interface and moisture

Gang Huang[a], Ariane Abou-Chakra[a,*], Sandrine Geoffroy[a], Joseph Absi[b]

[a]*LMDC (Laboratoire Matériaux et Durabilité des Constructions), INSA, UPS, Université de Toulouse, 135 Avenue de Rangueil, 31077 Toulouse, France*

[b]*UMR CNRS, IRCER, Université de Limoges, 12 rue Atlantis, 87068 Limoges, France*

Abstract

Bio-based materials are considered as one of the solutions to reduce energy consumption in buildings due to their excellent thermal insulation properties. However, previous studies often do not consider multiple complex microstructural characteristics in one model. In this study, a novel iterative multi-scale homogenization model was developed to predict the effective thermal conductivity of bio-based materials. This model is based on micro-geometric features at three scales and considers plant fiber orientation and shape, imperfect contact, moisture, and different pores' size. Further, the model was verified by comparison with finite element models and experimental data from the literature. The results show that the present model demonstrates reliable predictions on the scale of binder, plant fiber, and bio-based composites. The application on hemp verified the accuracy of the imperfect contact in the model, while the application on wheat straw showed the non-negligibility of moisture. Additionally, this study also has good applicability to other plant fibers. In conclusion, this model links microstructure and macroscopic behavior, which can effectively predict and evaluate the thermal conductivity of a wide range of bio-based materials, and thus contribute to reducing building energy consumption.

Keywords: Thermal conductivity; Bio-based material; Homogenization; Multi-scale modeling; Moisture; Finite Element Analysis.

https://doi.org/10.1016/j.conbuildmat.2023.131156

1. Introduction

Energy and carbon emissions are increasingly being discussed today. The building industry can play an important role in addressing the energy crisis and carbon emissions. According to a recent report by the International Energy Agency (IEA), building operations were responsible for 30% of global final energy consumption and 27% of total energy sector emissions in 2021 [1]. Building space heating and cooling (H & C) account for the largest share, about 60% of the total building energy consumption [2]. Moreover, heating systems emit 45% of building emissions, while it relies on fossil fuels to provide more than 55% of final

energy consumption [3]. These issues are more challenging especially considering the objectives of Net-Zero Energy Buildings (NZEB) [4,5] and Net-Zero Carbon Buildings (NZCB) [6,7]. Building insulation is the preferred solution for energy saving and emission reduction, which reduces energy demand for H & C and improves energy efficiency [8–11].

A large amount of plant waste is generated globally each year, and more than 30% of the waste from crop straw and forest crops is burned and discarded [12,13]. This results in environmental pollution and human health risks [14]. In fact, these wastes can be used as aggregates for concrete, known as bio-based material or lightweight concrete or plant fiber concrete, such as hemp [15], sunflower [16], miscanthus [17], and corn stalk [18] concretes, etc. Despite the low mechanical strength of bio-based concrete, it is mainly used in non-structural parts of buildings, such as floors, roofs, and walls [19,20]. These are the main areas where the building exchanges heat with the outside environment. Therefore, excellent thermal insulation is one of the keys to the application of bio-based concrete in buildings. The thermal conductivity of hemp concrete is 0.06 – 0.16 W/(mK) [21], compared to 1.6 – 3.2 W/(mK) [22] for conventional concrete. This indicates higher energy efficiency for indoor H & C. Bio-based buildings not only consume less energy, but also contribute in terms of carbon emissions. On the one hand, the application of bio-based materials significantly reduces the annual electricity consumption of buildings and thus indirectly reduces CO_2 emissions by 25% compared to conventional insulation materials [23]. On the other hand, plants are good materials for carbon sequestration, and many life cycle assessments (LCA) show the advantages of bio-based buildings in emissions [24–27]. In addition, bio-based building materials are characterized by acoustic absorption, low density, and moisture regulation [20,28,29].

The thermal conductivity of bio-based materials, a key indicator for improving the energy efficiency of buildings, is influenced by microstructural characteristics. Experimental studies [30,31] found different thermal conductivities of the bio-based samples in vertical and horizontal directions. This is caused by the anisotropic pore structure and orientation distribution of plant fibers. Due to the effect of compaction, the fibers tend to be distributed in the plane perpendicular to the compaction [32,33]. Plant fibers from different sources have different shapes, and fibers from the same source have different sizes depending on the processing method. [34] studied a variety of plant fibers such as hemp, sunflower, and corn husk, which vary in shape and porosity. Consequently, the thermal conductivity of the concrete from these plants differs. Moreover, most agricultural plant aggregates used in construction materials are composed of cellulose, hemicellulose, and lignin, which leads to weak compatibility of the aggregates with high alkaline binders [35,36]. Scanning electron microscopy (SEM) images in the literature also confirm the presence of an interfacial transition zone (ITZ) between the bio-aggregates and the binder [36–38], especially in the condition of dry-wet cycles [39]. Imperfect contact in the ITZ increases the resistance to heat transfer.

Moisture is another factor that greatly affects thermal conductivity. Bio-based concrete has high water absorption because of its high porosity. Specifically, the total porosity of bio-based concrete consists of three components: macropores between aggregates, intra-particle pores inside the aggregates, and micropores inside the binder [40]. These pores at different scales prevent heat transfer, but absorb moisture from the air in humid environments, which increases the thermal conductivity of the material [41,42]. Moreover, the volume percentage of the plant, the type of binder, the surface treatment of the plant, etc. can all affect the thermal conductivity of the bio-based material [28,36,43].

Figuring out the correlation between thermal conductivity and numerous microstructural factors requires a large number of experimental measurements, which undoubtedly takes a lot of time and cost. Moreover, it is difficult to quantitatively control some factors during the experiments, such as fiber orientation. The analytical homogenization model meets these needs by analyzing the quantitative relationship between the above microscopic characteristics and the thermal conductivity. Previous studies have made some achievements in the modeling of bio-based concrete, but there is still some need for improvement. For instance, early models of bio-based materials were based on the assumption of spherical inclusions, where different material phases were placed in composite spheres according to volume fraction [44]. This obviously lost features such as fiber shape, orientation, and anisotropy in the modeling [15,41,45]. Then, literature [46,47] took the shape of the inclusions into account in the model through the tensor transformation between global and local coordinate systems. The disadvantage is that the imperfect contact observed experimentally between the binder and the plant fiber is not addressed in these models. The model in [48] considered the imperfect contact on lime hemp concrete, but moisture was not involved. Also, to model the anisotropic orientation distribution, the probability density function of the orientation was introduced in the above study. Although this is an indirect way to obtain the orientation distribution of the fibers, i.e., data from X-ray tomography cannot be directly used.

Most of the current analytical models in this field are based on conventional mean-field methods, such as the Mori-Tanaka method. They have good approximations at low-volume fractions (<0.15 in the study of [49]). In contrast, its prediction for high inclusions volume has been criticized [50,51]. For instance, the study in the literature [49] demonstrated that the Mori-Tanaka-based micromechanical model well predicts the effective piezoelectric strain constants at low volume fractions (0.15). But beyond this, the average relative difference is up to about 30%. Although when the volume of the inclusions is higher than that of the matrix, the “inverse Mori-Tanaka method” [52] can be used, i.e., the matrix is considered as an inclusion. However, this is only a compromise solution because it does not completely solve the problem of high volume and the inclusions may have a complex orientation distribution and shape. The iterative approach can reduce the volume fraction at each step. [53] implemented an iterative homogenization for hemp concrete, but the

macropores were not counted. Generally, the macropore increases with the percentage of plant aggregates due to its elongated shape. Thus, it is more realistic to consider both macropore and aggregate in each step of the iteration.

Some methods based on 3D numerical models are also applicable to bio-based concrete. [54] developed a numerical model with spatial distribution, size, and shape to predict the thermal conductivity and mechanical behavior of straw concrete. This model performs well with an intuitive visualization, but has limitations in terms of volume fraction and computational cost compared to the analytical method. With the development of 3D X-ray reconstruction techniques, a 3D realistic structure based on a bio-based concrete sample can also be used for modeling various properties [55]. It is closer to the real material structure than the traditional numerical model. Nevertheless, this model cannot be used for parametric analysis and material optimization because of the immutability of the structure.

It is clear that there is a gap between current models and actual experiments on the thermal conductivity of bio-based materials. Also, most of the existing studies focus only on specific cases and are not generalizable to a wide range of plant fibers. Therefore, this study aims to develop an analytical model of thermal conductivity that incorporates all the above factors, especially considering anisotropy, imperfect interface, moisture, and different pores' size. This model relates thermal conductivity to microstructural characteristics to predict and evaluate the thermal insulation of a wide range of bio-based materials. An iterative mean-field homogenization approach (I–MFH) involving both macropores and plant aggregates was developed for the model. Moreover, the fiber orientation method in this study can make use of data directly from X-ray tomography, which is lacking in the commonly used probability density function. Then, the model was verified at different scales, i.e., binder, aggregate, and bio-based composite. This verification was performed by comparison with finite element models and experimental data from the literature. Finally, the model was applied to a wide range of agricultural by-products.

Nomenclature

Latin symbols		**Superscripts**	
$\underline{\underline{A}}$	Concentration tensor	*m*	m-th iteration
b	Parameter related to the fiber shape in depolarization matrix	*MT*	Mori-Tanaka scheme
e	Euler's number (constant, 2.71828)	*X, Y, Z*	X, Y, Z-axis direction in global coordinates

$\underline{e_3}$	The unit vector in the axis direction of fiber
$\underline{E}$	Macroscopic thermal gradient field (K/m)
f	Volume fraction
$F(L)$, $F(W)$	Weibull functions of length and width
n	Iterations
N	Division of fiber angle φ
$\underline{\underline{P}}$	Interaction tensor (mK/W)
$\underline{q}$	Microscopic thermal flux (W/m^2)
$\underline{Q}$	Macroscopic thermal flux (W/m^2)
R	Rotation matrix
$\underline{\underline{S}}$	Depolarization tensor
T	Temperature (K)
w	Water saturation ($\in [0, 1]$)
X	Aspect ratio of the bio-aggregates

Greek symbols

α, β	Parameters related to fiber length and width
$\underline{\underline{\delta}}$	Kronecker symbol
η	Imperfect contact degree (≥0)
θ	Angle between fiber and Z-axis (°)
λ	Thermal conductivity (W/(mK))
$\tilde{\lambda}$	Thermal conductivity with imperfect contact (W/(mK))
φ	Angle between fiber's projection and Y-axis (°)
Ω	Domain of RVE
ρ	Density (kg/m^3)

$\parallel$	Parallel to the compaction (For bio-based composites) or fiber axis (For aggregates)
$\perp$	Perpendicular to the compaction (For bio-based composites) or fiber axis (For aggregates)

Subscripts

A	Aggregates
A^S	Aggregate solid
b	Binder
b^S	Binder solid
hom	Homogeneous materials
L	Length of the fiber (mm or cm)
p	Macropores
p^A	Intra-particle pores in aggregates
p^b	Micropores in binder
r	r-th phase
w	Water
W	Width of the fiber (mm or cm)

Abbreviations

FEM	Finite Element Method
H & C	Building Space Heating and Cooling
IEA	International Energy Agency
ITZ	Interfacial Transition Zone
LCA	Life Cycle Assessment
NZCB	Net-Zero Carbon Buildings
NZEB	Net-Zero Energy Buildings

RVE	Representative Volume Element
SEM	Scanning Electron Microscopy

2. Theoretical basis of the multi-scale homogenization method

2.1. Heat conduction problem

The complex microstructural and morphological characteristics of bio-based building materials can influence macroscopic behavior. Homogenization techniques can relate microscopic characteristics to macroscopic behavior and quantify their correlation. The general basic homogenization approach is first presented in this section and then developed in later sections with regard to the multi-scale microstructure of bio-based materials. Consider a Representative Volume Element (RVE) (domain Ω) containing a homogeneous matrix (thermal conductivity tensor $\underline{\underline{\lambda}}_0$) and inclusions (volume fraction f_I, thermal conductivity tensor $\underline{\underline{\lambda}}_I$). The boundary of the RVE, $\partial\Omega$, is subjected to a macroscopic uniform thermal gradient field $\underline{E}$. In this case, the thermal conduction problem can be expressed by the microscopic and macroscopic Fourier's law as:

$$\underline{q}(\underline{x}) = -\underline{\underline{\lambda}}(\underline{x}) \cdot \underline{grad}\, T(\underline{x})$$

$$\underline{Q} = -\underline{\underline{\lambda}}_{hom} \cdot \underline{E} \quad (1)$$

where $\underline{q}(\underline{x})$ and $\underline{Q}$ denote the microscopic and macroscopic heat fluxes, $\underline{grad}\, T(\underline{x})$ denotes the microscopic heat gradient field, $\underline{\underline{\lambda}}_{hom}$ is the effective thermal conductivity tensor.

Thanks to the concentration tensor $\underline{\underline{A}}(\underline{x})$, which is also known as localization tensor, the macroscopic and microscopic thermal gradient field can be converted using the following equation:

$$\underline{grad}\, T(\underline{x}) = \underline{\underline{A}}(\underline{x}) \cdot \underline{E} \quad (2)$$

Then, volume averaging of the microscopic heat flux and the combination of Eqs. (1) and (2) yield:

$$\underline{\underline{\lambda}}_{hom} = \langle \underline{\underline{\lambda}}(\underline{x}) \cdot \underline{\underline{A}}(\underline{x}) \rangle \quad (3)$$

For a composite consisting of a matrix and r-phase inclusions, Eq. (3) can be rewritten by the classic Mori-Tanaka scheme [48,56,57] as:

$$\underline{\underline{\lambda}}_{hom} = \sum_{r=0}^{N} f_r \cdot \underline{\underline{\lambda}}_r \cdot \underline{\underline{A}}_r^{MT} \quad (4)$$

with

$$\underline{\underline{A}}_r^{MT} = \underline{\underline{A}}_r^0 \cdot (\sum_{r=0}^{N} f_r \underline{\underline{A}}_r^0)^{-1} \quad (5)$$

$\underline{\underline{A}}_r^0$ in Eq. (5) represents the concentration tensor of the r-th phase, a value of 0 for r represents the matrix, while 1 represents the first phase of inclusions, and so on. The concentration tensor of the matrix $\underline{\underline{A}}_0^0$ is $\underline{\underline{\delta}}$. In the case of single inclusions, all inclusions have the same properties. Therefore, the concentration tensor of the inclusion $\underline{\underline{A}}_r^0$ (r = 1, 2, …) is expressed as follows:

$$\underline{\underline{A}}_r^0 = [\underline{\underline{\delta}} + \underline{\underline{P}}_r \cdot (\underline{\underline{\lambda}}_I - \underline{\underline{\lambda}}_0)]^{-1} \quad (6)$$

where $\underline{\underline{P}}_r$ in Eq. (6) is interaction tensor of corresponding inclusion, which is similar to the Hill tensor in the mechanics problem [58]. But it is a second-order tensor compared to the fourth-order tensor in the mechanics. $\underline{\underline{P}}_r$ can be expressed by the symmetric second-order depolarization tensor $\underline{\underline{S}}_r$ as follows:

$$\underline{\underline{P}}_r = \underline{\underline{S}}_r \cdot (\underline{\underline{\lambda}}_0)^{-1} \quad (7)$$

$\underline{\underline{S}}_r$ depends on the shape of the inclusions. In the case of three-dimensional sphere-like inclusions, it can be expressed in the Cartesian coordinate system as:

$$\frac{x^2}{{a_1}^2} + \frac{y^2}{{a_2}^2} + \frac{z^2}{{a_3}^2} = 1 \quad (8)$$

where

$$a_1 = a_2 < a_3 \; with \; a_1 = a_2 = a, a_3 = Xa. \quad (9)$$

X is the ratio of the length to the diameter of the inclusions, which is referred to as the aspect ratio in this paper. Moreover, the depolarization tensor $\underline{\underline{S}}_r$ in Eq. (7) can be obtained from the equations containing *X*, as detailed in 0

2.2. Tensor transformation of inclusions between global and local coordinate systems

The generic homogenization method described above is only applicable in the case of unidirectional inclusions. However, during the casting or spraying of bio-based concrete, fibers are embedded in the matrix in various orientations. The orientation distribution of the fibers in bio-based concrete depends on the manufacturing technology, fiber shape, etc., which will be discussed in detail in subsequent sections. In this section, a fiber orientation transformation method is introduced to cover all possible orientations in 3D space. As shown in **Fig. 1**, the orientation of the fiber in the matrix can be defined in terms of two angles: θ is the angle between the principal axis of the inclusion and the Z-axis in global coordinates, whereas φ is the angle

between the projection of the inclusion in the XY-plane and the Y-axis. According to [47], the second-order tensor λ_{ij} can be transformed from local to global coordinates by:

$$\lambda_{ij}^{G} = \lambda_{mn}^{L} R_{mi} R_{nj} \tag{10}$$

where R can be expressed in the form of a matrix as:

$$R = \begin{vmatrix} 1 & 0 & 0 \\ 0 & \cos\theta & -\sin\theta \\ 0 & \sin\theta & \cos\theta \end{vmatrix} \cdot \begin{vmatrix} \cos\varphi & -\sin\varphi & 0 \\ \sin\varphi & \cos\varphi & 0 \\ 0 & 0 & 1 \end{vmatrix} \tag{11}$$

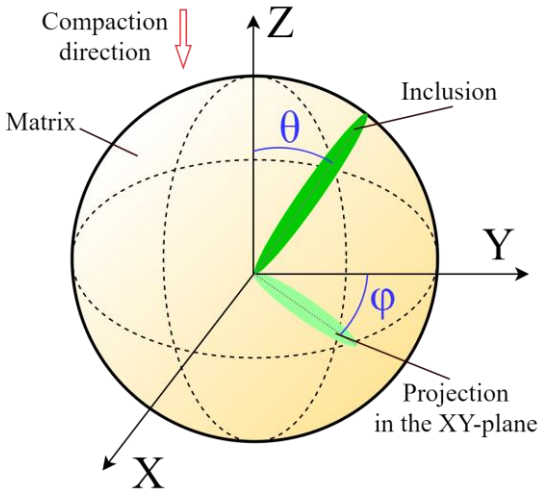

Fig. 1. Definition of inclusion direction.

As described above, in the later sections dealing with inclusions in different directions, the tensor associated with the inclusions will all be transformed by Eq. (10).

2.3. Multi-scale homogenization of bio-based building materials

As shown in **Fig. 2**, bio-based concrete has three components on a scale of 10^0 to 10^2 mm: macropores, homogenized bio-aggregates, and binder. Moreover, there is imperfect contact in the ITZ between the binder and the bio-aggregate, which will be discussed in Section 2.3.3. Further on a scale of 10 to 10^2 μm, experimental observations [59–61] found that some plant aggregates, such as hemp and wheat straw, have a directional pore distribution. On the scale of 10^{-2} to 10^0 μm, there are micropores in the binder. In addition,

the moisture in the bio-based concrete will be discussed in Section 2.3.2. The homogenization methods and calculations on scales 1, 2, and 3 will be described separately in the next subsections.

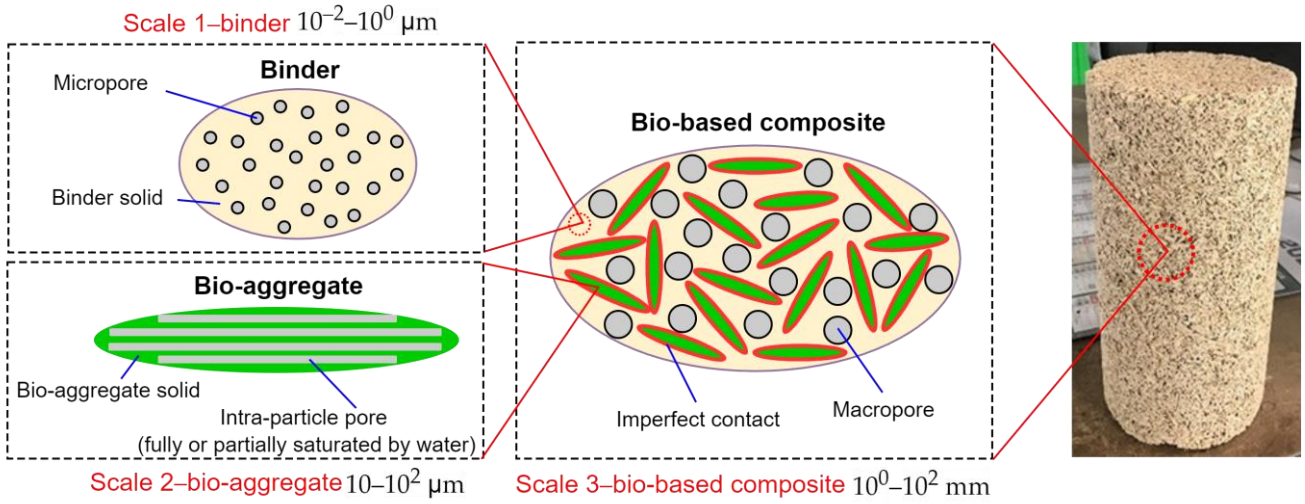

Fig. 2. Multi-scale structure of bio-based building materials for modeling (The photograph of the sample on the right: [62]).

2.3.1. Binder with micro pores (Scale 1: 10^{-2}–10^{0} μm)

As shown in **Fig. 2**, the porous binder on scale 1 consists of micropores and binder solids. The effective thermal conductivity of the binder is expressed in Eq. (12) and the detailed calculation procedure is shown in Appendix B.

$$\underline{\underline{\lambda_b}} = \lambda_b \underline{\underline{\delta}} = \left[\lambda_{bs} + \frac{f_{pb}\lambda_{bs}(\lambda_p - \lambda_{bs})}{\lambda_{bs} + \frac{1}{3}(1 - f_{pb})(\lambda_p - \lambda_{bs})}\right]\underline{\underline{\delta}} \tag{12}$$

where $\underline{\underline{\lambda_b}}$ denotes the effective thermal conductivity tensor of porous binder, while λ_{bs} and λ_p denote that of binder solid and air pore. f_{pb} is the porosity in the binder.

2.3.2. Individual bio-aggregate in wet condition (Scale 2: 10–10^{2} μm)

On the one hand, bio-based aggregates have high porosity, these pores have various shapes and orientations in different types of plants. For example, they have aligned cylindrical pores in hemp [59] and straw [61,63], while sunflower pith [64] has spherical pores with an approximately random distribution. In the present model, the different pores can be represented by varying X in Eq. (9) based on the specific plants. On the other hand, bio-based building composites have strong water absorption due to high porosity and volume fraction [40]. The presence of water can significantly increase the thermal conductivity of the composite [15,42,65]. Therefore, it is necessary to consider water saturation in the bio-based model.

Assume that $\underline{e_3}$ is the unit vector oriented in the symmetrical axis of the transversely isotropic inclusion. According to [66], the bio-aggregate can be considered to contain aggregate solid and pore inclusion saturated

fully or partially by water (see scale 2 in **Fig. 2**), the effective thermal conductivity of individual wet bio-aggregate can be expressed as:

$$\underline{\underline{\lambda}}_A = \lambda_A^{\perp}\left(\underline{\underline{\delta}} - \underline{e_3} \otimes \underline{e_3}\right) + \lambda_A^{\parallel}\underline{e_3} \otimes \underline{e_3} \tag{13}$$

with

$$\lambda_A^{\perp} = \left(\frac{(1-w)f_{p^A}}{\lambda_p + \lambda_{A^S}} + \frac{wf_{p^A}}{\lambda_w + \lambda_{A^S}} + \frac{1 - f_{p^A}}{2\lambda_{A^S}}\right)^{-1} - \lambda_{A^S}$$

$$\lambda_A^{\parallel} = (1-w)f_{p^A}\lambda_p + wf_{p^A}\lambda_w + \left(1-f_{p^A}\right)\lambda_{A^S} \tag{14}$$

where $\underline{\underline{\lambda}}_A$ denotes the effective thermal conductivity tensor of the aggregates. The magnitudes of its two components, $\lambda_A^{\perp}$ and $\lambda_A^{\parallel}$, denote the effective thermal conductivity perpendicular and parallel to the axial direction of aggregates. f_{A^S} and f_{P^A} represent the volume fraction of bio-aggregate solid and intra-particle pore. The water saturation noted by w is the volume ratio of water to the intra-particle pore. λ_w, and λ_{A^S} are the thermal conductivities of water, and aggregate solid, respectively.

2.3.3. Imperfect contact between bio-aggregates and binder

Due to the imperfect contact between the aggregate and the binder [36–38], it is necessary to consider the effect of the thermal resistance at the interface in the modeling of bio-based composites. Special attention is paid on a scale of 10^0 to 10^2 mm in **Fig. 2**, where the red outline represents the imperfect contact between the bio-aggregate and the binder. Due to the elongated profile in most cases, the plant fibers are in contact with the binder almost through the axial side instead of the two tips. This suggests that ITZ is basically considered to appear on the axial side, as can be seen from the SEM image [36]. Moreover, from the point of view of heat transfer, the passage of temperature laterally through the fibers is accompanied by greater thermal resistance, while the passage axially along the fibers can be achieved in an easier way along the outer walls of the fibers or the binder. This has been confirmed by the thermal flux distribution maps of the finite element simulations in our previous work [67]. Given the above, a method based on thermal jumping [48,68,69] is adopted in this paper, as shown in the following equations:

$$\tilde{\lambda}_A^{\perp} = \frac{\lambda_A^{\perp}}{1 + \eta\frac{\lambda_A^{\perp}}{\lambda_b}}$$

$$\tilde{\lambda}_A^{\parallel} = \lambda_A^{\parallel} \tag{15}$$

where $\tilde{\lambda}_A^{\perp}$ denotes the effective thermal conductivity perpendicular to the axial direction and with the imperfect contact.

η is a parameter describing the degree of imperfect contact. η = 0 indicates a perfect contact. $\lambda_A^{\perp}$ and $\lambda_A^{\parallel}$ can be obtained from Eq. (14). Then, the effective thermal conductivity tensor $\underline{\underline{\tilde{\lambda}}}_A$ for aggregates with imperfect contact is:

$$\underline{\underline{\tilde{\lambda}}}_A = \frac{\lambda_A^{\perp}}{1+\eta\frac{\lambda_A^{\perp}}{\lambda_b}}\left(\underline{\underline{\delta}} - \underline{e_3}\otimes\underline{e_3}\right) + \lambda_A^{\parallel}\underline{e_3}\otimes\underline{e_3} \tag{16}$$

2.3.4. Three-phase bio-based building materials (Scale 3: 10^0–10^2 mm)

On scales 1 (10^{-2}–10^0 μm) and 2 (10–10^2 μm), the binder and bio-aggregates have been homogenized based on micromorphology. Further on scale 3 (10^0–10^2 mm) in **Fig. 2**, bio-based composite is considered to contain an isotropic binder, macropores, and transversely isotropic bio-aggregate. Its effective thermal conductivity of bio-based material can be expressed by Eqs. (4) and (5) as:

$$\underline{\underline{\lambda}}_{hom} = \left(\sum_{r=0}^{N} f_r \cdot \underline{\underline{\lambda}}_r \cdot \underline{\underline{A}}_r^0\right) \cdot \left(\sum_{r=0}^{N} f_r \underline{\underline{A}}_r^0\right)^{-1} = \left[(1-f_p-f_A)\underline{\underline{\lambda}}_b + f_p\underline{\underline{\lambda}}_p \cdot \underline{\underline{A}}_p^0 + \sum_{r=2}^{N} f_r \underline{\underline{\lambda}}_r \cdot \underline{\underline{A}}_r^0\right] \cdot \left[(1-f_p-f_A)\underline{\underline{\delta}} + f_p\underline{\underline{A}}_p^0 + \sum_{r=2}^{N} f_r \underline{\underline{A}}_r^0\right]^{-1} \tag{17}$$

f_A and f_p denote the volume fraction of aggregates and macropores on scale 3. The value of r in Eq. (17) represents the specific phase, and the matrix and macropores are represented by 0 and 1. When r is greater than 1, it relates to inclusions in different orientations, i.e., specific θ and φ according to the method in Section 0. Also, X-ray tomography in the literature [16,32,33] shows a specific anisotropy of the bio-based material, that is, the fibers tend to be uniformly distributed in the plane perpendicular to the compaction. In detail, φ in **Fig. 1** is equally distributed in the interval 0 to 360°, whereas θ tends to be 90°. This is due to the fact that the fibers always tend to be distributed in the plane perpendicular to the compaction under pressure. As described, the fiber-related terms $\sum_{r=2}^{N} f_r \underline{\underline{\lambda}}_r \cdot \underline{\underline{A}}_r^0$ and $\sum_{r=2}^{N} f_r \underline{\underline{A}}_r^0$ in Eq. (17) can be rewritten as:

$$\sum_{r=2}^{N} f_r \underline{\underline{\lambda}}_r \cdot \underline{\underline{A}}_r^0 = \lim_{N\to\infty} \frac{f_A}{N}\left(\underline{\underline{\tilde{\lambda}}}_A^1(\theta^*,\varphi) \cdot \underline{\underline{A}}_A^1(\theta^*,\varphi) + \ldots + \underline{\underline{\tilde{\lambda}}}_A^N(\theta^*,\varphi) \cdot \underline{\underline{A}}_A^N(\theta^*,\varphi)\right)$$

$$\sum_{r=2}^{N} f_r \underline{\underline{A}}_r^0 = \lim_{N\to\infty} \frac{f_A}{N}\left(\underline{\underline{A}}_A^1(\theta^*,\varphi) + \ldots + \underline{\underline{A}}_A^N(\theta^*,\varphi)\right) \tag{18}$$

where θ^* is the effective angle between the compaction and the fiber axial direction in the corresponding bio-based concrete. $\underline{\underline{\tilde{\lambda}}}_A^N(\theta^*,\varphi)$ and $\underline{\underline{A}}_A^N(\theta^*,\varphi)$ are obtained based on Eq. (10). In theory, an infinite value of *N* in Eq. (18) can cover all possible directions, which makes the same thermal conductivity of the bio-based material in the *X* (λ^X) and Y (λ^Y) directions in **Fig. 1**. However, this leads to a high computational cost. Therefore, a reasonable value can balance the computational cost and accuracy. The case of 0.5 f_A and 0.35 f_p proves that *N* of 10 is sufficient for this calculation because the relative error between λ^X and λ^Y is only 1.21×10^{-8}%.

2.3.5. Iterative approach

Conventional mean field methods do not predict well for high inclusions volumes [50,51]. A novel iterative mean-field homogenization method (I–MFH) as shown in **Fig. 3** provides a good solution to the problem of high inclusions volume. Firstly, the macropore and bio-aggregate are divided into n portions. Subsequently, the first portion of macropore and bio-aggregate are homogenized with the binder to obtain an equivalent medium 1. Further, the homogenization operation is performed in medium 1, and the second portion of the macropore and bio-aggregate to obtain an equivalent medium 2. Eventually, the equivalent bio-based material can be achieved after the targeted n-step homogenization. In contrast to the literature [53], this method considers both macropore and aggregate in each step of the iteration.

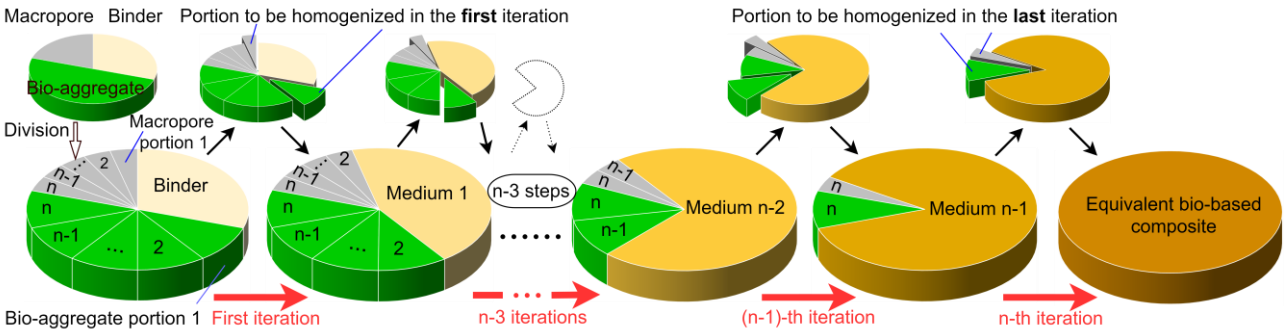

Fig. 3. Process of the iterative homogenization approach.

Fig. 4 illustrates the computational process to implement the above iterative scheme. Note that only the medium and one portion of the aggregate and macropore are considered in each step of the iteration. Therefore, the volume fraction of the aggregate (f_A^m) and macropore (f_p^m) at the n-th iteration step can be calculated using the equation in **Fig. 4**. In addition, a number of iterations n needs to be set before the calculation. A large value of n can overcome the weaknesses of the mean-field approach at high fiber volumes, which in turn improves the prediction accuracy. However, this also increases the computational cost. Therefore, a test on the number of iterations is used to determine a suitable value of n (see **Fig. 5**). This test is based on high-volume fractions of aggregates and macropores which are 0.5 and 0.35. A total volume fraction of 0.85 is sufficient to cover most cases. It can be seen from **Fig. 5** that the vertical and parallel thermal conductivity decreases sharply within 10 and especially within 5. When n is greater than 20, the thermal conductivity is almost independent of the iteration. Therefore, 20 is selected as the value for this iterative scheme. Additionally, it can be probably deduced that in this case the reliability of the conventional MT method is doubtful with inclusions volumes higher than 0.085 and especially 0.170. This also

coincides with the findings of the literature [49] mentioned in the introduction.

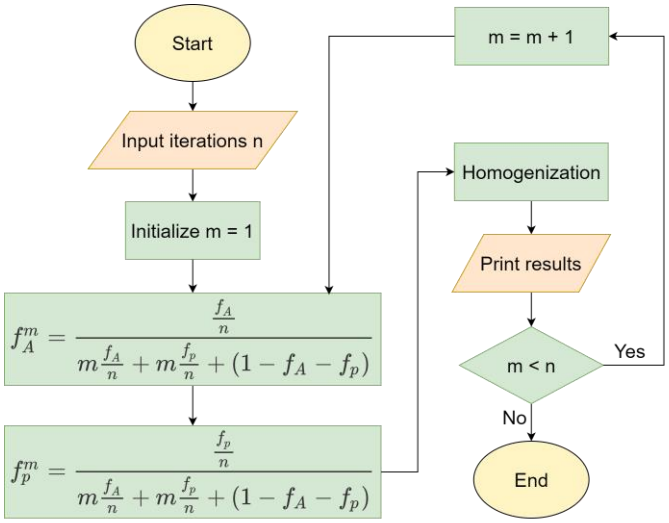

Fig. 4. Flowchart of the iterative computation.

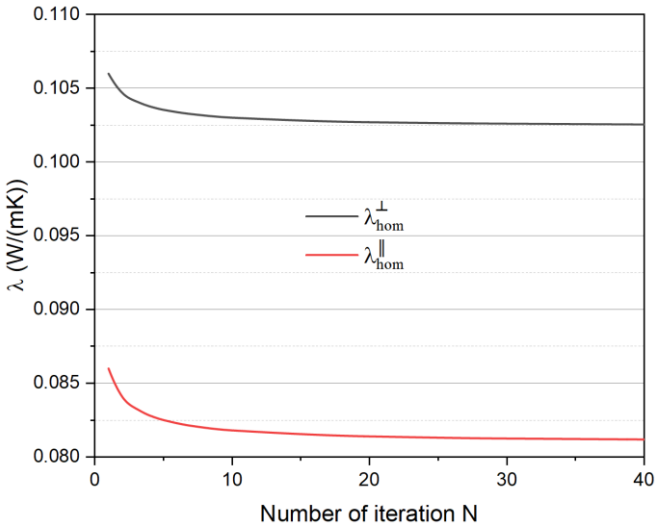

Fig. 5. Iteration test.

2.4. Shape of bio-aggregates

As with mineral aggregates, the size of bio-based aggregates is usually measured by gradation rather than by a constant value. This makes it difficult to obtain the aspect ratio *X* in Eq. (9). This section presents a method to calculate the equivalent aspect ratio based on the cumulative percentage of length and width. The cumulative distribution function of the fiber length can be represented by the Weibull function [48,70] in Eq.

(19), which gives the proportion of particles whose length is not greater than L.

$$F(L) = 1 - e^{-\alpha_L L^{\beta_L}} \tag{19}$$

where α_L and β_L are parameters that reflect the length distribution, which can be obtained from the fitting of experimental data.

Likewise, this method can be used for width as follows:

$$F(W) = 1 - e^{-\alpha_W W^{\beta_W}} \tag{20}$$

Subsequently, the effective length ($\overline{L}$) and width ($\overline{W}$) can be calculated by the following equations:

$$\overline{L} = \int_0^{+\infty} L\alpha_L\beta_L L^{\beta_L - 1} e^{-\alpha_L L^{\beta_L}} dL$$

$$\overline{W} = \int_0^{+\infty} W\alpha_W\beta_W W^{\beta_W - 1} e^{-\alpha_W W^{\beta_W}} dW \tag{21}$$

Ultimately, the effective aspect ratio in Eq. (9) is $X = \overline{L}/\overline{W}$.

3. Model verification and application

3.1. Effective aspect ratio of bio-aggregates

The method described in Section 0 was used to calibrate the particle size distribution of wheat straw from [61]. **Fig. 6** shows a comparison of simulation and experimental data for length and width. It can be seen from R^2 that the simulation based on the Weibull function gets a good match with the experimental data. This implies that this method can effectively utilize the existing and commonly used cumulative distributions to develop a size model for bio-aggregates. Then the average length ($\overline{L}$) and width ($\overline{W}$) calculated by Eq. (21)

are 2.80 and 0.43 cm, respectively. Finally, the effective aspect ratio of wheat straw is 6.51.

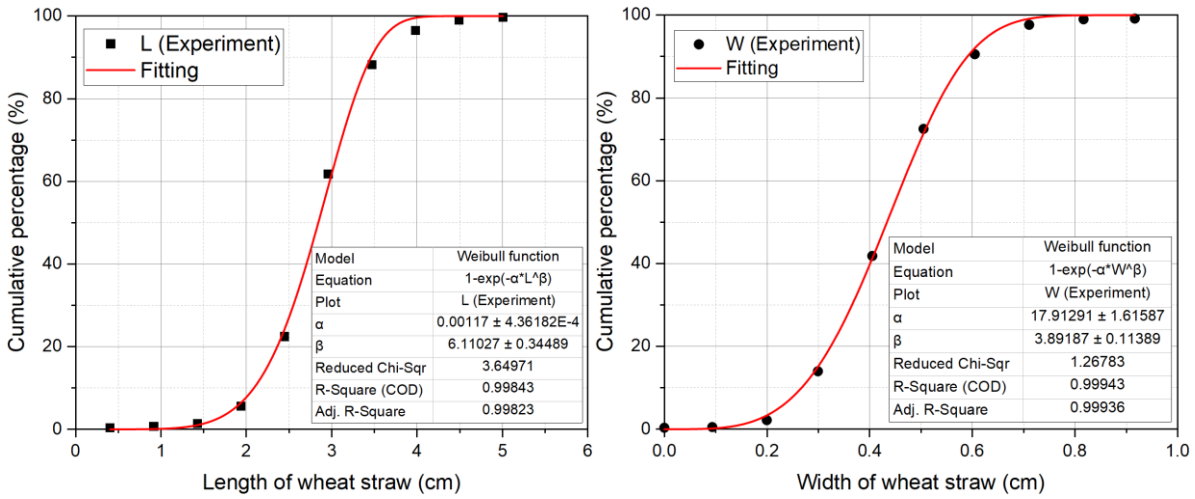

Fig. 6. Comparison of experimental data [61] and fitting based on Weibull functions.

In the same way, the length and width of the hemp from [60] were fitted and the results are shown in **Fig. 7**. The average length and width were calculated to be 5.48 and 1.53 mm based on the obtained parameters α and β. The effective aspect ratio of hemp particles for construction materials was thus calculated to be 3.59. On the other hand, literature [71] analyzed the dimensions of eight types of hemp shivs by 2D-images, where the median lengths and widths were 3.42–8.62 mm and 1.02–1.95 mm. Afterward, the average aspect ratios ranged from 3.26 to 4.42. It can be seen that the results of the present model are in this range.

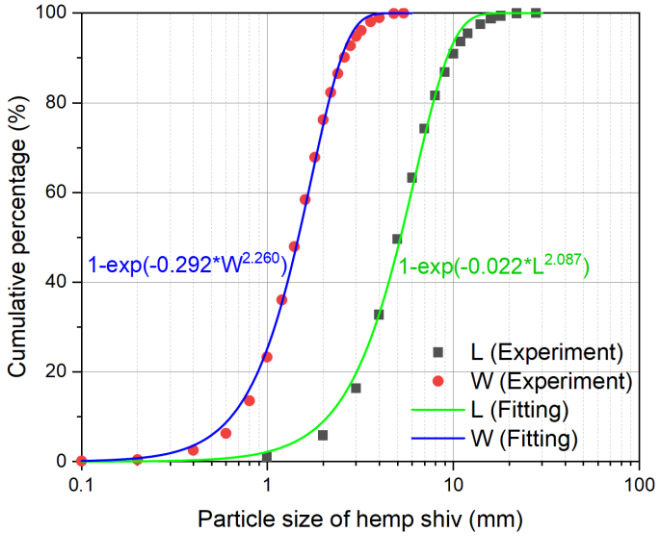

Fig. 7. Fitting of the size of hemp (Experimental data: [60]).

3.2. Effective thermal conductivity of porous binder

On scale 1, the effective thermal conductivity of the binder can be obtained using Eq. (12) and

shown with the curve in **Fig. 8**. Note that lime-based binder is a common choice for bio-based concrete because of its compatibility and low emissions in the manufacturing process [19]. Therefore, the thermal conductivity of the binder solid used for the simulations is 0.56 W/(mK) [48] from lime. The Finite Element Method (FEM) results are taken from our previous study [67] as a comparison and verification. It can be seen from **Fig. 8** that the present simulation matches the FEM results perfectly. Further comparison with different types of lime used in [44] for plant concrete also demonstrates good applicability.

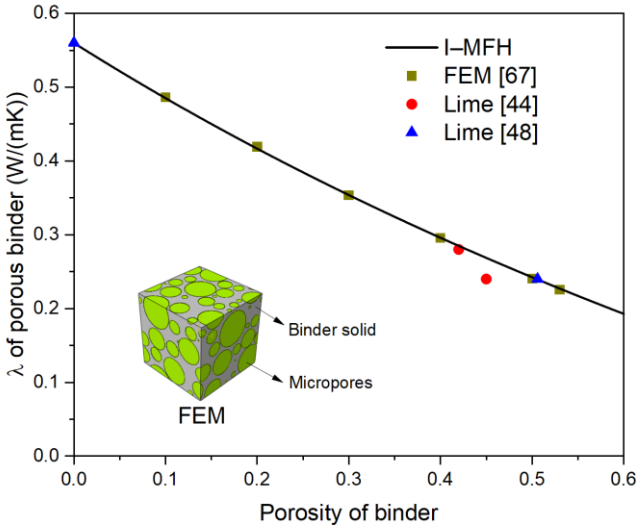

Fig. 8. Model validation on binder: I-MFH versus FEM [67].

3.3. Effective thermal conductivity of porous bio-aggregates

Fig. 9 shows the comparison of the present model with the FEM and experimental results on scale 2. The thermal conductivity of aggregate solid and porosity used for model input was cited from hemp concrete [71], which is 0.564 W/(mK) and 81.8%. As can be seen from **Fig. 9**, both parallel and perpendicular thermal conductivities decrease with porosity, which can be explained by the fact that the thermal conductivity of air (0.026 W/(mK)) is much lower than that of the aggregate solid (0.564 W/(mK)). Furthermore, the parallel thermal conductivity is greater than the perpendicular one because the heat flow tends to transfer axially along the fiber rather than transversely across it. Generally, the present model agrees well with the FEM and

experimental results. This implies the reliability of the present model on individual bio-aggregate.

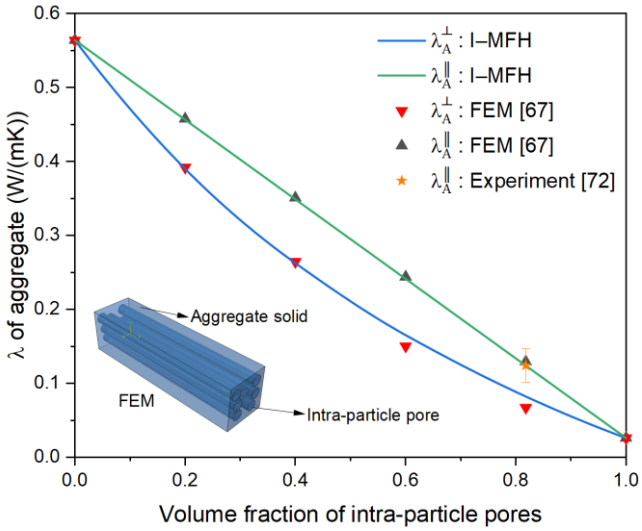

Fig. 9. Model validation on bio-aggregates with intra-particle pores (FEM: [67], experimental data: [72]).

3.4. Effective thermal conductivity of bio-based composite

3.4.1. Verification on binder-aggregates with orientation

After the model has been validated on binders and aggregates, this section aims to verify the reliability of the fiber orientation conversion to provide an additional basis for subsequent case applications. For this purpose, a finite element model of a two-phase material, i.e., binder-aggregate, is developed and compared with the analytical solution. In this finite element model, the transversely isotropic inclusions are embedded in an isotropic binder. According to the simulation of the shape of the hemp in Section 3.1, an aspect ratio of 3.59 was adopted for the inclusions. Moreover, the only variable for all cases is the orientation (defined in terms of θ and φ in **Fig. 1**). The number and volume fraction of inclusions are 75 and 0.25. **Fig. 10** shows the thermal conductivity of the binder-aggregates as a function of orientation for φ and θ of 30°. Note that the three curves represent the thermal conductivity of the binder-aggregates in the X, Y, and Z directions in the global coordinate system, respectively. When φ is 30°, λ^X reaches its maximum value at θ of 0 and 180°, while λ^Y and λ^Z reach it at θ of 90. This can be explained by the heterogeneity of bio-aggregates, where the thermal conductivity in the axial direction is greater than that in the transverse direction. In other words, the smaller the angle (acute angle) between the measured direction and the axial direction of the inclusions, the greater the thermal conductivity. When θ is 30°, it is noted that λ^Z is independent of φ, because the angle between the axial direction of inclusions and the Z-axis is always 30° regardless of φ. Also, a good agreement can be seen from the comparison of the FEM and the analytic solution in **Fig. 10**, the maximum relative errors for the two cases are 0.88% and 0.77%. Although the binder-aggregates is a simplified example in this section, this enables this section to exclude other factors and to better investigate the influence of fiber orientation on macroscopic behavior. Returning to the subject, this verification result shows that the quantitative description

of fiber orientation by the analytical scheme in Section 2.2 is reliable.

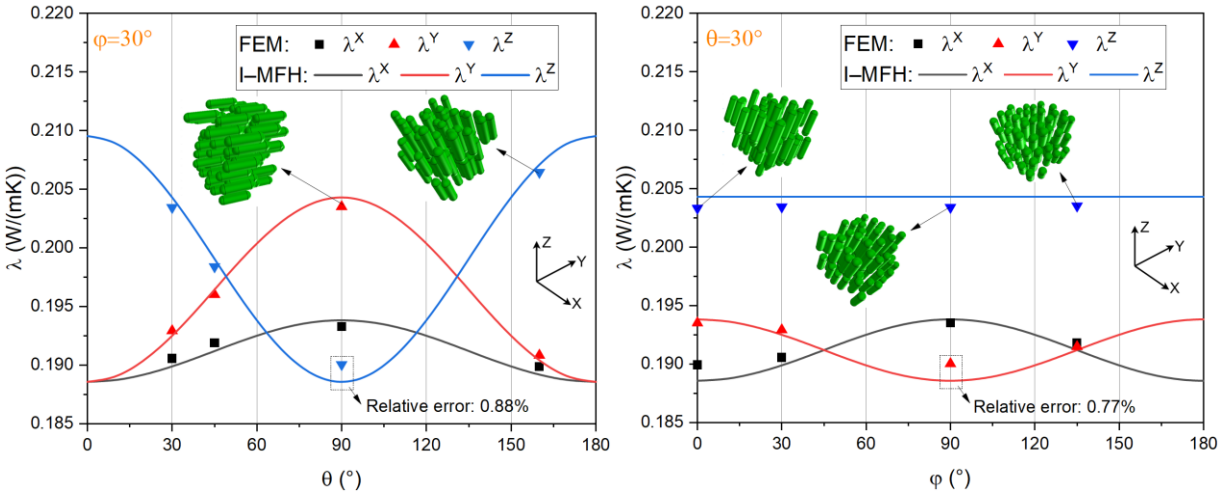

Fig. 10. Model verification on binder-aggregates with orientation.

3.4.2. Case 1 for dry hemp concrete

The above verifies the present model on scales 1 and 2. Good predictability was also achieved in the simulations of shape and orientation. In this section, the model containing the three scales is applied to dry hemp concrete. The input parameters of this model were obtained from different literature and are presented in **Table 1**.

Table 1. Parameters of hemp concrete.

Property	Value	Reference
ρ_b (kg/m^3)	1079	[16]
f_p^b (%)	50.6	[48]
λ_b^s (W/(m·K))	0.56	[48]
ρ_A (kg/m^3)	265	[72]
f_p^A (%)	81.8	[71]
λ_A^s (W/(m·K))	0.564	[71]
X	3.59	Calculated from [60]
θ	75°	[58]
f_p	0.15	[59]

It can be seen from the simulation results shown in **Fig. 11** that the thermal conductivity perpendicular to the compaction is higher than that parallel to the compaction. In fact, this is caused

by the arrangement of hemp particles and its own anisotropy. The comparison of experiments and simulations shows that the present model predicts thermal conductivity well in both perpendicular and parallel directions. The dotted line in **Fig. 11** was from an empirical equation: $\lambda = 0.0002\rho + 0.0194$ W/(mK) [44], which was used to calculate the effective thermal conductivity of hemp concrete from the density. Although the equation approximately agrees with the experimental results, it does not take into account the effect of orientation. In contrast, the present method is able to predict thermal conductivity for different orientations.

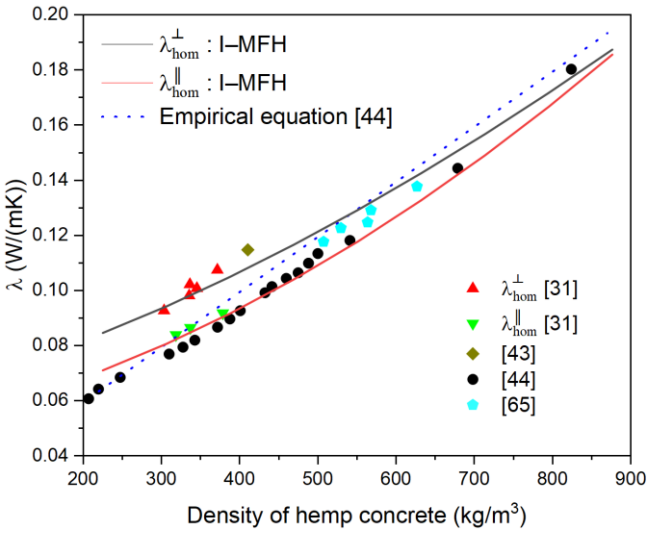

Fig. 11. Model validation on dry hemp concrete with density (Experimental data: [31,43,44,65]).

Note that the parameter of imperfect contact here is 0.15 by inverse analysis, but this is related to the type of binder and aggregate, and the treatment of the aggregate. Many studies [73–75] have been devoted to treating the surface of the aggregates to improve the ITZ. The parameter of imperfect contact used in this study can quantify this behavior. In the application, for instance, this parameter is first obtained from the inverse analysis according to several sets of experimental data, which in turn can be used to predict the effective thermal conductivity of other concretes with the same surface treatment method.

3.4.3. Case 2 for dry and wet wheat straw concrete

Further, the present model is applied to wheat straw concrete and considers the effect of moisture and imperfect contact. The experimental data in this section are obtained from the study by Ismail et al. [54,61]. The main input data for this model are shown in **Table 2** and **Table 3**. Note that the binder used in straw composite 1 is lime-based binder, while in straw composite 2 it is lime and 20% gelatin. The thermal conductivity of the solid phase of wheat straw was obtained by inverse analysis to be 0.80 W/(mK) at an intra-particle porosity of 86%.

Table 2. Volume fraction of each component of wheat straw concrete [54,61].

An example of a column heading	Binder (%)	Straw (%)	Macropores (%)
Straw composite 1	33	30	37
Straw composite 2	11	35	54

Table 3. Properties of wheat straw concrete [54,61].

Property	X	λ_p (W/(mK))	λ_w (W/(mK))	λ_b in composite 1 (W/(mK))	λ_b in composite 2 (W/(mK))
Value	4	0.026	0.598	0.168	0.143

Fig. 12 shows a comparison between the simulation and experiment for dry wheat straw concrete. It demonstrates the non-negligible relative error between the simulation and the experiment in the case of perfect contact, with a maximum of 26.07%. A good agreement was then achieved in subsequent operations considering imperfect contact. The imperfect coefficients for straw composites 1 and 2 are 2.58 and 0.30. This indicates a better contact between the aggregate and binder in composite 2. The facts from the literature [54,61] support this conclusion, i. e, 20% of the gelatin was added to the binder in composite 2 compared to composite 1, which improved the imperfect contact in the ITZ. This indicates the potential of this model in measuring the contact degree.

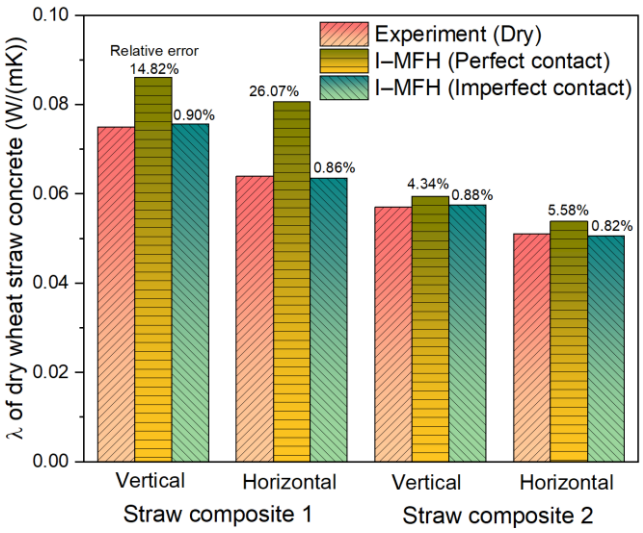

Fig. 12. Calibration of the thermal conductivity of wheat straw concrete with imperfect contact.

In order to verify whether the water saturation in this model can be applied to bio-based concrete, wheat straw concrete in a wet state was added to the comparison, as shown in **Fig. 13**. Inverse analysis in the model

gives a water saturation percentage of 24.84% and 12.38% in composites 1 and 2. It is clear that composite 2 has a lower percentage of water saturation. This can be explained by the effect of gelatin in composite 2, where the better contact between the bio-aggregates and the binder restricts the absorption of water. Moreover, from a dry to a humid environment, the thermal conductivities of the straw composites 1 and 2 increase by about 20%. The raising from dry to wet states suggests that it is important to consider water saturation when studying the thermal conductivity of bio-based building composites.

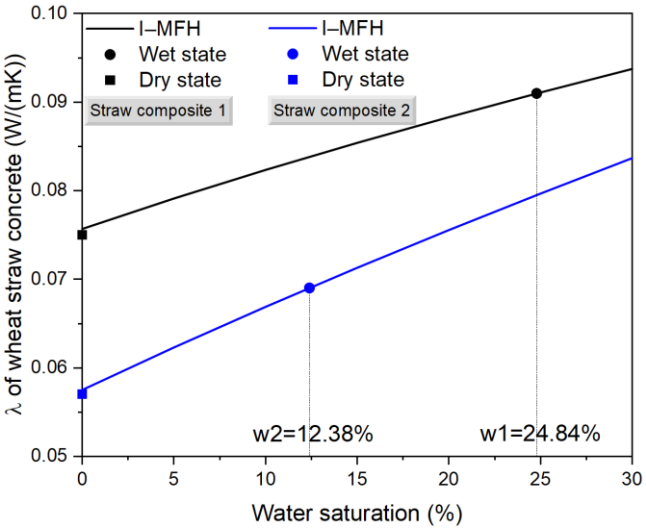

Fig. 13. Calibration of the thermal conductivity of wheat straw concrete with moisture.

3.4.4. Case 3 for other bio-based building materials

The parameters in Section 0 were further used to approximately predict the effective thermal conductivity of building materials containing various plant aggregates. The predicted results were then compared with several experimental observations [28,76–79] as shown in **Fig. 14**. It can be seen that when η is equal to 0, i.e., perfect contact, the curves of thermal conductivity in both directions cover a narrower range. In fact, due to the imperfect contact between the aggregate and the binder discussed earlier, η should be greater than 0. When η = 2, the thermal conductivity in both directions decreases compared to the perfect contact, which is due to the thermal resistance of the interface and the special arrangement of the plant fibers. In addition, η of 2 covers a larger area where more experimental data are located. This also indicates that in practical situations, imperfect contact is not negligible.

Due to the different types of plant fibers and binders used in these studies, aggregate surface treatment methods, etc., the value of η varies accordingly. The best way to do this is to obtain the coefficients by inverse operation for the corresponding working conditions and use them to predict the behavior of other materials under the same conditions. It is interesting to note that this operation can also be used to quantify the degree of surface treatment of plant fibers. **Fig. 14** shows a variety of plant fibers, so the model gives a range of

predictions rather than specific values. It can be seen that the area of η from 0 to 2 covers most cases, which demonstrates the applicability of this model to various plant fiber building materials.

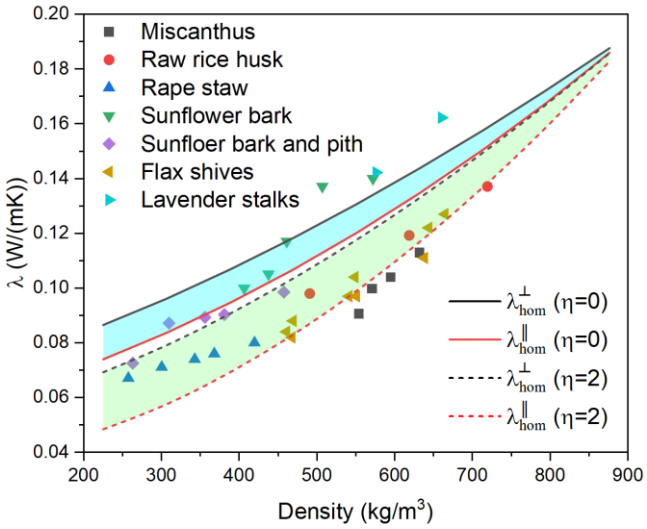

Fig. 14. Validation on various plant aggregates (Experimental data: [28,76–79]).

4. Conclusion

The use of bio-based materials in buildings is mainly due to their low thermal conductivity. Previous experimental studies have identified the effects of plant fiber type, orientation, imperfect contact, pores on different scales, and moisture on thermal conductivity. However, so far, no study has perfectly combined all these factors in one model to predict the effective thermal conductivity. Therefore, this study developed a multiscale model based on an iterative homogenization method and considered the above factors simultaneously. In particular, a new iterative approach was used for the model, which iterates over both macropores and bio-aggregates, compared to the conventional iterative approach that considers only aggregates. Also, the approach of fiber orientation in this study can utilize the fiber orientation distribution from X-ray tomography, while the commonly used probability density function is an indirect way to describe the orientation.

A series of comparisons with experimental data from literature and finite element models were performed on different scales and cases. Firstly, the model agrees well with the experimental results in terms of binder and individual fibers. Secondly, a finite element model of the binder-aggregate was developed to compare with the analytical model, then the results implied that the approach for plant fiber orientation was accurate. Thirdly, the model was applied to dry hemp concrete, which verified the predictive ability of the model in both perpendicular and parallel directions. Further, the successful application of the model on wet wheat straw concrete demonstrated the significant effect of moisture on thermal conductivity. Therefore, for modeling thermal conductivity under non-drying conditions, consideration of moisture is essential. Finally,

in order to investigate the applicability of the present model on other plant aggregates, a prediction range based on an imperfect contact coefficient was given. The results showed that most of the experimental data were covered by this prediction area. This suggests that the present model can be used for a wide range of plant sources, which facilitates the effective recycling of local agricultural by-products. Moreover, noting that some experiments investigated aggregate surface treatment to improve the interface with the binder, the imperfect contact coefficient can also be used to quantify this operation by inverse analysis. In addition, the fits to the shapes of hemp and wheat straw were consistent with the literature data.

In this study, a three-phase iterative model was developed to predict the effective thermal conductivity of various bio-based materials. In future work, this model may be used for sensitivity analysis and thus optimizing the thermal insulation of bio-based materials based on porosity, volume fraction of each phase, fiber orientation, shape, etc. Moreover, the application of bio-based concrete requires a comprehensive performance in terms of mechanical and thermal properties, thus contributing to the improvement of sustainability and to the reduction of energy consumption.

CRediT authorship contribution statement

Gang Huang: Methodology, Software, Formal analysis, Investigation, Data Curation, Writing - Original Draft, Writing - Review & Editing, Visualization. **Ariane Abou-Chakra:** Conceptualization, Methodology, Software, Validation, Resources, Writing - Review & Editing, Supervision. **Sandrine Geoffroy:** Conceptualization, Methodology, Validation, Writing - Review & Editing, Supervision, Project administration. **Joseph Absi:** Conceptualization, Methodology, Software, Validation, Writing - Review & Editing, Supervision.

Declaration of Competing Interest

The authors declare that they have no known competing financial interests or personal relationships that could have appeared to influence the work reported in this paper.

Appendix A. Depolarization tensor

In reference to [80], the depolarization tensor $\underline{\underline{S_r}}$ can be expressed in a form of matrix,

$$S = \begin{bmatrix} b & 0 & 0 \\ 0 & b & 0 \\ 0 & 0 & 1-2b \end{bmatrix} \quad \text{(A.1)}$$

For spherical inclusion, $X = 1$ and $b = 1/3$.

For prolate inclusion, $X > 1$,

$$b = \frac{1}{2}\left\{1+\frac{1}{X^2-1}\left[1-\frac{1}{2\chi_b}\ln\left(\frac{1+\chi_b}{1-\chi_b}\right)\right]\right\} \quad \text{(A.2)}$$

For oblate inclusion, $X < 1$,

$$b = \frac{1}{2}\left\{1+\frac{1}{X^2-1}\left[1-\frac{1}{\chi_a}\tan^{-1}(\chi_a)\right]\right\} \quad \text{(A.3)}$$

with

$$\chi_a^2 = -\chi_b^2 = \frac{1}{X^2} - 1 \quad \text{(A.4)}$$

Additionally, cylindrical inclusions can be regarded as ellipsoids with *X* of infinity. Therefore, according to Eq. (A.1), (A.2), and (A.4), the depolarization tensor for cylindrical inclusion can be written as a form of matrix as:

$$S_{Cylinder} = \begin{bmatrix} \frac{1}{2} & 0 & 0 \\ 0 & \frac{1}{2} & 0 \\ 0 & 0 & 0 \end{bmatrix} \quad \text{(A.5)}$$

Appendix B. Effective thermal conductivity of porous binder

According to Eq. (A.1), the depolarization tensor of the spherical pores in binder can be expressed as

follows.

$$\underline{\underline{S}}_{Sphere} = \frac{1}{3}\underline{\underline{\delta}} \tag{B.1}$$

Then, Eq. (7) can be rewritten as:

$$\underline{\underline{P}}_{Sphere} = \underline{\underline{S}}_{Sphere} \cdot (\underline{\underline{\lambda}}_b s)^{-1} = \frac{1}{3}\underline{\underline{\delta}} \cdot \frac{1}{\lambda_b s}\underline{\underline{\delta}} = \frac{1}{3\lambda_b s}\underline{\underline{\delta}} \tag{B.2}$$

Substituting Eq. (B.2) into (6):

$$\underline{\underline{A}}_p^0 = [\underline{\underline{\delta}} + \underline{\underline{P}}_{Sphere} \cdot (\underline{\underline{\lambda}}_p - \underline{\underline{\lambda}}_b s)]^{-1} = [\underline{\underline{\delta}} + \frac{1}{3\lambda_b s}\underline{\underline{\delta}} \cdot (\underline{\underline{\lambda}}_p - \underline{\underline{\lambda}}_b s)]^{-1} = (\frac{3\lambda_b s}{\lambda_p + 2\lambda_b s})\underline{\underline{\delta}} \tag{B.3}$$

Next, substituting Eq. (B.3) into (5) yields:

$$\underline{\underline{A}}_b^{MT} = \underline{\underline{A}}_b^0 s \cdot [(1-f)\underline{\underline{A}}_b^0 s + f\underline{\underline{A}}_p^0]^{-1} = \frac{\lambda_p + 2\lambda_b s}{(1-f)\lambda_p + (2+f)\lambda_b s}\underline{\underline{\delta}}$$

$$\underline{\underline{A}}_p^{MT} = \underline{\underline{A}}_p^0 \cdot [(1-f)\underline{\underline{A}}_b^0 s + f\underline{\underline{A}}_p^0]^{-1} = \frac{3\lambda_b s}{(1-f)\lambda_p + (2+f)\lambda_b s}\underline{\underline{\delta}} \tag{B.4}$$

As a result, the effective thermal conductivity of porous binder is as follows:

$$\underline{\underline{\lambda}}_b = \lambda_b s\underline{\underline{\delta}} + f_{pb}(\lambda_p - \lambda_b s)\frac{3\lambda_b s}{(1-f_{pb})\lambda_p + (2+f_{pb})\lambda_b s}\underline{\underline{\delta}} = [\lambda_b s + \frac{f_{pb}\lambda_b s(\lambda_p - \lambda_b s)}{\lambda_b s + \frac{1}{3}(1-f_{pb})(\lambda_p - \lambda_b s)}]\underline{\underline{\delta}} \tag{B.5}$$

References

[1] Buildings, IEA. (2022). https://www.iea.org/reports/buildings (accessed October 31, 2022).

[2] O. Kaynakli, A review of the economical and optimum thermal insulation thickness for building applications, Renewable and Sustainable Energy Reviews. 16 (2012) 415–425. https://doi.org/10.1016/j.rser.2011.08.006.

[3] Is cooling the future of heating? – Analysis, IEA. (n.d.). https://www.iea.org/commentaries/is-cooling-the-future-of-heating (accessed November 2, 2022).

[4] B. Lin, Z. Chen, Net zero energy building evaluation, validation and reflection – A successful project application, Energy and Buildings. 261 (2022) 111946. https://doi.org/10.1016/j.enbuild.2022.111946.

[5] W. Wu, H.M. Skye, Residential net-zero energy buildings: Review and perspective, Renewable and Sustainable Energy Reviews. 142 (2021) 110859. https://doi.org/10.1016/j.rser.2021.110859.

[6] Green Buildings, World Economic Forum. (2021). https://www.weforum.org/realestate/green-buildings/ (accessed November 2, 2022).

[7] E. Ohene, A.P.C. Chan, A. Darko, Prioritizing barriers and developing mitigation strategies toward net-zero carbon building sector, Building and Environment. 223 (2022) 109437. https://doi.org/10.1016/j.buildenv.2022.109437.

[8] P. Arumugam, V. Ramalingam, P. Vellaichamy, Effective PCM, insulation, natural and/or night ventilation techniques to enhance the thermal performance of buildings located in various climates – A review, Energy and Buildings. 258 (2022) 111840. https://doi.org/10.1016/j.enbuild.2022.111840.

[9] J.E.F.M. Ibrahim, O.B. Kotova, S. Sun, E. Kurovics, M. Tihtih, L.A. Gömze, Preparation of innovative eco-efficient composite bricks based on zeolite-poor rock and Hen's eggshell, Journal of Building Engineering. 45 (2022) 103491. https://doi.org/10.1016/j.jobe.2021.103491.

[10] J. Allegrini, V. Dorer, J. Carmeliet, Influence of the urban microclimate in street canyons on the energy demand for space cooling and heating of buildings, Energy and Buildings. 55 (2012) 823–832. https://doi.org/10.1016/j.enbuild.2012.10.013.

[11] N. Llantoy, M. Chàfer, L.F. Cabeza, A comparative life cycle assessment (LCA) of different insulation materials for buildings in the continental Mediterranean climate, Energy and Buildings. 225 (2020) 110323. https://doi.org/10.1016/j.enbuild.2020.110323.

[12] N. Asim, Z. Emdadi, M. Mohammad, M.A. Yarmo, K. Sopian, Agricultural solid wastes for green desiccant applications: an overview of research achievements, opportunities and perspectives, Journal of Cleaner Production. 91 (2015) 26–35. https://doi.org/10.1016/j.jclepro.2014.12.015.

[13] D. Jiang, S. Lv, S. Cui, S. Sun, X. Song, S. He, J. Zhang, P. An, Effect of thermal insulation components on physical and mechanical properties of plant fibre composite thermal insulation mortar, Journal of Materials Research and Technology. 9 (2020) 12996–13013. https://doi.org/10.1016/j.jmrt.2020.09.009.

[14] G. He, T. Liu, M. Zhou, Straw burning, PM2.5, and death: Evidence from China, Journal of Development Economics. 145 (2020) 102468. https://doi.org/10.1016/j.jdeveco.2020.102468.

[15] F. Collet, S. Pretot, Thermal conductivity of hemp concretes: Variation with formulation, density and water content, Construction and Building Materials. 65 (2014) 612–619. https://doi.org/10.1016/j.conbuildmat.2014.05.039.

[16] M. Lagouin, C. Magniont, P. Sénéchal, P. Moonen, J.-E. Aubert, A. Laborel-préneron, Influence of types of binder and plant aggregates on hygrothermal and mechanical properties of vegetal concretes, Construction and Building Materials. 222 (2019) 852–871. https://doi.org/10.1016/j.conbuildmat.2019.06.004.

[17] F. Wu, Q. Yu, H.J.H. Brouwers, Long-term performance of bio-based miscanthus mortar, Construction and Building Materials. 324 (2022) 126703. https://doi.org/10.1016/j.conbuildmat.2022.126703.

[18] M.R. Ahmad, B. Chen, S. Yousefi Oderji, M. Mohsan, Development of a new bio-composite for building insulation and structural purpose using corn stalk and magnesium phosphate cement, Energy and Buildings. 173 (2018) 719–733. https://doi.org/10.1016/j.enbuild.2018.06.007.

[19] T. Jami, S.R. Karade, L.P. Singh, A review of the properties of hemp concrete for green building applications, Journal of Cleaner Production. 239 (2019) 117852. https://doi.org/10.1016/j.jclepro.2019.117852.

[20] S. Barbhuiya, B. Bhusan Das, A comprehensive review on the use of hemp in concrete, Construction and Building Materials. 341 (2022) 127857. https://doi.org/10.1016/j.conbuildmat.2022.127857.

[21] B. Seng, C. Magniont, S. Lorente, Characterization of a precast hemp concrete. Part I: Physical and thermal properties, Journal of Building Engineering. 24 (2019) 100540. https://doi.org/10.1016/j.jobe.2018.07.016.

[22] H.R. Talebi, B.A. Kayan, I. Asadi, Investigation of Thermal Properties of Normal Weight Concrete for Different Strength Classes, 8 (2020) 7.

[23] J. Zhao, S. Li, Life cycle cost assessment and multi-criteria decision analysis of environment-friendly building insulation materials - A review, Energy and Buildings. 254 (2022) 111582. https://doi.org/10.1016/j.enbuild.2021.111582.

[24] F. Ntimugura, R. Vinai, A.B. Harper, P. Walker, Environmental performance of miscanthus-lime lightweight concrete using life cycle assessment: Application in external wall assemblies, Sustainable Materials and Technologies. 28 (2021) e00253. https://doi.org/10.1016/j.susmat.2021.e00253.

[25] G.M. Cappucci, V. Ruffini, V. Barbieri, C. Siligardi, A.M. Ferrari, Life cycle assessment of wheat husk based agro-concrete block, Journal of Cleaner Production. 349 (2022) 131437. https://doi.org/10.1016/j.jclepro.2022.131437.

[26] K. Ip, A. Miller, Life cycle greenhouse gas emissions of hemp–lime wall constructions in the UK, Resources, Conservation and Recycling. 69 (2012) 1–9. https://doi.org/10.1016/j.resconrec.2012.09.001.

[27] A. Galimshina, M. Moustapha, A. Hollberg, P. Padey, S. Lasvaux, B. Sudret, G. Habert, Bio-based materials as a robust solution for building renovation: A case study, Applied Energy. 316 (2022) 119102. https://doi.org/10.1016/j.apenergy.2022.119102.

[28] Y.X. Chen, F. Wu, Q. Yu, H.J.H. Brouwers, Bio-based ultra-lightweight concrete applying miscanthus fibers: Acoustic absorption and thermal insulation, Cement and Concrete Composites. 114 (2020) 103829. https://doi.org/10.1016/j.cemconcomp.2020.103829.

[29] P.S. de Carvalho, M.D. Nora, L.C. da Rosa, Development of an acoustic absorbing material based on sunflower residue following the cleaner production techniques, Journal of Cleaner Production. 270 (2020) 122478. https://doi.org/10.1016/j.jclepro.2020.122478.

[30] T.T. Nguyen, V. Picandet, P. Carre, T. Lecompte, S. Amziane, C. Baley, Effect of compaction on mechanical and thermal properties of hemp concrete, European Journal of Environmental and Civil Engineering. 14 (2010) 545–560. https://doi.org/10.1080/19648189.2010.9693246.

[31] J. Williams, M. Lawrence, P. Walker, The influence of the casting process on the internal structure and physical properties of hemp-lime, Mater Struct. 50 (2017) 108. https://doi.org/10.1617/s11527-016-0976-4.

[32] J. Williams, M. Lawrence, P. Walker, A method for the assessment of the internal structure of bio-aggregate concretes, Construction and Building Materials. 116 (2016) 45–51. https://doi.org/10.1016/j.conbuildmat.2016.04.088.

[33] J. Williams, M. Lawrence, P. Walker, The influence of constituents on the properties of the bio-aggregate composite hemp-lime, Construction and Building Materials. 159 (2018) 9–17. https://doi.org/10.1016/j.conbuildmat.2017.10.109.

[34] H.H. Ratsimbazafy, Évaluation du potentiel de co-produits agricoles locaux valorisables dans le domaine des matériaux de construction (PALOMAC), phdthesis, Université Paul Sabatier - Toulouse III, 2022. https://tel.archives-ouvertes.fr/tel-03699668 (accessed September 30, 2022).

[35] M.R. Ahmad, B. Chen, S.F. Ali Shah, Mechanical and microstructural characterization of bio-concrete prepared with optimized alternative green binders, Construction and Building Materials. 281 (2021) 122533. https://doi.org/10.1016/j.conbuildmat.2021.122533.

[36] M.R. Ahmad, B. Chen, M.A. Haque, S.M. Saleem Kazmi, M.J. Munir, Development of plant-concrete composites containing pretreated corn stalk bio-aggregates and different type of binders, Cement and Concrete Composites. 121 (2021) 104054. https://doi.org/10.1016/j.cemconcomp.2021.104054.

[37] G.M. Amantino, N.P. Hasparyk, F. Tiecher, R.D. Toledo Filho, Assessment of bio-aggregate concretes' properties with rice residue, Journal of Building Engineering. 52 (2022) 104348. https://doi.org/10.1016/j.jobe.2022.104348.

[38] R. Zerrouki, A. Benazzouk, M. Courty, H. Ben Hamed, Potential use of matakaolin as a partial replacement of preformulated lime binder to improve durability of hemp concrete under cyclic wetting/drying aging, Construction and Building Materials. 333 (2022) 127389. https://doi.org/10.1016/j.conbuildmat.2022.127389.

[39] N. Belayachi, D. Hoxha, M. Slaimia, Impact of accelerated climatic aging on the behavior of gypsum plaster-straw material for building thermal insulation, Construction and Building Materials. 125 (2016) 912–918. https://doi.org/10.1016/j.conbuildmat.2016.08.120.

[40] M.S. Abbas, E. Gourdon, P. Glé, F. McGregor, M.Y. Ferroukhi, A. Fabbri, Relationship between hygrothermal and acoustical behavior of hemp and sunflower composites, Building and Environment. 188 (2021) 107462. https://doi.org/10.1016/j.buildenv.2020.107462.

[41] M. Rahim, O. Douzane, A.D. Tran Le, T. Langlet, Effect of moisture and temperature on thermal properties of three bio-based materials, Construction and Building Materials. 111 (2016) 119–127. https://doi.org/10.1016/j.conbuildmat.2016.02.061.

[42] E. Gourlay, P. Glé, S. Marceau, C. Foy, S. Moscardelli, Effect of water content on the acoustical and thermal properties of hemp concretes, Construction and Building Materials. 139 (2017) 513–523. https://doi.org/10.1016/j.conbuildmat.2016.11.018.

[43] V. Barbieri, M. Lassinantti Gualtieri, T. Manfredini, C. Siligardi, Lightweight concretes based on wheat husk and hemp hurd as bio-aggregates and modified magnesium oxysulfate binder: Microstructure and technological performances, Construction and Building Materials. 284 (2021) 122751. https://doi.org/10.1016/j.conbuildmat.2021.122751.

[44] V. CEREZO, Propriétés mécaniques, thermiques et acoustiques d'un matériau à base de particules végétales : approche expérimentale et modélisation théorique, These de doctorat, INSA Lyon, 2005. https://www.theses.fr/2005ISAL0037.

[45] S.C. Somé, A. Ben Fraj, A. Pavoine, M. Hajj Chehade, Modeling and experimental characterization of effective transverse thermal properties of hemp insulation concrete, Construction and Building Materials. 189 (2018) 384–396. https://doi.org/10.1016/j.conbuildmat.2018.08.210.

[46] Q.V. Huynh, ESTIMATION DES PROPRIETES POROMECANIQUES EFFECTIVES DES ARGILITES: APPORT DES METHODES D'HOMOGENEISATION, (n.d.) 131.

[47] A. Giraud, I.-C. Gruescu, D.P. Do, F. Homand, D. Kondo, Effective thermal conductivity of transversely isotropic media with arbitrary oriented ellipsoïdal inhomogeneities, International Journal of Solids and Structures. 44 (9) (2007) 2627–2647. https://doi.org/10.1016/j.ijsolstr.2006.08.011.

[48] A.D. Tran-Le, S.-T. Nguyen, T. Langlet, A novel anisotropic analytical model for effective thermal conductivity tensor of dry lime-hemp concrete with preferred spatial distributions, Energy and Buildings. 182 (2019) 75–87. https://doi.org/10.1016/j.enbuild.2018.09.043.

[49] N. Mishra, K. Das, A Mori–Tanaka Based Micromechanical Model for Predicting the Effective Electroelastic Properties of Orthotropic Piezoelectric Composites with Spherical Inclusions, SN Appl. Sci. 2 (2020) 1206. https://doi.org/10.1007/s42452-020-2958-y.

[50] A. Jain, Micro and mesomechanics of fibre reinforced composites using mean field homogenization formulations: A review, Materials Today Communications. 21 (2019) 100552. https://doi.org/10.1016/j.mtcomm.2019.100552.

[51] M. Ferrari, Asymmetry and the high concentration limit of the Mori-Tanaka effective medium theory, Mechanics of Materials. 11 (1991) 251–256. https://doi.org/10.1016/0167-6636(91)90006-L.

[52] A.F. Fedotov, Mori-Tanaka experimental-analytical model for predicting engineering elastic moduli of composite materials, Composites Part B: Engineering. 232 (2022) 109635. https://doi.org/10.1016/j.compositesb.2022.109635.

[53] S. Dartois, S. Mom, H. Dumontet, A. Ben Hamida, An iterative micromechanical modeling to estimate the thermal and mechanical properties of polydisperse composites with platy particles: Application to anisotropic hemp and lime concretes, Construction and Building Materials. 152 (2017) 661–671. https://doi.org/10.1016/j.conbuildmat.2017.06.181.

[54] B. Ismail, N. Belayachi, D. Hoxha, L. Arbaret, Modelling of thermal conductivity and nonlinear mechanical behavior of straw insulation composite by a numerical homogenization approach, Journal of Building Engineering. 43 (2021) 103144. https://doi.org/10.1016/j.jobe.2021.103144.

[55] F. Bennai, K. Abahri, R. Belarbi, Contribution to the Modelling of Coupled Heat and Mass Transfers on 3D Real Structure of Heterogeneous Building Materials: Application to Hemp Concrete, Transp Porous Med. 133 (2020) 333–356. https://doi.org/10.1007/s11242-020-01426-9.

[56] T. Mori, K. Tanaka, Average stress in matrix and average elastic energy of materials with misfitting inclusions, Acta Metallurgica. 21 (1973) 571–574. https://doi.org/10.1016/0001-6160(73)90064-3.

[57] Z. Tian, A. Abou-Chakra, S. Geoffroy, D. Kondo, The effective elastic properties and thermal conductivity of porous fired clay bricks, European Journal of Environmental and Civil Engineering. 26 (2022) 547–569. https://doi.org/10.1080/19648189.2019.1666303.

[58] G. Huang, A. Abou-Chakra, J. Absi, S. Geoffroy, Optimization of mechanical properties in anisotropic bio-based building materials by a multiscale homogenization model, Journal of Building Engineering. 57 (2022) 104890. https://doi.org/10.1016/j.jobe.2022.104890.

[59] F. Bennai, C. El Hachem, K. Abahri, R. Belarbi, Microscopic hydric characterization of hemp concrete by X-ray microtomography and digital volume correlation, Construction and Building Materials. 188 (2018) 983–994. https://doi.org/10.1016/j.conbuildmat.2018.08.198.

[60] G. Delannoy, S. Marceau, P. Glé, E. Gourlay, M. Guéguen-Minerbe, D. Diafi, I. Nour, S. Amziane, F. Farcas, Aging of hemp shiv used for concrete, Materials & Design. 160 (2018) 752–762. https://doi.org/10.1016/j.matdes.2018.10.016.

[61] B. Ismail, N. Belayachi, D. Hoxha, Optimizing performance of insulation materials based on wheat straw, lime and gypsum plaster composites using natural additives, Construction and Building Materials. 254 (2020) 118959. https://doi.org/10.1016/j.conbuildmat.2020.118959.

[62] M.S. Abbas, F. McGregor, A. Fabbri, M.Y. Ferroukhi, The use of pith in the formulation of lightweight bio-based composites: Impact on mechanical and hygrothermal properties, Construction and Building Materials. 259 (2020) 120573. https://doi.org/10.1016/j.conbuildmat.2020.120573.

[63] M. Bouasker, N. Belayachi, D. Hoxha, M. Al-Mukhtar, Physical Characterization of Natural Straw Fibers as Aggregates for Construction Materials Applications, Materials. 7 (2014) 3034–3048. https://doi.org/10.3390/ma7043034.

[64] N. Mati-Baouche, Conception d'isolants thermiques à base de broyats de tiges de tournesol et de liants polysaccharidiques, phdthesis, Université Blaise Pascal - Clermont-Ferrand II, 2015. https://tel.archives-ouvertes.fr/tel-01226208 (accessed January 14, 2022).

[65] R. Walker, S. Pavía, Moisture transfer and thermal properties of hemp–lime concretes, Construction and Building Materials. 64 (2014) 270–276. https://doi.org/10.1016/j.conbuildmat.2014.04.081.

[66] Modeling thermal conductivity of hemp insulation material: A multi-scale homogenization approach, Building and Environment. 107 (2016) 127–134. https://doi.org/10.1016/j.buildenv.2016.07.026.

[67] G. Huang, A. Abou-Chakra, S. Geoffroy, J. Absi, A Multi-Scale Numerical Simulation on Thermal Conductivity of Bio-Based Construction Materials, Construction Materials. 2 (2022) 148–165. https://doi.org/10.3390/constrmater2030011.

[68] H. Le Quang, Estimations and bounds of the effective conductivity of composites with anisotropic inclusions and general imperfect interfaces, International Journal of Heat and Mass Transfer. 99 (2016) 327–343. https://doi.org/10.1016/j.ijheatmasstransfer.2016.03.116.

[69] C.-W. Nan, R. Birringer, D.R. Clarke, H. Gleiter, Effective thermal conductivity of particulate composites with interfacial thermal resistance, Journal of Applied Physics. 81 (1997) 6692–6699. https://doi.org/10.1063/1.365209.

[70] S.-Y. Fu, B. Lauke, Effects of fiber length and fiber orientation distributions on the tensile strength of short-fiber-reinforced polymers, Composites Science and Technology. 56 (1996) 1179–1190. https://doi.org/10.1016/S0266-3538(96)00072-3.

[71] P. Glé, T. Lecompte, A. Hellouin de Ménibus, H. Lenormand, S. Arufe, C. Chateau, V. Fierro, A. Celzard, Densities of hemp shiv for building: From multiscale characterisation to application, Industrial Crops and Products. 164 (2021) 113390. https://doi.org/10.1016/j.indcrop.2021.113390.

[72] T. Pierre, M. Carin, Characterization of the thermal properties of millimeter-sized insulating materials, International Journal of Thermal Sciences. 135 (2019) 247–255. https://doi.org/10.1016/j.ijthermalsci.2018.09.009.

[73] F. Wu, Q. Yu, C. Liu, Durability of thermal insulating bio-based lightweight concrete: Understanding of heat treatment on bio-aggregates, Construction and Building Materials. 269 (2021) 121800. https://doi.org/10.1016/j.conbuildmat.2020.121800.

[74] F. Wu, Q. Yu, C. Liu, H.J.H. Brouwers, L. Wang, Effect of surface treatment of apricot shell on the performance of lightweight bio-concrete, Construction and Building Materials. 229 (2019) 116859. https://doi.org/10.1016/j.conbuildmat.2019.116859.

[75] A. Sellami, M. Merzoud, S. Amziane, Improvement of mechanical properties of green concrete by treatment of the vegetals fibers, Construction and Building Materials. 47 (2013) 1117–1124. https://doi.org/10.1016/j.conbuildmat.2013.05.073.

[76] M. Chabannes, J.-C. Bénézet, L. Clerc, E. Garcia-Diaz, Use of raw rice husk as natural aggregate in a lightweight insulating concrete: An innovative application, Construction and Building Materials. 70 (2014) 428–438. https://doi.org/10.1016/j.conbuildmat.2014.07.025.

[77] Y. Brouard, N. Belayachi, D. Hoxha, S. Méo, W. Abdallah, Hygrothermal Behavior of Clay - Sunflower (Helianthus annuus) and Rape Straw (Brassica napus) Plaster Bio-Composites for Building Insulation, Advanced Engineering Forum. 21 (2017) 242–248. https://doi.org/10.4028/www.scientific.net/AEF.21.242.

[78] F. Benmahiddine, R. Cherif, F. Bennai, R. Belarbi, A. Tahakourt, K. Abahri, Effect of flax shives content and size on the hygrothermal and mechanical properties of flax concrete, Construction and Building Materials. 262 (2020) 120077. https://doi.org/10.1016/j.conbuildmat.2020.120077.

[79] R.V. Ratiarisoa, C. Magniont, S. Ginestet, C. Oms, G. Escadeillas, Assessment of distilled lavender stalks as bioaggregate for building materials: Hygrothermal properties, mechanical performance and chemical interactions with mineral pozzolanic binder, Construction and Building Materials. 124 (2016) 801–815. https://doi.org/10.1016/j.conbuildmat.2016.08.011.

[80] S. Torquato, Random Heterogeneous Materials, Springer New York, New York, NY, 2002. https://doi.org/10.1007/978-1-4757-6355-3.

CHAPTER IV ：Performance optimization of bio-based concrete through a multi-objective approach

Chapter introduction

The preceding chapters have presented models for predicting the mechanical and thermal properties of bio-based concrete, but a single-objective optimization approach may not guarantee optimal performance for both properties. For example, an increase in the volume fraction of bio-aggregate may improve thermal insulation but reduce mechanical performance. Thus, this chapter proposes a multi-objective optimization approach that combines both models to optimize the overall performance of bio-based concrete.

Three optimization strategies are presented based on the structural differences of bio-based concrete in main industrial applications, including bio-based blocks or filler materials, bio-based roofs, and bio-based shotcrete. The optimization was first performed in a broad decision space and then extended to specific situations, including high-volume bio-aggregates, low-density roofs, and humid environments. As a result, the optimal solution for each situation was provided.

By applying a multi-objective optimization approach to the previously developed models, this chapter can provide an optimal solution for the comprehensive performance of bio-based concrete. This approach enhances the application potential of this sustainable material by allowing us to optimize multiple properties simultaneously, rather than focusing on a single property in isolation. In conclusion, this study provides a valuable contribution to the field of sustainable construction by demonstrating the potential of bio-based concrete and providing a framework for optimizing its performance.

This chapter is formatted as a manuscript for submission to a journal, and its final version is subject to possible revisions during the journal review process.

Article D: Improving the Mechanical and Thermal Performance of Bio-Based Concrete Through Multi-Objective Optimization

Gang Huang[a], Ariane Abou-Chakra[a,*], Sandrine Geoffroy[a], Joseph Absi[b]

[a]*LMDC, INSA, UPS, Université de Toulouse, 135 Avenue de Rangueil, 31077 Toulouse, France*
[b]*UMR CNRS, IRCER, Université de Limoges, 12 rue Atlantis, 87068 Limoges, France*

Abstract

Bio-based concrete, which utilizes recycled agricultural waste as aggregates, has emerged as a sustainable alternative material in the construction industry. Optimizing its combined mechanical and thermal performance can promote its environmental and energy benefits. To achieve this, this paper presents a multi-objective optimization approach to improve the overall performance of bio-based concrete based on multiscale structural features, considering the porosity, shape, orientation, and volume fraction. Optimization strategies are provided for three main industrial applications. Furthermore, this study addresses multiple design requirements, including high-volume bio-aggregates, more demanding performance requirements, low densities, and humid environments. The optimization results demonstrate that the optimal solution varies with industrial applications and requirements. Consequently, we provide specific optimal solutions for each case, and offer designers three preferences for mechanical properties, insulation, or balanced performance. Overall, this study optimizes the comprehensive performance of bio-based concrete in terms of multiscale structures, thereby contributing to a more sustainable construction industry.

Keywords: Bio-based material; Mechanical properties; Thermal conductivity; Multi-objective optimization; Multi-scale modeling.

1. Introduction

In recent years, the construction industry has been exploring sustainable alternatives to traditional building materials in response to the urgent need to reduce the carbon emissions and energy consumption [1,2]. One promising solution for low-load building components is bio-based concrete [3]. It is a composite material consisting of recycled agricultural waste, such as hemp [4], sunflower [5], and flax [6], as well as low-carbon binders including lime and metakaolin [7]). Bio-based concrete represents a new generation of sustainable building materials that have gained significant attention for their low-carbon footprint [8,9] and energy efficiency [10]. Studies assessing the life cycle of bio-based constructions have shown that they offer environmental benefits [9–11]. This sustainable material has the potential to support the European Green

Deal's goal of reducing greenhouse gas emissions by at least 55% by 2030 and achieving climate neutrality by 2050 [12].

Bio-based concrete's excellent thermal insulation is one of its main advantages for use in construction. Its thermal conductivity can be as low as 0.06 W/m·K [13] compared to 1.28 W/m·K for normal concrete, 0.81 W/m·K for clay bricks, 0.26 W/m·K for hollow blocks, and 0.22 W/m·K for aerated concrete [14]. Nevertheless, it performs weakly in terms of mechanical properties, for example, its compressive strength is generally less than 5 MPa [15]. This limits its use to non-load-bearing parts [16] and greatly hinders its potential for more applications. Therefore, it is important to improve and optimize the mechanical properties of bio-based concrete. However, improving the material's mechanical properties may come at the expense of its thermal insulation. For instance, reducing the volume of bio-aggregates can enhance the mechanical properties, but at the same time the thermal insulation decreases [6]. In addition, binder, pretreatment, and fiber orientation all have varying degrees of influence on both properties [17,18]. Thus, it is necessary to improve the combined mechanical and thermal properties through a multi-objective optimization approach.

The macroscopic behavior of a material is closely related to its multi-scale structural characteristics. Several experimental studies have demonstrated that the complex microscopic features of bio-concrete can influence its performance. [18,19] found that bio-fibers in concrete are often distributed in the plane perpendicular to compaction, which creates differences in properties between the horizontal and vertical directions. Moreover, the properties of concrete can be affected by the different shapes of bio-aggregates. As an example, the aspect ratio can influence the thermal conductivity and compressive strength of wheat straw [20]. Therefore, it is possible to optimize bio-based concrete by considering multi-scale structural features. To achieve a comprehensive optimization, it is essential to establish quantitative relationships between mechanical and thermal properties and the aforementioned factors. Traditional experimental methods are time-consuming and cannot quantify the effects of factors such as orientation on performance.

The analytical method has several advantages in this case, including reduced cost, faster results, and greater control over variables [21]. It enables the analysis of complex systems that are challenging to replicate experimentally. Nevertheless, previous models are inadequate for the intricate microstructure of bio-based concrete. The composite sphere assumption-based model was employed initially for bio-based concrete [22–24]. This scheme is simple to execute and can approximately anticipate concrete behavior. However, it overlooks the fibers' shape and orientation distribution. Subsequently, researchers such as [25] enhanced the model by incorporating more microstructural features. But they do not encompass moisture, imperfect contact, and comprehensive multiscale structure in one model.

Our previous study [26,27] proposed multiscale models for the mechanical properties and thermal conductivity of bio-based concrete, respectively. The models considered several factors, i.e., the volume fraction of each phase, shape and orientation of plant aggregates, moisture, pore size, and imperfect contact. In this study, we optimize the combined mechanical and thermal performance of bio-based concrete using a

multi-objective approach. This optimization contains four decision variables: aspect ratio, porosity, volume fraction, and orientation, as well as two objectives: higher mechanical properties and thermal insulation. Moreover, we propose three optimization strategies based on the main industrial applications of bio-based concrete. To cover a wider range of design possibilities, the optimization was first carried out in the general case and then in more practical design requirements, such as high-volume bio-aggregates, more demanding performance requirements, low densities, and wet environments. The results provide specific optimal solutions for different applications and requirements, with three preferences offered: mechanical properties, thermal insulation, and balanced performance. This study aims to improve the overall performance of bio-based concrete by means of a multi-objective optimization approach, increasing its potential for applications and contributing to a more sustainable and efficient construction industry.

2. Methodology

2.1. Multi-scale models

Bio-based concrete is a sustainable building material composed of agricultural waste and low-carbon binders. It has a more complex microstructure than traditional concrete due to the shape and high-volume fraction of the plant aggregates. In previous research [26,27], we proposed homogenization models based on the multi-scale structure of bio-based concrete, focusing on its mechanical and thermal performance, respectively. They were developed from the classical Mori-Tanaka homogenization theory [28] and considered several factors, including the multi-scale structure, shape and orientation of the bio-aggregates, volume fractions of each component, different pore sizes, water content, and imperfect contact. The effective mechanical and thermal properties of the homogenized material can be summarized by Eqs. (1) [26] and (2) [27]. In this study, we will combine both to optimize the overall performance of bio-based concrete.

$$\mathbb{C}_{hom} = \sum_{r=0}^{N} f_r \, \mathbb{C}_r : [\mathbb{A}_r : (\sum_{r=0}^{N} f_r \, \mathbb{A}_r)^{-1}] \quad (1)$$

$$\underline{\underline{\lambda}}_{hom} = \sum_{r=0}^{N} f_r \, \underline{\underline{\lambda}}_r \cdot [\underline{\underline{A}}_r \cdot (\sum_{r=0}^{N} f_r \, \underline{\underline{A}}_r)^{-1}] \quad (2)$$

In the above equations, $\mathbb{C}_{hom}$ and $\underline{\underline{\lambda}}_{hom}$ denote the effective fourth-order stiffness tensor and second-order thermal conductivity tensor. The volume fraction of the r-th phase is represented by f_r, where $r = 0$ corresponds to the binder and r ranging from 1 to *N* represents the inclusions (bio-aggregates) in different directions. $\mathbb{A}$ and $\underline{\underline{A}}$ denote the fourth-order and second-order concentration tensor. It depends on the Hill

tensor $\mathbb{P}$ (mechanical problem) or the interaction tensor $\underline{\underline{P}}$ (thermal problem), which contains information about the shape of bio-aggregates.

Additionally, the thermal model considered moisture (W) and imperfect contact (η), where bio-aggregates were assumed to be made up of aggregate solids and pore inclusions partially or fully saturated with water. Detailed calculations can be found in [27].

2.2. Multi-objective optimization problem

The concept of multi-objective optimization is based on the idea of simultaneously optimizing multiple objectives that are often in conflict with each other [29]. In such cases, finding a single optimal solution that satisfies all objectives is often not possible, and a trade-off between conflicting objectives must be made. To deal with such problems, the domination-based approach proposed by Goldberg D. E. [30] is widely used. In this approach, the decision variables $X = (x_1,\ x_2,..,x_m)$ and the objective functions $f(X) = (f_1(X),\ f_2(X),..,f_n(X))$ are defined, and then the general multi-objective optimization problem can be expressed mathematically as follows:

$$\min f(X) = \big(f_1(X),f_2(X),\dots,f_n(X)\big), or\ \max\ (-f(X))$$

with two types of constraint functions $g_i(X)$ and $h_i(X)$ as follows

$$g_i(X) \geqslant 0 \quad (i = 1,2,\dots,k)$$

$$h_i(X) = 0 \quad (i = 1,2,\dots,l)$$

and the boundaries of the decision variables

$$X^{Lower} \leqslant X \leqslant X^{Upper}$$

In multi-objective optimization, the solutions can be categorized as dominated or non-dominated. A dominated solution is one that is worse than at least one other solution in all objectives. A non-dominated solution, on the other hand, is one that is not dominated by any other solution. The set of non-dominated solutions is called the Pareto optimal set [31]. The Pareto optimal solution set cannot be improved in any objective without worsening at least one other objective. The Pareto optimal solution set forms a front in the objective space, which is called the Pareto front. The Pareto front represents the trade-offs between the objectives and shows the best possible compromise solutions for different preferences or scenarios. In the context of bio-based concrete, the objectives of interest typically include both mechanical and thermal performance. Therefore, this study aims to find the Pareto optimal solution set under different constraints to improve the overall performance of bio-based concrete for various industrial applications.

2.3. Optimization strategy for bio-based concrete

After identifying the mechanical and thermal insulation properties as the two main objectives for multi-objective optimization of bio-based concrete, it is crucial to note that the specific optimization targets may vary depending on the intended application of the concrete. Based on the investigation the main industrial applications of bio-based concrete [15,32,33], three main types have been identified, classified by their anisotropic microstructures:: bio-based block (BB) or bio-based wall filling materials, bio-based roofing (BR), and bio-based shotcrete (BS). **Fig. 1** illustrates the structures and corresponding optimization strategies for these three types.

In BB, concrete blocks are generally stacked horizontally into walls, with load-bearing primarily along the compaction direction. Therefore, $E^{\parallel}$ is chosen as the mechanical optimization target. Thermal insulation properties are mainly determined by the heat transfer inside and outside the wall, which is represented by $\lambda^{\perp}$ in the direction perpendicular to the compaction.

In BF, the load bearing direction is the same, i.e., $E^{\parallel}$. But thermal insulation properties are determined by the thermal conductivity in the direction perpendicular to the roof surface, i.e., $\lambda^{\parallel}$. It should be noted that this study focuses on horizontal roofs.

In BS, fibers tend to be randomly distributed on the sprayed wall surface [34]. Therefore, the optimization targets are $E^{\perp}$ and $\lambda^{\parallel}$.

The optimization strategy for bio-based concrete is to find the Pareto optimal solution for multiple industrial applications, thus to improve the overall performance of bio-based concrete based on different constraints.

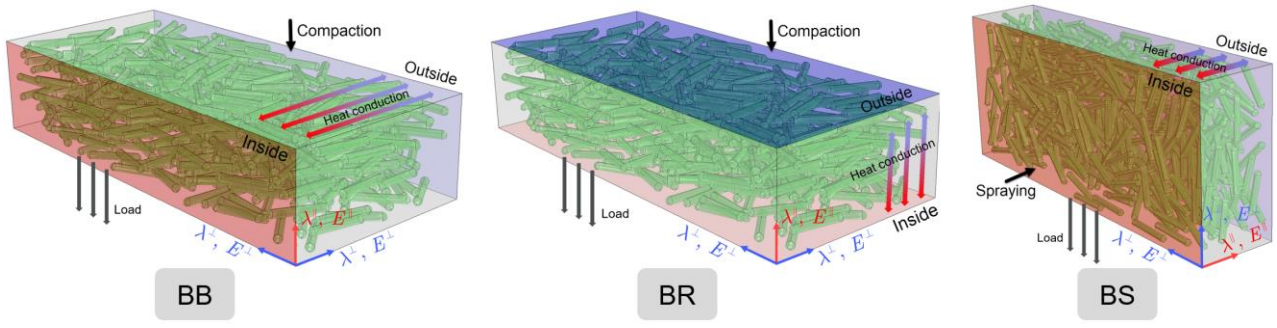

Fig. 1. Three optimization strategies for bio-based concrete.

2.4. Decision variables and constraints

The optimization of bio-based concrete involves selecting suitable decision variables and constraints to ensure that the resulting meets the requirements of different applications. In this study, four decision variables were chosen: aspect ratio (X), porosity in binder (f_p^b), volume fraction of fibers (f_A), and fiber orientation (θ). The boundaries of these decision variables, i.e., their minimum and maximum values, were determined based on a literature survey, as presented in **Table 1**. These values were selected to cover and slightly exceed those

reported in the literature, which can compensate for any omissions in the literature survey and provide a more comprehensive exploration of the design space.

Moreover, the performance requirements of bio-based concrete vary depending on its intended application, such as the dosage of bio-aggregates, mechanical and thermal insulation properties requirements, environmental humidity, and density. Therefore, corresponding constraints were proposed to optimize the performance of bio-based concrete for specific requirements, as detailed in sections 2 to 5.

The sampling density (SD) shown in **Table 1** represents the number of points sampled between the minimum and maximum values of each decision variable. For example, SD-3 indicates that three equally spaced points are sampled in each decision space, i.e., X (3, 7, 11), f_p^b (0.2, 0.425, 0.65), f_A (0.1, 0.5, 0.9), and θ (45º, 67.5º, 90º). It affects the accuracy of the Pareto front. A higher sampling density results in a more accurate Pareto optimal solution, but also increases the computation time and cost. Hence, determining an appropriate sampling density is the first step in optimization. In this study, we compared five sampling densities (SD = 3, 6, 9, 12, and 15), with the corresponding number of objective points being the quadratic of the sampling density. Additionally, the fixed parameters for the model inputs are shown in **Table 2**.

Table 1. Decision variables and boundaries.

Decision variable	Literature review	Min	Max	SD-3*	SD-6	SD-9	SD-12	SD-15
X	Hemp: 3.3-4.4 [35], 9.6 [36]. Flax: 7.8 [36]. Maize bark: 3.7 [36].	3	11	3	6	9	12	15
f_p^b	Lime T70: 0.45 [22]. Metakaolin-based binder: 0.562, lime-based binder 0.548 [37]. Cement–lime: 0.20 – 0.23 [38].	0.20	0.65	3	6	9	12	15
f_A	Sunflower concrete: 40, 46 [13].	0.1	0.9	3	6	9	12	15
θ	Tends to be perpendicular to the direction of compaction or spraying [19,34,37].	45°	90°	3	6	9	12	15
Total point count				81	1296	6561	2073	5065

* SD refers to the sampling density, or the number of points across decision variable range evenly, for each decision values.

Table 2. Fixed parameters in this model.

Parameter	Value	Reference

ρ_A (kg/m^3)	265	[39]
ρ_A^s (kg/m^3)	1454	[35]
ρ_b^s (kg/m^3)	2327	Calculated from [37]
λ_A^s (W/m·K)	0.564	[35]
λ_b^s (W/m·K)	0.56	[40]
E_A (MPa)	1.5	[25]
ν_A	0.1	[25]
E_b^s (MPa)	1318	Calculated from [22]
ν_b^s	0.2	Calculated from [22]
λ_w (W/m·K)	0.598	[41]
λ_p (W/m·K)	0.026	[42]
η	1	[27]

3. Results and discussions

3.1. Sampling density (SD)

Fig. 2 shows the point distributions of the generated objective values and the corresponding Pareto fronts in BB for five sampling densities, namely, SD-3, SD-6, SD-9, SD-12, and SD-15. As can be observed, the Pareto fronts become more densely packed with points as the sampling density. Higher sampling densities lead to more accurate approximations of the true Pareto fronts. It is worth noting that the amplitude of the lines decreases as the sampling density increases. This implies that some Pareto optimal solutions may have been missed at lower densities, but they were found as the density increased. Thus, the use of higher sampling

densities is crucial to ensure that all relevant Pareto optimal solutions are identified, especially when dealing with complex multi-objective optimization problems.

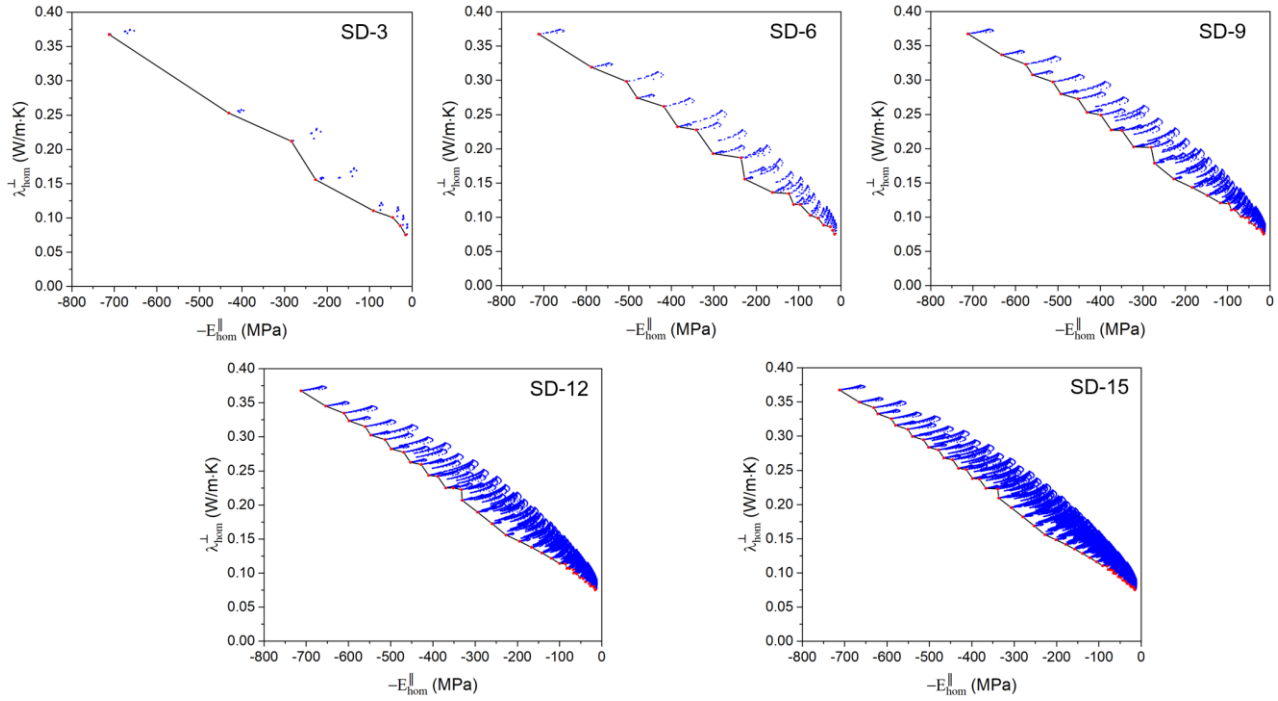

Fig. 2. Point distribution and Pareto front (Line) at varying sampling densities.

Furthermore, the Pareto fronts under the five sampling densities were compared in BB, BR, and BS to determine a suitable sampling density that meets all cases, as shown in **Fig. 3**. As expected, the Pareto front approaches the origin of the coordinate axis as the sampling density increases, indicating that a low sampling density is inadequate to locate all optimal solutions. The comparison of adjacent sampling densities shows that the Pareto front advances more slowly with increasing sampling density, suggesting that it is close to the true Pareto solution set at a moderate sampling rate.

In terms of BB, the comparison of SD-9 and SD-12 reveal that the Pareto front of SD-9 is less accurate at approximately -300 MPa, whereas the Pareto front of SD-12 and SD-15 are nearly identical. Therefore, SD-12 satisfies the requirements of BB. Similarly, the minimum sampling density requirements for BR and BS are SD-9 and SD-12. In summary, SD-12 was chosen as the sampling density for the subsequent optimization

analyses. The results demonstrate that a density of SD-12 is adequate for identifying the Pareto-optimal solutions for this optimization problem, striking a balance between accuracy and computational cost.

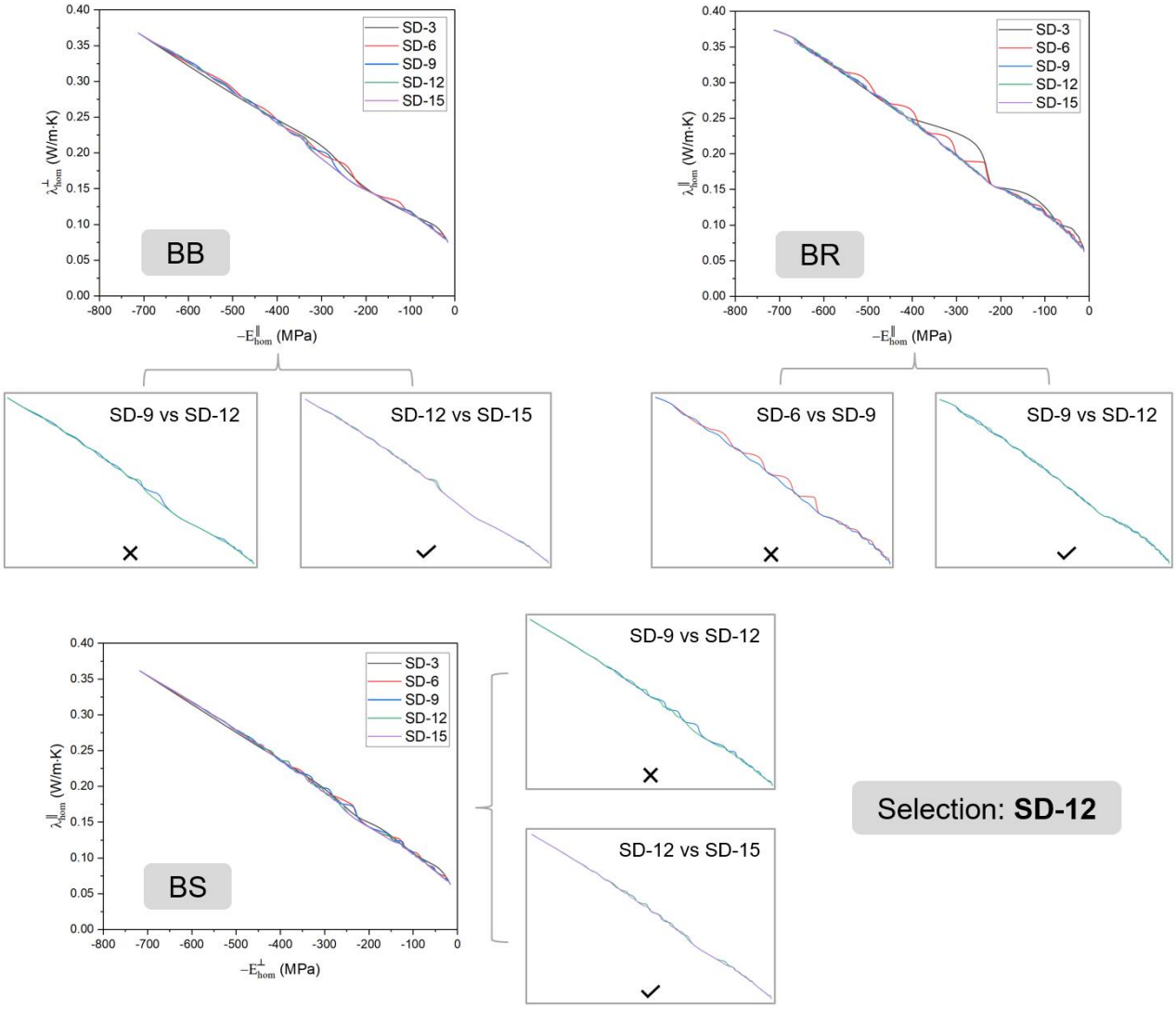

Fig. 3. Comparison of Pareto fronts at different sampling densities for three applications (Icons × and ✓ represent inadequate and adequate sampling density in the comparison).

3.2. Point distribution of the objectives

The selected sampling density SD-12 was implemented to represent the objectives in three main applications. The resulting point distribution was plotted in **Fig. 4**. While the decision variables were uniformly selected, the density of the point distribution was significantly higher in the lower-right corner of the plot. This means that the overall sensitivity of the objectives to the decision variables is not uniform, and is more pronounced when the thermal conductivity and mechanical properties are high. A comparative analysis of the three applications reveals that the high point density region in BS is closest to the Pareto front,

followed by BR and BB. This finding suggests that the optimal or suitable formula for BS offers more possibilities than the other two applications.

The point distribution reflects the general sensitivity of the objectives to the decision variables. To investigate this phenomenon in detail, further studies in Section 3.3 could examine the specific decision that contribute to the point distribution.

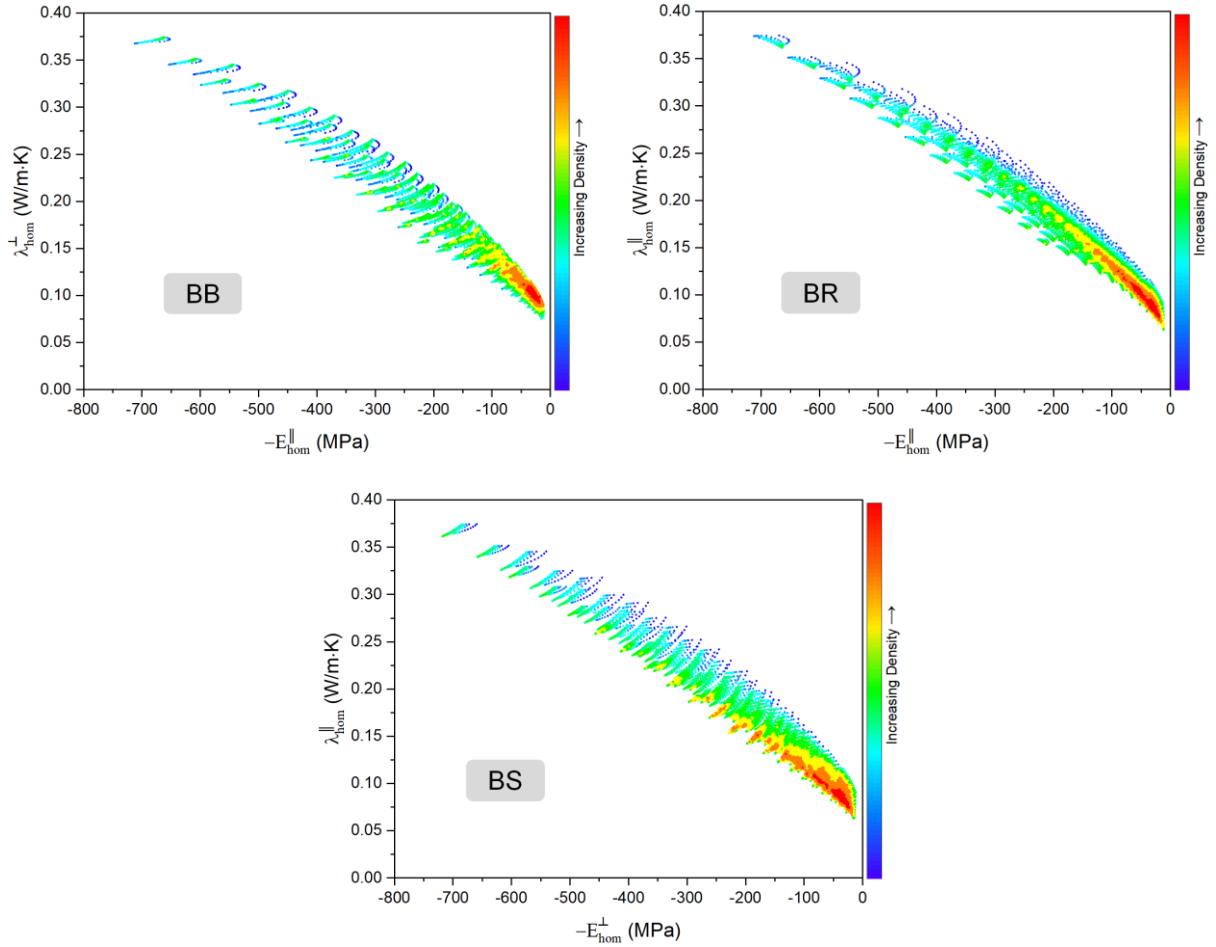

Fig. 4. Density plot of the objective values.

3.3. Sensitivity analysis and multi-objective optimization in the general case

3.3.1. BB

This section aims to analyze and optimize bio-based concrete in the general case by providing overall recommendations for all possible decisions. The distribution of objectives with decision variables marked in different colors is shown in **Fig. 5**. The analysis of the color distribution shows that different values of X and θ are spread over all the objective ranges, while the point distribution of the other variables depends on the thermal or mechanical properties. This indicates that X and θ can work in all cases. However, increasing the values of f_A and $f_p{}^b$ leads to a loss in mechanical properties, which cannot be compensated by the optimization of X and θ. Further comparison of X and θ reveals that the distribution of X is uniform, while θ is distributed

in a gradient from the lower left to the upper right corner. This can be explained by the fact that X has a relatively small and uniform effect on all cases and low θ is the optimal solution for BB.

The coverage of the same color represents the optimization potential through the other three variables, with larger coverage indicating larger optimization space. In **Fig. 5**, the red color of f_A and f_p^b is more widely distributed, i.e., concrete at low f_A and f_p^b has greater optimization potential through four decision variables. This can be explained by the higher sensitivity of concrete performance in this case.

When comparing the colors of the Pareto fronts, it can be observed that high X and low θ are optimal solutions for BB. But, the suboptimal solution of X (from 6 to 8) is also worth considering when the bio-aggregate shape has been determined because it is very close to the Pareto front. Moreover, the optimal solutions for f_A and f_p^b vary with thermal conductivity. Lower values of f_A and f_p^b are optimal for mechanical performance preference, while higher values are optimal for thermal insulation preference, regardless of the values of X and θ.

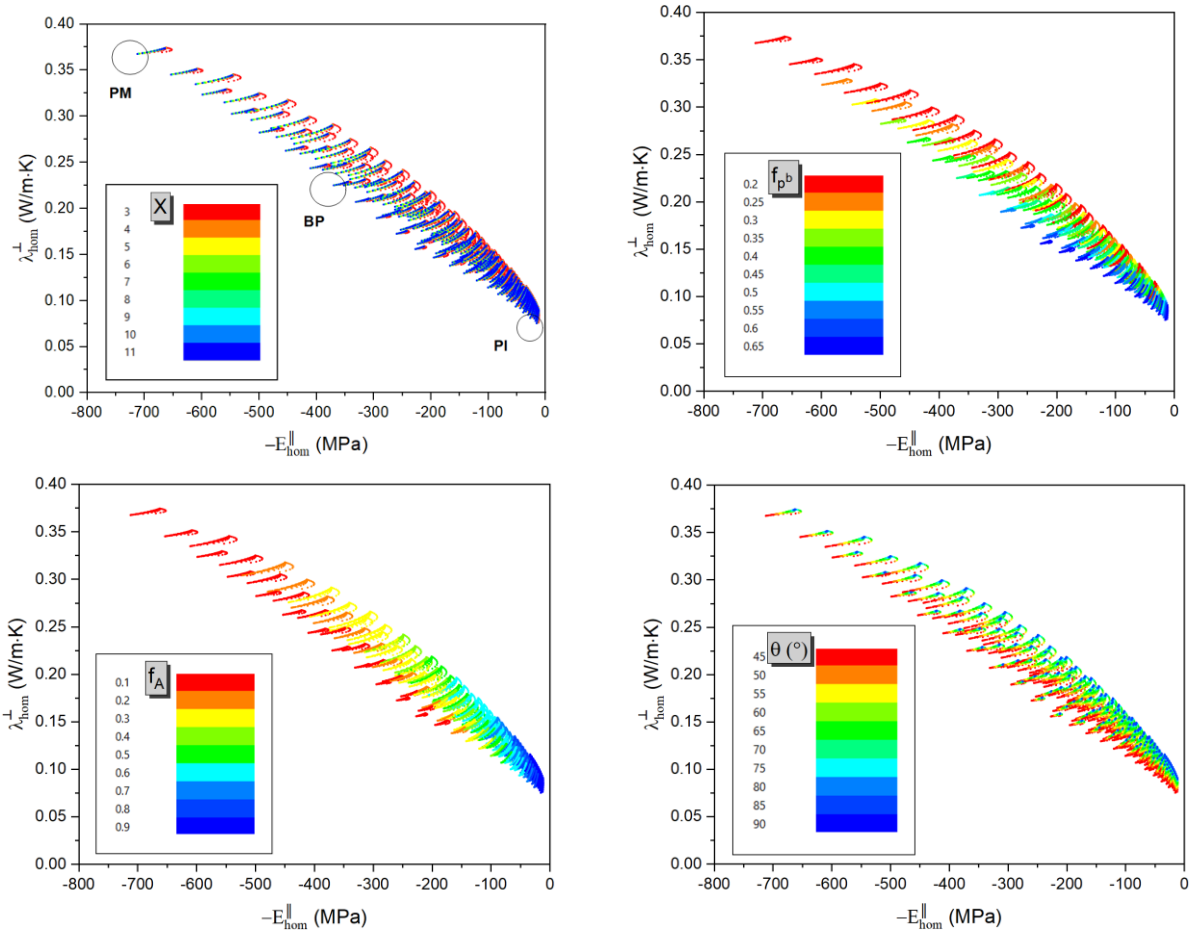

Fig. 5. Color-coded point distribution of objectives in BB (PM: preference for mechanical properties, BP: balanced performance, PI: preference for insulation).

As mentioned earlier, multi-objective optimization leads to a set of solutions without prioritization. However, recognizing that different stakeholders may have distinct preferences regarding the objectives, we

define three distinct preference scenarios. The first preference scenario, referred to as 'preference for mechanical properties' (PM), places a higher priority on maximizing mechanical properties while accepting a certain trade-off in thermal insulation. The second preference scenario, denoted as 'balanced performance' (BP), reflects a balanced compromise between thermal insulation and mechanical properties, acknowledging an equal preference for both objectives. Lastly, 'preference for insulation' (PI) represents a strong emphasis on achieving optimal thermal insulation performance while allowing for a moderate compromise in mechanical properties. By considering these three preference scenarios (**Fig. 5**), we aim to provide a comprehensive understanding of the trade-offs and optimal solutions that cater to a range of stakeholder preferences in this multi-objective optimization problem. **Table 3** presents the detailed optimal solution for BB, BR, and BS in the general case.

Table 3. Optimal solution for the general case.

Applications	Preferences	X	f_p^b	f_A	θ (º)	E (MPa)	λ (W/m·K)
BB	PM	11	0.20	0.10	45	712	0.37
	BP	11	0.49	0.10	45	370	0.23
	PI	11	0.65	0.90	45	16	0.08
BR	PM	11	0.20	0.10	45	712	0.37
	BP	11	0.49	0.10	57	358	0.23
	PI	11	0.65	0.90	90	12	0.06
BS	PM	11	0.20	0.10	90	718	0.36
	BP	11	0.49	0.10	90	372	0.22
	PI	11	0.65	0.90	90	16	0.06

PM: preference for mechanical properties, BP: balanced performance, PI: preference for insulation.

3.3.2. BR

The point distribution for application BR in the general case is depicted in **Fig. 6**. Unlike BB, the point distribution of BR is more continuous from the upper left to the lower right. It can be inferred that the influence of decision variables on mechanical and thermal performance is more balanced. A modification in one factor is more clearly reflected in both performances. Additionally, the color distribution of f_p^b and f_A in **Fig. 6** is similar to that in BB, but more concentrated. At the low conductivity, the comparison of **Fig. 5** and

Fig. 6 for θ exhibit opposite color distributions due to the distinct microstructures. **Table 3** provides three specific optimal solutions.

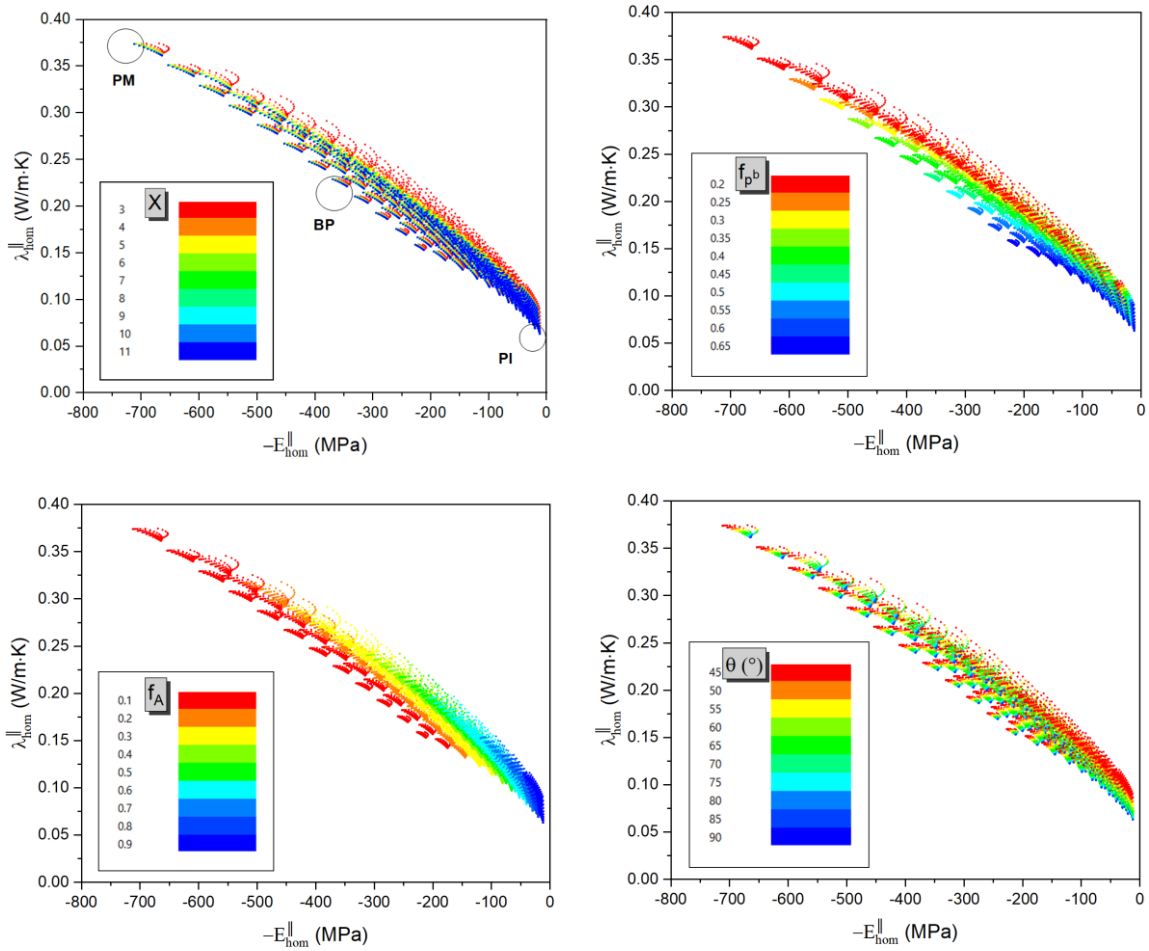

Fig. 6. Color-coded point distribution of objectives in BR.

3.3.3. BS

Fig. 7 illustrates the point distribution for the application BS. The points are arranged from the upper left to the lower right and their continuity is between BB and BF. The distribution for f_A and f_p^b is consistent with that observed in BB. For concrete with a priority on mechanical performance, it is recommended to take low values of f_p^b and f_A. For high thermal insulation concrete, the opposite is recommended. The color distribution of θ is the opposite of that observed in BB. Hence, high θ values are suggested in BS. The optimal solutions for this case are listed in **Table 3**.

The optimal point distribution shares some similarities across different applications. The large X value is the optimal solution for all cases although the lifting effect through X is weak. Moreover, the color maps of f_A are consistent across all three applications. The bio-aggregate volume fraction plays a crucial role in determining the mechanical properties of concrete. High bio-aggregate content often leads to inferior mechanical performance. The pursuit of improved strength presents opportunities for replacing traditional

construction materials in load-bearing structures. To achieve this, research should focus on a novel binder with enhancing mechanical properties and moderate micropores. Additionally, it is important to evaluate the environmental benefits of novel binders. These factors give possible directions for the experimental study.

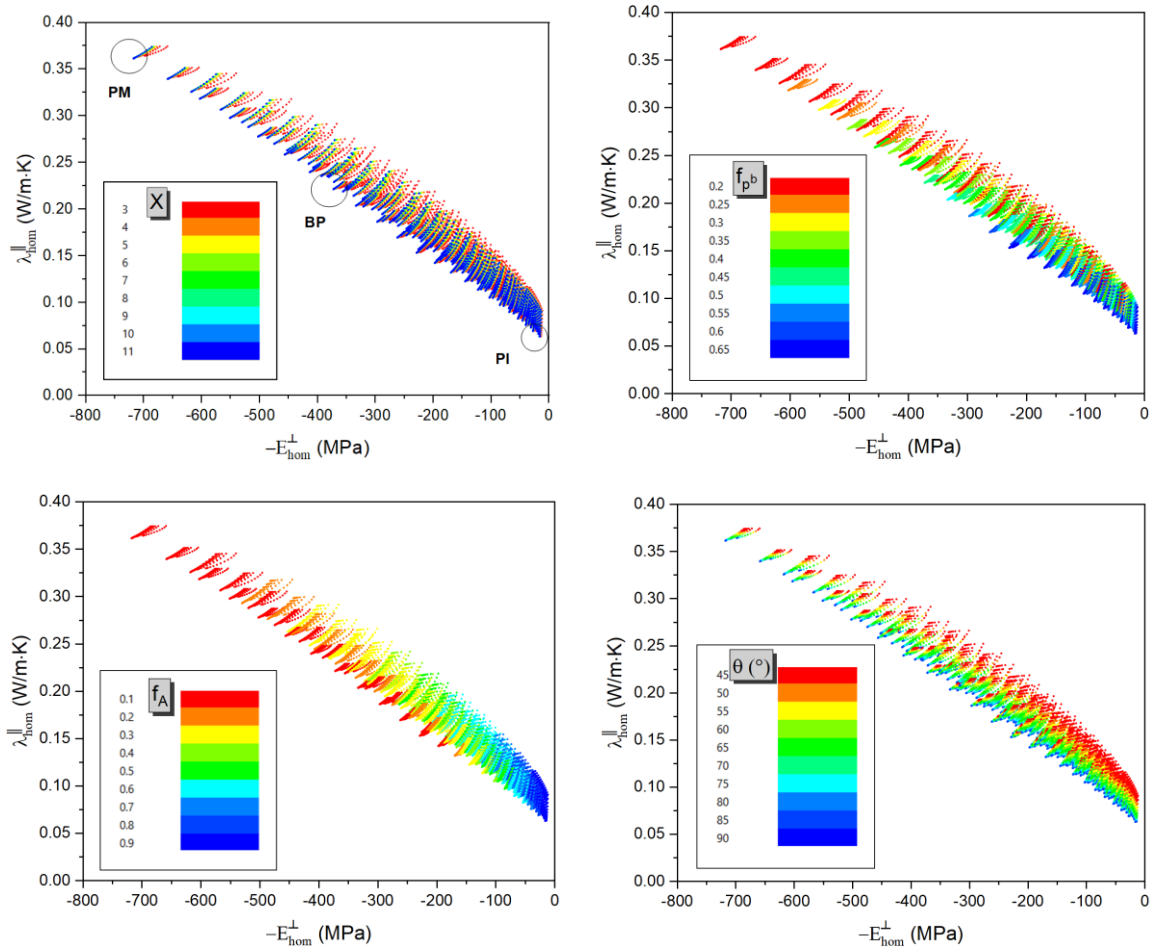

Fig. 7. Color-coded point distribution of objectives in BS.

3.4. Constraints on bio-aggregates

The volume fraction of bio-aggregates used in the formulations analyzed in Section 3.3 ranged from 0.1 to 0.9, which covers both structural and non-structural applications. However, recent laboratory formulations have primarily focused on non-structural applications, where the volume fraction of bio-aggregates is relatively high, such as 0.40, 0.46 [13]. Therefore, this section specifically examines cases where the volume fraction is greater than 0.4. **Fig. 8** shows the point distributions and Pareto fronts in high-volume bio-aggregates for BB, BF, and BS. The concrete with high-volume bio-aggregates has approximately the same point distribution as the general case but exhibits lower mechanical performance and better thermal insulation. As an example, comparing the PM points of BB for the two cases shows that high-volume bio-aggregates exhibit a 47% reduction in mechanical strength and a 12% improvement in thermal insulation.

Although formulations with high-volume bio-aggregate are typically used for non-load bearing structures and can lead to improved thermal insulation, increasing the fraction of bio-aggregate requires careful consideration of the resulting changes in mechanical properties.

The corresponding optimal solutions are listed in **Table 4**.

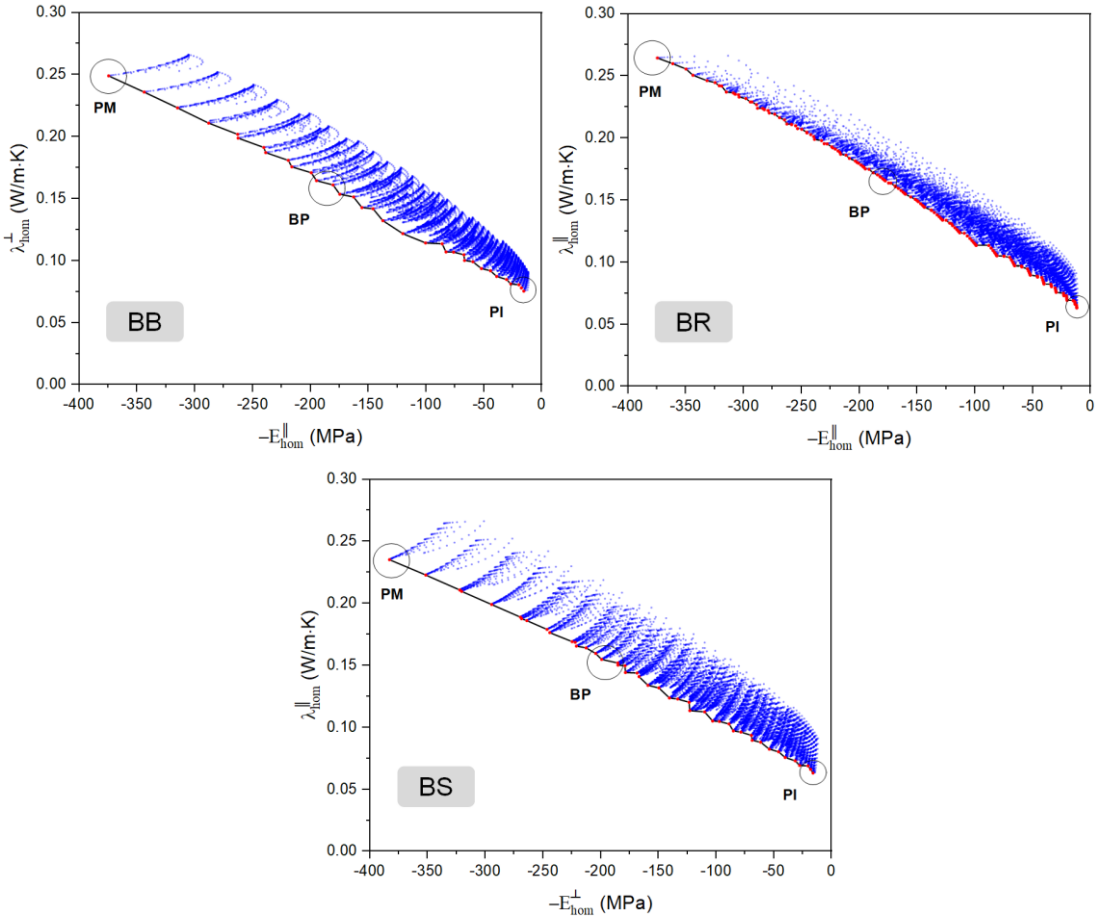

Fig. 8. Point distribution in high-volume bio-aggregates.

Table 4. Optimal solution in high-volume bio-aggregates.

Applications	Preferences	X	f_p^b	f_A	θ (º)	E (MPa)	λ (W/m·K)
BB	HM	11	0.20	0.39	45	375	0.25
	HT	11	0.45	0.46	45	180	0.16
	BP	11	0.65	0.90	45	16	0.08
BR	HM	11	0.20	0.39	45	375	0.26
	HT	11	0.45	0.39	78	180	0.17

	BP	11	0.65	0.90	90	12	0.06
BS	HM	11	0.20	0.39	90	383	0.24
	HT	11	0.45	0.46	90	185	0.15
	BP	11	0.65	0.90	90	16	0.06

3.5. Performance Constraints

Bio-based concrete is a building material that possesses superior thermal insulation and weak mechanical properties. Compared to commonly used building materials, bio-based concrete has an advantage in terms of thermal conductivity, which can reach about 0.06 W/m·K [13], while that of aerated concrete and hollow bricks is 0.22 and 0.26 W/m·K [14] (**Fig. 9**). Meanwhile, the modulus of elasticity for hemp concrete is typically between 32 to 95 MPa when used in moderate dosage [22]. Bio-based concretes with mechanical properties higher or lower than this range can be defined as high or low mechanical performance, respectively (**Fig. 9**). To limit the impact of these trade-offs, performance constraints are set at a thermal conductivity of 0.22 W/m·K and a modulus of 95 MPa.

The plot in **Fig. 9** shows three zones that represent different combinations of thermal insulation and mechanical performance. Zone 1 represents solutions that exhibit both high thermal insulation and improved mechanical performance, whereas Zone 2 represents improved mechanical performance and low thermal insulation, and Zone 3 shows high thermal insulation but weak mechanical performance. Given the

performance constraints, the optimal solutions from Zone 1 are selected. Accordingly, **Table 5** lists the three optimal solutions in this zone.

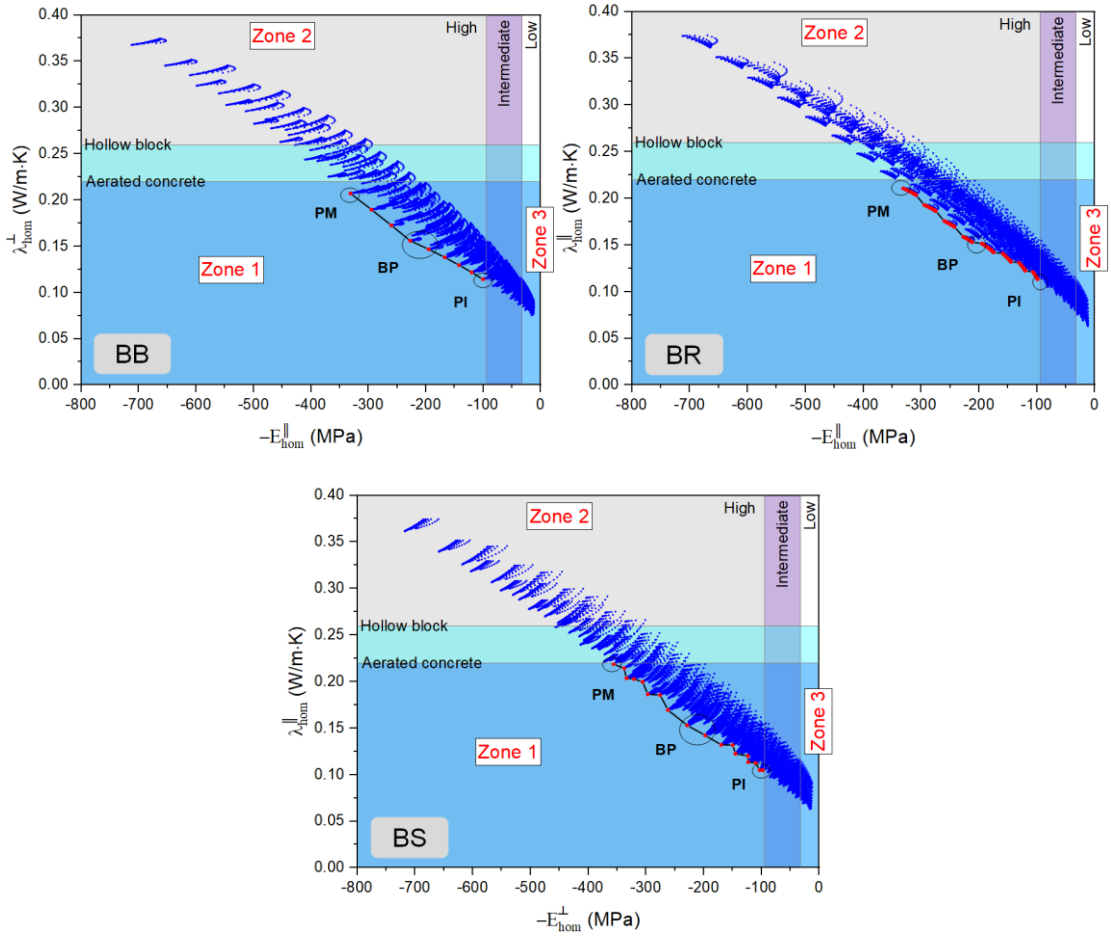

Fig. 9. Optimization under performance constraints.

Table 5. Optimal solution under performance constraints.

Applications	Preferences	X	f_p [b]	f_A	θ (º)	E (MPa)	λ (W/m·K)
BB	PM	11	0.53	0.10	45	331	0.21
	BP	11	0.65	0.10	45	227	0.16
	PI	11	0.65	0.46	45	100	0.11
BR	PM	11	0.53	0.10	45	331	0.21
	BP	11	0.65	0.10	90	212	0.15
	PI	11	0.65	0.39	90	99	0.11
BS	PM	11	0.45	0.17	90	356	0.22

BP	11	0.65	0.17	90	197	0.14
PI	11	0.61	0.54	90	97	0.10

3.6. Density constraint

Roof structures generally have a lower load-bearing capacity compared to other parts of a building. The utilization of bio-based materials in roofing systems must be meticulously designed to ensure that the structure can safely support the weight of the roofing material and any additional loads, such as snow or wind. The density of bio-based materials can vary depending on the specific formulation. The density of bio-based roofing does not exceed 300 kg/m^3 [43], making it a lightweight concrete. Therefore, this section sets the density constraint to 300 kg/m^3. The left side of **Fig. 10** shows the distribution of points in the decision space under the density constraint, where the lightweight zone and the decision space are marked in red and black. The optional range of the bio-based roofing occupies a small portion of the decision space, featuring outstanding thermal insulation and very low mechanical strength. Fortunately, bio-based roofing does not have a large load-bearing role, which allows the advantages of thermal insulation to be fully exploited in this case.

To further investigate the point distribution and the Pareto front, the lightweight Zone is magnified and displayed on the right side of **Fig. 10**. The variation of the Pareto front from PM to BP to PI shows a rapid decrease in mechanical performance, ending at 12 MPa. Hence, this weak bio-based roofing is often utilized with load-bearing frames (Tradical ® [44]). As a result, the optimal solutions for bio-based roofing within this density range are presented in **Table 6**.

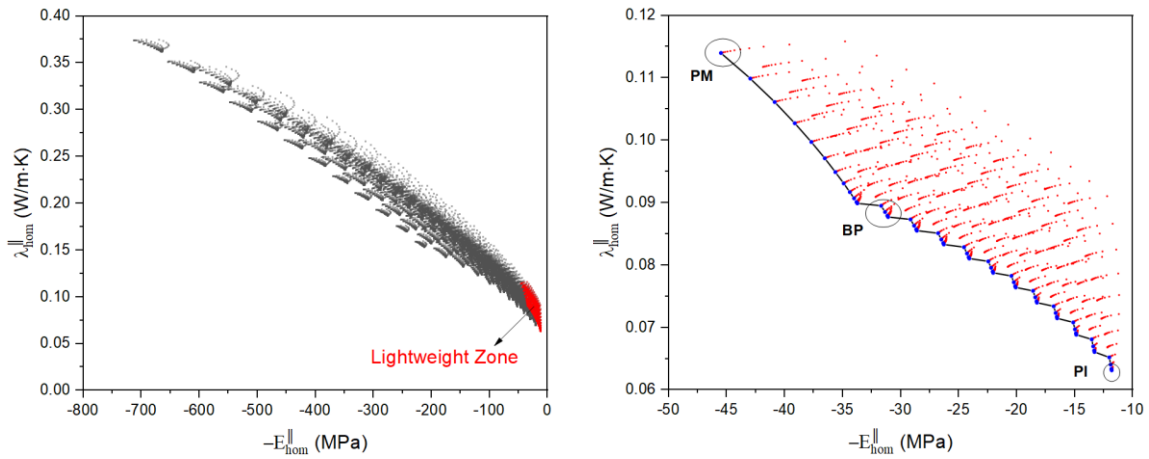

Fig. 10. Optimization of bio-based concrete for lightweight roofing.

Table 6. Optimal solution for lightweight roofing.

Preferences	X	f_p^b	f_A	θ (º)	E (MPa)	λ (W/m·K)
PM	11	0.20	0.90	45	45	0.11
BP	11	0.24	0.90	86	31	0.09
PI	11	0.65	0.90	90	12	0.06

3.7. Optimization in humid environments

The behavior of bio-based materials in humid environments is a crucial factor in their design. Bio-based concrete has a porous structure that results in a strong water absorption capacity [45], and several experimental studies [46,47] have demonstrated the significant influence of water content on thermal conductivity. Given that bio-based concrete structures may often be exposed to humid environments, it is essential to investigate the differences in multi-objective optimization under varying levels of humidity. This section explores three distinct water saturation levels: 0, 0.3, and 0.6, which respectively represent dry, low humidity, and high humidity building environments. Water saturation refers to the volume ratio of water to intra-particle pores.

As **Fig. 11** shows, the Pareto front gradually moves away from the origin with moisture in wet environments. Also, it is found that the differences of three Pareto fronts are minor from -800 to -200 MPa, but increased significantly from -200 MPa to 0 MPa. The curve's slope also decreased when the modulus was greater than -200 MPa, particularly for BB, as thermal conductivity decreased. These findings suggest that the decision variables have a more significant impact on mechanical performance than insulation properties in low-density concrete. Lower density concrete is more sensitive to humidity changes, whereas increasing

density can help resist the effects of changing humidity levels in the environment. It should be noted that this measure must meet the requirements of performance or density.

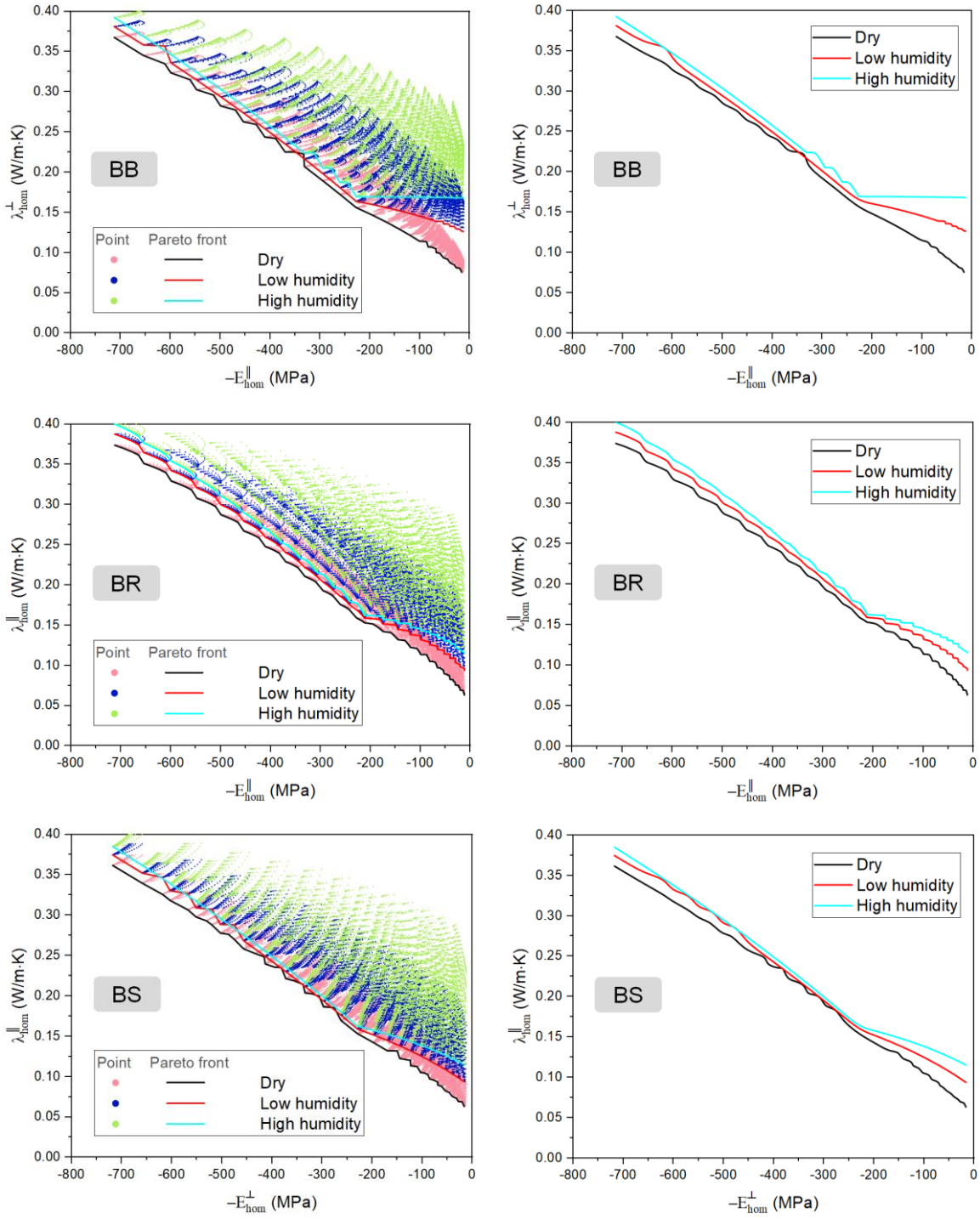

Fig. 11. Optimization of bio-based concrete under dry, low humidity, and high humidity conditions for three industrial applications.

3.8. Summary of optimal solutions for varied requirements

In this section, we provide a comprehensive summary of the optimal solutions obtained through multi-objective optimization for different requirements in bio-based concrete. The multi-objective optimization process was conducted separately for distinct sets of design requirements, including high-volume aggregates, higher performance requirements, and lightweight considerations. Addressing these specific requirements individually allowed designers to tailor the optimization strategies more effectively to meet the desired objectives.

Fig. 12 illustrates the distribution of objective values under the three different requirements. In the general case, the point distribution ranges from -800 to -11 MPa, while under the more specific requirements, the distribution ranges from -400 to -11 MPa. The thermal insulation properties of bio-based concrete play a crucial role in various applications. Moreover, there are overlapping regions between the high-volume aggregates area and the performance-oriented area, as well as between the lightweight area and the high-volume aggregates area. This indicates the possibility of optimal solutions that simultaneously meet both requirements. For example, optimal solutions satisfying both volume and performance can be found in the range of -330 to -100 MPa. Notably, around -105 MPa, the optimal solution aligns with the Pareto-optimal solutions for both requirements. Similarly, within the range of -45 to -11 MPa, the optimal solutions fulfill the requirements for lightweight and high volume. However, when comparing the lightweight and performance-oriented areas, no overlapping region is observed, suggesting a trade-off between these two requirements. It is worth mentioning that lightweight concrete is commonly utilized in applications such as roofs, where exceptional performance is not critically required.

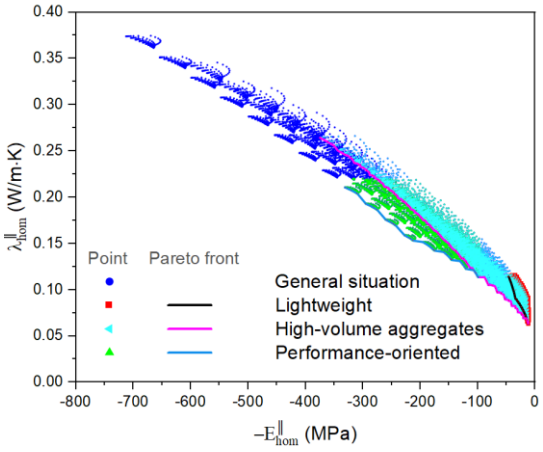

Fig. 12. Optimal solutions for varied requirements.

Furthermore, our study delved into optimizing bio-based concrete performance in humid environments. By incorporating environmental factors into the optimization process, we found that the optimal solution varies with ambient humidity, particularly in low-density concrete. Increasing the density of bio-based concrete contributes to

mitigating the impact of ambient humidity. These optimized solutions provide valuable insights for applications in regions characterized by high humidity levels or exposure to moisture.

Collectively, the multi-objective optimization results demonstrate the versatility and adaptability of bio-based concrete in meeting diverse design requirements. The tailored solutions offer designers a range of options to enhance mechanical strength, insulation properties, or achieve a balance between different performance aspects.

4. Conclusion

Bio-based concrete is gaining attention due to its excellent thermal insulation and eco-friendliness. Optimizing the properties of bio-based concrete facilitates the expansion of its application, especially considering the weak mechanical properties. However, single-objective optimization cannot meet the requirements of practical applications. To address this challenge, our previous study presented a novel multi-scale model for mechanical and thermal properties of bio-based concrete, which has been verified through comparison with finite element and experimental data. In this study, we applied the model to optimize the combined performance of bio-based concrete in terms of its mechanical and thermal insulation properties, using a multi-objective optimization approach customized for bio-based construction.

We identified three main industrial applications of bio-based concrete through a literature survey and developed three optimization strategies to optimize the performance of bio-based concrete for each application. The optimization included four decision variables, including aspect ratio, porosity, volume fraction, and orientation. The boundaries of the decision variables are given in the general case, i.e., the range of values in the reference and slightly beyond it. This can give more possibilities for formulation design. Correspondingly, we first performed the optimization in the general case and then extended it to more realistic situations, such as those involving high-volume bio-aggregates, more stringent performance requirements, low densities, and humid environments. Results showed that the optimal solution varied with each application and situation. As a key result, this study provided the optimal solutions for specific applications and requirements, as well as three preferences for improved mechanical performance, outstanding thermal insulation, and balanced performance, respectively. This gives different decision makers more flexibility in choosing the best option for their needs.

In conclusion, this study provides essential design parameters for optimizing the combined performance of bio-based concrete across various industrial applications, requirements, and preferences. This has the potential to enhance its practicality and maximize its contributions to reducing carbon and energy consumption in the construction industry.

CRediT authorship contribution statement

Gang Huang: Methodology, Software, Formal analysis, Investigation, Data Curation, Writing - Original Draft, Writing - Review & Editing, Visualization. **Ariane Abou-Chakra:** Conceptualization, Methodology,

Software, Validation, Resources, Writing - Review & Editing, Supervision. **Sandrine Geoffroy:** Conceptualization, Methodology, Validation, Writing - Review & Editing, Supervision, Project administration. **Joseph Absi:** Conceptualization, Methodology, Software, Validation, Writing - Review & Editing, Supervision.

Declaration of Competing Interest

The authors declare that they have no known competing financial interests or personal relationships that could have appeared to influence the work reported in this paper.

References

[1] Z. He, A. Shen, H. Wu, W. Wang, L. Wang, C. Yao, J. Wu, Research progress on recycled clay brick waste as an alternative to cement for sustainable construction materials, Construction and Building Materials. 274 (2021) 122113. https://doi.org/10.1016/j.conbuildmat.2020.122113.

[2] A. Jeanjean, R. Olives, X. Py, Selection criteria of thermal mass materials for low-energy building construction applied to conventional and alternative materials, Energy and Buildings. 63 (2013) 36–48. https://doi.org/10.1016/j.enbuild.2013.03.047.

[3] S. B., N. Patil, K.K. Jaiswal, T.P. Gowrishankar, K.K. Selvakumar, M.S. Jyothi, R. Jyothilakshmi, S. Kumar, Development of sustainable alternative materials for the construction of green buildings using agricultural residues: A review, Construction and Building Materials. 368 (2023) 130457. https://doi.org/10.1016/j.conbuildmat.2023.130457.

[4] M.S. Abbas, E. Gourdon, P. Glé, F. McGregor, M.Y. Ferroukhi, A. Fabbri, Relationship between hygrothermal and acoustical behavior of hemp and sunflower composites, Building and Environment. 188 (2021) 107462. https://doi.org/10.1016/j.buildenv.2020.107462.

[5] V. Nozahic, S. Amziane, Influence of sunflower aggregates surface treatments on physical properties and adhesion with a mineral binder, Composites Part A: Applied Science and Manufacturing. 43 (2012) 1837–1849. https://doi.org/10.1016/j.compositesa.2012.07.011.

[6] F. Benmahiddine, R. Cherif, F. Bennai, R. Belarbi, A. Tahakourt, K. Abahri, Effect of flax shives content and size on the hygrothermal and mechanical properties of flax concrete, Construction and Building Materials. 262 (2020) 120077. https://doi.org/10.1016/j.conbuildmat.2020.120077.

[7] R. Zerrouki, A. Benazzouk, M. Courty, H. Ben Hamed, Potential use of matakaolin as a partial replacement of preformulated lime binder to improve durability of hemp concrete under cyclic wetting/drying aging, Construction and Building Materials. 333 (2022) 127389. https://doi.org/10.1016/j.conbuildmat.2022.127389.

[8] G.M. Cappucci, V. Ruffini, V. Barbieri, C. Siligardi, A.M. Ferrari, Life cycle assessment of wheat husk based agro-concrete block, Journal of Cleaner Production. 349 (2022) 131437. https://doi.org/10.1016/j.jclepro.2022.131437.

[9] K. Ip, A. Miller, Life cycle greenhouse gas emissions of hemp–lime wall constructions in the UK, Resources, Conservation and Recycling. 69 (2012) 1–9. https://doi.org/10.1016/j.resconrec.2012.09.001.

[10] A. Galimshina, M. Moustapha, A. Hollberg, P. Padey, S. Lasvaux, B. Sudret, G. Habert, Bio-based materials as a robust solution for building renovation: A case study, Applied Energy. 316 (2022) 119102. https://doi.org/10.1016/j.apenergy.2022.119102.

[11] F. Pittau, F. Krause, G. Lumia, G. Habert, Fast-growing bio-based materials as an opportunity for storing carbon in exterior walls, Building and Environment. 129 (2018) 117–129. https://doi.org/10.1016/j.buildenv.2017.12.006.

[12] European Green Deal, (n.d.). https://climate.ec.europa.eu/eu-action/european-green-deal_en (accessed May 1, 2023).

[13] H.H. Ratsimbazafy, Évaluation du potentiel de co-produits agricoles locaux valorisables dans le domaine des matériaux de construction (PALOMAC), phdthesis, Université Paul Sabatier - Toulouse III, 2022. https://tel.archives-ouvertes.fr/tel-03699668 (accessed September 30, 2022).

[14] Y. Pan, L. Deng, S. Li, J. Wang, F. Zhang, A study using a combined method of scientometric and manual analysis to review the present research of plant fibres reinforced concrete, Construction and Building Materials. 341 (2022) 127551. https://doi.org/10.1016/j.conbuildmat.2022.127551.

[15] T. Jami, S.R. Karade, L.P. Singh, A review of the properties of hemp concrete for green building applications, Journal of Cleaner Production. 239 (2019) 117852. https://doi.org/10.1016/j.jclepro.2019.117852.

[16] H. Wadi, S. Amziane, E. Toussaint, M. Taazount, Lateral load-carrying capacity of hemp concrete as a natural infill material in timber frame walls, Engineering Structures. 180 (2019) 264–273. https://doi.org/10.1016/j.engstruct.2018.11.046.

[17] M.R. Ahmad, B. Chen, S.F. Ali Shah, Mechanical and microstructural characterization of bio-concrete prepared with optimized alternative green binders, Construction and Building Materials. 281 (2021) 122533. https://doi.org/10.1016/j.conbuildmat.2021.122533.

[18] J. Williams, M. Lawrence, P. Walker, The influence of constituents on the properties of the bio-aggregate composite hemp-lime, Construction and Building Materials. 159 (2018) 9–17. https://doi.org/10.1016/j.conbuildmat.2017.10.109.

[19] J. Williams, M. Lawrence, P. Walker, A method for the assessment of the internal structure of bio-aggregate concretes, Construction and Building Materials. 116 (2016) 45–51. https://doi.org/10.1016/j.conbuildmat.2016.04.088.

[20] L. Liu, S. Zou, H. Li, L. Deng, C. Bai, X. Zhang, S. Wang, N. Li, Experimental physical properties of an eco-friendly bio-insulation material based on wheat straw for buildings, Energy and Buildings. 201 (2019) 19–36. https://doi.org/10.1016/j.enbuild.2019.07.037.

[21] A. Jain, Micro and mesomechanics of fibre reinforced composites using mean field homogenization formulations: A review, Materials Today Communications. 21 (2019) 100552. https://doi.org/10.1016/j.mtcomm.2019.100552.

[22] V. CEREZO, Propriétés mécaniques, thermiques et acoustiques d'un matériau à base de particules végétales : approche expérimentale et modélisation théorique, These de doctorat, INSA Lyon, 2005. https://www.theses.fr/2005ISAL0037.

[23] F. Collet, S. Pretot, Thermal conductivity of hemp concretes: Variation with formulation, density and water content, Construction and Building Materials. 65 (2014) 612–619. https://doi.org/10.1016/j.conbuildmat.2014.05.039.

[24] A. Djoudi, M.M. Khenfer, A. Bali, T. Bouziani, Effect of the addition of date palm fibers on thermal properties of plaster concrete: experimental study and modeling, Journal of Adhesion Science and Technology. 28 (2014) 2100–2111. https://doi.org/10.1080/01694243.2014.948363.

[25] S. Dartois, S. Mom, H. Dumontet, A. Ben Hamida, An iterative micromechanical modeling to estimate the thermal and mechanical properties of polydisperse composites with platy particles: Application to anisotropic hemp and lime concretes, Construction and Building Materials. 152 (2017) 661–671. https://doi.org/10.1016/j.conbuildmat.2017.06.181.

[26] G. Huang, A. Abou-Chakra, J. Absi, S. Geoffroy, Optimization of mechanical properties in anisotropic bio-based building materials by a multiscale homogenization model, Journal of Building Engineering. 57 (2022) 104890. https://doi.org/10.1016/j.jobe.2022.104890.

[27] G. Huang, A. Abou-Chakra, S. Geoffroy, J. Absi, A multiscale homogenization model on thermal conductivity of bio-based building composite considering anisotropy, imperfect interface and moisture, Construction and Building Materials. 377 (2023) 131156. https://doi.org/10.1016/j.conbuildmat.2023.131156.

[28] T. Mori, K. Tanaka, Average stress in matrix and average elastic energy of materials with misfitting inclusions, Acta Metallurgica. 21 (1973) 571–574. https://doi.org/10.1016/0001-6160(73)90064-3.

[29] C.A.C. Coello, G.B. Lamont, Applications of Multi-Objective Evolutionary Algorithms, World Scientific Publishing Company, Hackensack, NJ, 2004.

[30] D.E. Golberg, Genetic algorithms in search, optimization, and machine learning, Addion Wesley. 1989 (1989) 36.

[31] V. Pareto, Manual of Political Economy: A Critical and Variorum Edition, OUP Oxford, 2014.

[32] M.P. Sáez-Pérez, M. Brümmer, J.A. Durán-Suárez, A review of the factors affecting the properties and performance of hemp aggregate concretes, Journal of Building Engineering. 31 (2020) 101323. https://doi.org/10.1016/j.jobe.2020.101323.

[33] S. Barbhuiya, B. Bhusan Das, A comprehensive review on the use of hemp in concrete, Construction and Building Materials. 341 (2022) 127857. https://doi.org/10.1016/j.conbuildmat.2022.127857.

[34] J. Kaufmann, K. Frech, P. Schuetz, B. Münch, Rebound and orientation of fibers in wet sprayed concrete applications, Construction and Building Materials. 49 (2013) 15–22. https://doi.org/10.1016/j.conbuildmat.2013.07.051.

[35] P. Glé, T. Lecompte, A. Hellouin de Ménibus, H. Lenormand, S. Arufe, C. Chateau, V. Fierro, A. Celzard, Densities of hemp shiv for building: From multiscale characterisation to application, Industrial Crops and Products. 164 (2021) 113390. https://doi.org/10.1016/j.indcrop.2021.113390.

[36] S. Arufe, A. Hellouin de Menibus, N. Leblanc, H. Lenormand, Physico-chemical characterisation of plant particles with potential to produce biobased building materials, Industrial Crops and Products. 171 (2021) 113901. https://doi.org/10.1016/j.indcrop.2021.113901.

[37] M. Lagouin, C. Magniont, P. Sénéchal, P. Moonen, J.-E. Aubert, A. Laborel-préneron, Influence of types of binder and plant aggregates on hygrothermal and mechanical properties of vegetal concretes, Construction and Building Materials. 222 (2019) 852–871. https://doi.org/10.1016/j.conbuildmat.2019.06.004.

[38] M. Arandigoyen, J.I. Alvarez, Pore structure and mechanical properties of cement–lime mortars, Cement and Concrete Research. 37 (2007) 767–775. https://doi.org/10.1016/j.cemconres.2007.02.023.

[39] T. Pierre, M. Carin, Characterization of the thermal properties of millimeter-sized insulating materials, International Journal of Thermal Sciences. 135 (2019) 247–255. https://doi.org/10.1016/j.ijthermalsci.2018.09.009.

[40] A.D. Tran-Le, S.-T. Nguyen, T. Langlet, A novel anisotropic analytical model for effective thermal conductivity tensor of dry lime-hemp concrete with preferred spatial distributions, Energy and Buildings. 182 (2019) 75–87. https://doi.org/10.1016/j.enbuild.2018.09.043.

[41] The Engineering ToolBox, Water - Thermal Conductivity vs. Temperature, (n.d.). https://www.engineeringtoolbox.com/water-liquid-gas-thermal-conductivity-temperature-pressure-d_2012.html (accessed May 19, 2022).

[42] The Engineering ToolBox, Air - Thermal Conductivity vs. Temperature and Pressure, (n.d.). https://www.engineeringtoolbox.com/air-properties-viscosity-conductivity-heat-capacity-d_1509.html?vA=20&degree=C&pressure=1bar# (accessed February 16, 2023).

[43] S. Mom, Modèle d'homogénéisation itérative numérique pour des milieux non linéaires morphologiquement riches : application aux comportements de bétons de chanvre, These de doctorat, Paris 6, 2013. https://www.theses.fr/2013PA066558 (accessed December 16, 2022).

[44] How to Insulate a Roof ?, Weber Tradical. (n.d.). https://www.weber-tradical.com/en/hempcrete/beton-de-chanvre-toiture-isolante/ (accessed December 12, 2022).

[45] F. Wu, Q. Yu, C. Liu, H.J.H. Brouwers, L. Wang, Effect of surface treatment of apricot shell on the performance of lightweight bio-concrete, Construction and Building Materials. 229 (2019) 116859. https://doi.org/10.1016/j.conbuildmat.2019.116859.

[46] M. Rahim, O. Douzane, A.D. Tran Le, T. Langlet, Effect of moisture and temperature on thermal properties of three bio-based materials, Construction and Building Materials. 111 (2016) 119–127. https://doi.org/10.1016/j.conbuildmat.2016.02.061.

[47] M.R. Ahmad, B. Chen, M.A. Haque, S.M. Saleem Kazmi, M.J. Munir, Development of plant-concrete composites containing pretreated corn stalk bio-aggregates and different type of binders, Cement and Concrete Composites. 121 (2021) 104054. https://doi.org/10.1016/j.cemconcomp.2021.104054.

Conclusions and perspectives

This thesis aims to propose a multi-scale homogenization model for predicting and optimizing the mechanical and thermal properties of bio-based concrete. This objective is achieved in two steps: the first step proposes separate models for the mechanical and thermal properties, while the second step combines the two models through a multi-objective optimization approach.

Both models are based on the multiscale microstructure of bio-based concrete and consider several factors such as the volume fraction of each phase, the shape and orientation of the bio-aggregate, and pores. Additionally, the mechanical model takes into account the mechanical properties of the binder, while the thermal model considers imperfect contact and moisture. These additional factors have been shown in previous experimental studies to significantly influence the performance of individual objective.

The mechanical behavior of bio-based concrete is influenced by several factors, as revealed by the parametric study. These include E-Binder, volume fraction, orientation, shape ($R < 8$), shape ($R > 8$), and E-Aggregate, in order of decreasing impact. upgrading the binder and reducing aggregate volume fraction are two significant ways to enhance the mechanical properties of bio-based concrete. Further investigations showed that orientation optimization, achieved by increasing the level of compaction, is beneficial for low aspect ratios (such as sunflower pith and maize). The volume fraction has a similar effect regardless of high or low aspect ratios. Moreover, for high volume bio-aggregates, the optimization potential in terms of shape and orientation is significant. This can be explained by the cumulative influence of plant fibers. In this case, a 32% increase in the modulus perpendicular to the compaction direction can be achieved through shape and orientation optimization for a given component characteristic.

Bio-based concrete is used in buildings mainly due to its high thermal insulation. Its thermal conductivity is related to volume fraction, porosity, shape, orientation, imperfect contact, and moisture. The thermal conductivity of hemp and bio-based construction material increases with water saturation in both parallel and perpendicular directions. However, the parallel thermal conductivity of hemp increases linearly with water saturation, whereas that of bio-based materials increases nonlinearly.

Regarding the effect of inclusion shape on thermal conductivity, three shapes were investigated: length/width = 2, 4, and 10. The results show that for bio-based materials, the thermal conductivity is almost independent of shape in the direction of compaction. However, in the direction perpendicular to compaction, the thermal conductivity at low length/width is lower than that of other shapes, and the difference increases with water saturation.

The anisotropy of bio-based materials is a non-negligible feature, which leads to mechanical and thermal properties that exhibit large differences horizontally and vertically. Due to the compaction or spraying of the process, the plant fibers tend to be distributed in a direction perpendicular to the compaction or spraying. The average angle of the fibers depends on the degree of compaction or spraying during the construction process. Heavy compaction leads to unidirectional optimal mechanical properties for a constant mixture, while moderate compaction achieves balanced optimal mechanical properties in all directions.

The slender structure of the individual fibers also increases the anisotropy of the concrete in terms of thermal conductivity. The thermal conductivity of the fibers is greater in the axial direction than in the transverse direction. Based on the analysis of plant fiber orientation, it can be observed from the finite element analysis that heat tends to flow axially along the fiber rather than transversely across it. The heat flux on the fiber decreases as the angle (acute angle) between the fiber and the initial heat flow increases. This behavior can be attributed to the transversely isotropic structure of the plant fibers. Moreover, the anisotropy of both individual fiber and bio-based construction material initially increases, reaches a maximum of approximately 0.4 water saturation, and then decreases with further water saturation. Anisotropy decreases as the scale increases from pore-moisture, to bio-aggregate, to concrete.

The comparison of finite element models, analytical models, and experimental data from the literature showed a high agreement across various scales and cases.

Although the multiscale model for bio-based concrete performs well in terms of individual mechanical and thermal properties, practical applications often require an overall performance of the material. To address this need, a multi-objective optimization method was proposed to simultaneously consider both mechanical performance and thermal insulation. The optimization involves four decision variables: shape, porosity, volume fraction, and orientation, and two optimization objectives: high mechanical performance and thermal insulation. The distribution of points in the two objectives suggests that the combined performance of the material is more sensitive to the decision variables at low densities.

Since optimization schemes for bio-based concrete should correspond to different industrial applications, three optimization strategies based on the classification of structural were proposed for three different industrial applications: bio-based blocks or wall filling materials, bio-based roofs, and bio-based shotcrete. Sensitivity analysis reveals that the optimal solutions with respect to the decision variables differ for the three industrial applications, confirming the need for classification of optimization strategies.

To provide more flexibility for the formulation design of bio-based concrete, we also give the optimal solution for the general case, which involves a larger range of values for the decision variables. This can provide a better perspective to analyze the impact of decision variables on the overall performance. However,

practical applications may have specific requirements, such as more demanding performance, high-volume bio-aggregates, low density roofs, and humid environments. Corresponding constraints for these specific requirements were developed for optimization, and optimal solutions were subsequently given.

The optimal solution in a multi-objective optimization problem is a solution set, namely a Pareto solution set. There is no difference in quality between the optimal solutions in the set. For bio-based concrete, we divide the Pareto solution set into three specific cases: high mechanical performance, high thermal insulation, and balanced performance, providing practitioners with more options in actual construction.

The findings presented in this thesis provide valuable insights into the prediction and optimization of bio-based concrete for practical applications. By providing a better understanding of the material's properties and a multi-objective optimization approach for improving its overall performance, this research has the potential to advance the development of such sustainable and eco-friendly materials, and could ultimately contribute to the reduction of carbon emissions in the construction industry.

There are still some aspects that could be improved in future work. Specifically, for the shape and orientation of bio-aggregates, this model used an effective fiber aspect ratio and orientation to simplify the calculations. Although these values were derived from length and width distribution curves from image analysis, and orientation distribution curves from X-ray tomography, a more realistic distribution would be closer to reality. Thus, future work could consider incorporating real distributions directly into the model. Moreover, this study only focused on the linear mechanical behavior of bio-based concrete, and future work could expand upon this by modeling its nonlinear mechanical properties through analytical or numerical approaches. This would allow for a more comprehensive understanding of the material's behavior under varying loads and conditions. Fracture, shrinkage, and creep behavior of bio-based concrete are also potential topics that need to be investigated. Furthermore, carbon emissions and energy consumption throughout the entire lifecycle are supplementary to objectives of mechanical and thermal performance, which can lead to a more comprehensive optimization.